nagra.

TECHNICAL REPORT 23-02 Rev. 1

The Geochemical Evolution of the HLW Repository Near-Field

September 2024

Nagra | National Cooperative for the Disposal of Radioactive Waste
Hardstrasse 73 | 5430 Wettingen | Switzerland
T. +41 56 437 11 11 | info@nagra.ch | nagra.ch

nagra.

TECHNICAL REPORT 23-02 Rev.1

The Geochemical Evolution of the HLW Repository Near-Field

September 2024

Nagra | **National Cooperative for the Disposal of Radioactive Waste**
Hardstrasse 73 | 5430 Wettingen | Switzerland
T. +41 56 437 11 11 | info@nagra.ch | nagra.ch

The report "The Geochemical Evolution of the HLW Repository Near-Field" has been elaborated by E. Curti[1], T. Thoenen[1], G. Kosakowski[1], B. Baeyens[1], L.R. Van Loon[1], O.X. Leupin[2] & L. Martin[2].

[1]Paul Scherrer Institute
[2]Nagra

This report has been revised due to findings made during the course of the project development. As a result, certain formulations have been adjusted to reflect updated information and ensure consistency across the reports. In documents published before September 2024, this document is referenced as Curti et al. (2023).

ISSN 1015-2636

Abstract

This report addresses the chemical processes occurring during the spatial-temporal evolution of the HLW repository near-field in the Opalinus Clay formation. It represents an update of a previous report (Bradbury et al. 2014) and is part of the documentation for the general licence application.

The HLW near-field is understood to be the multicomponent system of engineered barriers in the repository drifts after sealing and closure, as well as the adjacent host rock. According to the provisional design, the barriers consist of a HLW disposal canister (for spent fuel or reprocessed high-level waste), made of a carbon-steel, compacted bentonite as buffer, the drift support structure made of concrete materials, and the surrounding Opalinus Clay host rock. In the presence of water or water vapour, the various near-field components will chemically interact with one another, potentially modifying the material properties and their functionality. It is therefore required to identify and evaluate the effects of such chemical near-field interactions during the entire period of assessment, which is one million years according to regulatory requirements.

The report is structured as a series of chapters dedicated to specific topics. After a general introduction (Chapter 1), a preliminary part (Chapter 2 – Section 5.1) presents descriptions of the key properties, initial states and thermal evolution of the intact HLW near-field. The geometry and functions of the various components are described along with the expected geochemical and geomechanical evolution of the HLW repository system. This part also includes an overview of the initial states of the chemical composition of engineered barrier materials and the reacting porewater. This is followed by a discussion, based on model calculations of the predicted post-closure temperature evolution.

The following part (Sections 5.2 – 9.4) focuses on the chemical evolution and mutual interactions between the components in the repository near-field (mineralogical changes, evolution of the porewater chemistry, effects on radionuclide solubility/sorption properties and functionality of the engineered barriers, particularly the bentonite buffer). Sections 5.2 – 5.4 discuss the effects of temperature on the mineral stability, radionuclide retention and diffusivities in bentonite. Based on experimental data and reactive transport models, Chapter 6 describes the chemical interactions between the tunnel support structure, Opalinus Clay and bentonite buffer. In Chapter 7, bentonite porewater compositions and characteristics (pH, Eh, ionic strength) are modelled and discussed. Chapter 8 is devoted to the chemical interactions at the bentonite/canister interface under water-saturated conditions, with the focus on the impact of formation of Fe-silicates onto the buffer function. In Chapter 9, chemical conditions inside a failed canister are modelled, assuming fully saturated conditions. Moreover, the potential influence of boron released via dissolution of vitrified waste on the solubility of dose-relevant radionuclides is assessed. Finally, Chapter 10 provides a summary of the entire report and the main conclusions relevant to the performance assessment. These are also briefly summarised in the following paragraphs.

Compared to Stage 2 of the Sectoral Plan, the updated calculations of the thermal evolution in the HLW repository section predict higher transient temperatures for longer periods. Temperatures slightly exceeding 100 °C are predicted across the entire bentonite section over several hundred years. At 10,000 years after repository closure, temperatures in the bentonite are predicted to be in the range of ~ 55 °C, the temperatures in the undisturbed host-rock ~ 47 °C. In contrast, the scenario discussed in the previous report (Bradbury et al. 2014) assumed a shallower repository depth, and the near-field was also predicted to be close to thermal equilibrium with the undisturbed host rock. Despite the slightly higher temperatures compared to the previous study, it could be concluded, based on ample experimental evidence from laboratory tests and natural analogues, that mineralogical transformations in the bentonite due to illitisation or the supply of

dissolved iron from the corroding canisters will remain limited. A consequent loss of the buffer functionality due to reduced swelling capacity and modification of radionuclide retention/ diffusion properties can be excluded.

Updated reactive transport calculations to simulate the mineral and porewater evolution at the interfaces of the cementitious drift support structure with the Opalinus Clay and bentonite indicate similar results to those presented in Bradbury et al. (2014). Specifically, alteration zones in the clay do not exceed 10 – 20 cm on either side, and the total amount of dissolved clay minerals is predicted to be small at the end of the simulation time (50,000 years). The predicted precipitation of secondary minerals will reduce porosity within both clay domains close to the interfaces. Moreover, the simulations predict that alkaline water (pH > 9) from the tunnel support moving towards bentonite and Opalinus Clay will propagate no more than 10 cm from the respective interfaces and will not move further after around 100,000 years. Eventually, near-neutral conditions (pH ~ 8) will be reached across the entire section (bentonite – tunnel support – Opalinus Clay).

The geochemical "ClaySor" model, which follows a "classical" thermodynamic approach, was applied to predict composition and characteristics of porewaters in equilibrium with compacted bentonite. This serves as a basis for determining solubility limits and sorption coefficients of considered dose-relevant radionuclides for the safety assessment. The model takes into account cation exchange reactions in the interlayer of montmorillonite, protonation/deprotonation of amphoteric surface sites and dissolution/precipitation of reactive minor minerals. Despite wide but still realistic variations of key input parameters, such as bentonite dry density, initial occupancies of amphoteric surface sites, and pCO_2, the results show narrow ranges of dissolved element concentrations, Eh values (-227 to -135 mV) and pH values (6.8 to 7.5). The low sensitivity of the results is explained by robust internal chemical buffering mechanisms, specifically carbonate and Fe(II)-Fe(III) mineral equilibria in conjunction with cation exchange.

Thermodynamic equilibrium calculations were also carried out to predict the chemical conditions inside the carbon steel canister after breaching and intrusion of bentonite porewater. Two cases were calculated, representing the initial and advanced stages of canister degradation. The former case leads to a mildly alkaline, strongly reduced (pH = 8.4, Eh = -495 mV) hydrogen-rich water, while the calculation representative of advanced degradation conditions produces a nearly neutral, moderately reducing hydrogen-poor water (pH = 7.2, Eh = -222 mV).

Based on the above model, the effect of boron release due to dissolution of the vitrified waste on complexation/solubility of radionuclides, as well as on pH, was evaluated. The results indicate that the strongest borate complexes should be formed with cations of transition metals (Fe and Ni). Depending on the pH, cations of alkaline-earth metals (Mg, Ca, Sr, Ba, Ra) and of trivalent actinides (Am, Cm) could also form borate complexes to a limited extent. In contrast, monovalent (Na, Cs, K) and tetravalent to hexavalent cations (U, Np, Pu, Tc) should not form borate complexes in significant concentrations. Overall, the results indicate that the effect of borate complexation and local pH increase induced by the dissolution of borosilicate glass on the solubility limits of dose-relevant radionuclides will be negligible.

Zusammenfassung

Dieser Bericht befasst sich mit den chemischen Prozessen, die sich während der räumlich-zeitlichen Entwicklung des Nahfelds des Lagerteils für hochaktive Abfälle (HAA) des von der Nagra im Opalinuston geplanten Tiefenlager abspielen. Er stellt eine Aktualisierung eines früheren Berichts dar (Bradbury et al. 2014) und ist Teil der Dokumentation für das Rahmenbewilligungsgesuch.

Unter HAA-Nahfeld versteht man das geologische und technische Mehrfachbarrierensystem nach Versiegelung und Verschluss der Tiefenlagerstollen, sowie das angrenzende Wirtgestein. Gemäss der beispielhaften Umsetzung des Lagerkonzepts besteht das HAA Nahfeld aus dem Abfallgebinde (für abgebrannte Brennelemente oder verglaste hochaktive Abfälle), das wiederum von einem Endlagerbehälter aus Karbonstahl umschlossen wird, dem Verfüllmaterial aus verdichtetem Bentonit, dem Stollenausbau aus Betonmaterialien und das umgebende Wirtgesteins (Opalinuston). Die Präsenz von Wasser oder Wasserdampf verursacht zwischen den verschiedenen Nahfeldkomponenten chemische Wechselwirkungen, was potenziell Auswirkungen auf die Materialeigenschaften und ihre Funktionalität haben kann. Daher ist es notwendig, die Auswirkungen solcher chemischer Nahfeldwechselwirkungen während des gesamten für den Sicherheitsnachweis relevanten Zeitraums zu identifizieren und zu bewerten. Gemäss regulatorischen Anforderungen beträgt diese Zeitspanne eine Million Jahre.

Der Bericht ist in Kapiteln gegliedert, die jeweils spezifischen Themen gewidmet sind. Auf die generelle Einleitung (Kapitel 1) folgt ein einführender Teil (Kapitel 2 – Abschnitt 5.1), der die wichtigsten Eigenschaften, Ausgangszustand und Temperaturentwicklung des intakten HAA-Nahfelds beschreibt. Geometrie und Funktionen der verschiedenen Komponenten werden zusammen mit der erwarteten geochemischen und geomechanischen Entwicklung des HAA-Tiefenlagersystems beschrieben. Dieser Teil des Berichts vermittelt auch einen Überblick über die anfängliche chemische Zusammensetzung der für die technischen Barrieren verwendeten Materialien sowie des Porenwassers. Es folgt eine auf Modellrechnungen basierende Diskussion der Temperaturentwicklung im Nahfeld während der Nachverschlussphase des Tiefenlagers.

Der Fokus des folgenden Teils (Abschnitte 5.2 – 9.4) liegt auf der chemischen Entwicklung sowie den gegenseitigen Wechselwirkungen der HAA-Tiefenlager-Nahfeldkomponenten (mineralogische Veränderungen, Entwicklung der Porenwasserchemie, Auswirkungen auf die Löslichkeit/Sorptionseigenschaften von Radionukliden und die Funktionalität der technischen Barrieren, insbesondere der Bentonitverfüllung). In den Abschnitten 5.2 – 5.4 werden die Auswirkungen der Temperatur auf Mineralstabilität, Radionuklidretention und deren Diffusionskoeffizienten im Bentonit erörtert. Kapitel 6 beschreibt anhand experimenteller Daten und reaktiver Transportmodelle die chemischen Wechselwirkungen zwischen Tunnelausbau, dem Opalinuston und der Bentonit-Verfüllung. In Kapitel 7 werden die Zusammensetzung und weitere Eigenschaften des Bentonit-Porenwassers (pH, Eh, Ionenstärke) modelliert und diskutiert. Kapitel 8 ist den chemischen Wechselwirkungen an der Grenzfläche zwischen dem Bentonit und dem Endlagerbehälter im wassergesättigten System gewidmet, wobei der Schwerpunkt auf dem Einfluss der Bildung von eisenhaltigen Silikaten auf der Bentonitverfüllung liegt. In Kapitel 9 werden die chemischen Bedingungen innerhalb des wassergesättigten Endlagerbehälters (nach dessen Versagen) modelliert. Darüber hinaus wird der potenzielle Einfluss von durch Auflösung verglaster Abfälle freigesetztem Bor auf die Löslichkeit dosisrelevanter Radionuklide evaluiert. Abschliessend bietet Kapitel 10 eine ausführliche Zusammenfassung des gesamten Berichts mit den wichtigsten für die Sicherheitsanalyse relevanten Schlussfolgerungen. Letztere werden auch in den folgenden Absätzen kurz zusammengefasst.

Im Vergleich zur Studie von Bradbury et al. (2014) sagen die aktualisierten Berechnungen zur thermischen Entwicklung im HAA-Lagerteil höhere und länger dauernde Übergangstemperaturen voraus. Für die gesamte Bentonitverfüllung werden über mehrere Jahrhunderte hinweg Temperaturen von etwas über 100 °C vorhergesagt. Nach 10'000 Jahre nach Verschluss des Tiefenlagers werden im Bentonit höhere Temperaturen (~ 55 °C) als im ungestörten Wirtgestein (~ 47 °C) vorhergesagt. Im Gegensatz dazu basierte das frühere Szenario, dokumentiert in Bradbury et al. (2014), auf der Annahme, dass das Tiefenlager in einer geringeren Tiefe gebaut wird, sowie auf der sich daraus ergebenden Vorhersage, dass das Nahfeld zu diesem Zeitpunkt thermisch nahezu im Gleichgewicht mit dem ungestörtem Wirtgestein liegt. Trotz der höheren Temperaturen im Vergleich zu Vorstudie konnte auf der Grundlage zahlreicher experimenteller Daten aus Labortests und Naturanaloga der Schluss gezogen werden, dass mineralogische Umwandlungen im Bentonit, sei es durch Illitisierung oder Zufuhr von gelöstem Eisen aus den korrodierenden Behältern, begrenzt bleiben werden. Ein daraus entstehender Verlust der Funktionalität der Verfüllung durch eine verringerte Quellfähigkeit oder durch veränderte Eigenschaften der Radionuklidrückhaltung, bzw. der Diffusion kann ausgeschlossen werden.

Aktualisierte reaktive Transportberechnungen zur Simulation der Mineral- und Porenwasserentwicklung an den Grenzflächen zwischen dem zementhaltigen Stollenausbau und dem Opalinuston sowie dem Bentonit zeigen ähnliche Ergebnisse wie im Bericht von Bradbury et al. (2014). Insbesondere sind die Alterationszonen im angrenzenden Ton auf beiden Seiten maximal 10 – 20 cm dick, und am Ende der Simulationszeit (50'000 Jahre) ist die Gesamtmenge der gelösten Tonminerale gering. Die vorhergesagte Ausfällung von Sekundärmineralen führt zu einer Verringerung der Porosität in beiden Tondomänen in der Nähe der Grenzflächen zum Tunnelausbau. Darüber hinaus prognostizieren die Simulationen, dass sich alkalisches Wasser (pH > 9) vom Tunnelausbau aus in Richtung Bentonit und Opalinuston weniger als 10 cm ausbreiten und sich nach etwa 100,000 Jahren nicht mehr weiter verschieben wird. Schliesslich werden im gesamten Abschnitt (Bentonit – Tunnelausbau – Opalinuston) nahezu neutrale Bedingungen (pH ~ 8) erreicht.

Das geochemische Modell «ClaySor», das einem «klassischen» thermodynamischen Ansatz folgt, wurde angewendet, um die Zusammensetzung und Eigenschaften von Porenwässern im Gleichgewicht mit verdichtetem Bentonit vorherzusagen. Dies dient als Grundlage für die Bestimmung von Löslichkeitslimiten und Sorptionskoeffizienten der zu betrachtenden dosisrelevanten Radionuklide für die Sicherheitsanalyse. Das Modell berücksichtigt Kationen-Austauschreaktionen in der Zwischenschicht von Montmorillonit, die Protonierung/Deprotonierung amphoterer Oberflächenstellen und die Auflösung/Ausfällung reaktiver Minerale. Trotz grosser, doch immer noch realistischer Variationen wichtiger Parameter wie die Bentonit-Trockendichte, die Anfangsbelegung amphoterer Oberflächenstellen und pCO_2, zeigen die Ergebnisse nur eine geringe Variation der Konzentrationen gelöster Elemente, der Eh-Werte (-227 bis -135 mV) sowie der pH-Werte (6,8 bis 7,5). Die geringe Empfindlichkeit der Ergebnisse lässt sich durch robuste interne chemische Puffermechanismen erklären, insbesondere durch Karbonat- und Fe(II)-Fe(III)-Mineralgleichgewichte in Verbindung mit dem Kationenaustausch.

Weiter wurden auch thermodynamische Gleichgewichtsberechnungen durchgeführt, um die chemischen Bedingungen im Inneren des Endlagerbehälters aus Karbonstahl nach dessen Versagens und nach dem Eindringen von Bentonit-Porenwässern vorherzusagen. Es wurden zwei Fälle berechnet, die jeweils dem Anfangsstadium bzw. dem fortgeschrittenen Stadium der Endlagerbehälter-Korrosion entsprechen. Im ersten Fall resultiert ein leicht alkalisches, stark reduziertes, wasserstoffreiches Wasser (pH = 8,4, Eh = -495 mV), während die zweite Berechnung, die auf fortgeschrittenen Abbaubedingungen basiert, ein nahezu neutrales, mässig reduziertes Wasser (pH = 7.2, Eh = -222 mV) mit geringem Wasserstoffgehalt ergibt.

Auf der Grundlage des obigen Modells wurde die Auswirkung der durch die Auflösung verglaster Abfälle verursachte Borfreisetzung auf den pH-Wert, sowie auf Komplexierung und Löslichkeit der Radionuklide, bewertet. Die Ergebnisse deuten darauf hin, dass die stärksten Boratkomplexe mit Kationen der Übergangsmetalle (Fe und Ni) gebildet werden sollten. Abhängig vom pH-Wert könnten auch Kationen der Erdalkalimetalle (Mg, Ca, Sr, Ba, Ra) und dreiwertiger Aktiniden (Am, Cm) in begrenztem Umfang Boratkomplexe bilden. Im Gegensatz dazu sollten einwertige (Na, Cs, K) und vierwertige bis sechswertige Kationen (U, Np, Pu, Tc) keine Boratkomplexe in nennenswerten Konzentrationen bilden. Insgesamt deuten die Ergebnisse darauf hin, dass die Auswirkungen der Boratkomplexierung und des lokalen pH-Anstiegs, die durch die Auflösung von Borosilikatglas hervorgerufen werden, auf die Löslichkeitslimiten der dosisrelevanten Radionuklide vernachlässigbar sein werden.

Table of Contents

List of Tables

List of Figures

List of Acronyms

AAP	Anion-accessible porosity
ABM	Alternative Buffer Materials in-situ experiment in the Aspö Hard Rock Laboratory, Sweden
BFE	Bundesamt für Energie (engl. Swiss Federal Office of Energy)
B.E.	Best estimate
BET	Technique for surface area determination based on the Brunauer-Emmett-Teller theory
BPW	Bentonite Porewater
BWR	Boiling water reactor
CEC	Cation exchange capacity
CEM II/A-D	Portland cement, blended with up to 10 wt.% of silica fume
CI	Cement-Clay Interaction experiment at the Mont Terri URL
COx	Callovo-Oxfordian argillite
CRZ	Containment-providing rock zone
C-S-H	Cement phase containing Ca-Si-OH in various stoichiometric proportions
DDL	Diffuse double layer
EBS	Engineered barrier system
EDL	Electrical double layer
EDX	Energy dispersive X-ray spectroscopy
EDZ	Excavation-damaged zone
ENSI	Swiss Federal Nuclear Safety Inspectorate
ESDRED	Low-pH cement formulated in the EU ESDRED project
FE	Full-scale emplacement demonstration experiment at the Mont Terri Rock Laboratory
FEBEX	Full-scale engineered barriers experiment at the Grimsel Test Site
FTIR	Fourier-Transform Infrared Spectrometry
GEM	Gibbs Energy Minimisation
HLW	Vitrified high-level waste
HTO	Tritiated water
IC-A	Iron Corrosion in Bentonite experiment at the Mont Terri Rock Laboratory
ICP-AAS	Inductively coupled plasma atomic absorption spectroscopy
ILW	Long-lived intermediate-level waste
INCAN	In-canister porewater
JO	Evaluated siting region Jura Ost

KEG	Kernenergiegesetz (engl. nuclear energy act)
LAC	Low alkalinity cement
L/ILW	Low- and intermediate-level waste
MIRAM	Model inventory of radioactive materials
M-S-H	Cement phase containing Mg-Si-OH in various stoichiometric proportions
MX-80	Wyoming bentonite type
NL	Nördlich Lägern
NPP	Nuclear power plant
NW	Canton Nidwalden, Switzerland
MOX	Mixed oxide fuel
OM	Organic matter
OPA	Opalinus Clay host rock
OPAw	Opalinus Clay porewater
OPC	Ordinary Portland Cement
PWR	Pressurised water reactor
RBG	Rahmenbewilligungsgesuch (engl. general licence application)
RP-HLW	High-level waste from reprocessing
REE	Rare earth elements (lanthanides)
SGT	Sectoral Plan for Deep Geological Repositories
SGT-E2	Stage 2 of the Sectoral Plan
SGT-E3	Stage 3 of the Sectoral Plan; general licence application (RBG) stage
SF	Spent fuel
SIT	Specific Ion Interaction activity model
SD	Standard Deviation
SEM	Scanning Electron Microscopy
TDB	Thermodynamic database
TEM	Transmission Electron Microscopy
THM	Thermo-hydro-mechanical
THMC	Thermo-hydro-mechanical-chemical
URL	Underground Research Laboratory
VIS	Visible light spectrophotometry
XRD	X-ray diffraction analysis
XRF	X-ray fluorescence spectroscopy
ZNO	Evaluated siting region Zürich Nordost
ZWILAG	Zwischenlager Würenlingen AG (Interim storage facility for radioactive waste)

1 Introduction

1.1 Context

In Switzerland, legal regulations (Nuclear Energy Act (KEG 2003) and Nuclear Energy Ordinance (KEV 2004)) and guidelines are in place for the management of radioactive waste. The Nuclear Energy Ordinance (KEV) classifies Switzerland's radioactive waste into low- and intermediate-level waste (L/ILW), alpha-toxic waste[1] (ATW) and high-level waste (HLW), the latter comprising spent fuel (SF) and vitrified HLW from reprocessing (RP-HLW). The Nuclear Energy Act (KEG) requires the disposal of all these types of radioactive waste in deep geological repositories. The feasibility of this disposal solution has been demonstrated for L/ILW in Nagra (1985) and for long-lived intermediate-level waste and HLW in Nagra (2002).

The Sectoral Plan for Deep Geological Repositories (SGT) regulates the search for suitable siting regions for deep geological repositories in Switzerland. This site selection process is conducted in three stages (BFE 2008). Stages 1 and 2 have already been completed and Nagra is currently in Stage 3 (SGT-E3). Clarifications on the safety-related specifications for this stage are provided in ENSI 33/649 (ENSI 2018), while ENSI Guideline G03 and the corresponding explanatory report (ENSI 2023, ENSI 2020) specify the protection objective, protection criteria and design principles for deep geological repositories.

In SGT-E3, three siting regions located in Northern Switzerland have been considered – Jura Ost (JO), Nördlich Lägern (NL) and Zürich Nordost (ZNO) – with the objective of selecting one siting region for an HLW repository, one for an L/ILW repository, or one for a combined repository for all waste types.

Following a comparison of these siting regions, Nagra concluded that NL is the safest and most flexible siting region and is therefore applying for a general licence for a combined repository for both HLW and L/ILW at the Haberstal site.

The justification for this selection and the safety demonstration for a repository at the site are submitted as part of the general licence application (RBG[2]). The reports relating to post-closure safety, shown in Fig. 1-1, are structured as follows:

- The overall safety-related argumentation, including post-closure and operational safety, is summarised in an overarching safety report ("*Sicherheitsbericht*") NTB 24-01 (Nagra 2025b) shown at the top of Fig. 1-1.
- The upper left side of Fig. 1-1 shows the reports supporting Nagra's site comparison. The available options are compared with respect to safety and technical feasibility and the results are synthesised in NTB 24-03 (Nagra 2025a) ("*Bericht zur Begründung der Standortwahl*").
- The upper right side of Fig. 1-1 shows the reports documenting the post-closure safety case for the combined repository at the site, including its synthesis in the post-closure safety report NTB 24-10 (Nagra 2024e).
- The lower part of Fig. 1-1 shows a report that presents the safety and repository concept, including the provisional design, and reports providing the assessment basis.

---

[1] According to Nagra (2024a), ATW can coexist with L/ILW within the same emplacement caverns. As a result, for the sake of simplicity, the term L/ILW encompasses ATW without explicit mention.

[2] From the German *Rahmenbewilligungsgesuch*.

The present report is bordered in red in Fig. 1-1 and provide an overview of the geochemical processes and phenomena expected during the evolution of the HLW near-field.

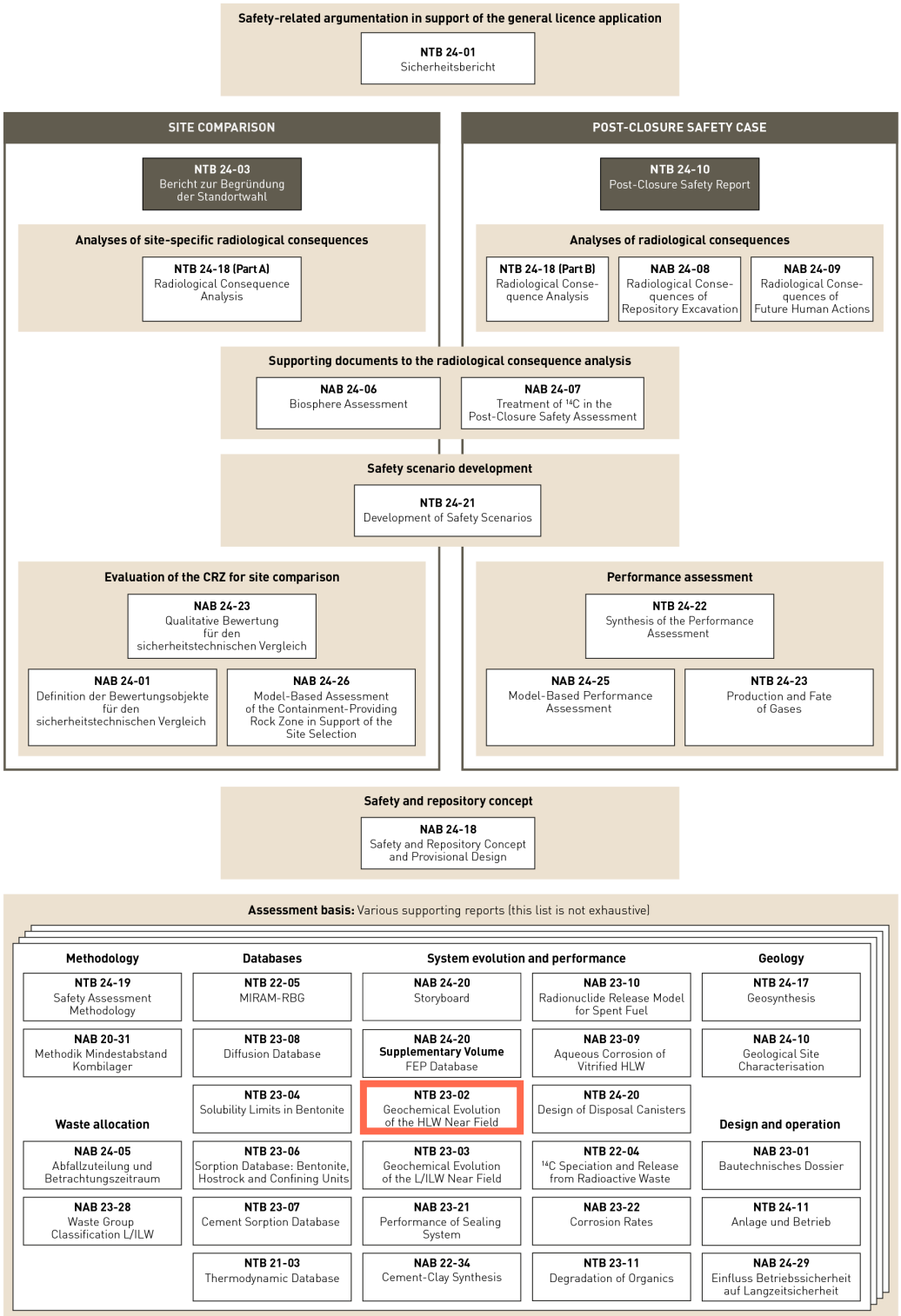

Fig. 1-1: Structure of reports covering post-closure safety aspects of the site comparison and the post-closure safety case

1.2 Scope of the present report

The main objective of this report is to provide an overview of the geochemical processes and phenomena expected during the evolution of the HLW near-field and to discuss the potential impact of such processes on the properties of the near-field components.

The HLW near-field is understood as a multicomponent system made up of the materials present in the emplacement drifts after sealing and closure, including the immediately adjacent host rock. More specifically, the provisionalary design consists of the waste package (spent fuel or vitrified high-level waste (RP-HLW)), the carbon-steel HLW disposal canister encasing the waste package, the compacted bentonite backfill material, the drift support structure made of concrete materials and the surrounding (a few metres thick) zone of Opalinus Clay host rock that undergoes mechanical and chemical disturbances following repository construction, the so-called excavation-disturbed zone (EDZ). The initial boundary conditions of the undisturbed rock, as well as the processes related to excavation and construction, are considered when describing the evolution of the near-field properties for the entire assessment period. This period is set by the authorities at one million years for the HLW repository section. This report also supports the simplified description of the properties of the near-field components within the framework of the safety case. The overview is guided by a state-of-the-art understanding of chemical-physical processes under relevant conditions.

Although generally applicable to all three sites selected in SGT-E2, since the relevant chemical processes and features considered refer to a common engineered barrier system, this evaluation also takes into account some peculiarities of the proposed site provided by the recently conducted site characterisation campaigns:

- The selection of the Opalinus Clay porewater composition reacting with bentonite (see Chapter 7) which has distinct chemistries in the NL/ZNO and JO siting regions (Mäder & Wersin 2023). This distinction reflects regional differences in the lithology of the Opalinus Clay, particularly the content and availability of soluble species such as chloride and sulphate.
- The selection of a thermal history referring to the greater depth (~ 800 to 940 m) foreseen for construction of the HLW repository section in the NL region compared to ZNO and JO (~ 600 m).

More specifically, this report focuses on the chemical thermodynamic stability of the near-field materials during the elevated temperature phase (particularly the bentonite buffer), the reactivity at material interfaces (bentonite/concrete liner, HLW disposal canister/bentonite and HLW disposal canister/waste) and porewater chemistry. The topics of canister and waste degradation kinetics, and of the associated radionuclide release, are not treated because these are the subject of separate reports (Nagra 2024b, Curti 2022, Johnson et al. 2023). The hydromechanical evolution of the near-field is taken from the expected repository evolution and alternative scenarios are not considered unless they are judged relevant for assessing the ranges of radionuclide release and transport rates[3].

As noted above, safety assessments for the HLW repository section are carried out for a period of one million years, during which chemical and other characteristics of the repository near-field will evolve in time and space. In order to obtain as realistic a picture as possible of such evolution, the main chemical transformations that could occur over the widely different timescales involved

[3] E.g. the question of whether bentonite intrusion into the empty spaces could occur after breaching of the waste canister. Such a process could impact the water chemistry inside the failed canister and enhance the dissolution kinetics of vitrified waste. Based on a Swedish model on bentonite erosion and expert judgments on the evolution of canister degradation, it can be concluded that intrusion of wet bentonite into the canister interior is very unlikely (see App. B and reference therein).

(construction, waste emplacement, post-closure evolution) have to be identified and their potential effects on the outcome of safety assessments accounted for. Specifically, the effects of these processes on waste degradation kinetics, radionuclide solubilities and sorption, diffusion and swelling characteristics of the bentonite buffer, and engineered barrier/host rock interface (EDZ) must be evaluated.

The main processes that may affect the long-term barrier performance of the HLW repository near-field, also taking into account the relatively short post-closure high temperature transient, are: the interaction of the cementitious HLW emplacement drift support structure with the adjacent Opalinus Clay and bentonite; the corrosion of the carbon-steel canister[4] and its reaction with bentonite on the external side and with waste/structural materials on the internal side; the dissolution of spent fuel or reprocessed high-level waste (RP-HLW). All these topics have been considered in a previous report (Bradbury et al. 2014) prepared in the context of SGT-E2. A major aim of the present report is to update and complete the information presented in Bradbury et al. (2014) based on the new knowledge gathered since its publication, and taking into account specific questions addressed by the regulators (Nagra 2017). The focus of the report is on mineral and water chemistry. Both factors directly affect solubility, sorption and diffusion of dose-relevant radionuclides, which are key parameters to be specified to calculate dose rates in safety assessment calculations.

1.3 Structure of this report

The report is structured as a series of chapters dedicated to specific topics. The first introductory part (Chapters 2 – 5) presents descriptions of key properties, initial states and expected evolution of the HLW near-field:

Chapter 2: Description of the planned HLW repository section, including geometry and functionality of the foreseen components.

Chapter 3: Description of the expected geomechanical and thermal evolution of the HLW repository system.

Chapter 4: Overview of the chemical properties of engineered barrier materials and of the reacting aqueous solutions in their initial states (i.e. prior to any interaction following construction, sealing and post-closure evolution).

Chapter 5: Overview of the predicted temperature evolution during the relatively short post-closure high-temperature transient, with the focus on possible effects on the chemical stability, sorption and transport properties of bentonite under non-saturated to partially saturated conditions.

[4] Cu/steel canisters or copper-coated steel canisters are alternative options being considered by Nagra during the optimisation phase.

The aforementioned chapters follow the current plans for, and evolution of, the HLW repository according to the expected evolution as described in detail in Nagra (Nagra 2024d). They are concise and thus do not provide updated information, apart from details on the repository construction/emplacement phases and on the characterisation/variability of initial materials (e.g. mineralogy of bentonite). They are followed by more extensive chapters focusing on the chemical evolution and mutual interactions among the various components in the repository near-field (mineralogical changes, porewater chemistry evolution, effects on radionuclide solubility/sorption properties and functionality of the engineered barrier materials, particularly bentonite):

Chapter 6: Description of chemical interactions between the concrete tunnel liner, Opalinus Clay host rock and bentonite buffer and the effects of such interactions on porewater chemistry and radionuclide mobility.

Chapter 7: Modelling and calculation of bentonite porewater compositions and characteristics (pH, Eh, ionic strength) in the anion-accessible porosity after full resaturation, as a basis for the calculation of radionuclide sorption coefficients and solubility limits.

Chapter 8: Chemical interactions occurring at the bentonite/canister interface after resaturation of the bentonite buffer with porewater, with the focus on potential loss of functionality of the bentonite, based on the results of recent laboratory and underground facility experiments. An estimation of the potential extent of alteration is provided.

Chapter 9: Assessment of chemical conditions inside a failed canister hosting spent fuel assemblies, assuming fully saturated conditions in the canister cavities, and evaluation of the potential influence of boron released during the dissolution of RP-HLW, with the focus on radionuclide complexation by borate.

Chapter 10: Overall summary and conclusions.

In addition, three Appendices are provided to (re-)evaluate specific questions related to two of the previous chapters:

App. A: (related to Chapter 8) Estimation of the extent of bentonite alteration due to interaction with the degrading HLW disposal canister made of carbon-steel. This is an update of the previous mass balance model (Bradbury et al. 2014) to an Fe diffusive flux model driven by concentration gradients.

App. B: (related to Chapter 9) Application of the "bentonite erosion" model of (Birgersson & Karnland 2009) to evaluate the likelihood of bentonite intrusion into the cavities of a failed canister.

App. C: Comparison betweeen the provisional calculations for Opalinus Clay porewater (used to calculate the bentonite porewater in Chapter 7) and the final ones (released later, based on the complete set of borehole data after completion of the bentonite porewater calculations).

2 Description of the HLW repository section and its components

The safety concept for the post-closure phase of a deep geological repository must ensure the permanent protection of humans and the environment using staged, passive barriers (Art. 3c KEG 2003). In Switzerland, the safety concept for the HLW and L/ILW repository sections is based on a multibarrier system. This includes, according to the provisionalary design, engineered barriers consisting of the waste matrix and their containement, disposal canisters, backfilling and sealing materials, as well as a suitable rock formation as a natural barrier.

The multibarrier system ensures that the repository fulfils the required safety functions over time periods set by the regulators (one million years in the case of the HLW repository planned in Switzerland). In line with Guideline ENSI-G03 (ENSI 2023), safety functions are overarching functional requirements on the multibarrier system that, taken together, ensure long-term safety. The safety functions include:

- **S1: Isolation** of radioactive waste from humans and the environment;
- **S2: Complete containment** of radionuclides for a period of time;
- **S3: Immobilisation, retention, and slow release** of radionuclides;
- **S4: Compatibility** of the components of the repository system;
- **S5: Long-term stability** of the multi-barrier system regarding long-term geological and climatic evolution.

The provisional repository design envisages a combined repository site with two disposal areas, one for spent fuel (SF) and reprocessed vitrified high-level waste (RP-HLW), which will be disposed of in the HLW repository section, and one for low- and intermediate-level waste (L/ILW) in the L/ILW repository section, co-located at the same site.

In the provisional repository, as illustrated in Fig. 2-1, the emplacement drifts for SF and RP-HLW would be spatially separated from the emplacement caverns for L/ILW. Because of the large distance (several hundred meters, Nagra 2022) between the two sections, the HLW section and the L/ILW section of the repository will not interact. Thus, the phenomenology of both repository sections can be treated separately. The present report specifically addresses the phenomena in the HLW section. While some of the processes under consideration apply to both sections, those specifically involving the waste and its containment refer only to the HLW section.

The underground part of the repository will be constructed in the Jurassic Opalinus Clay formation at a depth of ca. 800 – ca. 940 m below ground level at the Haberstal site. It will include a series of dead-end emplacement drifts for SF and RP-HLW with initial outer excavated diameters of around 3.9 m, supported by cementitious segmental lining elements and annular gap-filling material according to the provisional design. The repository will also include dead-end emplacement caverns for L/ILW with internal widths of around 11.5 m, heights of around 12.5 m and lengths of around 230 to 245 m, which will also be reinforced by a tunnel support system consisting of shotcrete towards the Opalinus Clay and an inner-shell tunnel support emplaced by formwork.

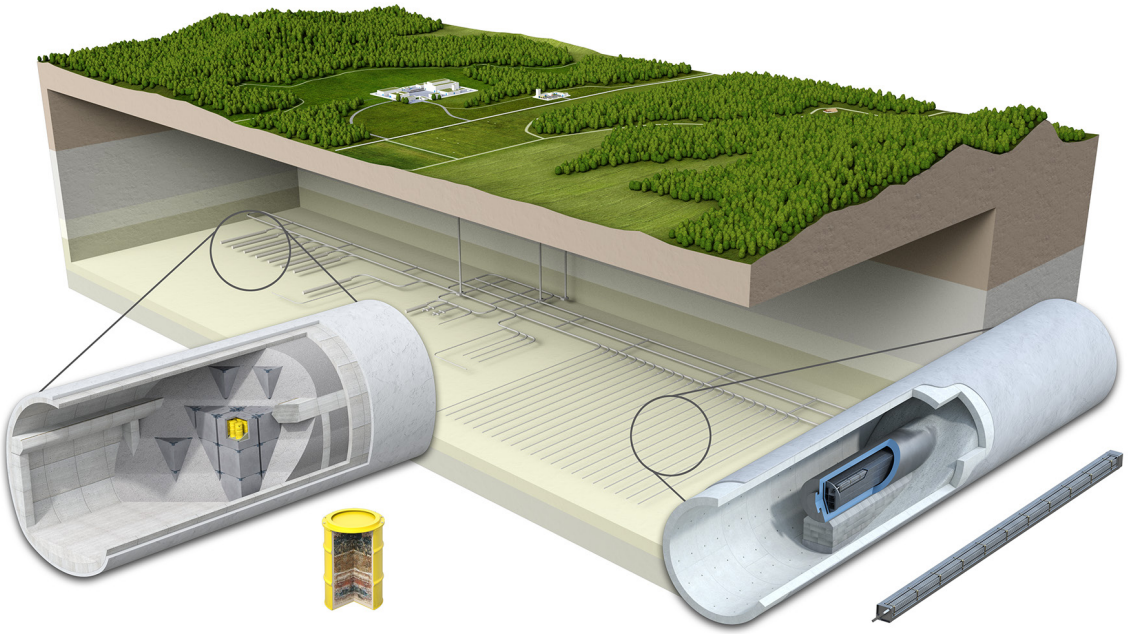

Fig. 2-1: Schematic representation of a provisional combined repository design for HLW (right section) and L/ILW (left section)

The figure shows schematically the components of the multiple barrier system.

In the surface interim storage facility (ZWILAG), spent fuel assemblies and RP-HLW in their fabrication flasks will be loaded into disposal canisters, which, according to the provisional Nagra disposal project, will be made of carbon steel (Fig. 2-2). The HLW disposal canisters will be around 5 m (SF) and 4 m (vitrified HLW) long. They will each have a diameter of around 1.1 m (SF) or 0.72 m (RP-HLW), and a wall thickness of about 14 cm (Nagra 2024b). The loaded disposal canisters will be transported underground through the shaft and emplaced co-axially at the centre of the drifts on pedestals of compacted bentonite blocks. Immediately after emplacement of a canister, the respective drift section will be backfilled with highly compacted granular bentonite. The bentonite blocks and granular bentonite will together form a protective mechanical and chemical buffer around the HLW disposal canisters. Fig. 2-3 shows a section of a HLW emplacement drift during the emplacement of a HLW disposal canister for SF.

Conceptually, the repository consists of multiple engineered and natural barriers that provide component-specific safety functions and collectively ensure the safety of the entire repository system. The components and environmental conditions for the provisionalary repository concepts considered to be relevant for providing the safety functions are:

- The deep underground location of the repository in a setting that is unlikely to attract human intrusion and is not prone to being affected by disruptive geological events and processes unfavourable to post-closure safety.
- The containment-providing rock zone, including the host rock as well as its confining geological units, which are of similar high quality in terms of safety functions (low hydraulic conductivity, homogeneous nano- to microporous structure, high sorption capacity for most dose-relevant radionuclides, self-sealing capacity and long-term chemical stability), thus providing a strong and long-lived barrier to radionuclide transport and a geologically stable physical and chemical environment around the engineered barrier system.

- The backfill and seals of the disposal areas and repository access structures, which together provide a strong and stable barrier to radionuclide transport, reduce the likelihood of inadvertent human intrusion into the repository and provide, for L/ILW, a gas transport system preventing the build-up of potentially damaging gas pressures within the disposal areas and, for the HLW repository, bentonite seals which prevent the ingress of water and physically separate the HLW repository section from the L/ILW repository section.
- The bentonite buffer (for SF and RP-HLW) with similar properties to the host rock, thus providing a strong and stable barrier to radionuclide transport, as well as a suitable physical and chemical environment favouring the longevity of the disposal canisters. Furthermore, the buffer provides mechanical support for the host rock after degradation of the tunnel support system, protects the disposal canisters and, by separating them from one another, provides compartmentalisation of the waste, mitigating the impact of any inadvertent human intrusion and reducing the potential impact of heat output from the SF/HLW disposal canisters on the radionuclide retention properties of the containment-providing rock zone (CRZ).
- Waste forms (SF[5] and RP-HLW[6]) that degrade slowly in the expected environment. It has been demonstrated that spent fuel dissolution rates will be very low during the entire repository evolution: in the first phase due to the inhibiting effect of hydrogen preventing the (radiolysis induced) oxidative dissolution; later due to the vanishing effect of alpha radiolysis (Johnson et al. 2023). In the case of vitrified HLW, dissolution rates will be high only for a very short time after first contact with water and will rapidly decrease by 3 – 4 orders of magnitude (Curti 2022).
- HLW disposal canisters (Fig. 2-2) that are mechanically strong and corrosion-resistant in the expected environment. They provide complete containment of radionuclides for a period, sufficient to allow for decay of most short-lived radionuclides prior to canister failure.

---

[5] Spent fuel rods consist of stacks of cylindrical ceramic pellets of irradiated UO_2 or MOX fuel containing a wide variety of fission products, activation products and minor actinides. A single fuel pellet is about 1 cm in diameter and 1 cm in length. The pellets are inserted in tubes of zirconium alloy cladding (Zircaloy), which serves as rigid mechanical confinement with high neutron cross-section during in-reactor irradiation. Various fuel bundles make up an assembly.

[6] RP-HLW arises from the treatment and reprocessing of spent fuel, which is first dissolved into a highly radioactive liquid, then evaporated, calcined and mixed at high temperatures with borosilicate glass-forming additives to produce a nearly homogeneous borosilicate glass melt. The melt is poured into stainless steel flasks and allowed to solidify before sealing by welding. During cooling, the glass monolith undergoes unavoidable fragmentation, causing an increase in the geometric surface area (Curti 2022).

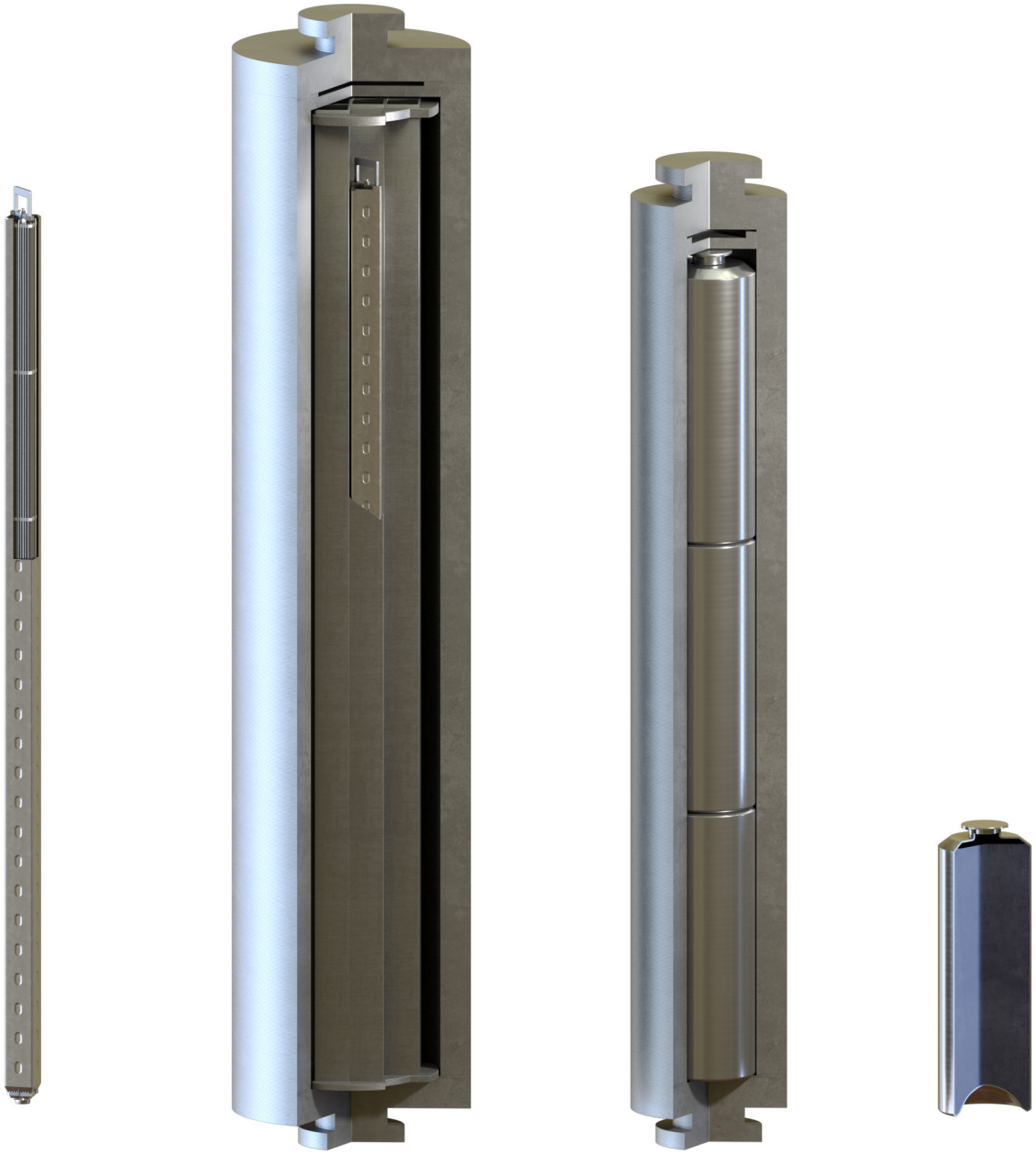

Fig. 2-2: Schematic cross-sections (to scale) of the provisional design for disposal canisters encasing spent fuel (centre left) and RP-HLW (centre right)

The leftmost image shows an individual boiling water reactor fuel assembly, the rightmost image shows a single vitrified waste form with its flask (“coquille”).

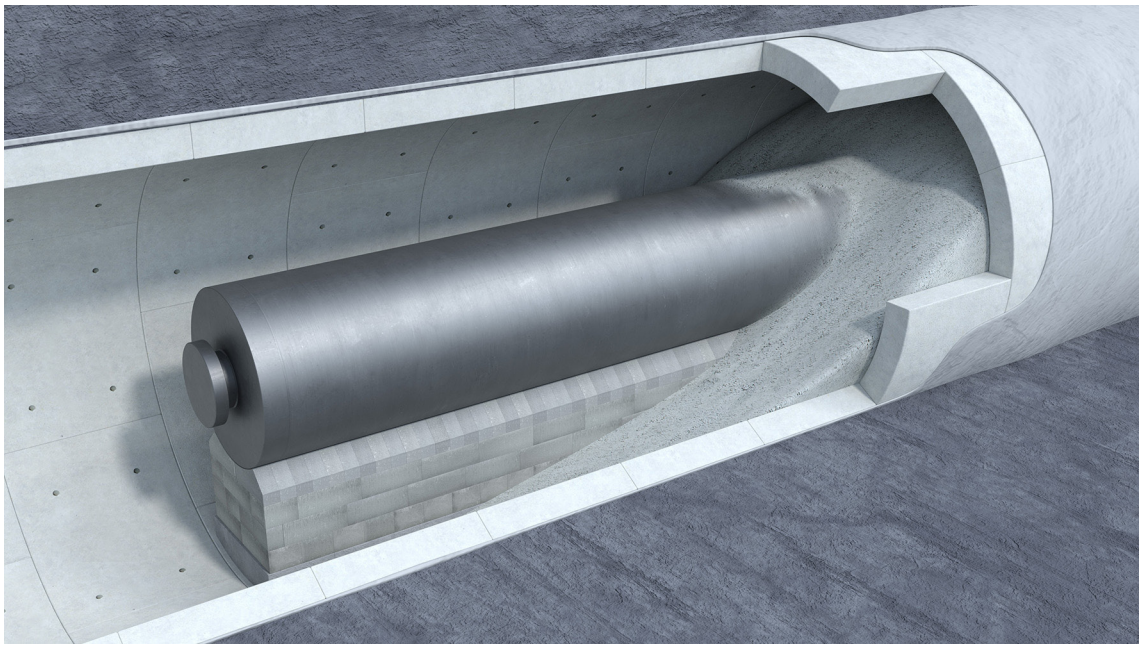

Fig. 2-3: Artistic rendering of an emplacement drift with a HLW disposal canister after emplacement on a pedestal of bentonite blocks and partial backfilling with granular bentonite

The drift is supported by a segmental liner made of precast concrete elements.

3 Expected evolution of the HLW repository near-field

3.1 Construction phase

The provisional HLW repository system design includes the main drifts and other underground structures (for example operating tunnels, construction tunnels, ventilation tunnels, pilot repository, vertical shafts, etc.) as shown in Fig. 2-1. The construction of all these structures will unavoidably affect the mechanical and structural properties of the surrounding Opalinus Clay host rock to some degree, creating a zone a few metres thick of "damaged" rock around the excavated structures, the so-called excavation-damaged-zone (EDZ). The major structural change in the host rock induced by the excavation work is the formation of a network of fractures in response to unloading, which locally increases the hydraulic conductivity (Bossart et al. 2004, Marschall et al. 2018). The construction also modifies in-situ chemical conditions: dry and cooled air will be introduced from outside through ventilation, causing local evaporation (desaturation) that will induce a local salinity increase in the porewater, eventually causing salt precipitation in the EDZ. The oxygen introduced by the excavation will trigger oxidation reactions, notably the oxidation of pyrite dispersed in the Opalinus Clay to ferric oxy-hydroxides. This reaction releases acidity, inducing calcite/dolomite dissolution and gypsum precipitation through the following reactions (Vinsot et al. 2014, Bock et al. 2010):

$$4\,FeS_2 + 15\,O_2 + 8\,CaCO_3 + 26\,H_2O \rightarrow 4\,FeO(OH) + 8\,CaSO_4 \cdot 2H_2O + 8\,HCO_3^- + 8\,H^+ \quad (3\text{-}1)$$

$$4\,FeS_2 + 15\,O_2 + 4\,CaMg(CO_3)_2 + 26\,H_2O \rightarrow 4\,FeO(OH) + 4\,CaSO_4 \cdot 2H_2O + 8\,HCO_3^- + 8\,H^+ + 4\,Mg^{2+} + 4\,SO_4^{2-} \quad (3\text{-}2)$$

These reactions may also lead to minor local changes in the exchange cation populations in illite, the major clay mineral in the Opalinus Clay.

Excavation in a rock such as Opalinus Clay will require reinforcement of the HLW drift walls. It is therefore planned to use precast annular concrete elements and a grout filling open spaces behind the concrete elements (see Section 4.5.2). The relatively large amounts of concrete introduced will affect the long-term geochemical evolution of the near-field, as discussed in detail in Chapter 6. In addition, a short-term geochemical response is expected during the construction phase, in the form of incipient carbonation of the surface of the cementitious material due to persistent contact with CO_2 from the ventilation air. This effect will however be limited to the drift surface and will not be invasive (Alheid et al. 2005). Another chemically relevant effect of the excavation work is the unavoidable contamination with microorganisms, which may later mediate redox reactions that would otherwise not proceed under sterile conditions (Leupin et al. 2018). This topic is briefly discussed in Section 7.4.5. Overall, the evidence collected from experiments in underground research laboratories (URLs) indicates that chemical changes in the host rock and support structures during the construction phase will be minor and local.

3.2 Waste emplacement, backfilling and closure phase

Several decades will elapse from the start of waste emplacement in the first drift to the final sealing and closure of the repository, and a monitoring phase of about 40 years is foreseen beyond repository closure according to the provisional time schedule (Nagra 2024d). Chemical changes in the engineered barrier materials are expected during this pre-closure phase due to persisting aerobic conditions. Limited oxidative corrosion (rusting) of the exposed surfaces of the HLW disposal canisters made of carbon steel is possible, leading to formation of Fe(III) oxy-hydroxides. Surnam et al. (2016) list, besides Fe_3O_4 (magnetite), several ferric oxy-hydroxides as typical corrosion products of carbon steel under atmospheric conditions: γ–Fe_2O_3 (maghemite, isostructural with magnetite), α-Fe_2O_3 (haematite), α-FeOOH (goethite), β–FeOOH (akaganeite), γ-FeOOH (lepidocrocite), δ-FeOOH (feroxyhyte), $Fe(OH)_2$ (ferrous hydroxide) and $Fe(OH)_3$ (ferrihydrite). The extent of corrosion seems to increase with temperature, relative humidity and atmospheric salinity (Morcillo et al. 2015). Because humidity and atmospheric salinity will be low in the ventilated structures, rusting during the emplacement phase is expected to be weak.

Resaturation of the near-field will start as soon as a canister is emplaced and the corresponding drift section filled with compacted bentonite (Nagra 2024d). The humidity within the backfilled drift will continuously increase until water condenses and starts to saturate the bentonite. Upon saturation, the bentonite starts to swell, resulting in a porosity redistribution and homogenisation (Seiphoori 2014). Thanks to the stiff tunnel support, the EDZ will not propagate further and resaturation will result in self-sealing due to swelling of the clay minerals and formation of secondary minerals (Nagra 2024c).

3.3 Early post-closure phase

At the time of repository closure, the bentonite will be only partially saturated; it will take tens to hundreds of years after backfilling of a drift for resaturation to be complete (Nagra 2024f). The advance of the saturation front will probably be delayed by the steep thermal gradient towards the canister (Gens et al. 2004). The maximum heat power of canisters fully loaded with UO_2/MOX spent fuel will be about 1,500 W at the time of emplacement. For the scenarios assumed for the general licence documentation, temperatures in the bentonite surrounding UO_2/MOX spent fuel canisters are predicted to remain above 50 °C for about 30,000 years (cf. Fig. 5-2). However, bentonite temperatures exceeding 100 °C will be limited to less than 1,000 years after closure.

Because transport of Opalinus Clay porewater to the bentonite will occur across the concrete liner, steep chemical gradients at the bentonite / tunnel support / Opalinus Clay interfaces will be generated due to the high reactivity and alkalinity of the cementitious materials of the support. This will result in mineralogical changes, and potentially local clogging phenomena, and thus to a reduction in solute transport rates across the two boundaries. This topic is treated in detail in Chapter 6.

Redox conditions will gradually become anaerobic as several processes (diffusion of dissolved O_2 towards the Opalinus Clay, aerobic respiration and mineral oxidation) consume the entrapped oxygen (Leupin et al. 2021). In-situ experiments at the Mont Terri Rock Laboratory indicate that gaseous O_2 disappears rapidly (within weeks) after backfilling, however an pool of oxygen may remain stored as physisorbed O_2 on the external surfaces of the bentonite granulate (Giroud et al. 2018, Tomonaga et al. 2019).

As soon as the relative humidity at the canister surface reaches a threshold value, anaerobic corrosion of the canister steel will begin producing hydrogen gas and secondary Fe(II,III) solids. The thermodynamically most stable corrosion product of anaerobic corrosion is Fe_3O_4 (magnetite), according to the reaction

$$3\ Fe(0) + 4\ H_2O \rightarrow Fe_3O_4 + 4\ H_2(g) \quad (3\text{-}3)$$

Other ferrous solids are however conceivable, at least as transient metastable products. Laboratory and field experiments show evidence for $FeCO_3$ (siderite) or $Fe_2(OH)_2CO_3$ (chukanovite); see for example Kerleguer (2020). Experiments in underground laboratories also reveal formation of halos of ferric iron solids (e.g. goethite, FeOOH) in the bentonite, possibly as a consequence of the reaction between released Fe(II) and the aforementioned residual O_2 sorbed on bentonite (Leupin et al. 2021). In addition to oxy-hydroxides, Fe-silicates may form at the bentonite/canister interface. Details on the mineralogy of Fe corrosion products formed under repository conditions are presented in Chapter 8.

Pressure build-up in the near-field may result from hydrogen gas accumulation if H_2 production from anaerobic Fe corrosion exceeds the dissipation rate (Diomidis et al. 2016). In-situ corrosion rates reach a near steady-state of about 0.3 µm/a within a few years (Diomidis et al. 2023). However, due to the initial high consumption of water and H_2 production induced by the anaerobic Fe corrosion (up to about 30 µm/a during the first few months, see Smart et al. 2017b), local desiccation cracks are likely to form, extending a few mm from the canister surface (Leupin et al. 2021). Although these cracks may offer preferential pathways for solutes, they should be rapidly sealed by swelling bentonite upon resaturation and/or by Fe corrosion products (oxides, oxy-hydroxides, or silicates) since these have a much larger molar volume than metallic Fe and will thus fill any formed open space.

A high temperature transient will characterise the early post-closure time. In HLW emplacement drifts, where UO_2/MOX SF is emplaced, current simulations for a repository depth of ~ 900 m predict temperatures at the canister surface decreasing from a maximum of around 135 °C (five years after closure) to around 95 °C within the first 1,000 years after repository closure (see Fig. 5-2). The bentonite buffer temperature will then continue to decrease slowly and reach about 50 – 60 °C after 10,000 years, i.e. about 10 – 20 °C above background host rock temperatures. The high temperature transient will lead to increased pore pressures in the host rock. The pressure increase will probably not be sufficient to induce further fracturing beyond the EDZ, although reactivation and further development of already existing EDZ fractures cannot be excluded (Nagra 2024d). The impact of temperature on the host rock will be discussed in Section 5.6.

3.4 Long-term evolution after canister failure

The HLW diposal canisters made of carbon steel required to maintain their integrity for at least 1,000 years. Once the canister is breached, porewater will enter the canister, but intrusion of bentonite can be largely excluded (see App. B). The strong chemical resistance of structural materials encasing the waste (Zircaloy for spent fuel and Cr-Ni steel coquille for vitrified waste) will delay the release of fission products and actinides from the waste, as long as they are physically intact[7].

[7] No credit is however taken for the corrosion resistance of these materials in safety assessments, as the Zircaloy cladding encasements are thin, so that mechanical failures at the time of water ingress in the canister cavity cannot be excluded.

As long as metallic Fe from the canister is corroding, conditions will remain anoxic and very reducing, even in the presence of radiolytic oxidants (mainly H_2O_2) produced via alpha radiolysis of the water in contact with the fuel surface. This protection mechanism is ascribed to chemical activation of H_2, mainly catalysed by the noble metal particle inclusions present in spent fuel, ensuring that the dissolution rates of the $U(Pu)O_2$ fuel matrix and consequently the release rates of redox-sensitive dose-relevant nuclides remain low (Johnson et al. 2023). Persistent reducing conditions will contribute to maintaining low release rates of surface-accessible redox-sensitive nuclides (e.g. U, Pu, Np, Se) since the solubilities of reduced species of these elements are low compared to the oxidised forms. The prompt release from SF (Instant Release Fraction, IRF) of easily accessible and soluble radionuclides such as ^{129}I and ^{135}Cs are not expected to be directly affected by the redox potential, nor the dissolution rates of waste. Because some elements (e.g. Ni) will be dissolved simultaneously from the radioactive waste and from structural materials, the effective solubility limit of the respective dose-relevant nuclides (e.g. ^{59}Ni) will be greatly reduced via dilution with stable and short-lived isotopes. The effective mobility of radionuclides from the near-field to the host rock will also depend on complex, not fully resolved chemical effects such as competitive sorption (see for example Bradbury & Baeyens 2005, Pfingsten et al. 2011), or the presence of soluble ligands, e.g. borate from vitrified waste (Section 9.3).

After breaching, the canister will continue to corrode for at least several tens of thousands of years, until all metallic Fe is consumed. The corrosion process at the inner canister side will produce additional H_2 and consume water, in analogy with the previously described evolution at the external canister side. Similarly, this could lead temporarily to partial desaturation and formation of a separate gas phase.

Upon losing its integrity, the canister will no longer prevent the bentonite porewater from entering the internal open spaces. The infiltrating water will start to react with the waste package. As already mentioned, the ingress of porewater will initially induce a significant pH increase at the Opalinus Clay/tunnel support/bentonite interfaces and mineralogical changes due to chemical reactions of cementitious materials with the clay. Eventually, the pH gradient will be strongly mitigated, and the porewater chemistry will become uniform across the bentonite. Reactive transport calculations have been carried out to address this topic (Kosakowski 2023) and are discussed in Section 6.7, including a comparison with the older calculations (Bradbury et al. 2014, Berner et al. 2013) and with other modelling work for similar systems. New bentonite porewater compositions for use in safety assessment calculations are also provided (Chapter 7) based on the new Opalinus Clay porewater data derived from the recent borehole campaign (Mäder & Wersin 2023) and the update of the PSI-Nagra thermodynamic database (Hummel & Thoenen 2023). Finally, the long-term chemical evolution at the canister/bentonite interface (Chapter 8) and at the waste/canister interface (Chapter 9) is addressed. This is done based on the analysis of newly published literature on these topics and dedicated geochemical calculations.

4 Initial states

4.1 Preliminary remarks

The purpose of this chapter is to describe the *chemical state* of the HLW repository near-field before any perturbations caused by construction or other repository-induced effects. By *initial states* we thus refer to the chemical inventories of the engineered barrier materials and of the adjacent host rock. The "material compartments" considered are the waste packages (the waste matrices, structural materials encasing the waste, and the HLW disposal canister made of carbon-steel, protecting the waste packages), the compacted bentonite as a buffer material in the excavated drifts, and the tunnel support structure, consisting of a concrete liner with annular gap-filling materials at the drift/host rock interface and the adjacent Opalinus Clay host rock.

This list includes the materials specified in Chapter 4 of Bradbury et al. (2014). Analogous figures and tables are presented here for the sake of comparability between the two reports. Some of the chemical data presented in this chapter have used as input parameters for the porewater calculations presented in Section 7.4 (bentonite porewater) and Section 9.2 ("inside canister" water).

4.2 Waste packages

4.2.1 Spent fuel

In Switzerland, four nuclear power plants (NPP) with a total of five light water reactors have been operating to date: Beznau (2 PWRs, Pressurised Water Reactor), Mühleberg (1 BWR, Boiling Water Reactor, currently being decommissioned), Gösgen (1 PWR) and Leibstadt (1 BWR). According to the current base scenario for final disposal, 12,797 spent fuel assemblies with UO_2 fuel and 380 spent fuel assemblies with MOX fuel will have to be disposed of according to the Model Inventory of Radioactive Materials (MIRAM) RBG database (Nagra 2023).

Due to the different types of reactors, fuel and enclosing structural materials, assembly geometries and their chemical compositions are not uniform. Six different spent fuel waste sorts have thus been defined in the scope of the MIRAM RBG database (Nagra 2023), requiring two distinct types of spent fuel canisters with different internal arrangements, one hosting BWR SF, the other hosting PWR SF (Nagra 2024b). The chemical heterogeneity concerns both the fuel itself (UO_2 and MOX fuels with different burnups) and the enclosing structural materials (different types of Zircaloy cladding and metal alloys). The inventories of structural materials for the different SF waste categories, together with the expected numbers of assemblies for each sort, have been determined and can be found in Johnson et al. (2023).

The determination of the bulk chemical composition of spent fuels is more difficult, as the MIRAM RBG database lists detailed inventories of radionuclides for all waste types, but data on stable isotopes are not given in the public document (Nagra 2023). In order to provide representative time-dependent bulk chemical inventories of LWR spent fuels, calculations were carried out using the webKORIGEN++ code[8]. The calculations involved first simulating the fission reactions in a PWR operated with UO_2 fuel up to a burnup of 55 GWd/t_{iHM}, followed by the modelling of in-situ decay.

[8] This is a development of the Oak Ridge National Laboratory ORIGEN code available at the Nucleonica portal (Magill & Dreher 2009) under https://nucleonica.com/Application/webKORIGEN/KorigenPlus.aspx

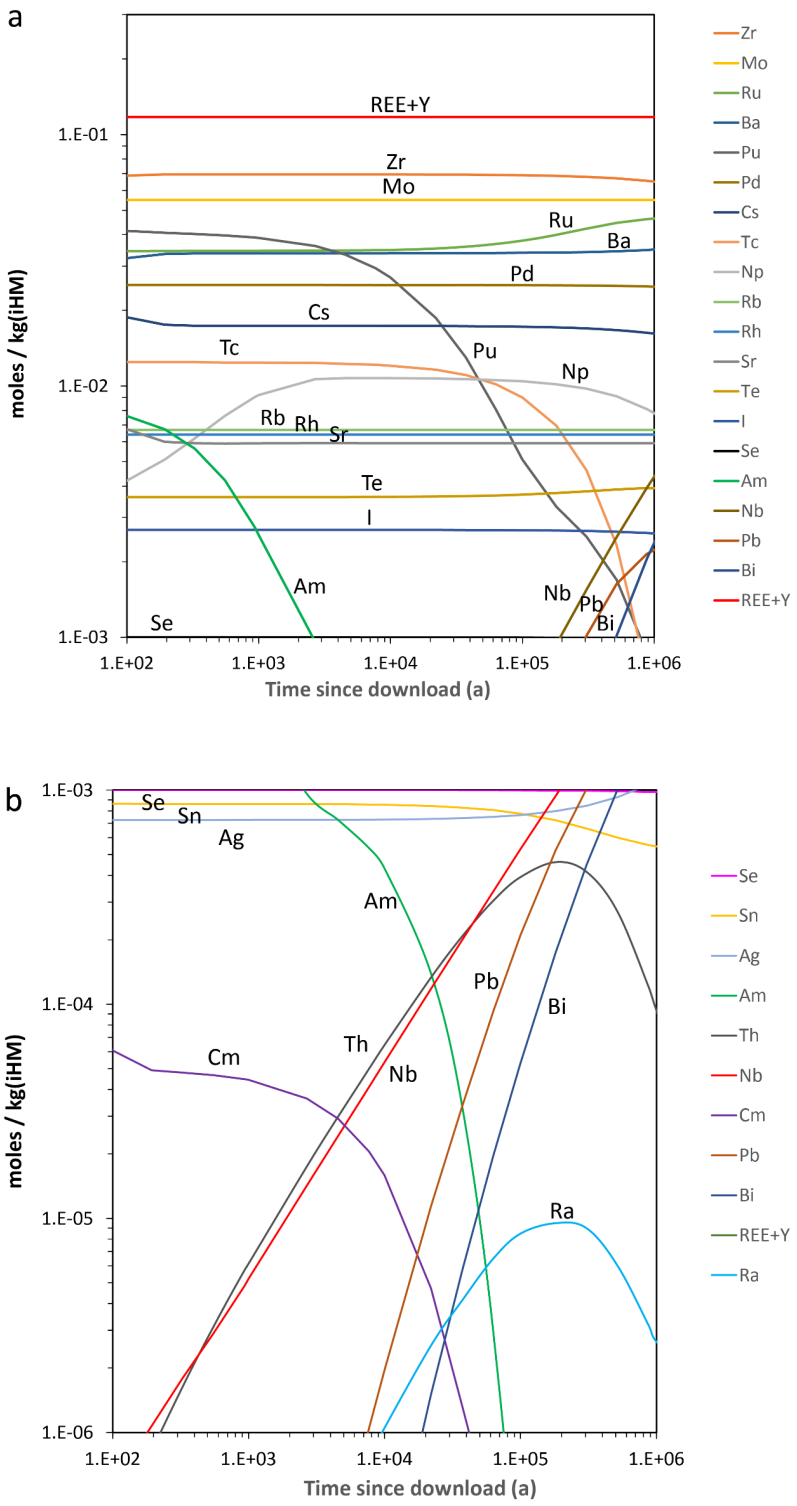

Fig. 4-1: Total element concentrations of fission products for a burnup of 55 GWd/t_{iHM} UO_2 PWR spent fuel as a function of time from reactor download

a) major elements, b) intermediate elements. U, O, He, Xe, Kr and trace elements are not shown.

Fig. 4-1 shows the obtained total element contents as a function of time, starting from 100 years after fuel download (~ time of repository closure) up to one million years (final time of repository evolution required by the Swiss regulators to be considered in safety assessments). The results indicate that rare earth elements (REE) and Y areat all times the major contributors among the fission products, followed by Zr, Mo, Ru, Pu, Ba, Pd, Cs, Rb, Rh, Sr, Te and I. Because stable or very long-lived isotopes dominate the inventories of all these elements, their total concentrations are quite insensitive to decay and remain nearly constant. This is exemplified in Fig. 4-2 for Ba and Cs. During the interim storage and repository construction phase (up to about 100 years after fuel download), the total Cs inventory decreases while the Ba inventory increases due to decay of ^{137}Cs (half-life = 30.7 years) to ^{137}Ba. Afterwards, the elemental concentrations of both elements remain almost constant since they are controlled by stable isotopes. Only after 10^5 years do the Cs and Ba inventories start to change due to the decay of the long-lived (dose-relevant) ^{135}Cs.

Data on stable isotopes are of relevance not only for determining bulk element concentrations, but also for quantifying isotope dilution effects that reduce the effective solubility limit of any specific radionuclide of the same element. As an example, consider the case of selenium. Our calculations indicate that the dose-relevant nuclide ^{79}Se makes up, at any time, less than 5% of the total Se inventory in spent fuel, the remaining part consisting of the stable isotopes ^{77}Se, ^{78}Se, ^{80}Se and ^{82}Se. This means that whenever the solubility limit of Se is reached during the evolution of near-field porewaters, the effective isotope-specific solubility limit of ^{79}Se will be at least 20 times smaller than the elemental solubility limit. If considered, this isotope dilution effect may have a significant impact on the results of safety assessment calculations for ^{79}Se.

In contrast to fission products, actinides do not have stable isotopes. Consequently, the concentrations of Pu and of the minor actinides Np, Am, Cm in the waste are subject to strong time-dependent variations owing to decay and ingrowth. Towards the end of the evolution, decay products such as Nb, Bi, Pb and Th isotopes become important (Fig. 4-1b).

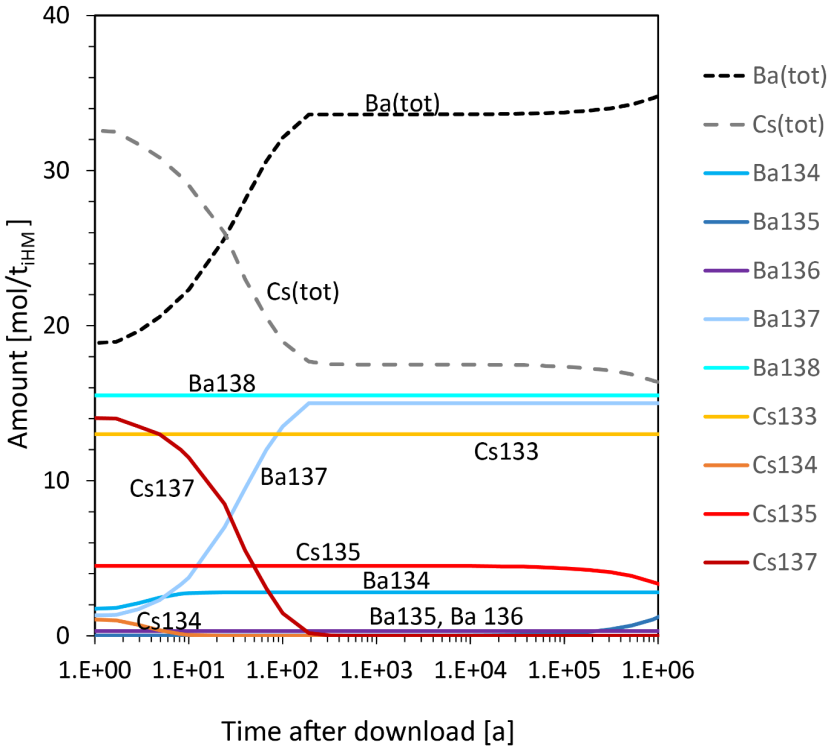

Fig. 4-2: Isotopic and total element concentrations of caesium and barium fission products calculated for a burnup of 55 GWd/t_{iHM} UO_2 PWR spent fuel as a function of time elapsed since reactor download

4.2.2 Reprocessed high-level waste (RP-HLW)

Two types of RP-HLW from spent fuel reprocessing, produced in the plants of La Hague in France (ORANO, formerly COGEMA/AREVA) and Sellafield Ltd. in the U.K. (formerly BNFL), will have to be disposed of in the planned HLW repository. According to the current base scenario (reference year 2075[9]), 632 packages, each consisting of 0.15 m^3 vitrified HLW waste encased in a thin stainless steel flask will have to be disposed of (Nagra 2023a). Tab. 4-1 shows the chemical inventories of these materials as specified in McGinnes (2002). According to the current material inventory data (Nagra 2023), each waste package consists of about 400 kg RP-HLW encased in stainless steel cylindrical flasks of ca. 133 cm height and 43 cm diameter with 0.18 m^3 void volume.

[9] In the MIRAM-RBG database, projections for the full waste inventory for the year 2075 have been made, as at that time no further waste is expected to be produced. Note that in 2006 the Swiss federal government enforced a reprocessing moratorium. From that date on, reprocessing of waste from Swiss reactors was prohibited and Nagra had to pursue a disposal strategy involving, in addition to RP-HLW, direct disposal of spent fuel.

Tab. 4-1: Chemical composition in wt.% of RP-HLW, as specified by ORANO (France) and Sellafield Ltd. (U.K.), and of the steel flask after McGinnes (2002)

The chemical compositions of the inactive reference glasses SON68 and MW used for laboratory experiments are given for comparison.

	ORANO glass (F)		**Sellafield Ltd. glass (UK)**		**Flasks (coquille)**		
	CSD-V J-Z-005000 Old notation: **WA-COG-1**	**SON68**	**VR-SL J-Z-005002** Old notation: **WA-BNF-1**	**MW**		**Z15 CN 24.13[#] (ORANO)**	**316 L@ (BNFL)**
Al_2O_3	4.53	4.91	1.38	5.33	C	0.15	0.015
B_2O_3	14.14	14.02	16.78	16.65	Cr	23	15
CaO	4.04	4.04	0.01	0.03	Fe[**]	61.05	71.57
Fe_2O_3	1.10	2.91	0.88	2.69	Mn	2	1
Li_2O	2.02	1.98	4.00	3.79	Ni	13	12
MgO	0	0	1.40	5.85	P	0.035	0.023
MoO_3	2.15	1.70	2.38	1.76	S	0.015	0.015
Na_2O	9.23	9.86	8.33	8.10	Si	0.75	0.38
P_2O_5	0.30	0.28	0.15	0.18	Mo	-	2.5
SiO_2	45.70	45.48	45.95	46.20			
ZnO	2.50	2.50	0.02	0			
ZrO_2	3.13	2.65	2.35	1.71			
RN[*]	11.14	9.67	16.38	7.71			

* RN = sum of fission products and actinides, or analogue elements for inactive glass
** Calculated by balance
\# https://www.steel-grades.com/metals/85/214771/AFNOR-NF-Z15CN24-13.html
@ https://www.azom.com/article.aspx?ArticleID=2382

The specifications provided for the RP-HLW (CSD-V and VR-SL) show only minor differences in the glass matrix compositions of the two waste sorts. The UK glass contains significant amounts of Mg oxide, which is absent in the French glass and is replaced by Ca and Zn oxides (not present, or only in minor amounts, in the UK glass). The other major oxides occur in similar amounts in both glasses. The main soluble components having the potential to affect the composition of the aqueous phase in contact with RP-HLW are Na_2O and, in particular, B_2O_3. The potential effect of boron release on the complexation and solubility of dose-relevant radionuclides is treated in Chapter 9.

Although the flasks encasing the waste contain significant amounts of Cr and Ni, the release of these elements due to corrosion will have little influence on the bulk chemical composition of the porewater due to the very slow corrosion rates of stainless steel and the low solubility of these transition metals (Hummel & Thoenen 2023, Hummel et al. 2023).

4.3 Carbon steel canister

Nagra's provisional desing for the HLW/SF disposal canister assumes a cylindrical, 14 cm-thick canisters made from forged carbon steel (Nagra 2024b). A series of requirements has been identified to guide the selection of appropriate materials and designs (Nagra 2024b), including the need to maximise long-term integrity, to avoid stresses that could induce cracking, to minimise hydrogen embrittlement during manufacture and to optimise weldability.

Based on these requirements, a low-carbon steel with restricted concentrations of key elements, with the specifications shown in Tab. 4-2, has been selected.

Tab. 4-2: Compositional limits (in wt.%) for carbon steel material to be used for the fabrication of SF/HLW disposal canisters according to the provisional design

Modified from Patel et al. (2012)

Element	C	Si	Mn	P	S	Cr	Ni	Cu	Fe
wt.%	0.12 max.	0.3 max.	0.8 max.	0.015 max.	0.01 max.	0.2 max.	0.2 max.	0.02 max.	≥ 98.3 (balance)

4.4 Bentonite: safety functions, mineralogy and physical-chemical properties

As previously mentioned, the loaded canisters will be emplaced in the middle of the HLW emplacement drifts on pedestals of compacted dry bentonite blocks. Thereafter, the excavated repository drifts will be backfilled with compacted dry granular bentonite according to the provisionalary repository concept. The compacted bentonite contributes to multiple safety functions in the current repository design. When water resaturation starts, the bentonite buffer will gradually expand and seal open spaces, ensuring a low-permeability hydraulic environment around the canisters, and providing support through the swelling pressure. Swelling will also help to further homogenise the density distribution within the bentonite buffer. After canister breaching and the onset of waste dissolution, the compacted bentonite will ensure very low diffusivities and strong sorption capacities for almost all solutes, thereby retarding the release of to be considered dose-relevant radionuclides. Retardation will allow for substantial decay of short-lived and many long-lived radionuclides within the buffer, thus strongly attenuating the effective release of most considered dose-relevant radionuclides into the Opalinus Clay host rock. Finally, the nanoporous nature of the buffer material will also be beneficial as a radiocolloid filter and in limiting or even suppressing microbial activity.

Natural bentonites are clay formations produced through surface alteration of volcanoclastic silica-rich rocks (Ross & Shannon 1926). Bentonites are mainly composed of smectites and in particular montmorillonite, a sheet silicate with the following ideal structural formula (Newman 1987):

$$X^{z+}_{(0.425/z+)} <Al_{1.575}Mg_{0.425}> [Si_4O_{10}] (OH)_2 \cdot nH_2O \quad (4\text{-}1)$$

where < > denotes octahedrally coordinated sites, [ ] denotes tetrahedrally coordinated sites and X stands for exchangeable interlayer cations (Na^+, K^+, Mg^{2+}, Ca^{2+}, etc.) of charge z+. Structurally, montmorillonite is a dioctahedral 2:1 clay mineral of the smectite group (Borchardt 1989). The

term '2:1' means that it consists of units made of 2 tetrahedral and 1 intercalated octahedral sheets (TOT) alternating with layers of charge compensating interlayer cations X^{z+}. In Wyoming MX-80 bentonite, the provisional representative buffer material, the dominant interlayer cation is Na^+.

The term “dioctahedral” implies that only 2/3 of the available octahedral sites are occupied, in contrast to “trioctahedral” clay minerals, where all available octahedral sites are occupied. In montmorillonite, a limited proportion of divalent octahedral cations (Mg^{2+} in the above formula) generates a small negative charge in the octahedral sheet that must be compensated by the interlayer cations. If the octahedral sites in the previous formula were fully occupied by Al^{3+}, the TOT sheets would be uncharged and no compensating interlayer cations would be required, resulting in the mineral pyrophyllite, $<Al_2>\ [Si_4O_{10}]\ (OH)_2$. In montmorillonite, no or only negligible substitution of trivalent cations occurs in the $[Si_4O_{10}]$ layers, i.e. the tetrahedral layers are not charged. If no divalent cations substitute into the octahedral layer and Al^{3+} substitutes for Si^{4+} in the tetrahedral layer, another smectite with high exchange capacity forms, beidellite:

$$X^{z+}_{(0.425/z+)} <Al_2> [Si_{3.575}\ Al_{0.425}O_{10}]\ (OH)_2 \cdot nH_2O \qquad (4\text{-}2)$$

Beidellite has a weaker swelling capacity than montmorillonite owing to the significant tetrahedral charge (Newman 1987, Yariv 1992) and is therefore of concern since it has been reported as a potential alteration product of montmorillonite during the high-temperature period in the expected evolution scenario of the HLW repository (Leupin et al. 2014), see Section 5.2.2 for a discussion.

In addition to montmorillonite, bentonites contain a variety of accessory minerals, which, despite their small quantities, may play a significant role in determining porewater chemistry in a compacted state. This is because compaction reduces the amount of external porewater to a small fraction of the total solid volume, allowing even small amounts of solids to dissolve up to their solubility limits and thus to control the composition of the porewater. Cation exchange reactions also greatly affect the porewater composition. Chapter 7 deals with this topic in detail, presenting the results of model calculations used to determine representative bentonite porewater compositions.

In the Swiss programme, the provisional representative buffer material for evaluating bentonite properties and its chemical behaviour is Wyoming MX-80 sodium bentonite. The host rock will be the Opalinus Clay formation. Tab. 4-3 provides representative mineralogical compositions for the bentonite. The representative mineralogy of MX-80 bentonite was determined through the characterisation work described in Bradbury & Baeyens (2002).

Tab. 4-3: Representative mineral compositions of MX-80 bentonite

Minerals considered to be reactive in the bentonite porewater calculations (Chapter 7) are in bold face.

Minerals [wt.%]	**MX-80 bentonite mineralogy***
Montmorillonite	75
Illite	-
Illite/smectite mixed layer	-
Kaolinite	< 1
Chlorite	-
SiO_2 (mostly **quartz**)	15.2
Calcite	0.7
K-feldspar	5 – 8
Plagioclase	-
Dolomite	-
Siderite	0.7
Gypsum	0.4*
Pyrite	0.3

* Calculated from aqueous extract analyses based on data in Bradbury & Baeyens (2002), Tab. A-2.

The types of minor minerals and their inventories can vary significantly in natural bentonites, even within the same formation (Dixon 2019). Because Nagra has taken no decision on the type of bentonite to be considered as a buffer material in their provisional design, it is of relevance to consider such variations in mineralogy and evaluate the possible consequences for porewater chemistry. To this end, we reviewed selected literature data on well characterised bentonites (Gates et al. 2002, Karnland 2010 & Damian et al. 2021) originating from different localities and geological terrains: MX-80 Wyoming bentonite (Müller-Vonmoos & Kahr 1983), Milos bentonite and Ashapura bentonite (Karnland 2010), Australian Miles bentonite (Gates et al. 2002) and Romanian Oraşu-Nou bentonite.

A total of 24 analyses (mostly XRD) were evaluated and the data collected in Tab. 4-4 and Fig. 4-3. It appears that reactive[10] minor minerals such as carbonates (calcite, siderite and dolomite), Fe hydrous oxides (goethite, maghemite or other Fe(III) solids), gypsum and silica phases (mostly quartz) are ubiquitous across all samples. Therefore, the MX-80 mineral assemblage is representative. Relatively large variations of the mineral contents mostly do not play a role, because the very high solid:water ratios ensure that saturation equilibria are reached even when small amounts of these minerals are present (see Chapter 7 for more details). Other occasionally observed minerals such as anatase, feldspars, and muscovite are not stable at low temperatures. They usually persist as sparingly soluble metastable phases that do not significantly affect porewater compositions. In the model predicting composition and characteristics of bentonite porewaters (Chapter 7), these minerals are therefore considered to be chemically inert.

[10] Reactive minerals are those assumed to reach thermodynamic equilibrium with the porewater (via dissolution or precipitation) in our model calculations.

Among the clay minerals, montmorillonite is the dominant phase in bentonite. Illite and kaolinite are also common up to about 10 wt.%. However, their effect on porewater chemistry is limited due to their low solubilities and lower cation exchange capacities compared to montmorillonite. Nevertheless, kaolinite, probably the only clay mineral phase with well-defined solubility product (Hummel & Thoenen 2023), is used as a reactive phase in our bentonite porewater model (Chapter 7) in order to set a control on the Al(III) concentration.

Tab. 4-4: Mineral composition of MX-80 and five other bentonites, showing minimum (Min.) average (Avg.) and maximum (Max.) contents from the analysed samples

N = number of analyses, Det.% = percentage of analyses in which a mineral was detected. Minimum values refer to samples in which the mineral was detected.

	MX-80 bentonite (N=8)				**All samples (N=24)** (6 bentonites)			
Mineral	**Min. wt.%**	**Avg. wt.%**	**Max. wt.%**	**Det. %**	**Min. wt.%**	**Avg. wt.%**	**Max. wt.%**	**Det. %**
Montmorillonite	75	80.6	83.9	100	60.0	80.3	95.0	100.0
Illite	0.7	0.8	0.8	88	0.6	2.4	10.4	95.8
Anatase (TiO_2)	-	-	-	0	0.2	0.8	1.2	25.0
Carbonates*	0.1	0.8	1.4	50	0.1	3.3	7.5	62.5
Fe oxy-hydroxides	0.1	0.1	0.1	13	0.1	1.7	3.4	66.7
Feldspars	2.4	3.9	6.5	100	0.2	3.1	8.0	70.8
Gypsum	0.4	0.9	1.4	100	0.3	0.9	2.2	58.3
Zeolites	-	-	-	0	1	1.5	2.0	8.3
Kaolinite	1	1	1	13	1	4.0	10.0	25.0
Muscovite	2.4	3.4	5.1	88	0.1	2.3	5.1	75.0
Pyrite	0.3	0.6	0.9	100	0.3	0.8	1.5	95.8
SiO_2**	4.5	8.6	15.2	100	0.5	9.4	41.0	79.2

* Mostly calcite, dolomite, siderite
** Mostly quartz, otherwise tridymite, cristobalite, opal

In summary, these data confirm that the MX-80 mineralogy is representative and consistent with the findings of Dixon (2019), who quotes the same minor mineral assemblages (except for the additional presence of biotite in a single sample) and similar variations in their contents for various samples of MX-80 bentonite analysed in three different laboratories. As already noted, the absolute contents should play a minor role in determining porewater composition due to the high solid/water ratio in saturated compacted bentonite. A sensitivity analysis to substantiate this expectation has been carried out and the results are presented in Section 7.4.7.

Cation exchange reactions between porewater and interlayer cations of montmorillonite also play a role in determining the equilibrium composition and characteristics of bentonite porewaters. For the calculations presented in Chapter 7, we used the cation exchange capacities (CEC) and initial cation occupancies determined by Bradbury & Baeyens (2002), with slight corrections to account for Sr and Ba exchange (Tab. 4-5).

Dohrmann et al. (2012a) and Dohrmann et al. (2012b) carried out CEC and exchangeable cation determinations on different types of bentonite selected by various countries as potential repository buffer materials. The analyses were conducted using different methods in different laboratories, taking precautions to avoid contamination by dissolution of reactive minor minerals[11]. As for the mineralogy, the question arises to what extent the variations in CEC and initial exchangeable cation populations may affect porewater chemistry. It can be anticipated that both parameters will affect chemical equilibria in the porewater, at least during the initial stages[12] of water-bentonite interaction. The determination of CEC values for clays and soils is in general a difficult task as it may be easily biased by inappropriate sample treatment, different cation extraction and analysis methods, the dissolution of minor phases, and the presence of competitive charged components (e.g. organic matter). Therefore, great care must be taken when using and comparing exchange capacities determined in different laboratories.

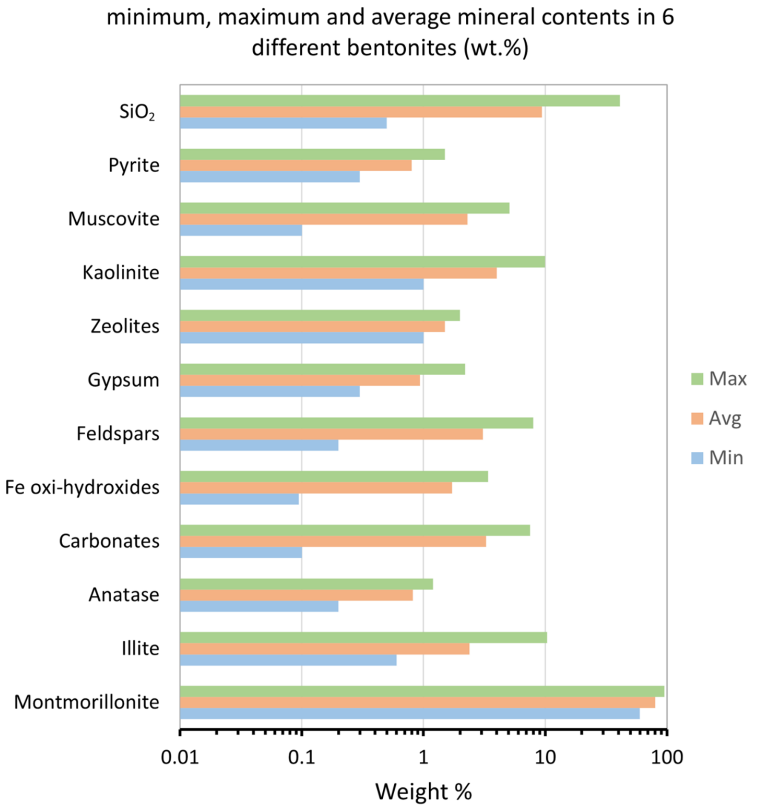

Fig. 4-3: Minimum, average and maximum contents of minerals detected in 24 analyses of six different bentonite types, including MX-80

Minimum contents refer to the smallest significant values above analytical detection limit. Analyses below detection limits are excluded.

[11] Dissolution of minor minerals such as gypsum or calcite would lead to overestimated exchanged Ca populations and thus falsify the CEC determination.

[12] For any cation exchanger subject to interaction with an increasing amount of water of fixed composition (e.g. multiple exchange cycles with Opalinus Clay porewater), the exchanged cation population will evolve until it is finally at equilibrium with the intruding water. After prolonged interaction, one may therefore assume a final bentonite porewater composition identical to that of the intruding Opalinus Clay porewater.

Tab. 4-5: Cation exchange capacity and initial cation occupancies composition of MX-80 bentonite used for the modelling of bentonite porewaters

(see Chapter 7)

Cation	**Initial occupancy** [meq kg^{-1}]	**Initial occupancy** [site fraction]
Na^+	668	0.843
K^+	13	0.016
Mg^{2+}	40	0.051
Ca^{2+}	66	0.083
Sr^{2+}	4	0.005
Ba^{2+}	1	0.001
CEC*	792	

* The original value quoted by Bradbury & Baeyens (2002) without Sr and Ba was 787 ± 48 meq kg^{-1}.

Dohrmann et al. (2012a) measured CEC values of three bentonites selected as potential backfill materials in various countries (MX-80, Milos and Ashapura). They used the "Cu-trien" method, in which a known amount of the highly selective Cu-triethylenetetramine complex is added to a slurry of clay. After reaction with the clay, the CEC was determined from the difference between initial and final concentration of the "Cu-trien" complex in the supernatant of the centrifuged slurry. The experiments were replicated by five different laboratories and the concentrations were measured both photometrically (VIS) and by ICP-AAS. The results, shown in the first two data rows of Tab. 4-6, indicate satisfactory agreement and, most importantly, surprisingly similar CEC values for all three types of bentonites. The range of variation including the bounding values of the analytical uncertainties is 791 – 902 meq kg^{-1}. In a companion study by Dohrmann et al. (2012b), the influence of using different high-selectivity exchange complexes (ammonium acetate or ammonium chloride instead of Cu-trien) was studied on the same bentonite samples. Higher CEC values, in the range 821 – 944 meq kg^{-1}, were obtained when such "alternative extraction methods" were used.

Tab. 4-6: Summary of results on CEC determinations from the interlaboratory study of Dohrmann et al., Dohrmann et al. (2012a, 2012b)

Averages (AVG) and standard deviations (± SD) from multiple analyses of duplicate determinations are given in meq kg^{-1}.

Bentonite / **Method**	**MX-80**		**Dep. CAN**		**ASHA**	
	AVG	**± SD**	**AVG**	**± SD**	**AVG**	**± SD**
Cu-trien (VIS)	839	15	822	19	865	22
Cu-trien (ICP-AAS)	848	42	826	35	863	39
Alternative methods	846	23	851	30	908	36

Dohrmann et al., Dohrmann et al. (2012a, 2012b) also determined the amounts of major exchangeable cations (Na, K, Ca and Mg) in the three bentonites. In the ideal case, the sum of exchangeable cations in charge equivalents should yield the CEC value obtained from the decrease in Cu-trien (or other selective complex) concentration. The sums, however, turned out to be systematically higher than CEC values determined via Cu-trien. The excess varies from 3% to 25% and can be ascribed to the effect of dissolving minor solids, particularly gypsum or NaCl impurities. This may explain the lower CEC of 787 ± 48 meq kg^{-1} determined by Bradbury & Baeyens (2002), who took care to explicitly determine the contributions of such minor solids and thus were able to correct for such effects. Adding the 70 meq kg^{-1} Ca contribution from gypsum dissolution and the 1 meq kg^{-1} contribution from NaCl, an uncorrected equivalent sum of 858 meq kg^{-1} is obtained from Bradbury & Baeyens (2002), which compares well with the MX-80 range determined in Dohrmann et al., Dohrmann et al. (2012a, 2012b).

In summary, it can be concluded that variations of CEC values of bentonites suitable for use as repository backfill materials are moderate, as they vary within a range of 10 – 20% in terms of absolute values, independently of the type of bentonite and the method used for the determination. Therefore, differences in CEC values arising from the choice of different bentonite types are not expected to greatly affect porewater chemistry. In contrast to this, a change in the major exchanged cation will certainly have a large impact. A Ca-dominated bentonite will react differently and have a reduced swelling capacity compared to a Na-dominated bentonite such as Wyoming MX-80 (Karnland et al. 2006).

4.5 Tunnel support structures

The HLW emplacement drifts must provide sufficient mechanical stability during the construction and operational phases, while minimising damage and changes in the adjoining host rock. As mentioned in Chapter 2, such stability will chiefly be provided by a segmental liner consisting of pre-cast concrete elements and adequate filling material to seal residual void spaces between the liner and Opalinus Clay host rock (annulus grout; see Fig. 4-4) according to the provisional design. The long-term support of the tunnel structure will be provided by the bentonite backfill which will become saturated over time.

4.5.1 Tunnel support materials considered for SGT-E2

In the Sectoral Plan Stage 2 (SGT-E2), shotcrete was considered as the material for rock support (see Bradbury et al. 2014). At that time, a generic low-pH shotcrete[13] formulation as defined within the scope of the ESDRED project was considered as a representative material (Alonso et al. 2009) (see Tab. 4-7). The equilibrium water chemistry for this shotcrete material, calculated at 25 °C and 1 bar total pressure, is given in Tab. 4-8, along with transport properties. These chemical compositions served as input for reactive transport calculations carried out in the context of SGT-E2 to predict chemical reactions with porewater at the liner/bentonite and liner/Opalinus Clay interfaces and are summarised in Section 6.6.

[13] The qualification "low-pH" may be confusing. Low pH cements are formulated such that portlandite is not part of the stable mineral assemblage. However, it is clear that porewater interacting with a drift support structure made of low pH cement will still become sufficiently alkaline to induce chemical changes in the adjacent bentonite and Opalinus Clay, leading to local pH increase and new secondary phases in the clay materials at both interfaces.

Tab. 4-7: Phase composition calculated for the low-pH ESDRED shotcrete

The total mass of 2,388.4 g includes 118.9 g of aqueous solution phase (after Berner et al. 2013).

Phase	**Stoichiometry**	**Mass** [g]
Solid solutions		
Jennite	$(SiO_2)(CaO)_{1.667}(H_2O)_{2.1}$	324.58
Tobermorite_II	$(SiO_2)(CaO)_{0.833}(H_2O)_{1.333}$	
Al-ettringite	$Ca_6Al_2(SO_4)_3(OH)_{12}(H_2O)_{26}$	38.88
Fe-ettringite	$Ca_6Fe_2(SO_4)_3(OH)_{12}(H_2O)_{26}$	
Hydrotalcite	$Mg_4Al_2(OH)_{14}(H_2O)_3$	11.31
Fe-hydrotalcite	$Mg_4Fe_2(OH)_{14}(H_2O)_3$	
Pure phase		
Gibbsite	$Al(OH)_3$	1.45
Barite	$BaSO_4$	3.27
Calcite	$CaCO_3$	10.56
Hydro-magnetite	$Fe_3O_4(H_2O)_2$	0.005
Ferrihydrite	$Fe(OH)_3$	7.27
Illite	$K_{0.6}Mg_{0.25}Al_{2.3}Si_{3.5}O_{10}(OH)_2$	17.42
Celestite	$SrSO_4$	0.004
Inert SiO_2*	SiO_2	1,784.7

* The term "Inert SiO_2" mainly includes non-reacting concrete aggregates. As the name suggests, this component does not undergo any chemical reaction in the calculations but was assigned the chemical and physical properties of quartz for keeping track of mass, volume and necessary physical parameters.

Tab. 4-8: Low-pH ESDRED shotcrete: calculated equilibrium pore solution
After Berner et al. (2013) and transport properties

pH	11.07
Eh	-180.7 mV
Ionic strength [M]	0.150
Element	**Concentration** [mmol/kg]
Al	0.12
Ba	2.2×10^{-4}
C	0.0168
Ca	5.39
Cl	124.3
Fe	3.9×10^{-5}
K	25.71
Mg	$1.2E \times 10^{-4}$
Na	104.9
S	7.88
Si	0.353
Sr	0.41
Transport properties	
Porosity (-)	0.18
D_p (m^2 s^{-1})	4.9×10^{-11}

4.5.2 Tunnel support by segmental liner and annulus grout

In the updated provisional design for the documentation for the general licence application, the HLW emplacement drifts will be supported by segmental liner elements manufactured from pre-cast concrete elements (tubbing), and the void space between the liner and the rock will be filled with an annulus grout material (Fig. 4-4). This is a low-viscosity two-compound mortar consisting of a mixture of cement, bentonite, sand, and a reactive component for hardening. The use of segmental liner and filling grout is related to the revised construction concept with a tunnel boring machine, which is considered to be more efficient and will result in more radially symmetric tunnel geometries.

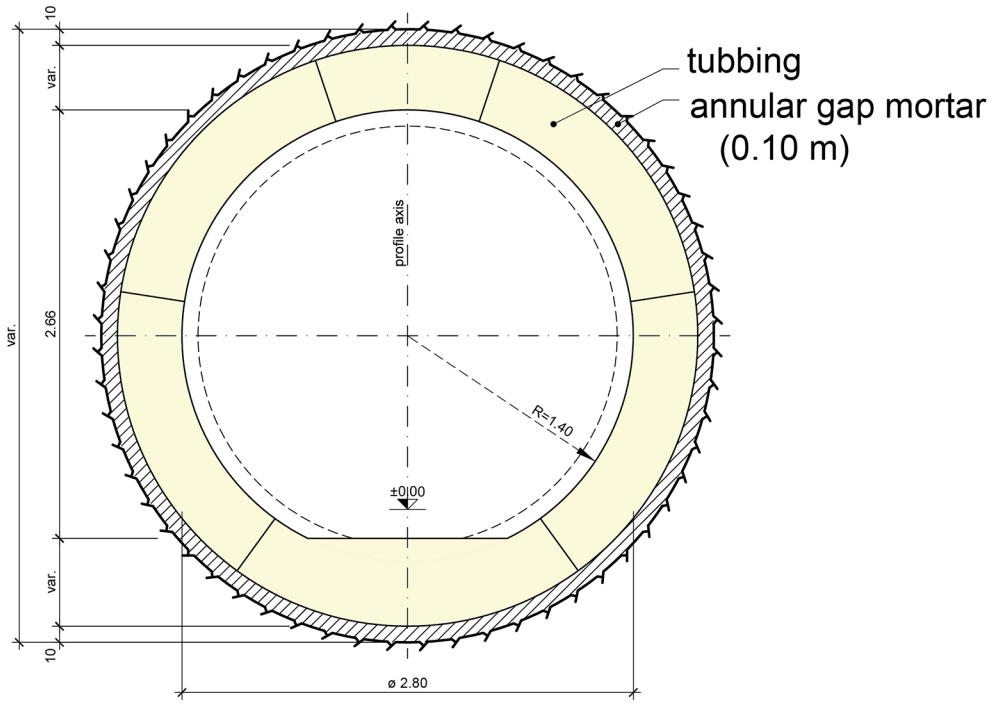

Fig. 4-4: Cross-section of a waste emplacement drift, showing the segmental tubbing liner (yellow, 0.4 m thick for NL according to the provisional design) and the external gap-filling material (cross-hatching)

4.5.2.1 Tubbing concrete

The tubbing will consist of a low-pH concrete, the composition of which is given in Tab. 4-9. The provisional composition is based on a Portland cement (CEM II/A-D, Fortico from Holcim, Switzerland) blended with silica fume to provide the necessary high mechanical strength and to ensure that all portlandite is dissolved[14] as a result of the pozzolanic reaction, through which the very fine silica from the microsilica reacts with portlandite to form C-S-H phases.

Tab. 4-9: Provisional composition of a tubbing concrete (strength class C60/75)

Material	**kg/m^3**
Cement (CEM II/A-D 52.5R)	339
Silica fume	41
Sand 0/1	570.02
Sand 0/4	294.2
Gravel 4/8	349.37
Gravel 8/16	625.18
Water/binder ratio	0.43
Superplasticiser	6.5

The porewater composition and the mineralogy after equilibration, calculated using the GEM/Selektor code (Kulik et al. 2013), are given in Tab. 4-10 and Tab. 4-11. The modelling approach is documented in Kosakowski (2023). The equilibrated system represents a typical freshly hydrated concrete, with a high pH due to the alkalis in the porewater. The mineralogical composition is characterised by the presence of large amounts of C-S-H in the form of jennite and tobermorite, with some additional ettringite, siliceous hydrogarnet, hydrotalcite and calcite. As expected, there is no portlandite present as the excess of silica fume leads to its complete dissolution. The phases denoted as “Inert quartz” and “quartz” represent parts of the aggregates considered to be inert and reactive, corresponding to large and small particle sizes, respectively.

[14] Note that if portlandite is in equilbrium with cement porewater, pH is buffered > 12.5 at 25 °C, 1 bar.

Tab. 4-10: Tubbing concrete pore water composition, and other water and system properties, calculated with GEM-Selektor at 25 °C and 80 bar

Elements/independent components	**Total elemental concentration** [mol/kg]
Al	2.92×10^{-3}
C	4.08×10^{-3}
Ca	1.18×10^{-4}
Cl	8.39×10^{-6}
Fe	4.89×10^{-7}
H	1.06×10^{2}
K	0.49
Mg	5.22×10^{-10}
Na	0.13
O	54.01
S	0.20
Si	9.78×10^{-4}
Sr	7.14×10^{-6}
Other properties	
Water/solid ratio [L kg^{-1}]	0.43
Liquid volume fraction [-]	0.135
Ionic strength [M]	0.683
pH [-]	13.1
Eh [V]	-0.242

Tab. 4-11: Mineralogical composition of tubbing concrete after equilibration, calculated with GEM-Selektor at 25 °C and 80 bar

	Volume fraction	**Mass** [kg]	**Mass fraction based on dry weight** [-]
Pore solution	0.135	0.14	
Jennite	0.149	0.345	0.156
Tobermorite-14Å	5.229×10^{-3}	0.0123	5.559×10^{-3}
C3AS0.84H4.32	8.647×10^{-3}	0.0242	0.0109
Ettringite	0.032	0.0568	0.0257
Calcite	1.346×10^{-3}	3.648×10^{-3}	1.651×10^{-3}
Magnetite	8.905×10^{-5}	4.631×10^{-4}	2.096×10^{-4}
Ferrihydrite (mc)	4.272×10^{-3}	0.0111	5.008×10^{-3}
OH-hydrotalcite	8.670×10^{-3}	0.0175	7.901×10^{-3}
Inert aggregate	0.557	1.48	0.668
Quartz aggregate	0.0995	0.264	0.119

4.5.2.2 Annulus grout

A two-component mortar (“annulus grout”) is foreseen for filling the void space behind the segmental liner according to the provisional design. Component A consists of cement, silica fume, limestone filler and sand and is mixed with pre-saturated bentonite and water. The bentonite maintains a very high amount of water in the cement. The annulus grout is activated by reactive component B, which, according to the current concept, is sodium-water glass. The injection of the components A and B behind the segmental liner will cause rapid setting of the material within about 20 – 30 seconds, to ensure a force-closure between the segmental liner and the host rock. This is necessary to ensure that the gripper of the tunnel-boring machine can be held onto the preliminarily emplaced tubbing ring for the next advance of 0.8 m. The composition of a provisional annulus grout, considered for the documentation of the current licence application, is given in Tab. 4-12.

Tab. 4-12: Composition of a provisional annulus grout

		Proposed system
	kg per m^3 of Comp. A	
Comp. A	CEM II/B-LL 32.5R	180 kg
	Bentonite	30 kg
	Quartz sand (coarse)	670 kg
	Limestone powder (fine)	300 kg
	Microsilica	6.5 kg
	Water	560 kg
	Retarder	4.0 kg
	Sum for 1 m^3 Comp. A	**1,750 kg = 1,000 L**
Comp. B	Sodium silicate (water glass)	110 kg

The generic recipe has been implemented accordingly in the GEM-Selektor (for details see Kosakowski 2023). After equilibration, the hydrated cement material has a very high water content, which results in a saturated porosity of 52.5 volume % (see Tab. 4-13). The pH is close to 14 due to the high sodium hydroxide concentrations induced by the water glass addition, which also explains the high ionic strength (1.85 M). The total dissolved carbonate content of the solution is very high, and is related to the stability of the $Na(CO_3)^-$ complex.

After the hydration reaction, the solid assemblage is dominated by calcite, tobermorite and jennite (Tab. 4-14). Minor amounts of hydrotalcite, strontianite and zeolite (sodalite) are also present. Iron is bound entirely to ferrihydrite, in line with the high Eh as a result of the model setup. The smectite and large parts of the quartz (aggregate) were kinetically controlled and were not allowed to react during equilibration (for details concerning the model setup see Kosakowski 2023).

Due to the calculated high ionic strength of the solution, the very simplistic representation of water glass as $((NaOH)_{2.5}SiO_2H_2O)_{0.2}$ in the thermodynamic database and the missing temperature-dependence of thermodynamic data, the calculation of the composition has to be made with care.

The reactive transport calculations indicate that the initially high ionic strength of the cementitious pore solution (actually outside the permitted limits of the Debye-Hückel activity model) will quickly decrease and equilibrate with the contacting solutions. Eventually, a uniform ionic strength across the whole section of materials at values well within the applicability limit of the activity model used is reached.

Tab. 4-13: Grout porewater composition and other system properties calculated with GEM-Selektor at 25 °C and 80 bar

Elements/independent components	**Total elemental concentration** [mol/kg]
Al	3.04×10^{-4}
C	0.51
Ca	2.72×10^{-5}
Cl	8.10×10^{-4}
Fe	2.02×10^{-6}
H	99.47
K	0.031
Mg	2.25×10^{-9}
Na	2.32
O	52.23
S	0.088
Si	0.024
Properties	
Water:solid ratio [L kg^{-1}]	0.55
Liquid volume fraction [-]	0.525
Ionic strength [M]	1.85
pH [-]	13.9
Eh [V]	0.4

Tab. 4-14: Mineralogical composition of the grout after equilibration with GEM-Selektor at 25 °C and 80 bar

	Volume fraction	**Mass** [kg]	**Mass fraction based on dry weight** [-]
aq_gen	0.524	0.593	0
Smectite_MX80	0.0142	0.0293	0.024
Jennite	0.0818	0.189	0.155
Tobermorite 14Å	1.380×10^{-3}	3.241×10^{-3}	2.656×10^{-3}
Calcite	0.114	0.309	0.253
Ferrihydrite-mc	1.810×10^{-3}	4.687×10^{-3}	3.841×10^{-3}
OH-hydrotalcite	3.340×10^{-3}	6.725×10^{-3}	5.512×10^{-3}
Sodalite (OH)	7.912×10^{-3}	0.0179	0.0146
Inert aggregate	2.384×10^{-3}	6.314×10^{-3}	5.175×10^{-3}
Quartz aggregate	0.247	0.654	0.536
Strontianite	2.363×10^{-8}	8.943×10^{-8}	7.329×10^{-8}

Modelling of these reactions with the generic material compositions presented above has been conducted with the help of reactive transport calculations (for details see Kosakowski 2023). These results are summarised in Section 6.7 and compared with those of analogous calculations for the tunnel support system with shotcrete.

4.6 Opalinus Clay porewater chemistry

Bentonite porewaters serving as a basis for the quantification of radionuclide solubility limits and sorption coefficients for safety assessment calculations have been calculated by modelling cation exchange and solubility equilibria after reaction between the intruding Opalinus Clay porewater and MX-80 bentonite with the initial state characteristics defined in Section 7.3. Therefore, the Opalinus Clay porewater compositions are also an integral part of the initial state of the repository system.

Because the bentonite porewater (BPW) calculations were carried out before the end of the bore-hole drilling campaign, preliminary Opalinus Clay water (OPAw) compositions had to be used. These are based on borehole data from the Nördlich Lägern and Zürich Nordost regions available at that time and differ only slightly from the final ones documented in Mäder & Wersin (2023). A comparison of the preliminary and finalised OPAw compositions is given in Tab. C-1, App. C, along with a short discussion.

Opalinus Clay porewaters sampled from the Nördlich Lägern and Zürich Nordost regions proved to be very similar to the extent that the specification of distinct porewaters for the two regions was judged unnecessary. Therefore, a unified OPAw (denoted NL-ZNO) was defined in four variants (Tab. 4-15): a reference OPAw in equilibrium with a pCO_2 of $10^{-2.2}$ bar, low and high pCO_2 variants thereof in equilibrium with pCO_2 of $10^{-2.8}$ bar and $10^{-1.8}$ bar, respectively, and a

high salinity water based on the data from the Bülach borehole. Compared to those extracted from Jura Ost (JO) borehole samples (not shown, see Mäder & Wersin 2023 for details), NL-ZNO OPAw are more saline and poorer in sulphate.

All Opalinus Clay waters were computed at 25 °C and 1 bar total pressure, assuming saturation equilibria with $CaCO_3$ (calcite), $CaMg(CO_3)_2$ (dolomite), SiO_2 (quartz), $SrSO_4$ (celestine), $FeCO_3$ (siderite) or Fe_3O_4 (magnetite)[15], FeS_2 (pyrite), CaF_2 (fluorite), $Al_2Si_2O_5(OH)_4$ (kaolinite), $BaSO_4$ (barite) and $MnCO_3$ (rhodochrosite). The imposed CO_2 partial pressures ($10^{-2.8}$, $10^{-2.2}$ or $10^{-1.8}$ bar) correspond closely to the range used in SGT-E2, for which a slightly higher lower limit of $10^{-2.5}$ bar was assumed (see Tab. C-1 in Bradbury et al. 2014).

Tab. 4-15: Opalinus Clay porewaters used as input for BPW calculations (25 °C, 1 bar)

Region =>	**Nördlich Lägern – Zürich Nordost (NL-ZNO)**		**Bülach (NL)**	
GEMS ID => Nagra ID =>	OPAw_NL-ZNO-28 E3-OPW_lowpCO2	OPAw_NL-ZNO-22 E3-OPW-Ref	OPAw_NL-ZNO-18 E3-OPW_highpCO2	OPAw_BUL-28 E3-OPW_sal
log $p(CO_2)$/bar	-2.79	-2.20	-1.80	-2.81
pH	7.40	7.10	6.90	7.37
pe	-3.22	-2.83	-2.58	-3.17
Eh	-0.190	-0.167	-0.152	-0.187
IS /m	0.317	0.319	0.321	0.509
Total element concentrations (molality)				
Al	2.13×10^{-8}	2.09×10^{-8}	2.86×10^{-8}	2.05×10^{-8}
Ba	1.56×10^{-7}	1.57×10^{-7}	1.58×10^{-7}	1.81×10^{-7}
C(IV)	1.07×10^{-3}	2.21×10^{-3}	3.68×10^{-3}	1.02×10^{-3}
Ca	2.01×10^{-2}	2.03×10^{-2}	2.05×10^{-2}	2.90×10^{-2}
Cl	0.239	0.240	0.241	0.407
F	1.74×10^{-4}	1.74×10^{-4}	1.74×10^{-4}	1.71×10^{-4}
Fe	7.14×10^{-6}	2.56×10^{-5}	5.95×10^{-5}	9.08×10^{-6}
K	2.13×10^{-3}	2.13×10^{-3}	2.14×10^{-3}	2.74×10^{-3}
Mg	1.43×10^{-2}	1.45×10^{-2}	1.46×10^{-2}	1.89×10^{-2}
Mn	8.16×10^{-5}	8.24×10^{-5}	8.33×10^{-5}	1.07×10^{-4}
Na	0.215	0.215	0.216	0.368
S(VI)	2.29×10^{-2}	2.29×10^{-2}	2.29×10^{-2}	2.98×10^{-2}
Si	1.73×10^{-4}	1.72×10^{-4}	1.72×10^{-4}	1.68×10^{-4}
Sr	3.67×10^{-4}	3.70×10^{-4}	3.73×10^{-4}	4.19×10^{-4}

[15] In the pH region of interest and specified pCO_2 range ($10^{-2.8}$ to $10^{-1.8}$ bar), siderite and magnetite cannot coexist at thermodynamic equilibrium. Magnetite is the stable Fe-solid along with pyrite. See discussions in Section 7.6.4 and App. C in Curti (2023) for details.

5 The elevated temperature period and its influence on the properties of bentonite

5.1 Temperature evolution in the HLW Near-field

5.1.1 Introduction

Even after decades of interim storage, the residual decay heat generated by the HLW will be sufficient to cause, after repository closure, a temporary rise in temperature within the engineered barrier system (EBS) and the surrounding host rock. Understanding the magnitude and duration of this high-temperature pulse is essential. It is the basis for predicting potential physical-chemical alterations of engineered barrier materials (particularly bentonite and, to a lesser extent, the host rock) that might affect the integrity of the barriers and consequently alter radionuclide pathways. Reliable predictions of the temperature evolution in the repository near-field require a careful assessment of boundary conditions and the coupling of heat transfer calculations with other hydro-mechanical processes. Necessary input data are, e.g., the amounts, initial states and geometry of the component materials, the heat produced by the radioactive waste at the time of repository closure and thereafter, the spatial separation between canisters along and across the emplacement drifts, the initial water contents of bentonite, thermal conductivities of engineered barrier materials and host rock, and knowledge of the baseline underground temperature.

In the first part of this chapter, previous predictions of thermal evolution for the "Entsorgungs-nachweis" feasibility demonstration and later for the SGT-E2 scenario reported in Bradbury et al. (2014) are briefly discussed. While the former calculations were carried out using a model based on heat conductivity only, the SGT-E2 calculations were carried out with a refined model that includes coupling of thermal-hydraulic processes (Senger & Ewing 2008, Papafotiou & Senger 2014). Finally, an update of the latter model, taking into account the increased repository depth for the repository at the Haberstal site, will be presented. This latter calculation will serve as a basis for the evaluation of long-term chemical processes operating in the near-field.

5.1.2 Thermal evolution calculations

In an earlier demonstration of disposal feasibility (Project "Entsorgungsnachweis"), the post-closure temperature evolution in the emplacement drifts of a HLW repository was assessed using a 3D finite-element model for two limiting cases with high and low water contents in bentonite (Johnson et al. 2002). For the latter case, a moisture content of 2 wt.% was assumed, corresponding to a thermal conductivity of 0.4 W m^{-1} K^{-1} and a heat capacity of 1.2 MJ m^{-3} K^{-1}. For the former case, water-saturated bentonite was assumed, with a thermal conductivity of 1.35 W m^{-1} K^{-1} and heat capacity of 2.4 MJ m^{-3} K^{-1}. These values were taken as constant over time. Heat transport was assumed to occur entirely by conduction, i.e. ignoring generation of water vapour at temperatures above 100 °C and heat transfer by convection.

In order to reduce uncertainties and introduce more realism, an updated model was developed by Senger & Ewing (2008). In contrast to the model of Johnson et al. (2002), the refined model included two-phase flow processes associated with the early post-closure period, as well as consideration of the two distinct types of buffer materials: bentonite blocks foreseen for support of the canisters during emplacement and granular bentonite (pellets) foreseen as drift backfill material. The blocks are denser and generate higher swelling pressures upon saturation than the bentonite pellets, for which an initial water content of 2 wt.% was assumed. In contrast, up to 18 wt.% initial water was assumed at the time of sealing for the bentonite blocks, due to the prolonged exposure to humid air during the construction phase. Thermal conductivities were assumed to vary linearly with the water content from 0.4 to 1.35 W m^{-1} K^{-1} for bentonite between

2 wt.% and 100 wt.% moisture content (fully saturated bentonite). Values for the heat generation from the waste canisters were the same as in Johnson et al. (2002). Conservatively, calculations were performed only for the canister type with the highest heat output (mixed UO_2/MOX assemblies).

Fig. 5-1 shows the temperature evolution predicted by Senger & Ewing (2008) at different locations in the near-field. At the upper canister/bentonite boundary, the temperature increases rapidly after repository closure, reaching a peak of ~ 130 °C after about 4 years (curve Bent1-WP in Fig. 5-1). The bottom of the waste canister, which sits on top of the water-rich and thus more conductive bentonite blocks, reaches only 115 °C (curve B2-WP). This leads to evaporation of the moisture in the pellets, initiating vapour convection processes. In the central and outer part of the bentonite, temperatures are always below 100 °C, allowing the saturation front from the host rock to advance.

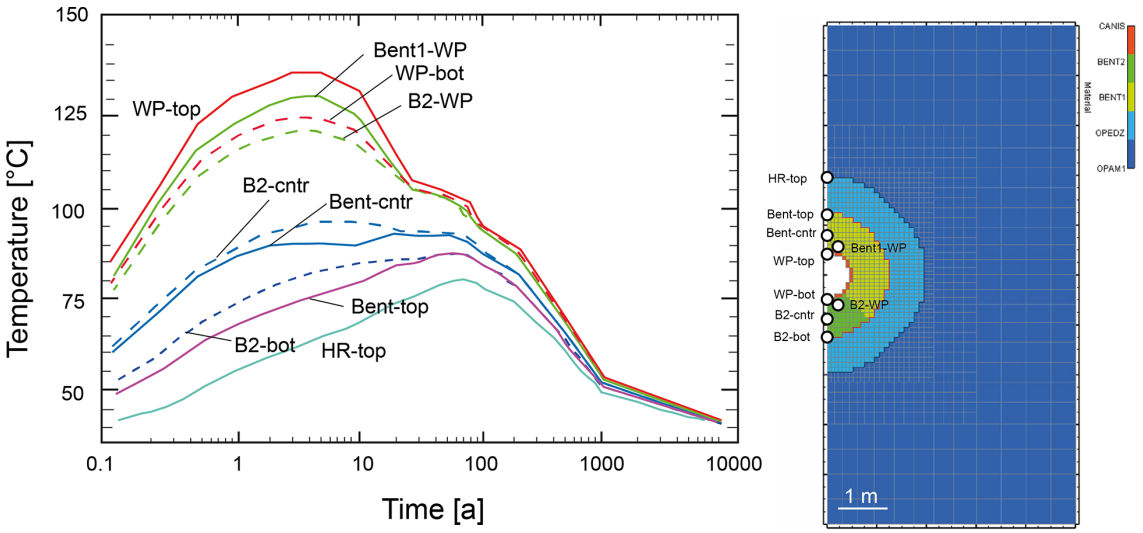

Fig. 5-1: Time-dependent temperature evolution in the vertical plane above (solid lines) and below (dashed lines) the axis of the UO_2/MOX canister

WP: canister hull, Bent1/B2-wp: bentonite next to WP, Bent/B2-cntr: in the centre of the bentonite, Bent/B2-top/bot: bentonite next to EDZ, HR-top: host rock. (Figure redrawn after Senger & Ewing 2008 Fig. 4-8 top right.)

Between 60 and 80 years, the temperature decreases to less than 100 °C everywhere in the near-field, and the bentonite becomes fully water-saturated. Senger & Ewing (2008) calculate a significantly lower peak temperature at the top of the canister surface (~ 135 °C) compared to the corresponding calculation for MOX fuel of Johnson et al. (2002) for unsaturated bentonite (~ 160 °C, low bentonite conductivity case, Fig. 17 in op. cit.) as a consequence of the heat-consuming water evaporation process included in their model. As expected, peak temperatures calculated by Johnson et al. (2002) assuming full bentonite saturation are lower (~ 100 °C, high bentonite conductivity case, Fig. 16 in op. cit.) than those predicted by Senger & Ewing (2008). The model of Senger & Ewing (2008) predicts that, during the first years, the gas phase in the bentonite consists of as much as 25% water vapour.

Although more advanced than earlier models relying solely on heat conduction, the model of Senger & Ewing (2008) still has some limitations. It is a purely thermal-hydraulic (TH) model that does not include chemically induced effects, e.g. hydrogen production due to canister corrosion and the evaporation-induced increase in porewater salinity, which could modify the solubilities of gases (CO_2, H_2) and minerals. These and other aspects were taken into account in the refined 3D model of Senger et al. (2014) who included, in addition to water evaporation, the effect of hydrogen gas evolution and of background temperature as a function of depth. Three cases were computed for 450 m, 600 m and 750 m repository depths using measured temperature profiles from boreholes. In spite of the consideration of the aforementioned effects, a temperature evolution similar to that predicted in the simpler model of Senger & Ewing (2008) was computed.

The model of Senger et al. (2014) was recently re-applied to the siting region for a repository depth of ~ 900 m, where rock background temperatures are higher (Nagra 2024g). The calculated thermal evolution is presented in Fig. 5-2 and a comparison of predicted temperatures at specific near-field locations for the three scenarios discussed so far is presented in Tab. 5-1.

While the former SGT-E2 calculations of Senger & Ewing (2008) and Senger et al. (2014) yield very similar results, the new calculations result in higher temperatures as a consequence of the greater depth of the repository. Specifically, in the updated calculations, near-field temperatures exceeding 100 °C last for several hundred years after repository closure. At 10,000 years after repository closure, thermal equilibrium with the host rock is not yet achieved. For instance, the temperature in the whole bentonite buffer at that time is still ~ 55 °C against a background temperature of ~ 47 °C in the Opalinus Clay (Nagra 2024g).

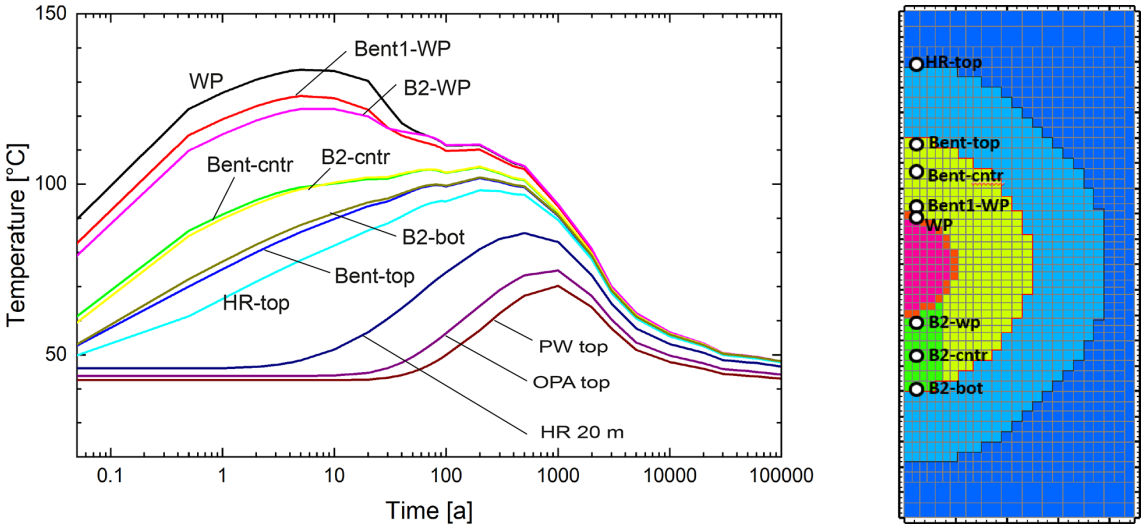

Fig. 5-2: Time-dependent temperature evolution in the HLW near-field for UO_2/MOX canisters according to the 3D model of Senger et al. (2014), recalculated for a repository excavated at ~ 900 m depth

The positions to which the curves refer are reported in the vertical cross-section shown on the right.

WP: canister hull; Bent1/B2-wp: bentonite next to WP; Bent/B2-cntr: in the centre of the bentonite; Bent/B2-top/bot: bentonite next to EDZ; HR-top (at 2 m distance from the tunnel axis); HR-20 m (at 20 m distance from the tunnel axis); OPA top (at 50 m distance from the tunnel axis); PW top (at 75 m distance from the tunnel axis in the overlying bedrock, corresponding to the outer end of the implemented model setup).

Tab. 5-1: Comparison of temperature evolution in the HLW repository near-field computed with the models of Senger & Ewing (2008) (SE08) and Papafotiou & Senger (2014) (SA14)

All temperatures are given in °C, in blue for T < 100 °C, in red for T ≥ 100 °C. The times when the indicated temperature maxima are reached are indicated (column "max"), as well as the periods during which temperatures are lower than 100 °C (column "T < 100 °C").

B-WP = bentonite-waste package interface (upper side)
B-cntr = centre of bentonite (upper side)
B-top = bentonite-Opalinus Clay interface (upper side)
HR-top = top of EDZ at 2 m distance from the tunnel axis
SE08 = Senger & Ewing (2008)
SE14 = Senger et al. (2014), Papafotiou & Senger (2014)
SA23 = Recalculated with the model of Papafotiou & Senger (2014) for a repository at ~ 900 m depth

Position	**SE08**		**SE14 (SGT-E2)**		**SA23 (RBG)**	
	max	T < 100 °C	max	T < 100 °C	max	T < 100 °C
B-WP	130 (4 a)	> 80 a	127 (5 a)	> 100 a	127 (5 a)	> 650 a
B-cntr	93 (60 a)	Always	95 (60 a)	Always	105 (200 a)	> 500 a
B-top	88 (65 a)	Always	87 (80 a)	Always	103 (200 a)	> 350 a
HR-top	80 (65 a)	Always	82 (98 a)	Always	98 (200 a)	Always

5.1.3 Summary

Three different calculations of thermal evolution coupled with hydro-mechanical processes applied to the Swiss HLW repository setup, based on two model variants, were discussed and compared. In all three calculations, a conservative heat output of ~ 1,500 W (mixed UO_2/MOX fuel canisters) has been assumed. In the first (simpler) model of Senger & Ewing (2008), already discussed in Bradbury et al. (2014), water evaporation and convection is coupled with heat conduction, but chemically induced effects are ignored. The second calculation (Senger et al. 2014), also applying to SGT-E2, relies on a more refined 3D model and, in addition to evaporation and convection, also takes into account the effect of hydrogen production. Both calculations relate to the setup defined in SGT-E2 and yield very similar temperature curves. Finally, the third calculation presents an update of the model of Senger et al. (2014) (SA14-RBG), by assuming a greater repository depth (~ 900 m vs. 600 m) and thus higher host rock background temperatures. Compared to the SGT-E2 calculations, the updated calculation leads to higher temperatures for longer periods of time. Temperatures slightly exceeding 100 °C are predicted to occur across the entire bentonite section and last over several hundred years. Moreover, bentonite temperatures at 10,000 a after repository closure are higher (~ 55 °C) than the background host rock temperatures (~ 47 °C, Nagra 2024g), while in the SGT-E2 calculations all near-field components are nearly in thermal equilibrium with the host rock at that time.

5.2 Chemical stability of bentonite at elevated temperatures

Section 5.2 focuses on the effects of the thermal transient period on the chemical stability of bentonite. It should be noted that the processes and phenomena occurring at the external (tunnel support/bentonite) and internal (bentonite/canister) interfaces during this period are discussed in other chapters (Chapter 6 and Chapter 8). The updated temperature evolution calculations for a repository at a depth of ~ 900 m in the siting region (Fig. 5-2) will serve as a basis for the evaluation. Specifically, they indicate that temperatures in the bentonite will constantly exceed 100 °C for up to 500 – 800 years after repository closure. During this period, water saturation will be high enough to allow for chemical processes to occur. The bentonite buffer temperature will decrease from a peak of 125 °C to about 90 – 95 °C within the first 1,000 years after repository closure, then continue to decrease slowly and reach about 55 °C after 10,000 years. At that time, the entire near-field and Opalinus Clay host rock system will still be warmer than the asymptotic background, (~ 56 °C compared to ~ 47 °C pre-repository background temperature, Nagra 2024g) i.e. the tail of the thermal pulse is still propagating.

5.2.1 Dissolution/reprecipitation of calcium sulphate and silica

The discussion in this section is largely based on a review of experimental data collected by Leupin et al. (2014) and other papers selected based on their relevance to the potential impact of the results on the mineralogy and safety-relevant properties of compacted bentonite in the Swiss HLW repository.

Sena et al. (2010) carried out reactive transport calculations to simulate chemical effects following granitic water intrusion into the compacted MX-80 bentonite buffer during the thermal pulse predicted for the representative setup of the Swedish repository. Two main temperature-induced effects affecting bentonite mineralogy were identified:

a) Redistribution of the native $CaSO_4$ inventory in the bentonite buffer due to dissolution of gypsum close to its interface with the host rock and re-precipitation as anhydrite near the advancing water front. The dissolution of gypsum is triggered by strong undersaturation in the inflowing granitic porewater (causing sulphate out-diffusion), while precipitation of anhydrite occurs due to evaporation-induced solute concentration coupled with a positive temperature gradient towards the canister.

b) Enhanced dissolution of SiO_2 (quartz) due to the increased solubility at higher temperatures, with diffusion and reprecipitation towards the cooler host rock.

In the absence of a cementitious tunnel support structure, similar solubility effects would be expected during the thermal pulse in the Swiss HLW repository. Bentonite porewaters contain 59 – 83 mmol/kgw sulphate due to partial dissolution of the gypsum inventory in MX-80 bentonite, against 23 – 30 mmol/kgw in the gypsum-undersaturated Opalinus Clay porewater (see Tab. 7-3 and Tab. 7-4 in Chapter 7), giving rise to out-diffusion of sulphate. During the thermal pulse, anhydrite would precipitate as long as the temperature remains above 58 °C, the gypsum to anhydrite conversion temperature (Hummel & Thoenen 2023). A negative concentration gradient towards the host rock would be established also for dissolved silica, even with porewaters permanently saturated with quartz. In contrast to the sulphate case, where the driving force for out-diffusion (of sulphate) was undersaturation with respect to gypsum/anhydrite in the Opalinus Clay, the silica concentration gradient would be induced solely by the increase in quartz solubility with temperature. Dissolved silica concentration in equilibrium with quartz would therefore be higher in the hot internal part of the bentonite compared to the cooler external part, leading to a net flux of silica and subsequent SiO_2 precipitation towards the host rock.

Such a model is, however, too simplistic when applied to the current setup of the HLW repository, as the design foresees a cementitious tunnel support structure with silica-rich aggregates acting as additional sources of sulphate and silica. Due to the strong enhancement of the solubility of silica at high pH and the fine grain size of the reactive aggregates, it can be anticipated that the mentioned solubility increase towards the canister induced by the temperature gradient would be overcompensated by an opposite gradient induced by the high pH in the support structure, thus leading to a flux of silica and precipitation within the nearby bentonite and Opalinus Clay. This expectation is confirmed by the reactive transport calculations discussed later in this report (Section 6.7, Fig. 6-8).

5.2.2 Stability of montmorillonite

One of the most significant issues related to temperature increase is its potential impact on the chemical stability of montmorillonite, the main mineral in bentonite. The properties of compacted bentonite are critical to several safety functions, including low hydraulic conductivity, high sorption capacity, and small diffusivities. In combination, these properties slow down solute transport, allowing the decay of short-lived and many long-lived radionuclides before they reach the host rock. Additionally, water-saturated bentonite provides sufficient swelling pressure, acts as a filter for radiocolloids, minimises microbial activity, and ensures a sufficiently high heat conductivity.

It is thus of relevance to understand whether mineralogical changes in montmorillonite potentially affecting the mentioned properties could occur as a response to the predicted thermal pulse. Geochemical reactions are typically faster at high temperatures and in the presence of water, making this issue particularly important during and after the resaturation of the bentonite buffer. According to the predicted thermal evolution for saturated conditions (Fig. 5-2), the temperature range of interest is approximately about 55 – 125 °C for the period up to 10,000 years.

This section discusses the potential effects of temperature increase on the chemical stability of smectite clay minerals, including montmorillonite, based on a previous review by Leupin et al. (2014) and recent geological evidence from diagenetically overprinted sedimentary basins. It is to be noted that other bentonite alteration processes, such as chemical reactions involving bentonite at the interfaces to the tunnel support structure and canister, are discussed separately in Chapter 6 and Chapter 8, respectively.

Natural bentonites are typical alteration products of Al/Si-rich volcanic ash. They are formed in low-temperature surface environments, such as soils and sediments (Huggett 2005, Inoue 1995). Smectitic clays may also form in hydrothermal systems below ~ 100 °C (Inoue 1995). During diagenesis, montmorillonite is progressively transformed via a series of complex reaction steps to illite, a dioctahedral clay mineral belonging to the mica group (Newman 1987). Compared to montmorillonite, illite has a higher interlayer charge due to substitution of tetrahedral Si^{4+} by Al^{3+}, as evident by comparing the following typical structural formulae:

montmorillonite (sample #6, Tab. 1.15 in Newman (1987)):

$$Na_{0.465} <Al_{1.58}Fe^{III}_{0.005}Mg_{0.40}> [Al_{0.015}Si_{3.985}O_{10}] (OH)_2 \cdot nH_2O \quad (5\text{-}1)$$

illite (sample #5, Table 1.22 in Newman (1987)):

$$K_{0.68}Ca_{0.05}Na_{0.03} <Al_{1.50}Ti_{0.05}Fe^{III}_{0.04}Fe^{II}_{0.07}Mg_{0.36}> [Al_{0.47}Si_{3.54}O_{10}] (OH)_2 \cdot nH_2O \quad (5\text{-}2)$$

Moreover, K^+ is always the dominant interlayer cation in illite, implying that in addition to the temperature increase, a potassium source is required in order to transform Na-montmorillonite into illite (Meunier & Velde 2004).

The reaction may proceed via two distinct mechanisms (Huggett 2005). In the first one, the integrity of the original TOT layers is conserved while tetrahedral Si^{4+} is partially replaced by Al^{3+}:

$$Na\text{-}montmorillonite + Al^{3+} + K^+ \rightarrow Illite + Si^{4+} \quad (5\text{-}3)$$

This mechanism requires external sources of both aluminium and potassium. The second mechanism requires dissolution of the pristine TOT layers and formation of new ones. The source of aluminium is internal, implying that more montmorillonite is dissolved than illite produced:

$$Smectite + K^+ \rightarrow Illite + Si^{4+} \quad (5\text{-}4)$$

In both cases, an excess of silica is produced, usually precipitating in the form of quartz or other SiO_2 solid. The SiO_2 precipitate frequently cements the stacks of clay minerals together, thereby reducing the swelling capacity and the ductility of the buffer.

With increasing temperature, the first step in the illitisation process is the transformation to beidellitic smectites (Sato et al. 1996, Meunier et al. 1998), implying an increase in interlayer charge induced by Al^{3+} for Si^{4+} substitution. This is followed by formation of illite/smectite mixed layers and, finally, complete conversion to illite (Galán & Ferrell 2013).

Beaufort et al. (2001) carried out experiments in which low-charge smectites were exposed to quartz-saturated solutions at temperatures of 100 – 200 °C over 330 days, resulting in partial transformation to beidellite and Mg-rich trioctahedral smectite. The amount of beidellite formed increased with time, temperature and K^+ concentration. Illite/smectite mixed layers were detected, but only at the highest temperature (200 °C) and highest K^+ concentration.

Experiments at elevated temperature were also conducted under unsaturated conditions in several studies. Considerable loss of swelling capacity was observed by Couture (1985) and by Oscarson & Dixon (1989) in the temperature range of 110 – 250 °C with uncompacted bentonite samples. In a later study, Oscarson & Dixon (1990) showed that such effects are not observed if compacted bentonite is used. Pusch (2000) detected only minor changes in swelling pressure and hydraulic conductivity for compacted dry bentonite powders exposed to steam at 90 – 110 °C over 30 days. In a later study carried out with highly compacted MX-80 bentonite pellets (Pusch et al. 2003), a significant reduction of the swelling capacity was observed upon exposure to water vapour at 150 °C. At lower temperatures (110 – 125 °C), the swelling pressure was not reduced compared to MX-80 saturated at room temperature. Electron microscope analyses revealed a contraction of the original clay particle aggregates and cementation with the silica expelled from the dissolved smectite. Although this effect was attributed to cooling-induced thermal stress (and thus probably an artefact), the segregation of silica implies that the original montmorillonite underwent mineralogical changes consistent with an incipient illitisation process. Under unsaturated conditions, smectite to illite conversion rates are considerably slower, as shown by the experimental study of Whitney (1990), at a temperature (250 °C) much higher than the highest temperature expected in the HLW repository near-field.

It is clear that illitisation requires temperatures well above ~ 100 °C and a sufficient supply of K^+ to proceed at rates observable in the laboratory. The crystal-chemical complexity of the montmorillonite-illite conversion process, as well as the lack of adequate thermodynamic models,

make it impossible to determine precise stability criteria. A well-defined temperature above which illite becomes thermodynamically stable probably does not exist, as clay minerals are complex multicomponent solid solutions rather than stoichiometric phases, implying that stability limits are highly composition-dependent. Another obstacle is the slow kinetics of smectite to illite conversion at the temperatures of interest (≤ 125 °C, see Fig. 5-2), which make laboratory observations and extrapolations to relevant time frames difficult.

A number of models have been developed based on the available knowledge to predict illitisation rates as a function of temperature and K^+ concentrations. Such models are based on activation energies derived from large-scale geological studies and use the theoretical framework of Pytte & Reynolds (1989). These authors developed an empirical equation to predict the rate of conversion of smectite to illite (*dS/dt*) as a function of the amount of smectite (*S*), the ratio of K^+ to Na^+ activities in the aqueous phase (*K/Na*), the activation energy (E_A) of the conversion reaction, and temperature (*T)*:

$$-\frac{dS}{dt} = S^a(K/Na)^b A \exp\left(-\frac{E_A}{RT}\right) \quad (5\text{-}5)$$

In eq. 5-5, *a* and *b* are integers describing the reaction order and *A* is the pre-exponential factor associated with the Arrhenius law used for the derivation of the activation energy. This model was calibrated using data on illite content in shales crossed by a thick basaltic dyke where the thermal history could be modelled quite precisely. At 15 m distance from the basalt/clay contact, a thermal pulse with a peak temperature of 150 °C after 10 years was predicted. For this situation, the model predictions of Pytte & Reynolds (1989) are in agreement with observations that 20% of the smectite was converted to illite. Although quite similar to the temperature evolution at the canister-bentonite interface (Fig. 5-1), the results from such models should be used with great caution, considering the number of fitting parameters and large uncertainties of key parameters. For instance, estimates of activation energies are subject to large uncertainties (see Tab. 2-2 in Leupin et al. 2014). Moreover, temperatures of 130 °C or higher are not expected in the Swiss HLW repository near-field (c.f. Nagra 2024f).

5.2.3 Geothermometry of illitisation during diagenesis in sedimentary basins

In order to predict illitisation rates as a function of physical-chemical conditions, regional-scale data on the diagenesis of bentonite beds in sedimentary basins appear to be more useful than the aforementioned models, particularly when multiple, complementary experimental techniques are used to cross-check the results. A considerable number of studies have been published on this subject that include not only a mineralogical description of the smectite-illite conversion, but also its correlation with temperature and duration of the process (Clauer et al. 2014, 2013, Vazquez et al. 2016). Some studies focus on geochemical factors such as salinity and organic matter content, apparently favouring the illitisation process at low temperatures (Li et al. 2016, Kirsimäe et al. 2020, Cifuentes et al. 2021, Ali et al. 2021).

Perhaps the most relevant studies are those of Clauer et al., Clauer et al. (2013, 2014) on the illitisation of bentonite beds from the Appalachians and East Slovak Basin, respectively. In both investigations, K-Ar crystallisation ages were determined on illite particles in combination with oxygen/hydrogen isotope data and other geothermometers. In the former study, fluid inclusions in authigenic feldspar and quartz from the Appalachians suggest illite crystallisation in relatively high-salinity fluids at 100 – 200 °C. Annealing of fission tracks in detrital zircons confirmed that temperatures exceeded 100 °C.

The evidence above is however indirect since these data were obtained from minerals of nearby carbonate rocks rather than from the bentonite itself. The data from the Slovak Basin appear to be more conclusive, since they refer directly to clay particles extracted from the bentonite beds sampled from deep boreholes. The data from Clauer et al. (2014) plotted in Fig. 5-3 indicate a clear correlation between degree of illitisation and present-day temperatures, particularly if the data from bentonites in contact with high-salinity water (green dots) are excluded. The latter points indicate that illitisation is facilitated in the presence of saline brines (possibly because of the increased availability of potassium). The reported temperatures range from 97 °C to 165 °C and correspond to specific borehole depths, which the authors claim to be *"close to the maximum burial"*. Consequently, the present-day temperatures indicated in Fig. 5-3 are considered to be estimates of maximum temperatures reached during illitisation. Consistent with the previous data, two additional independent geothermometers provide similar but somewhat lower temperature ranges for the partially illitised bentonite beds: vitrinite reflectance yielded a range of 70 – 135 °C, while oxygen isotope thermometry indicates a range of 50 – 140 °C.

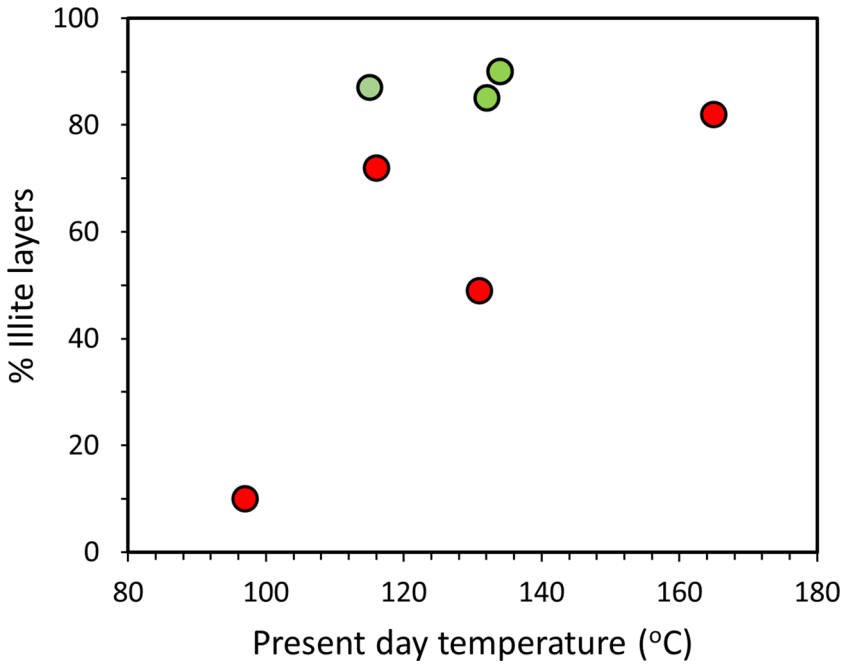

Fig. 5-3: Degree of illitisation as a function of present-day temperatures in bentonite beds from deep boreholes in the East Slovak Basin

Data taken from Tab. 1 in Clauer et al. (2014).
Red symbols: salt-free bentonites; green symbols salt-bearing bentonites.

Other more recent studies attempt to determine the temperature conditions of smectite illitisation and the role of geochemical factors favouring this reaction. Particular emphasis in recent years was given to the role of organic matter (OM). Li et al. (2016) investigated thirty red (oxidised) and black (OM-rich) mudstone samples from the Dongying basin (China) by X-ray diffraction and infrared spectroscopy across a 3,400 m thick stratigraphic column. The OM content was below 0.14% in the red mudstones and between 0.17% and 4.43% in the black samples. They found that, at shallow depths (i.e. at lower temperatures), the OM was preferentially incorporated into the interlayer of smectites. This process, prominent in the black mudstones, apparently delayed the illitisation by hindering dehydration of water from the smectite interlayer. At stratigraphic depths > 3,100 m (higher temperatures), maturation of the OM induced desorption

from the interlayer and release of organic acids, promoting dissolution of the smectite and its recrystallisation to illite. Thus, OM had apparently inhibited illite formation at low temperatures but catalysed the process at advanced diagenetic stages. Based on the maturation state of OM, Li et al. (2016) proposed a range of 80 – 120 °C for the illitisation process.

Kirsimäe et al. (2020) investigated the lower Cambrian Blue Clay formation in the northern Baltic Palaeobasin. They found high proportions of illite in illite-smectite mixed layers, gradually increasing from 85% to 92% up to a present-day burial depth of 1,000 m. The authors note that, despite the high degree of illitisation typical of advanced diagenesis, the low degree of compaction and low maturity of the OM suggest low temperatures not exceeding 50 °C. Based on the estimated maximum burial depth (1,500 m) and assumptions on the heat fluxes and erosion rates, the authors reconstructed the burial history of the illitisation process so that it is consistent with the estimated temperature. According to their model, illitisation proceeded continuously during a period of at least 500 million years, implying that smectite to illite conversion was exceedingly slow at 50 °C.

Cifuentes et al. (2021) investigated the ongoing low-temperature illitisation process in the Socahgota Lake (Colombia). The water has an average pH of 9.3, concentrations of about 65 mM Na, 22 mM sulphate and 7 mM potassium. Formation of illite and illite-vermiculite mixed layers occurs in the central and southern OM-rich part of the lake sediments in conjunction with an Fe-rich reduced environment, essentially at ambient temperatures (average lake temperature: 15 °C). According to the authors, trioctahedral vermiculite[16] forms outside the lake via weathering of mica in the adjacent subtropical soils and is then transported to the lake, where it is first converted to intermediate illite-dioctahedral vermiculite mixed layers. The latter serve as precursors, allowing illite formation at such low temperatures. Although the geochemical boundary conditions are different from those in the planned HLW repository (no vermiculite present), this investigation demonstrates that illite formation is possible even at ambient temperatures under particularly favourable circumstances.

5.2.4 Implication of geological data on illitisation for the stability of the bentonite buffer

A key for assessing the potential impact of illitisation on the safety function of the bentonite buffer is the evaluation of its long-term kinetics. The K-Ar ages determined on nanometric to micrometric illite particles by Clauer et al. (2014) can help in this assessment, as they directly measure the timing of K^+ uptake into the illite crystal lattice. For the smallest illite particles (< 0.02 μm), it may be assumed that the growth process had a very short duration and therefore their K-Ar age represents a "time stamp" for the *start* of illite particle growth. Usually, the larger the clay particle in a given sample, the larger the measured K-Ar particle age, due to the prolonged time needed for the illite to grow. It is therefore possible, by measuring K-Ar ages on particles of different size, to estimate illite growth rates. From a large number of such K-Ar data (Tab. 2 and Fig. 6 in Clauer et al. (2014)), the authors concluded that, for all bentonite horizons investigated (distributed over a region of several thousand km^2), the crystallisation of illite extended over time spans varying from < 1 Ma to 4.9 Ma, depending on the local temperature. Note that the highest K-Ar ages in a specific location are (with an unique exception[17]) 2 – 7 Ma younger than stratigraphic bentonite deposition ages (12 – 16 Ma). This age difference records the time necessary to reach a burial depth (and thus a temperature threshold) sufficient to start the smectite to illite conversion.

---

[16] Vermiculite is a 2:1 Mg-rich clay mineral similar to smectites.

[17] Suspected contamination of detrital clay.

In their paper, Clauer et al. (2014) mention that the thickness of the bentonite beds is centimetric to decimetric. Assuming that the duration of the illitisation process is governed by slow diffusion of (K-bearing) solutes from the confining units towards the centre of the bentonite bed, this information can be used to estimate the average rate of illitisation and compare it with the duration of the thermal pulse in the repository. This may be expressed as the thickness of bentonite undergoing (partial or complete) illitisation in 1,000 years. Using the reported K-Ar ages and assuming 30 cm as the maximum thickness of the bentonite beds studied by Clauer et al. (2014), penetration rates of the illitisation front ranging from 31 to 250 μm/1,000 years are obtained. The calculated duration of the thermal pulse in the repository being about 10,000 years (Fig. 5-2), these data imply that the amount of bentonite converted into illite would be negligible, corresponding to only a few mm of the entire thickness of several dm.

Another key requirement for illitisation to occur is a sufficient supply of potassium for the conversion of Na- or Ca-montmorillonite to illite via ion exchange. Given that any internal source in bentonite (e.g. K-feldspar) would not be sufficient due to exceedingly low dissolution rates and trace level amounts in bentonite, the only possible source of K^+ ions would be the intruding Opalinus Clay porewater, in which potassium concentrations are about 2 – 3 mM (Mäder & Wersin 2023, see also Tab. 4-17).

The predicted compositions of bentonite porewaters (Tab. 7-3 and Tab. 7-4) always indicate similar, but significantly lower K^+ contents as a result of the exchange of K^+ for Na^+ in the sodium-dominated MX-80 bentonite. Therefore, a small inward K^+ gradient from Opalinus Clay to bentonite can be assumed, from which it is possible to estimate the supply of dissolved K^+ to bentonite via diffusion. From the maximum difference in K^+ concentrations between Opalinus Clay and bentonite porewaters (2.13 mol m^{-3} – 1.83 mol m^{-3} = 0.3 mol m^{-3}, see Tab. 7-4) divided by the thickness of the bentonite annulus (0.625 m, see Tab. A3.4-5a, p. A-91 in Nagra 2014c), an upper limit of 0.48 mol m^{-4} can be derived for the linear concentration gradient. By applying Fick's law with an effective diffusion coefficient of 6×10^{-10} m^2 s^{-1} (reference value for K in Tab. A3.4-6 in Nagra 2014c), the amount of potassium "supplied" to bentonite during the 10,000 year thermal pulse was calculated. Assuming that the full amount of supplied K^+ exchanges for Na^+ in montmorillonite and is ultimately converted to illite, a maximum of 12.7% of the initial montmorillonite would be degraded, leaving 87.3% of montmorillonite intact.

The previous estimation ignores the effect of the cement-based liners foreseen as reinforcement of the drifts, which could provide an additional source of potassium for illitisation. This issue has already been treated in Bradbury et al. (2014) and Savage & Cloet (2018) by mass balance calculations (Section 6.3 in Bradbury et al. 2014). It was concluded that the amount of montmorillonite potentially converted to illite could not exceed 0.3 – 1.2 wt.%. Adding this contribution to the estimated contribution via K-diffusion from the Opalinus Clay results in a total maximum of ~ 14% of montmorillonite degraded, which still would leave ~ 86% of intact montmorillonite.

5.2.5 Concluding remarks

In summary, the data and models discussed above imply that illitisation of montmorillonite is theoretically possible at temperatures below 100 °C and could therefore be an issue during the elevated temperature pulse. However, an evaluation of the abundant geological data available on diagenesis-induced illitisation show that illitisation is dominated by kinetics, not by equilibrium thermodynamics. At the temperatures of interest (47 – 125 °C), illitisation rates are usually slow; several million years are required for the illitisation process to be complete. Moreover, a sufficient supply of potassium is required for the formation of illite. Mass balance and steady-state diffusion calculations considering the amounts of potassium potentially available to the bentonite, either from the cementitious drift support structures or from the Opalinus Clay porewater, show that the amounts of smectite that could be converted to illite during the elevated temperature period would not exceed ~ 13 – 14% of the initial bentonite, leaving 86 – 87% of the initial montmorillonite intact. These data are corroborated by experiments conducted either in the laboratory or in underground research facilities. The results from such experiments are presented in detail in the previous report (Section 6.2 of Bradbury et al. 2014) and will therefore not be discussed here. The overall conclusion from the available evidence is that illitisation during the transient temperature increase will not compromise the safety-relevant properties of the buffer in the HLW eplacement drifts.

5.3 Effect of temperature on radionuclide retention

This section discusses the effects of increased temperature on cation exchange and surface complexation of selected elements representing different classes of radionuclides. It is based both on work performed at PSI and elsewhere.

5.3.1 Cs sorption on clay minerals

Marques Fernandes et al. (2017) investigated the influence of temperature on the sorption of Cs on Milos montmorillonite and MX-80-bentonite. Sorption experiments were also carried out on a bentonite sample (ABM) that was heated for ~ 1 year at 135 °C at the Äspö Hard Rock Laboratory (Svensson et al. 2011). The sorption of Cs was investigated at 25 °C and 90 °C and was followed over a period of 100 days. A decrease of the distribution coefficient (R_d) by a factor of ~ 3 was observed for all studied clays with increasing temperature. The results are plotted in Fig. 5-4.

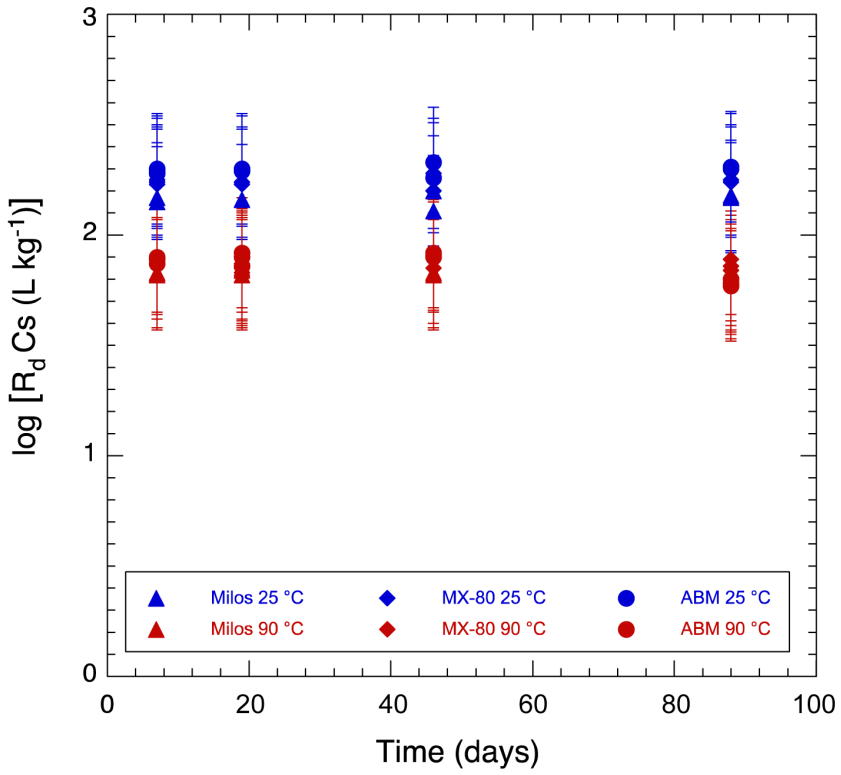

Fig. 5-4: Cs sorption coefficients on Milos montmorillonite, MX-80 bentonite and ABM bentonite at 25 °C and 90 °C in 0.1 M $NaClO_4$ at pH = 7.2, as a function of time

From Marques Fernandes et al. (2017)

This observation has been confirmed by studies carried out by Komarneni (1979) on montmorillonites, illites, micas, kaolinite and chlorites between 25 °C and 80 °C. A significant decrease in Cs sorption at 80 °C up to factor of ~ 3 was observed for all clay minerals and shales independent of the background electrolyte (NaCl or $CaCl_2$). The reduced sorption was explained by the decrease in the effective radius of the hydration sphere of cations at higher temperature.

The selectivity of cations sorbing by cation exchange depends mainly on ionic charge and hydration radius (Grim 1968). Cremers (1968) has shown that the selectivity coefficient (K_c) for Cs-Na exchange on montmorillonite decreased from K_c ~ 50 at 9.4 °C to Kc ~ 30 at 25 °C. Cs selectivity coefficients at elevated temperatures (T > 25 °C) can be calculated by means of the Van't Hoff equation (Novozamsky et al. 1976) if the exchange enthalpy ($\Delta_R H^o$) for the sorption reaction on a specific clay mineral and the selectivity coefficient at 25 °C are known:

$$\ln \frac{K_T}{K_{25°C}} = \frac{\Delta_R H^o}{R}\left(\frac{1}{298.15} - \frac{1}{T}\right) \qquad (5\text{-}6)$$

K_d-values at higher temperature can be then readily derived from the selectivity coefficients (Marques Fernandes et al. 2017).

5.3.2 Ni, Eu and Th sorption on montmorillonite

The study of Marques Fernandes et al. (2017) also provides temperature-dependent data for the sorption of the divalent (Ni^{II}), trivalent (Eu^{III}) and tetravalent (Th^{IV}) cations. These measurements serve as a model for the behaviour of activation/fission products with analogous oxidation states and chemical behaviour (transition metals, trivalent/tetravalent actinides). The results of experiments over a period of 5 years at 25 °C and 90 °C indicate no significant temperature effect for Eu and Th. In the case of Ni, the distribution coefficient (R_d) increases by up to one order of magnitude from 25 °C to 90 °C (Fig. 5-5). Because the sorption increases with temperature, it is a beneficial effect that makes the prediction of Ni sorption in safety assessment calculations (carried out with thermodynamic data for 25 °C) conservative. The main conclusion is that the surface complexation models developed for these elements at room temperature can be safely applied at higher temperatures (up to 90 °C) for the derivation of sorption databases.

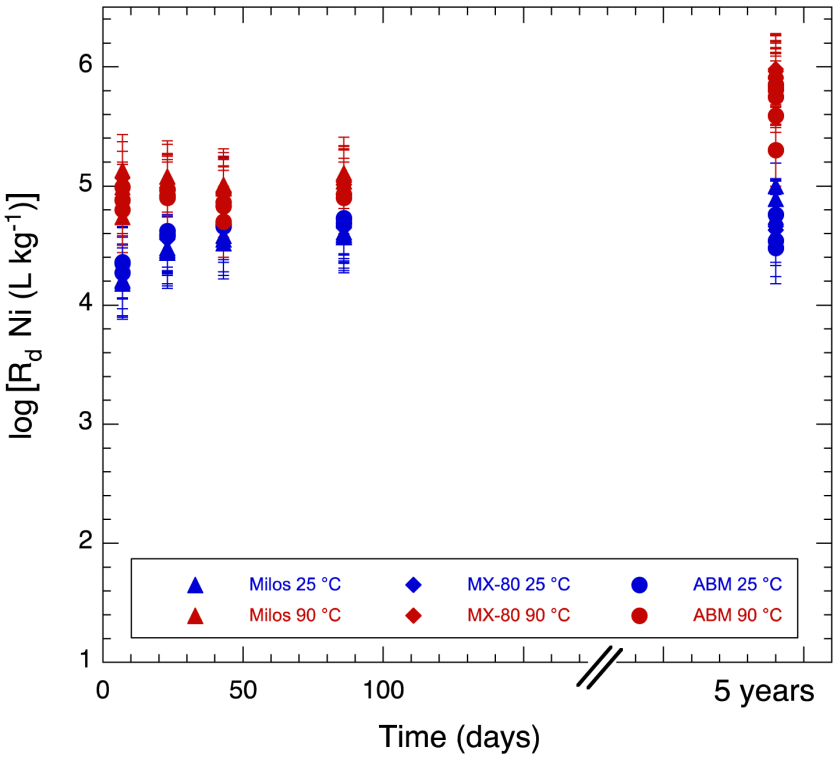

Fig. 5-5: Sorption of Ni(II) on Milos montmorillonite, MX-80 bentonite and ABM bentonite at 25 °C and 90 °C as a function of time

From Marques Fernandes et al. (2017)

5.3.3 Uranium(VI) sorption on heated bentonite

In a recent study by Fox et al. (2019), the effect of bentonite pre-heating on U(VI) adsorption was investigated at 25 °C[18]. Two bentonite samples were studied. The first sample was heated in situ up to 100 °C during 18 years, as part of a large-scale underground experiment (FEBEX) carried out at the Grimsel Test Site (Switzerland) between 1997 and 2015. The second sample was subjected to short-term heating in the laboratory (7 days), however at a much higher high temperature (300 °C). For both samples, U(VI) adsorption measurements indicate a small decrease of the distribution coefficient by less than a factor of 1.6 compared to control measurements with non-heated samples. The main reason for the decreased sorption was ascribed to different compositions of the aqueous phase during the sorption experiments. The heated bentonite samples released different amounts of Ca, Mg, carbonate and CO_2, leading to different concentrations of ternary uranyl-CO_3-Ca/Mg aqueous complexes, resulting in different K_d values measured for heated and non-heated samples.

In addition to the aqueous speciation effect, the authors also hypothesised that the heat treatment could have altered U(VI) adsorption by modifying the coordination environment and/or the available surface area of edge sites. Alternatively, the electrostatic properties of the basal surface, which influence the electrostatic potential of the edge sites through the spillover effect, may have affected the sorption of U(VI). However, none of these possibilities were quantified in this study. The authors conclude that one should account for at least a 30 – 50% decrease in K_d values in performance assessments due to pre-heating of clay buffer materials. This recommendation seems somewhat too conservative, considering that, according to the presented data, the *maximum* decrease in the K_d value of U(VI) was ~ 30%. Based on these data, it can be concluded that the effect of heating on the sorption of U(VI) on bentonite is minor.

5.3.4 General conclusions on elevated temperature effects for sorption

Studies on the effect of temperature on the sorption of cations on clays reveal general trends. There is clear evidence that the sorption of metals taken up preferentially via cation exchange (e.g. Cs^+, K^+, Na^+, Mg^{2+}) exhibit a significant decrease in sorption (up to a factor of three for Cs^+) when the temperature is raised from 25 °C to 90 °C. This behaviour can be explained with the fact that cation exchange reactions are exothermic and thus the reaction enthalpies are negative. According to the Van't Hoff equation (eq. 5-6), an increase in temperature must then induce a decrease in the cation exchange constant. Metals sorbing preferentially via surface complexation show either minor temperature dependence (e.g. U^{6+}, Eu^{3+}, Th^{4+}) or increased adsorption at elevated temperatures (Ni^{2+}). In this case, adsorption is endothermic, leading to an increase in sorption as the temperature rises.

[18] U(VI) sorption is discussed for the sake of completeness. As discussed in Johnson et al. (2023) and Chapter 9, due to the presesence of dissolved H_2 in the porewater entering into the canister, reducing conditions persist adjacent to the spent fuel and uranium will therefore be present as U(IV) and not as U(VI).

5.4 Effect of temperature on diffusion in bentonite

This section discusses the effects of increased temperature on the diffusion of selected aqueous species (cations, anions and HTO) in compacted bentonite. The contents of this section are largely based on experimental and theoretical work performed at PSI.

5.4.1 Theoretical background

Because molecular diffusion is caused by the random motion of atoms or molecules, it is evident that temperature must influence diffusion processes. This is reflected in the Stokes-Einstein relationship, applying to any diffusing species *i* in a medium *w*, apparently showing that the diffusion coefficient increases proportionally with temperature:

$$D_{w,i} = \frac{kT}{6\pi\eta r_i} \tag{5-7}$$

where k is Boltzmann's constant (1.381×10^{-23} J K^{-1}), T is temperature (K), η the dynamic viscosity of the medium (kg m^{-1} s^{-1}) and r_i is the ionic or atomic radius of species i (m). However, because the viscosity of the medium is related to the reciprocal of the temperature (Kampmeyer 1952), the temperature-dependence is not linear. Since the dynamic viscosity is normally not known, the effect of temperature on diffusion cannot be easily predicted and is usually described empirically with the help of measurements at various temperatures by means of an Arrhenius equation:

$$D_{w,i} = A \exp\left(\frac{-E_a}{RT}\right) \tag{5-8}$$

where A is the pre-exponential factor (m^2 s^{-1}), E_a is the activation energy (J mol^{-1}), R is the gas constant (8.314 J mol^{-1} K^{-1}) and T is temperature (K). The equation shows that the diffusion coefficients should increase exponentially with temperature. The activation energy for the diffusion of most dissolved species in bulk water and aqueous electrolytes has been determined to lie in the restricted range of 18 ± 1 kJ mol^{-1} (Mills 1973, Tanaka 1975), therefore the major task is the determination of the pre-exponential factor through diffusion coefficient measurements at different temperatures.

5.4.2 Experimental data

The effect of temperature on the diffusion of chemical species in compacted bentonite and montmorillonite has been studied for several cations (Na^+, Cs^+, Sr^{2+}, Ni^{2+}, Pb^{2+} and NpO^{2+}), anions (Cl^-, HS^-, SeO_3^{2-}, ReO_4^-) as well as neutral species (HTO, D_2O and He). In all studies, the dependence of the effective or apparent diffusion coefficient on temperature could be described by the Arrhenius equation. The activation energies for different elements were generally similar to those found in bulk water, i.e. close to 18 kJ mol^{-1}. However, weak dependencies of this parameter on the bulk dry density of bentonite were observed for some radionuclides. For anionic species, neutral species and Na^+, the activation energy depends only slightly on the bulk dry density. The variations appear to be within experimental uncertainties and are therefore not significant. Only in the case of Cs^+ a significant increase in the activation energy with bulk dry density, and in general higher E_a values compared to other species, were measured (from ~ 30 to ~ 50 kJ mol^{-1} in the dry density range 1,000 – 1,800 kg m^{-3}). This is probably a combined effect related not only to diffusion, but also to the fact that sorption of Cs^+ on Na-montmorillonite/ bentonite depends strongly on the degree of compaction (van Loon & Glaus 2008).

For all other species, it seems that activation energies do not depend on confinement. It can thus be assumed that the activation energy for diffusion in the confined porewater of compacted bentonite is similar (slightly higher) to that of diffusion in bulk water. Tab. 5-2 describes the effect of temperature on diffusion up to 80 °C. Changing the temperature from 20 °C to 80 °C results in an increase in D_e by a factor of four when using an activation energy of 20 kJ mol^{-1}.

Tab. 5-2: Effect of temperature on the effective diffusion coefficient

T °C	E_a = 10 kJ mol^{-1} D_e (m^2 s^{-1}) =	E_a = 20 kJ mol^{-1} D_e (m^2 s^{-1}) =	E_a = 30 kJ mol^{-1} D_e (m^2 s^{-1}) =
20	1.00×10^{-11}	1.00×10^{-11}	1.00×10^{-11}
50	1.46×10^{-11}	2.14×10^{-11}	3.14×10^{-11}
65	1.73×10^{-11}	2.98×10^{-11}	5.15×10^{-11}
80	2.01×10^{-11}	4.04×10^{-11}	8.11×10^{-11}

5.5 Implications of the effect of temperature on sorption and diffusion for the evolution of the HLW repository

The most recent heat transfer calculations for a repository at ~ 900 m depth (Fig. 5-2) predict temperatures only slightly (10 – 15 °C) above thermal equilibrium with the host rock at 10,000 years after emplacement. This means that temperature effects on radionuclide sorption and diffusion will be small and, as a first approximation, need not be taken into account in a normal evolution scenario.

On the other hand, temperature effects should be considered in the sensitivity analysis of safety assessment calculations, since reference case calculations are carried out using thermodynamic data for chemical reactions and diffusion coefficients determined at 25 °C. As seen in Tab. 5-2, diffusion coefficients increase by about a factor of two from 20 °C to 50 °C. Moreover, small but significant modifications of K_d values are expected in this temperature range for the sorption of two dose-relevant radionuclides, ^{135}Cs and ^{59}Ni. Particularly in the case of diffusion coefficients, the temperature-dependence is well assessed thanks to a large database.

5.6 Effects of high temperatures on the evolution of the concrete liner interfaces with Opalinus Clay and bentonite

According to the most recent thermal evolution predictions, peak temperatures of about 80 – 100 °C are predicted at the bentonite/EDZ/OPA interfaces between ~ 2 to ~ 2,000 years after closure (Fig. 5-2). Because resaturation will start soon after waste emplacement, temperature effects on chemical processes are thus expected at this interface. Cloet et al. (2019) studied the long-term evolution of an alternative HLW repository design, in which the bentonite buffer is replaced by a cementitious backfill, based on models that include the effect of a thermal pulse on solute transport and chemical reactivity. This study also addresses the potential effects of the thermal pulse on the evolution of the aforementioned interfaces for the provisionalary repository setup.

A faster chemical evolution is expected due to the increase with temperature of solute species diffusivities, kinetic dissolution/precipitation rates, and solubility products of many solids. The change in diffusivities directly affects solute fluxes. For instance, the water self-diffusion coefficient increases by a factor of three if temperature rises from 40 °C to 110 °C (Krynicki et al.

1978). Changes in mineral solubility with temperature are variable and depend on the type of mineral. In some cases, solubility products even decrease with temperature (retrograde solubility, e.g. calcium sulphate, magnesium silicate). Therefore, temperature-dependent variations of solubility and cement composition coupled with transport may potentially affect the mineralogy, porosity and position of the fronts originating from the interaction with clay porewaters.

The effect of temperature increase on the composition of hydrated cement is discussed in Section 4.2 of Cloet et al. (2019). Briefly, kinetic rates of dissolution/precipitation reactions are expected to be faster during the thermal pulse as they usually increase exponentially following an Arrhenius type dependency. The increase may be significant, e.g. quartz dissolution rates increase by two orders of magnitude from 50 °C to 100 °C (Palandri & Kharaka 2004). According to the calculations shown in Fig. 5-2, thermal peaks of about 90 – 100 °C are predicted in the EDZ at times between about 10 and 1,000 years after emplacement. The duration of the elevated temperature pulse in that region could thus last for several hundred years, significantly enhancing mineral dissolution reactions in the Opalinus Clay and bentonite adjacent to the concrete liner. In addition, the high pH values induced by reactions with cementitious materials should further enhance kinetic rates during this period, leading to fast conversion of clay minerals into zeolites and consequent porosity change.

In summary, temperature effects on chemical reactions within the bentonite – drift support – Opalinus Clay interface region are expected to be complex and hard to predict without specific experimental data and reactive transport models. In this report, the effect of elevated temperature on the geochemical evolution of this region is evaluated with the help of dedicated reactive transport calculations (Section 6.7).

6 Interaction of a concrete tunnel liner with Opalinus Clay and bentonite

6.1 Introduction

6.1.1 Objectives and background

The purpose of this chapter is to update the corresponding Chapter 5 in Bradbury et al. (2014). The focus is on the chemical reactions occurring across the interfaces of the drift support structure with the adjacent bentonite buffer and Opalinus Clay host rock as soon as porewater from the host rock resaturates these interfaces. The main objective is to evaluate, based on published experimental evidence and reactive transport calculations, how and to what extent the drift support materials and the adjacent clay materials are altered during their prolonged reciprocal interaction. Of particular importance is the question whether the mineralogy and physical properties of the bentonite buffer could be modified in such a way that its functionality would be compromised. Mineralogical changes are expected also within the Opalinus Clay, but these will presumably be less critical considering the much larger thickness of the host rock barrier. In addition, possible impacts on the hydraulic properties of the EDZ will be evaluated. Given the initial thermal pulse and the sharp pH gradients established between the clay materials and the cementitious tunnel support, the following effects are anticipated:

- Clay minerals may dissolve in both bentonite and Opalinus Clay. This could locally affect the radionuclide sorption capacity of both materials.
- Due to the release of alkalis during the hydration of cement in the tunnel support, changes in the exchanged cation population of montmorillonite are expected at the immediate contact (see e.g. Yokoyama et al. 2021). This could locally affect the swelling pressure of the bentonite.
- Local porosity will change due to precipitation/dissolution of minerals, affecting the transport properties (hydraulic conductivity, diffusivity).
- Changes in pH and composition of the bentonite and Opalinus Clay porewaters could locally modify radionuclide sorption (K_d) and solubilities.

This chapter is subdivided in several sections. Section 6.2 briefly summarises the contents of the corresponding section in Bradbury et al. (2014), with special emphasis on the results of the reactive transport calculations simulating the chemical evolution of bentonite and Opalinus Clay in contact with a concrete liner. Section 6.3 is devoted to an update based on literature published since Bradbury et al. (2014). Section 6.4 presents a synthesis of results from reactive transport models applied to other repository setups. Section 6.5 is devoted to recent reactive transport model calculations applied to the results of the CI experiment carried out in the Mont Terri Rock Laboratory, for which a thorough experimental characterisation is available. In this experiment, the evolution of cement/Opalinus Clay and cement/bentonite interfaces was studied over a period of 10 years. Section 6.6 presents a summary of reactive transport calculations applied to the HLW repository setup in the context of SGT-E2. Finally, Section 6.7 presents an update of the reactive transport calculations described in Bradbury et al. (2014) adapted to the currently envisaged tunnel support structure and repository depth. The chapter ends with a concise summary, including the main conclusions.

The present introductory section is completed by a summary and comparison of current approaches used to model chemical equilibrium in compacted clays, explaining the main differences, advantages and drawbacks, and justifying the choices made for the new geochemical calculations presented in this report. This is also relevant for the bentonite pore water calculations presented in Chapter 7.

6.1.2 Geochemical models for compacted clays

In Chapter 6 and Chapter 7, geochemical calculations involving compacted clays (bentonite and Opalinus Clay) are presented. The thermodynamic treatment of chemical equilibria coupled with transport in such systems has recently experienced (and is still experiencing) advances and it seems appropriate to discuss the approaches currently in use to predict the evolution of solid and porewater chemistry in highly compacted saturated clays. This section is intended as an introduction to this topic.

To date, there is no consensus on a scientifically sound approach for modelling aqueous solutions in equilibrium with compacted clays. This is mainly due to the complex nature of water/clay interactions and the intrinsic difficulties in measuring the properties of the aqueous phase under narrow confinement. As an aqueous solution saturates the (initially almost dry) bentonite buffer, the main fraction of the incoming water enters the interlayer space of montmorillonite, where exchangeable cations reside. The remaining minor fraction, usually denoted as "external water" or "interparticle" water, fills the interstitial pores between clay particles and can be further subdivided in two types (see e.g. Wersin et al. 2004):

a) water associated with the electrical diffuse double layer (DDL) characterised by a charge-compensating cation excess and anion depletion, and

b) electrically neutral interparticle water, approximately defining the so-called "anion-accessible porosity"

Classical models of porewater composition in compacted clays (including those used in the present report) follow a single-porosity approach, in which complexation and mineral dissolution/ precipitation reactions are limited to the external water (see e.g. Savage et al. 2010a). Sorption in the interlayer is considered by introducing selectivity coefficients to calculate the equilibrium distribution of exchangeable cations (e.g. Na^+, K^+, Ca^{2+}, Mg^{2+}) and specific adsorption on edge sites may be considered (including protonation/deprotonation) by introducing surface complexation constants. A shortcoming of this method is that selectivity coefficients must be transformed to *ad hoc* constants that depend on the CEC and must be scaled to the water/clay ratio of the system of interest.

An alternative to the classical approach has recently been developed (Birgersson & Karnland 2009, Birgersson 2017, Gimmi & Alt-Epping 2018, Birgersson et al. 2017) based on the Gibbs-Donnan membrane potential (Donnan 1995). The advantage of this approach is that the saturated clay can be treated as a single homogeneous phase in electrochemical equilibrium with an external bulk solution separated by a semi-permeable membrane (the "Donnan phase"). There is no need to specify different types of water or solids. This is appropriate particularly for bentonite at a very high degree of compaction. In more heterogeneous clays (e.g. Opalinus Clay), dual-porosity concepts are used, with the DDL represented as a Donnan layer (e.g. Alt-Epping et al. 2015, Tournassat & Steefel 2015, Soler et al. 2019, Tournassat & Steefel 2019, Tournassat & Steefel 2021, Jenni et al. 2017, Gimmi & Alt-Epping 2018). In the Donnan phase, which acts as semi-permeable membrane, cations, anions and neutral species concentrations are in equilibrium with an external water phase. The montmorillonite particles are regarded as immobile, negatively charged entities that are too large to cross the membrane. This generates an electric potential counteracting and limiting the mass flux of dissolved cations and anions across the membrane.

As a result, the concentration of cations inside the Donnan phase (the sum of exchanged and other dissolved cations) must be larger than the concentration of anions, generating an excess positive charge that compensates the negative charge carried by the immobile clay particles, leading to an electrically charge-balanced bulk system. In the case of bentonite, the negative charge of the clay is generated by substitution of divalent cations in the tetrahedral-octahedral-tetrahedral (TOT) units of montmorillonite (i.e. the octahedral charge). For each species of interest, concentrations in the Donnan phase can be related to the concentrations in the external water phase via equations dependent of the membrane potential, provided the activity coefficients in both phases are known (usually expressed as ratio of the activity coefficient in the external water to the activity coefficient in the clay, Γ_i).

Although Donnan equilibrium models capture essential features of water-clay interactions in compacted clays, they are presently not sufficiently implemented for the needs of safety assessments. Specifically, limitations of the Donnan approach include:

- The pH-dependent (non-permanent) surface charge is often ignored, although it is possible to account for this charge and accordingly vary the charge compensated in the Donnan layer. This is however a minor drawback since the non-permanent charge is usually only a fraction of the interlayer charge.
- Activity coefficients of cations and anions in the clay are hardly known, particularly in polyelectrolytes, so the Γ-factors (ratio of activity coefficients in external water and Donnan phase) are arbitrarily set to 1.
- Polyelectrolytes are difficult to treat (e.g. Opalinus Clay and the derived bentonite porewaters are NaCl-dominated, but still mixed electrolytes with significant sulphate and carbonate). While Donnan concentrations for single electrolytes can be calculated from (semi-) analytical solutions, numerical solutions are required for polyelectrolytes, making the treatment more difficult.
- Finding a set of appropriate model parameters for a given material is not easy. Typically, an independent estimation is not possible, and they have to be estimated inversely from specific experiments.

Recently, Gimmi & Alt-Epping (2018), Jenni et al. (2017), Jenni & Mäder (2021) proposed a dual-porosity model that explicitly uses both Donnan equilibria (for the DDL and interlayer) and a classical equilibrium approach for the separate uncharged interparticle water phase ("free" porosity). This method appears to be more appropriate to describe reactive transport in Opalinus Clay and clay/concrete interfaces than a single-porosity Donnan approach. However, in its present implementation, this method cannot be applied to all the chemical components of interest, which include, besides the dominant NaCl electrolyte, significant concentrations of other symmetric and asymmetric electrolytes (Mg-K-Ca-SO_4-CO_3) and trace elements (radionuclides).

An advantage of classical models is that critically evaluated thermodynamic data are available for all chemical components of interest, including trace element groups representing dose-relevant radionuclides. This capability is of relevance for safety assessment calculations, as it allows radionuclide solubility limits and sorption coefficients required for dose calculations to be determined. Therefore, for the tasks in this report it was decided to adopt a refined classical model that circumvents some limitations of classical single-porosity models. It is based on the "ClaySor" model (Kulik et al. 2018) and was used for the calculation of bentonite porewaters (Section 7.2) as well as for the reactive transport calculations presented later in this chapter (Section 6.7). A limitation of reactive transport models based on the classical approach is that they predict zero fluxes as a result of total clogging at advanced reaction times, which contradicts experimental evidence. For instance, it has been demonstrated that, in spite of total physical clogging, cation

transport does not stop in compact clays due to diffusion through the electrical double layer (EDL) (Luraschi et al. 2020). While this experimentally verified process is considered in Donnan models, this is not the case for classical single-porosity models.

6.2 Summary of previous work

Chapter 5 in Bradbury et al. (2014) starts with a general overview of the chemistry of concrete materials and clays. Concretes are artificial materials created by mixing cement with aggregates (sand, gravel) and other additives to obtain the desired mechanical and chemical properties. When ordinary Portland cement is flushed with increasing amounts of water, the initial porewater will be highly alkaline (pH > 13) due to release of KOH and NaOH (Berner 1992). After alkali hydroxides are eventually leached out, the pH will stabilise to ~ 12.5 as a result of equilibrating with $Ca(OH)_2$ (portlandite). In the long term, after consumption of portlandite, the pH will further decrease as the Ca:Si ratio of C-S-H phases progressively decreases. Eventually, equilibrium with calcium carbonate is reached under the assumption that concrete will become fully degraded and that sufficient CO_2 is available for the carbonation reaction.

Clays and clay rocks are fine-grained, plastic natural materials containing minor minerals and so-called "clay minerals" as the major component. These are sheet silicates characterised by loosely bound sheets of $(Si_{4-x},Al_x)O_4$ and octahedrally coordinated cations (T and O units). Some of them can swell by incorporating interlayer water (e.g. montmorillonite), others are non-swelling (illite, kaolinite). Under normal conditions (e.g. in contact with subsurface groundwater), clay minerals are less soluble and less reactive than cementitious materials and equilibrate at near-neutral pH. Upon interaction with alkaline water produced during cement alteration, however, clay minerals can be destabilised even at low temperatures. The result are changes in porosity and dissolution/precipitation reactions at the interface of both materials. Upon interaction with Na-montmorillonite, an increase in exchanged K^+ and Ca^{2+} at the expense of Na^+ is also expected.

The excavation phase during construction of the HLW repository will lead to the formation of a damaged zone around the drifts (EDZ), including microcrack formation following tunnel convergence. The EDZ could thus provide preferential pathways for the ingress of water into the bentonite after emplacement and sealing of the drifts, accelerating reaction progress in the initial resaturation stages. Later on, it is expected that cracks will be sealed by formation of secondary phases, re-establishing slow diffusion as the dominant solute transport regime. Because laboratory or underground facility experiments provide only short-term information on the evolution of clay-concrete interfaces, such experiments alone are not sufficient to prove this anticipation. The long-term chemical evolution of such complex systems can only be predicted based on reactive transport calculations calibrated with information from short-term experiments. The model predictions can be complemented by information from geological or industrial analogues as summarised in Prasianakis et al. (2022) .

An overview of early modelling studies on the chemical evolution at clay/concrete interfaces can be found in Gaucher & Blanc (2006). Various reactive transport models were developed and applied to different repository setups. Frequently, centimetre-thick zones with strongly reduced porosity (or even total clogging) at the clay side of the interface were predicted. Based on their literature review, Bradbury et al. (2014) summarise the main chemical-physical long-term effects of clay-interaction as follows, in agreement with Savage & Cloet (2018):

- Prolonged interaction of the concrete with in-diffusing water leads to a multi-stage leaching of the cementitious material, according to the sequence modelled in Berner (1992) with progressively decreasing pH (i.e. in the order of reaction progress: release of alkalis, consumption of portlandite, decrease in Ca:Si ratio of C-S-H phases, calcium carbonate precipitation).

- Sharp pH and pCO_2 gradients will be generated at the clay/cement interfaces, accompanied by precipitation of carbonates, hydroxides and C-S-H phases.
- In the case of MX-80 Na-bentonite, exchange of Ca^{2+} and K^+ for Na^+ is predicted, resulting in a reduction of bentonite swelling capacity.
- Deprotonation/protonation of edge sites in montmorillonite will significantly contribute to the neutralisation of hydroxyl ions released by the leached cementitious material, thus mitigating the propagation of a pH alteration front towards the inner side of the bentonite buffer.
- The high pH of cement porewater will enhance dissolution of minor silicates and montmorillonite, which will also consume hydroxyls, slowing down the advance of the high-pH front.
- Several secondary solids will form arranged in zoned patterns: C-(A)-S-H, illite, feldspars and zeolites.
- Porosity changes are predicted across the interface following the aforementioned dissolution/precipitation reactions; however, net changes in porosity should remain small.

Savage & Cloet (2018) carried out mass balance calculations to estimate the maximum amount of montmorillonite that could potentially dissolve due to the in-diffusion of hyperalkaline solution from a drift support structure consisting of ESDRED cement. They concluded that at most 8 % of the bentonite volume could be affected, corresponding to an alteration thickness of 13 cm. The same authors report that 1 m^3 of Opalinus Clay would be sufficient to neutralise the total hydroxide inventory of about 4 m^3 of typical OPC concrete. This translates into a 4 cm thick zone of altered Opalinus Clay in a drift supported by an ESDRED concrete liner.

Dedicated reactive transport calculations to simulate the interactions at the interface of ESDRED low-pH cement with MX-80 bentonite on one side and Opalinus Clay on the other side were carried out by Berner et al. (2013) (a similar model was developed for the L/ILW repository by Kosakowski & Berner 2013). Two cases were explored: in Case 1 the coupling of chemistry, porosity and transport was fully considered, whereas in Case 2 the porosity and the transport parameters (diffusivity, permeability), as well as the volume of the fluid phase, were assumed to remain constant. The net effect predicted in the (more realistic) Case 1 model was a slowing down of the reaction progress due to the overall reduction in porosity induced by the precipitation of secondary minerals. In the Case 2 model, solute transport continues at constant rates as no porosity reduction is taken into account, even when the volume of the precipitates exceeds the physically available pore space. Case 2 is less realistic; however, it yields more conservative results as it "accelerates" the chemical evolution. These calculations may be used to represent a pessimistic scenario involving microfracturing of the clogged zone or inhibition of mineral nucleation in small pores (Chagneau et al. 2015, Li et al. 2017, Fukatsu et al. 2017, Prasianakis et al. 2022, Luraschi et al. 2020). It is to be realised that, in the above calculations, dissolution/precipitation reactions were not kinetically controlled, i.e. a given mineral dissolves or precipitates instantaneously once it becomes thermodynamically unstable or stable, respectively. The time evolution of mineral assemblages is then exclusively controlled by solute diffusion. Selected results (mineralogical profiles) from the aforementioned two cases are shown in Fig. 6-1 (initial conditions), Fig. 6-2 (Case 1) and Fig. 6-3 (Case 2). These plots show the calculated mineral inventories across tunnel support and adjacent clay materials as cumulative mineral volume fractions (y-axis) with the liquid-filled volume fraction on top (porosity). The x-axis gives the distance from the centre of the emplacement drift.

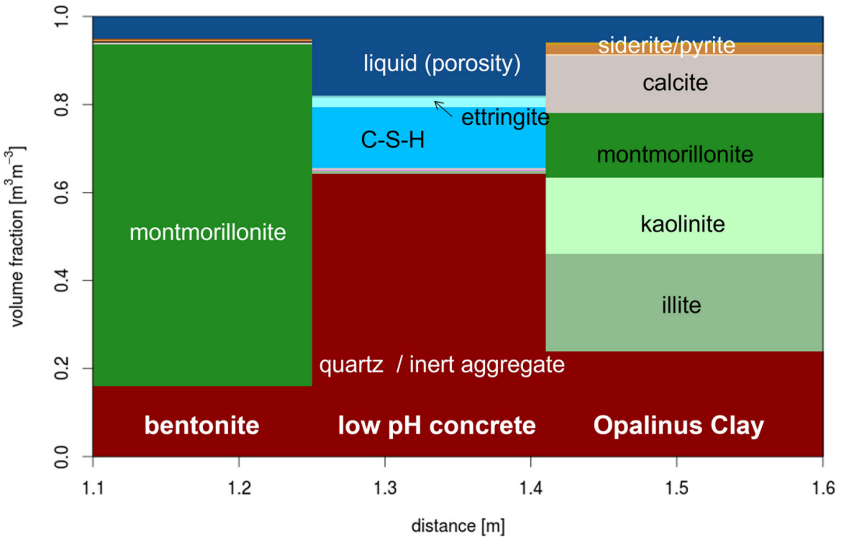

Fig. 6-1: Initial mineralogical profile across the drift support (consisting of low-pH ESDRED cement) and the adjacent bentonite and Opalinus Clay

From Bradbury et al. (2014) modified from Berner et al. (2013)

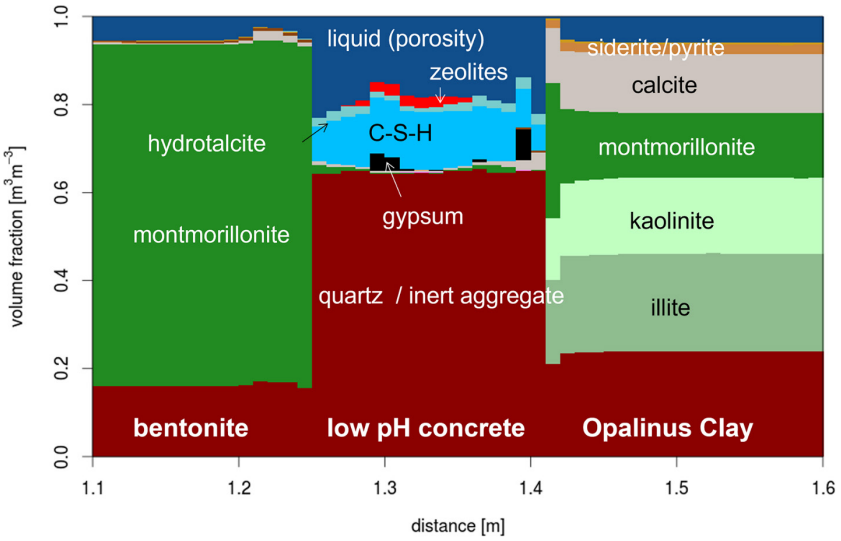

Fig. 6-2: Mineralogical profile across the drift support (consisting of low-pH ESDRED cement) and the adjacent bentonite and Opalinus Clay after ~ 10,000 years considering full coupling with porosity changes (Case 1)

From Bradbury et al. (2014) modified from Berner et al. (2013)

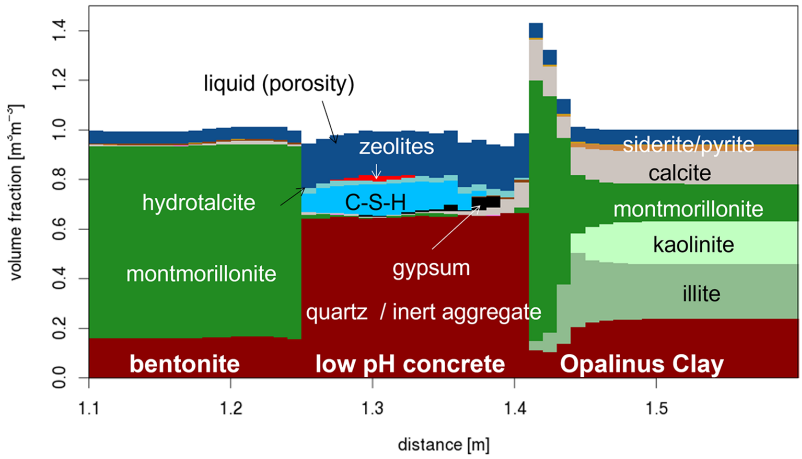

Fig. 6-3: Mineralogical profile across the drift support (consisting of low-pH ESDRED cement) and the adjacent bentonite and Opalinus Clay after ~ 10,000 years (Case 2, no porosity change considered)

Note: Because porosity change is not considered, the total volume is not conserved and may exceed 100%.

From Bradbury et al. (2014) modified from Berner et al. (2013)

The results of the model calculations show in both cases that, after 10,000 years, mineralogical modifications in the Opalinus Clay are restricted to a zone of a few centimetres thickness. Quartz, calcite, pyrite and kaolinite are partly dissolved, whereas illite and kaolinite are replaced by Na-montmorillonite. The volumetric changes indicate a strong tendency towards porosity reduction at the interface between drift support and Opalinus Clay. The porosity reduction strongly decreases the mass flux over the interface and effectively stops any mineralogical evolution in Case 1. Note that a similar conclusion was drawn from natural analogue studies of the Maqarin site (Jordan), based on the comparison of reactive transport modelling with isotopic data (Steefel & Lichtner 1998, Steefel & Lichtner 1994). The decrease in solute fluxes across a fracture filled with hyperalkaline fluid (equilibrated with natural cement-like rock) and the confining carbonate rock was correctly anticipated.

The evolution of the drift support structure is similar at both interfaces. Ettringite and C-S-H phases are dissolved; hydrotalcite, gypsum, phillipsite, montmorillonite and calcite precipitate. After the complete dissolution of the C-S-H phase, gypsum and hydrotalcite are replaced by calcite and clay minerals (see Case 2, Fig. 6-3). Mineral alteration is more pronounced and faster near the Opalinus Clay boundary. Once the porosity reduction approaches complete obstruction of the capillary pores at the interfaces, the concrete degradation rate is strongly reduced (Case 1). Only for Case 2, where the mass flux over the interfaces is not limited, does a complete degradation of the concrete occur, which is achieved after more than 50,000 years.

On the bentonite side, the altered zone extends up to 10 cm into the buffer when assuming full porosity feedback (Case 1). This zone is not expected to expand further since the mass flux over the interface rapidly decreases due to obstruction of the capillary pores. Note however that, based on new experimental and theoretical results, complete clogging of porosity in clay materials seems unlikely (see discussion in Prasianakis et al. 2022). Advanced reactive transport models that consider these findings are discussed in Section 6.5. In Case 2, a thicker alteration zone is predicted (> 20 cm at the end of the simulation run at ~ 52,900 years). The progress of the alteration front will nevertheless eventually slow down also in this case as the initially steep pH and chemical gradients are strongly reduced in the long term. Porosity changes induced by

dissolution/precipitation are less important compared to the liner/Opalinus Clay interface because in reality the molar volumes of the new minerals are comparable to those of the original minerals, whereas at the liner/Opalinus Clay interface the replacing solids have larger molar volumes than the primary ones. Within the first few centimetres from the liner/bentonite interface, a minor amount of montmorillonite is dissolved and quartz, calcite and hydrotalcite precipitate.

The exchanged cation populations in montmorillonite are slightly modified on a decimetre scale for Case 2. The exchanged Na^+ content is reduced towards the concrete liner by a few percent and replaced by Ca^{2+}, Mg^{2+} and K^+. In both calculations, the amount of montmorillonite dissolved and the thickness of this dissolution zone (< 1 cm for the conservative Case 2 calculation) are insignificant compared to the total amount of bentonite. In the Opalinus Clay, no net dissolution of clay minerals is observed, i.e. illite and kaolinite are replaced by an equivalent amount of montmorillonite. Since cement degradation has reached a mature stage at the end of the simulation time, decreasing to near-neutral pH, it is not expected that significantly more montmorillonite will be dissolved at later times.

In summary, the mineralogical changes and their spatial extent predicted by the reactive transport model are comparable to those described in Savage & Cloet (2018), but the amount of predicted montmorillonite dissolution is much less than the estimate of Savage & Cloet which was based on a simple and very conservative mass balance approach.

6.3 Synthesis of recent experimental and modelling studies on cement/clay interaction

This section reviews studies on cement/clay interaction published since the appearance of Bradbury et al. (2014). The focus is on investigations directly relevant to the behaviour of the bentonite – tunnel support – Opalinus Clay interfaces of the planned HLW repository. This includes a discussion of recent results from the Cement-Clay Interaction (CI) experiment carried out at the Mont Terri Rock Laboratory. Most of the information synthesised here is taken from recent reviews by Savage & Cloet (2018), Wilson et al. (2021) and Prasianakis et al. (2022).

Savage & Cloet (2018) synthesised a large number of modelling studies on cement/clay interactions. They point out that, while early models (up to ~ 2008) treated the presence of cement solids as a hyperalkaline boundary fluid with constant composition and fixed pH, later models explicitly represented the solid composition of cementitious materials. Such models are physically more realistic and account for complexities such as clinker hydration (Jenni et al. 2017) or C-S-H/M-S-H solid solution formation (Dauzeres et al. 2016, Watson et al. 2013). Typically, these models lead to much narrower pH alteration fronts than the older "boundary fluid" models due to the explicit consideration of porosity effects (clogging).

Savage & Cloet (2018) also note that much of the information generated in the simulations (e.g. aqueous species concentration/activities in each grid cell for all simulated times) is unfortunately not available in the reviewed publications. In most cases, detailed information is given only for the pH evolution as this is regarded as the master variable governing the solubility of clay minerals, which are frequently considered to be destabilised at pH > 11. Savage & Cloet (2018) criticise this simplistic view as solubility products depend also on other factors (*p, T* and activities of various ions). A parameter of particular importance governing the stability of clay minerals is the activity of silica, which must approach the solubility of amorphous silica (~ 2 mM Si at 25 °C and near-neutral pH) to stabilise smectites. Very low silica concentrations at the micromolar level, as buffered in some (silica-free) cementitious systems, will therefore unavoidably destabilise montmorillonite and cause dissolution of most clay minerals. Other critical factors sensitively affecting the results of cement/clay simulations are the completeness of the list of potentially forming solids and the reliability of associated thermodynamic data. Early models used a restricted number of solids, while newer models may include more than 40 potentially precipi-

tating phases, which in general results in more strongly buffered pH. An additional key factor is the kinetics of precipitation/dissolution reactions. In the absence of kinetic data for most mineral reactions, early simulations often assumed instantaneous equilibration, while state of the art simulation studies frequently include kinetic terms to be used in sensitivity analyses, partly supported by experimental data (e.g. Marty et al. 2015a). Even in the case of reliable kinetic data being available, large uncertainties remain due to the difficult quantification of reactive surface areas.

Considering the aforementioned accumulation of uncertainties in long-term simulations of cement-clay interactions, Savage & Cloet (2018) use an alternative (conservative) mass balance approach to evaluate the maximum amount of bentonite that could be dissolved via reaction with the concrete drift support structure. The evaluation is based on the conservative assumption that all hydroxyls that could potentially be released by the concrete liner are used to dissolve the montmorillonite in MX-80 bentonite, according to the reaction:

$$Na_{.33}Mg_{.33}Al_{1.67}Si_4O_{10}(OH)_2 + 2\ H_2O + 4.68\ OH^- \rightarrow 0.33\ Na^+ + 0.33\ Mg^{2+} + 1.67\ Al(OH)_4^- + 4\ HSiO_3^- \quad (6\text{-}1)$$

Using this conservative mass balance approach, the authors came to the conclusion (Fig. 3-5 in cited reference) that a liner 45 cm thick made of OPC concrete could induce dissolution of up to 35 cm of the bentonite backfill (about half the foreseen thickness), which could result in unacceptable reduction of the swelling pressure of the bentonite. If low-pH cement is used instead, the dissolution depth reduces to about 13 cm, which would still induce a very large reduction in swelling pressure. The results of more complex reactive transport calculations, however, point to alteration zones in the bentonite of no more than 5 cm thickness. Based on the latter estimate, Savage & Cloet (2018) calculate a decrease in swelling pressure from 5 MPa to 0.6 MPa in the altered zone, corresponding to a *local* dry density decrease from 1,400 to 1,030 kg m^{-3}. This large reduction in swelling pressure would however not induce canister sinking, since the effect is localised and concerns only a small fraction of the bentonite at its external boundary (Savage & Cloet 2018). Although activity of sulphate-reducing bacteria cannot be excluded in the reduced dry density region, the formation and diffusion of sulphide species to the canister surface has been determined to represent only a minor risk to the canister durability (Cloet et al. 2017). In the altered bentonite rim at the interface with the drift support structure, the hydraulic conductivity of the bentonite was estimated to decrease from ~ 10^{-13} to ~ 10^{-12} m s^{-1}, which still meets the safety function criteria of the buffer.

In a recent publication, Wilson et al. (2021) present a review of studies dealing with the impact of cement on the chemical and physical integrity of argillaceous rocks in the context of radioactive waste disposal. A declared objective was to "...identify the key processes and mechanisms associated with the chemical perturbation of argillaceous rocks; highlight the areas of uncertainty associated with these processes in the context of the safety assessment of repositories". After a general introduction, these authors first review recent laboratory studies on the interaction of mudstone porewaters with OPC pastes, and then present findings from the few studies available that were conducted with the focus on low-pH cements.

The work of Dauzères et al. (2014), in which the effects of OPC and a low-pH cement were studied under the same experimental conditions in a vessel with controlled pCO_2 and online pH measurement, is discussed in detail. These authors found that reaction pathways and extent of degradation of the two cements differed significantly after 5 months alteration with synthetic Callovo-Oxfordian (COx) water. Surprisingly, alteration and porosity increase were much larger for the low-pH cement (up to 1.5 mm) than for OPC (100 µm alteration thickness only). This was explained by the absence of portlandite in the low-pH cement, which favoured direct sulphate attack of C-S-H phases, with consequent formation of macroporosity and early amorphous silica

precipitation. In the case of OPC, an impervious carbonate crust formed that strongly limited the diffusive exchange of solutes (as observed in the Maqarin analogue). Such an impervious layer did not form in the low-pH cement, despite $CaCO_3$ precipitation, however dispersed across the entire alteration profile. The different types of cement carbonation are commonly associated with differences in the hydrate assemblage and pore solution chemistry, as well as in the pore structure and transport properties of the two cement materials (Greve-Dierfeld et al. 2020).

Even after 2 – 6 years interaction time, no formation of impervious layers was observed in the experiments of Shafizadeh et al. (2020) and Luraschi et al. (2020), in which OPC cement disks permeated with artificial cement porewater were placed in contact with compacted, saturated Na-montmorillonite. In the former study, neutron imaging was used to follow the development of porosity (represented by the water content) as a function of time. As expected, the data revealed a small but significant increase in porosity at the cement side of the interface, and a substantial decrease (from 0.4 – 0.5 to about 0.3) on the clay side. The total thickness of the altered layer was about 2 mm. In a companion study, Luraschi et al. (2020) studied the impact of the observed porosity changes on diffusivity. Both HTO and $^{36}Cl^-$ diffusivities (representing total and anion porosity, respectively) were considerably reduced after six years aging time. In some experiments, $^{36}Cl^-$ diffusivity approached zero after about 4 years, implying that anionic radionuclides would not be able to diffuse significantly through the altered montmorillonite-OPC interface (cf. Chagneau et al. 2015). In contrast, HTO diffusivity always remained significant (D_e was reduced from ~ 4×10^{-11} to ~ 2×10^{-11} $m^2 s^{-1}$), implying that selective pathways for diffusive transport of water and cationic/neutral solute species were still available at the end of the experiments.

Wilson et al. (2021) also reviewed studies dedicated to in-situ tests, including the Cement-Clay Interaction (CI) experiment conducted at the Mont Terri Rock Laboratory (Switzerland), documented in a series of papers dealing with different physical-chemical aspects (Jenni et al. 2014, Lerouge et al. 2017, Bernard et al. 2020, Mäder et al. 2018). In the CI experiment, the alteration of three concretes (OPC, low-pH ESDRED shotcrete and another low-pH cement) were studied in situ by placing them into two vertical boreholes drilled into Opalinus Clay and including a section of compacted MX-80 bentonite. Depending on the cement properties, up to six alteration zones developed over a thickness of approximately 2 – 4 mm. Samples were extracted from the experiment after several years of reaction time, namely at 2.2 years, 4.9 years, and 10 years.

Microprobe EDX analyses were carried out for a first chemical characterisation 2.2 years after the start of the experiment (Jenni et al. 2014). On the cement side, starting from the interface with the clay, the OPC developed a Ca-rich carbonated zone, followed by spotty Mg enrichment and a diffuse layer of sulphur enrichment. The low-pH concretes lacked such a clear S-rich layer and were characterised by higher concentrations of silica inherited from the added silica fume. In general, carbonated zones correlated with a reduction in porosity. Later examination of the OPC and low-pH concrete samples after 4.9 years of aging revealed a reduction in heterogeneity (i.e. better developed carbonated Mg-rich and S-rich zones) and extension of the altered zones into the cement up to about 10 mm.

In a recent study, cement samples from the CI experiment aged during 10 years were investigated using synchrotron-based micro-X-ray fluorescence and micro-X-ray diffraction (Bernard et al. 2020). The investigation showed that the porewater migrating into the OPC induced dissolution of portlandite, ettringite and C-S-H in 0.2 – 1 mm narrow zones at the interfaces. The low-pH ESDRED cement showed a larger zone (3 mm) of ettringite dissolution. In contrast to previous studies, calcite formation could not be detected in the altered OPC samples but was clear in the altered ESDRED sample. Overall, the authors state that *"the extent of reaction after 10 years is very small in both cases"*.

On the Opalinus Clay side, chemical changes were even less evident than on the cement side. Ca-enrichment was observed in a narrow zone close to the OPC-clay interface and measurable modifications of the exchanged cation populations were detected over 15 cm from the contact. The major effect after 2.2 years was the displacement of Mg^{2+} by Na^{+} and K^{+}, while Ca^{2+} populations remained almost unchanged due to buffering through calcite equilibrium (Jenni et al. 2014). In the OPC sample aged 10 years, however, Bernard et al. (2020) point to an enrichment of exchanged Ca in the Opalinus Clay, possibly as a result of calcite destabilisation. These authors summarise the main geochemical OPC-clay interface processes as follows: (i) hydration of unhydrated clinker phases due to penetration of Opalinus Clay porewater; (ii) out-diffusion of Ca from the cement, which induces release of exchanged Na^{+} from illite and diffusion into the cement; (iii) dissolution of portlandite, ettringite and C-S-H induced by the pH decrease; (iv) migration of carbonate from the Opalinus Clay into the cement, ultimately inducing calcite precipitation.

The CI experiment also included two samples of compacted MX-80 bentonite in contact with OPC on one side and low-pH cement on the other side. The latter is not the ESDRED formulation, but another low-alkalinity cement equilibrating at pH 12 and denoted “LAC” in the following. Detailed results of the chemical and mineralogical characterisation of thin sections comprising the cement-bentonite interfaces retrieved at 4.9 and 10 years after the start of the experiment are presented in a recent publication (Yokoyama et al. 2021) and will be discussed briefly below.

At the start of the CI experiment, the bentonite was saturated with an artificial solution of composition similar to the Opalinus Clay porewaters described in Chapter 7, although with a higher calculated pH of 9.6. Microprobe chemical analyses were carried out on samples aged 4.9 and 10 years. Only small differences in the element distribution pattern were detected between these samples, suggesting that most chemical reactions slowed down after the first 4.9 years or had even reached complete equilibrium. For both OPC and LAC, enrichment of Mg was observed on both sides of the interfaces. However, the thickness of the Mg-enriched zone is only ~ 1 mm on the cement side and more extended (~ 10 – 15 mm) on the bentonite side. Yokoyama et al. (2021) interpreted this zone as precipitated Mg-rich secondary products, such as magnesium silicate hydrates (M-S-H) or hydrotalcite. On the cement side, enrichment in S and Cl was observed. These zones extend deeper in the case of OPC compared to the LAC sample; they are interpreted as markers of monosulphate/ettringite and Friedel's salt precipitation, respectively, induced by the migration of the sulphate and chloride-rich porewater used to presaturate the bentonite. Therefore, the S and Cl enrichment derives directly from the presaturation with artificial porewater. This treatment does not however reflect the expected repository evolution: indeed, after bentonite emplacement and closure of the drifts, the bentonite would be still “dry” and saturation would proceed starting from the Opalinus Clay-cement interface. The sulphate and chloride in the Opalinus Clay porewater would first react and precipitate at the host rock-drift support interface, leaving a Cl- and S-poorer residual porewater. Probably no such Cl- and S-enrichment would therefore develop at the bentonite - drift support interface. Another effect observed was the partial dissolution of SiO_2 (cristobalite) present as a primary minor mineral in MX-80 induced by the increased solubility of silica at high pH. This effect would probably be less important in the case of the ESDRED formulation, which upon contact with water generates a lower initial pH (~ 11).

A critical issue addressed in the CI experiment was the long-term stability of bentonite, i.e. the question whether interaction with cementitious materials over 10 years would induce significant (safety-relevant) changes in the exchange capacity and mineralogy of MX-80 bentonite. To answer this question, the exchanged ion populations of the reacted bentonite were measured and XRD data were collected to determine any change in clay mineralogy (e.g. illite or beidellite formation). Treatment with NH_4Cl yielded significantly increased values of extracted Mg^{2+} and Ca^{2+} towards the contacts with both types of cement. However, because the K^{+} and Na^{+} populations remained constant, Yokoyama et al. (2021) attributed this result to the presence of

calcite and Mg-minerals formed soon after the contact between bentonite and cement materials was established. XRD data showed no sign of illitisation or beidellitisation; the content of montmorillonite remained stable at the initial values of 75 – 80%, except for a slight, barely significant decrease in the first 5 – 6 mm from the contact with OPC. From the above evidence, the authors conclude that neither the exchange capacity nor the mineralogical features of montmorillonite were significantly modified during the experiment and that dissolution of montmorillonite was insignificant.

Although encouraging, the results of the CI experiment cannot be considered to be conclusive, because of the short timescale and low temperatures to which the samples were subjected. As discussed in Section 5.2, illitisation is a very slow process that cannot be excluded over long timescales at the expected repository temperatures. Therefore, the results of the CI experiment must be complemented with information from advanced reactive transport models and geological analogues. Unfortunately, natural analogues of clay-cement transitions are rare and only partially conform to the geochemical/hydrological features of radioactive waste repositories. Specifically, there is no elevated temperature case and initial and/or boundary conditions are poorly known. The best-known natural analogue of clay-cement interface is found at the Maqarin site in Jordan. As shown by Martin et al. (2016), the observed maximum alteration extends to a maximum of 4 cm for the investigated samples. However the Maqarin site is characterised by limestone-rich lithology and an advective regime that strongly differ from the conditions expected in the Swiss HLW repository, thus limiting the relevance of this finding.

More useful for the prediction of the long-term evolution of clay-cement transitions appear to be reactive transport calculations, particularly if they are validated with the results of underground laboratory experiments. In such calculations, it is possible to set up the appropriate geometry and make use of increasingly reliable thermodynamic data on potentially precipitating phases (e.g. Steefel & Lichtner 1998, Shao et al. 2013, Soler 2016). The next sections are thus devoted to an extensive overview of advanced reactive transport modelling studies, both on the short-term (CI experiment) and long-term evolution of cement/clay interfaces (repository timescale).

6.4 Synthesis of long-term reactive transport modelling

Different approaches, assumptions, boundary conditions and primary materials make the comparison of results from various models difficult and sometimes even misleading. A cross-comparison is however useful as it allows identification of common results and the impact of key model assumptions, e.g. inclusion or exclusion of mineral dissolution/precipitation kinetics. The calculations summarised in Section 6.2, tailored to the SGT-E2 setup of the Swiss HLW repository, excluded mineral kinetics and instantaneous thermodynamic equilibration was assumed. Kosakowski & Berner (2013) justified this approach by arguing that in the system of interest *"most reactions are controlled by diffusive mass transfer rather than by kinetic constraints"*, i.e. that precipitation and dissolution rates are always faster than solute transport rates. This approach was judged appropriate for the initial stages of mineral reactions across cement-clay interfaces, based on the initially strong under- or oversaturation of the infiltrating solution with respect to many solids. This should favour fast dissolution or precipitation rates[19]. However, because diffusion coefficients of solute species in the adjoining compact clays (bentonite and Opalinus Clay) are very small, this assumption had to be revised in the updated calculations described in Section 6.7, based on results from the modelling studies listed further below in this section and from field experiments (e.g. Mont Terri CI experiment, cf. Section 6.5).

[19] Usually, precipitation rates increase exponentially with oversaturation. However, other factors, e.g. small pore sizes and the presence of inhibitors in solution, may prevent or retard nucleation of solids in oversaturated solutions.

Indeed, it was found that in order to capture the early evolution of mineral reactions across the cement/clay interfaces, considering the kinetics of reactions involving aluminosilicate minerals is of central importance.

The effects of dissolution-precipitation kinetics have been investigated by Marty et al. (2009), who modelled the chemical evolution of an alkaline plume diffusing from an aged concrete (pH ~ 12.5) through COx claystone, with full account of porosity variations on transport properties, using the reactive transport code TOUGHREACT. Two sets of model calculations were carried out and compared: one assuming instantaneous equilibration of solid phases, the second involving kinetic constraints for dissolution-precipitation, using a generic rate equation of the form:

$$R_i = \pm k_i \frac{A_i}{F} \left|1 - \Omega_i^{\Theta}\right|^{\eta} \quad (6\text{-}2)$$

Where for each mineral i, R_i is the bulk dissolution or precipitation rate (mol s^{-1}), k_i is the kinetic constant (mol m^{-2} s^{-1}), A_i is the reactive surface area (m^2), Ω_i the saturation ratio and θ, η are empirical parameters and F is a scaling factor introduced to investigate the effect of reduced reactive surface area. R (with i as subscript) is positive in the case of precipitation and negative for dissolution. In addition to the "instantaneous equilibrium" case, calculations were carried out for F = 1, 10, 100, 1,000 and 10,000 to describe increasingly slow reaction kinetics as the reactive surface area is progressively reduced. This slowdown effect is frequently observed in natural systems compared to rates obtained from laboratory experiments. The results of the calculations indicate a low impact of kinetics when $F < 100$. However, considerable effects on the final mineral assemblages, their extension, and clogging times were observed for $F \geq 100$. From this it was concluded that very slow kinetic rates or a low accessibility of reactive surfaces will lead to significantly different results than with fast kinetics or instantaneous equilibration. For instance, assuming fast clay dissolution rates led to "quick" porosity clogging (after 9,600 years) and maintenance of montmorillonite stability, whereas in the case of slow clay dissolution clogging was predicted to be delayed by several ten thousand years, allowing a large amount of montmorillonite to dissolve and new phases (e.g. clinochlore) to form.

In a more recent study (Marty et al. 2015b, see also Marty et al. 2015a), similar calculations were carried out within the framework of a benchmark exercise using six different reactive transport codes and databases. Two cases with different kinetic rates for dissolution/precipitation reactions were included, showing again substantially different outcomes between calculations with fast and slow kinetics. All the codes yielded consistently similar results in terms of solute concentrations and mineral distributions in both cases.

The codes used by Marty et al. (2009) and Marty et al. (2015b) did not include OpenGeoSys-GEM, the reactive transport code employed for the calculations presented in Berner et al. (2013) and in the updated calculations presented later in Section 6.7. It is therefore useful to compare the outcome of the three sets of calculations (Tab. 6-1), keeping in mind that the two exercises did not model the same clay lithology (COx vs. Opalinus Clay) nor the same concrete composition (ESDRED vs. OPC). Also, different assumptions on reaction kinetics were made (kinetic control of some reactions, e.g. clays in Marty et al. (2009, 2015b), vs. instantaneous equilibrium in the OpenGeoSys calculations). A summary of input and output data (times of porosity closure, mineral assemblages) is given for specific results of the three simulations.

In spite of different geometries, materials and initial conditions, the results of Berner et al. (2013) and Marty et al. (2009) are comparable, indicating similar porosity evolution and, to some extent, the same secondary minerals in the altered clay. A major difference emerges in the clay mineral assemblages. While montmorillonite is assumed to remain stable in Berner et al. (2013), it is

converted to saponite (a trioctahedral, Mg-rich smectite) in the calculations of Marty et al. (2009). Moreover, precipitation of zeolites is predicted in the latter calculations. These differences arise from fundamentally different assumptions on the thermodynamic behaviour of clay minerals and zeolites, which are considered to be non-reactive by Berner et al. (2013) (except for montmorillonite and kaolinite) due to the low temperature assumed in the simulations (25 °C in all cases) and/or uncertainties in thermodynamic data.

The analysis of the more recent results of Marty et al. (2015b) points to a much shorter clogging time and different secondary mineralogy compared to the other two simulations. The earlier porosity closure is probably to be ascribed to the lack of explicit porosity coupling in these calculations, which accelerates solute transport and thus reaction progress. In contrast, the reason for the substantial differences in the final mineral assemblages predicted by Marty et al. (2009) and Marty et al. (2015b) is not clear.

Overall, the different secondary mineral assemblages and contrasting developments predicted in the three studies make it evident that a major limitation of such predictions are uncertainties in thermodynamic and kinetic data of the minerals. One way to overcome, or at least to reduce, such uncertainties is to calibrate the models with experimental results from field tests, as exemplified in Section 6.5, devoted to the reactive transport modelling of the Mont Terri CI experiment.

Tab. 6-1: Comparison of input data and output data for three different simulations of clay-cement interfaces at the repository scale

Major minerals are indicated in bold.

	Berner et al. (2013)[%]	**Marty et al. (2009)[*]**	**Marty et al. (2015b)[**]**
Primary clay	Opalinus Clay	COx clay	COx clay
Concrete type	ESDRED	OPC	OPC
Domain length	5.6 m	10 m	43 m
Mesh size	0.01 m	0.1 m	0.05 m
Simulated time	30,000 a	25,270 a	10,000 a
Initial D_e (concrete) Initial D_e (clay)	4.9×10^{-12} m^2s^{-1} 2.6×10^{-11} m^2s^{-1}	1.5×10^{-12} m^2s^{-1} 1.5×10^{-11} m^2s^{-1}	9.0×10^{-12} m^2s^{-1}[#] 2.6×10^{-11} m^2s^{-1}[#]
Coupled porosity	YES	YES	NO
Clogging time	~ 30,000 a	25,270 a	< 10,000 a
Alteration width	0.07 m	0.2 m	0.1 – 0.2 m
Mineral assemblage in altered clay host rock at final simulated time	**Calcite** Siderite - Pyrite Magnetite **Montmorillonite** **Kaolinite** **Illite** **Quartz (inert)** - - - - - - - -	**Calcite** Siderite Dolomite Pyrite - Montmorillonite - **Illite** **Quartz** Daphnite **Phillipsite** **Saponite** - - - - -	**Calcite** - - - - Montmorillonite - **Illite** **Quartz** - - Saponite Microcline **Straetlingite** Hydrotalcite Chlorite Celestite

[%] Fig. 2 in reference, case (d),
[*] Fig. 2 in reference, case (A/100)
[**] Fig. 6 in reference, case 2 (slow kinetics) and Fig. 9 in reference case 3 (fast kinetics)
[#] Values remain constant, since (contrary to the other calculations) no dependence of diffusion coefficients on porosity is included.

6.5 Reactive transport modelling of the CI experiment

The previously discussed, still-ongoing CI experiment at the Mont Terri Rock Laboratory provides detailed mineralogical data on the chemical evolution of the cement/Opalinus Clay and cement/bentonite interface over a duration (> 10 years) sufficient to verify predictions of reactive transport models. Dedicated reactive transport simulations applied to the CI experiment have recently been carried out both using a classical and a Donnan-type approach to model chemical reactions in compacted clays (see Section 6.1.2). In this section, both types of simulations are discussed and compared.

Jenni et al. (2017) and Jenni & Mäder (2021) applied a "dual porosity" reactive transport model to simulate the chemical evolution of the OPC/Opalinus Clay interface in the CI experiment. The model is based on a Donnan approach, extended to include two distinct types of water (porosities) occurring in compacted clays: (i) anion-depleted porewater (representing the electrically charged interlayer with exchanged cations and the diffuse double layer water) and (ii) uncharged free water in macropores. In the classical approach used in all previously discussed simulations (Section 6.4), solute-mineral equilibria are limited to the free uncharged porewater. Interlayer cations are calculated via empirical exchange reactions that must be scaled to the amount of clay. Moreover the diffuse double layer (DDL) speciation cannot be calculated explicitly (nevertheless, in Berner et al. (2013) it is approximated by introducing charge-balancing cationic surface species). A relevant difference between classical approaches and Donnan models is that, in the latter, porosity clogging will reduce or eliminate anion diffusion, but not cation diffusion. Even at zero porosity, in a negatively charged Donnan phase such as clay, cations can continue to migrate through the clay via "surface diffusion" through the interlayer and the DDL. No such "surface diffusion" mechanism is included in classical models, therefore no solute can be further transported once total porosity clogging occurs.

In their reactive transport model, Jenni et al. (2017) implemented the geometry of the CI experiment, consisting of a concrete section of 80% single porosity in contact with a section of dual porosity clay (6.4% free porosity and 6.4% Donnan porosity). Initially, the OPC porosity is filled with pure water, causing rapid dissolution of the reactive clinker phases and precipitation of hydrated solids with consequent porosity reduction. After 1 day, about half of the clinker phases have dissolved and C-S-H, portlandite, ettringite and hydrotalcite precipitate. No pH reduction is predicted at the contact with Opalinus Clay, although the portlandite content is decreased close to the interface. The model indicates that Ca^{2+} diffuses out from the concrete to balance the opposite flux of Na^{+} from the Opalinus Clay. After 5 years, a high-pH alteration front has penetrated about 15 mm into the Opalinus Clay, causing dissolution of dolomite (replaced by calcite) and formation of small amounts of hydrotalcite and brucite. On the cement side, a disturbed region (about 1 mm wide) is predicted where portlandite has undergone total dissolution and ettringite partial dissolution. Changes in free and Donnan porosities are predicted to be small in the clay, whereas a strong porosity reduction occurs in OPC (from 80% down to 13 – 17%). Remarkably, after 5 years, the pH decrease within the clay is not smooth: it remains close to 13 in the altered clay zone and then drops abruptly to near-neutral values.

These model results were compared to multi-elemental microprobe analyses obtained from the CI experiment after 5 years interaction. The model reproduces the Ca profile across the interface quite well and also consistently predicts that no continuous carbonate layer forms in the cement. Instead, (as observed) diffuse precipitation of calcite is predicted following dissolution of dolomite. In contrast, the Mg-peak observed in the clay about 7 mm away from the interface is not correctly reproduced. The simulation predicts a diffuse, extended zone with slightly increased Mg content due to brucite and hydrotalcite precipitation correlated to the high pH. Jenni et al. (2017) conclude that *"The model predicts most trends observed in the samples well, except the false prediction of Mg hydrates precipitating in OPC close to the OPA"*.

The same dual-porosity Donnan model is used in the follow-up modelling study of Jenni & Mäder (2021) to simulate the interactions observed at the interface between Opalinus Clay and low-pH cement (ESDRED) during 4.8 years. Compared with the preceding simulation with OPC as concrete, the dual-porosity model now predicts hydrotalcite and talc as the major secondary phases (on both sides of the clay/ESDRED interface). Brucite is no longer stable due to the lower pH at equilibrium with the ESDRED concrete (pH ≤ 11). Surprisingly, porosity changes are predicted to be higher than in the case of the OPC/clay interface. The free porosity in the clay is completely clogged, and a zone of high porosity (> 80%) develops on the cement side of the interface, due to the partial dissolution of C-S-H phases. The authors conclude that *"It is striking that the predicted extent of alteration in terms of overall mass transfer in case of the ESDRED ("low-pH cement") was in fact larger than that in the OPC case..."* and give the following tentative explanation: *"In the ESDRED, the decrease of Ca-containing hydrates at the interface was higher than in OPC. More dissolved Ca may have diffused from ESDRED into the OPA and exchanged with Mg, which precipitated* [as hydrotalcite and talc] *within the narrow high-pH zone. The clogging of OPA's free porosity could not stop this cation exchange, because it could continue via the Donnan porosity"*.

Analogous reactive transport modelling of the CI experiment has also been carried out with OpenGeoSys-GEM as summarised in Prasianakis et al. (2022), using a classical single-porosity model for the clay. The plots showing mineral distribution and porosity, generated by the two models for 5 years interaction time, are compared in Fig. 6-4. This makes it possible to evaluate how the two conceptualisations perform against a common set of data. Overall, the results are comparable, however significant differences emerge. For instance, in Jenni et al. (2017) a decreasing amount of ettringite in the OPC is predicted towards the interface, while increasing amounts are predicted in the OpenGeoSys simulation. The latter prediction seems to be in better agreement with the S microprobe data than the dual-porosity model results (see Fig. 9 in Jenni et al. 2017). Another difference is the amount of C-S-H phases, which is strongly reduced towards the interface with clay in the calculations summarised in Prasianakis et al. (2022), while it remains constant across the OPC profile in the simulation of Jenni et al. (2017). Both models predict disappearance of portlandite close to the interface. In the calculations described in Prasianakis et al. (2022), Friedel's salt and M-S-H form. Both phases are absent in the concrete domain modelled by Jenni et al. (2017) after 5 years. Currently, an international group is modelling the CI-D experiment with the focus on capturing the anisotropic diffusion and anion exclusion effects in Opalinus Clay. To date, only results for the transport of ions and anions across the cement-Opalinus Clay interface without considering mineral reactions are available (Su et al. 2022).

Neither model correctly predicts the sharp peak in Mg content detected inside the clay by microprobe analyses (Fig. 10 in Jenni et al. 2017).While Jenni et al. (2017) predict a diffuse, slight Mg increase, explained by minor precipitation of brucite and hydrotalcite, in the model described in Prasianakis et al. (2022) practically no change in clay mineralogy occurs, which is explained by the slow rates of dissolution/precipitation assumed for clay and zeolite phases. Slow kinetics were introduced on purpose to comply with the observation that there is *"little evidence for chemical interaction on the claystone side"*. The latter statement makes clear that a fully meaningful comparison of the two simulations is not possible due to different assumptions concerning diffusion coefficients, thermodynamic data and kinetic constraints.

The sensitivity of the results on diffusion coefficient and mineral kinetics has been clearly demonstrated by the model described in Prasianakis et al. (2022), which reproduced the aforementioned Mg anomaly by decreasing the diffusion coefficient and simultaneously increasing clay dissolution rates (Fig. 25 in cited reference), leading to formation of hydrotalcite and brucite as predicted in Jenni et al. (2014).

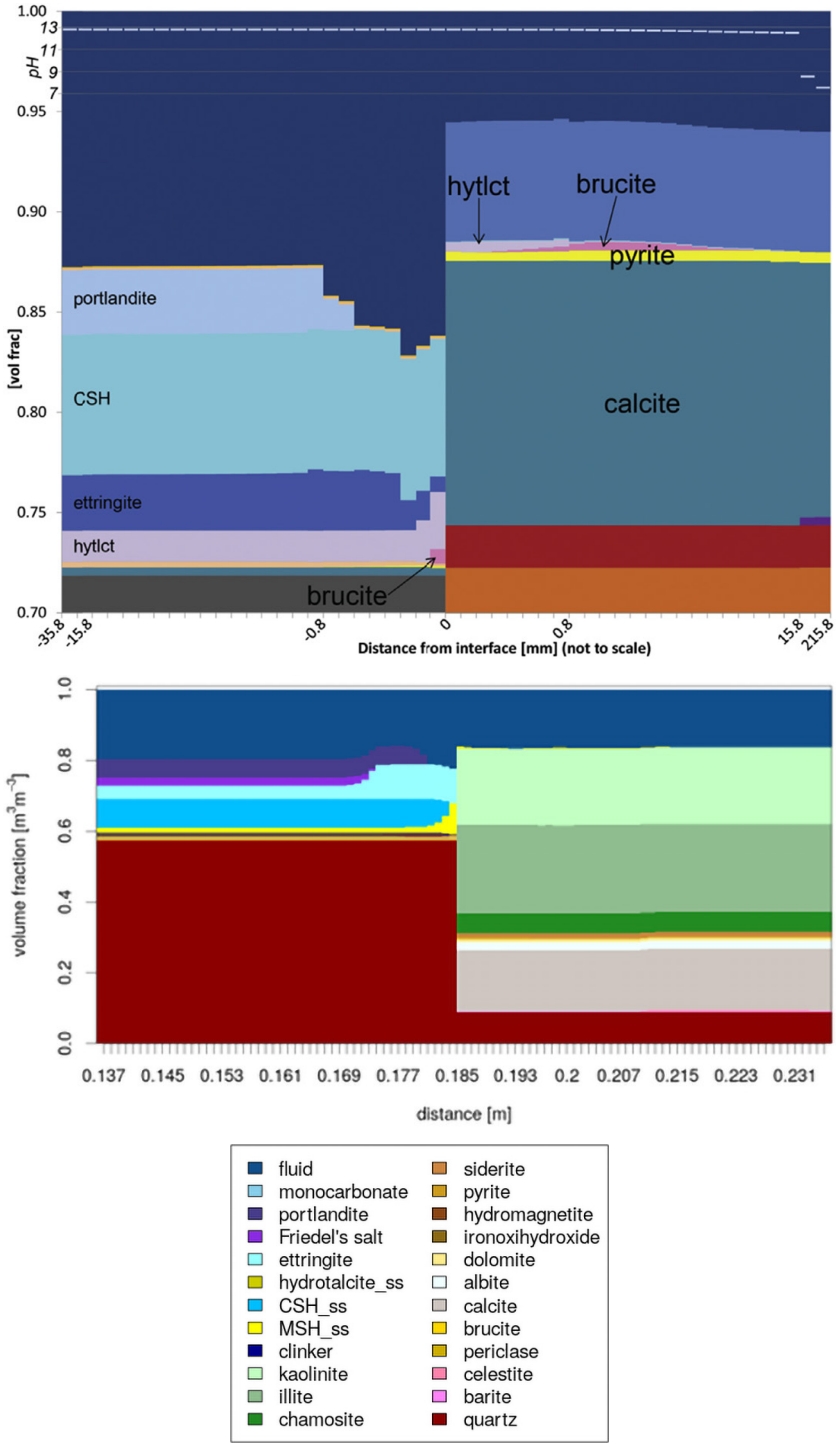

Fig. 6-4: Comparison of reactive transport calculations simulating the results of the CI experiment (low-pH cement / Opalinus Clay interface), after 5 years reaction time using different clay models

(top) results obtained using the dual porosity Donnan model (from Jenni et al. (2017) reproduced with permission from the publisher), (bottom) results obtained using a classical single-porosity model (described in Prasianakis et al. (2022)). Note that different x-axis (distance) and y-axis (vol.%) scales are used in the two plots.

6.6 Predicted evolution of porosity and porewater chemistry across the bentonite/low pH shotcrete/Opalinus Clay transition

In Stage 2 of the Sectoral Plan (SGT-E2), Nagra envisaged the use of low-pH shotcrete as tunnel support material. Such cements allow all portlandite to be consumed during the cement hydration process, so that the pH subsequently decreases below 12.5. ESDRED, a cement consisting of OPC blended with microsilica, was selected as a representative formulation to be used in SGT-E2 model calculations.

In view of a comparison with updated calculations (Section 6.7), this section briefly summarises earlier modelling results obtained in the context of SGT-E2 to predict the evolution of porosity and porewater chemistry across the Opalinus Clay/ESDRED liner/bentonite interface. These results are described in more detail in Berner et al. (2013) and Sections 5.4.2 to 5.4.5 of Bradbury et al. (2014). All calculations were carried out at isothermal-isobaric conditions (25 °C, 1 bar). Two cases were considered, both assuming instantaneous equilibration of minerals, i.e. ignoring kinetics of mineral dissolution/precipitation reactions:

Case 1, in which porosity feedback is considered.

Case 2, in which the porosity is assumed to remain constant and not affected by mineral dissolution/precipitation.

Case 2 is conservative since solute transport and thus reaction progress is not restricted by zones of reduced porosity.

Fig. 6-5 shows the predicted porosity evolution after 10,000 and 30,800 years for the more realistic case 1. These simulations indicate a localised increase in porosity within the drift support structure close to the interfaces, whereas thin regions of strongly reduced porosity are predicted in the adjacent bentonite and Opalinus Clay.

Fig. 6-6 shows the predicted pH evolution at selected reaction times for case 1 (blue lines) and case 2 (red curve at 10,000 years), in which porosity feedback is considered as in Fig. 6-5. In both cases, a pH peak of about 11 is reached soon after saturation (black line), decreasing to ~ pH 10 after 10,000 years. For case 2, a further decrease to pH ~ 9.5 is predicted, and significant pH gradients are maintained up to the end simulation time (56,200 years) between the tunnel support and both clay sides. By that time, no significant pH rise is predicted in the Opalinus Clay, whereas a region of increased pH (alteration front) of about 20 cm has progressed on the bentonite side. Note that assuming porosity coupling (case 1), the altered bentonite zone is considerably thinner. It is not expected that the pH alteration front in bentonite will extend further at later times, since after hydrotalcite is completely dissolved, the pH in the concrete liner and in the adjacent clay materials will have decreased to ~ 8, eliminating any pH contrast in the three materials (see Kosakowski et al. 2014 for details).

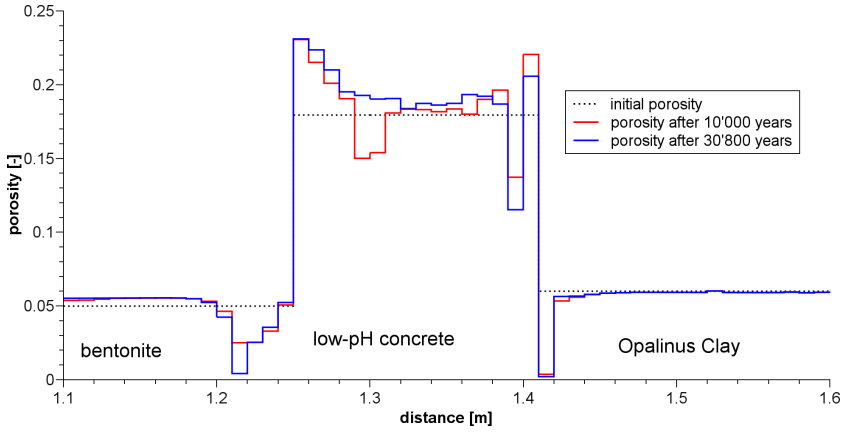

Fig. 6-5: Porosity evolution across the Opalinus Clay/ESDRED liner/bentonite interfaces for different repository evolution times assuming instantaneous equilibration of minerals, compared with initial values

Case 1: with porosity feedback

After Bradbury et al. (2014)

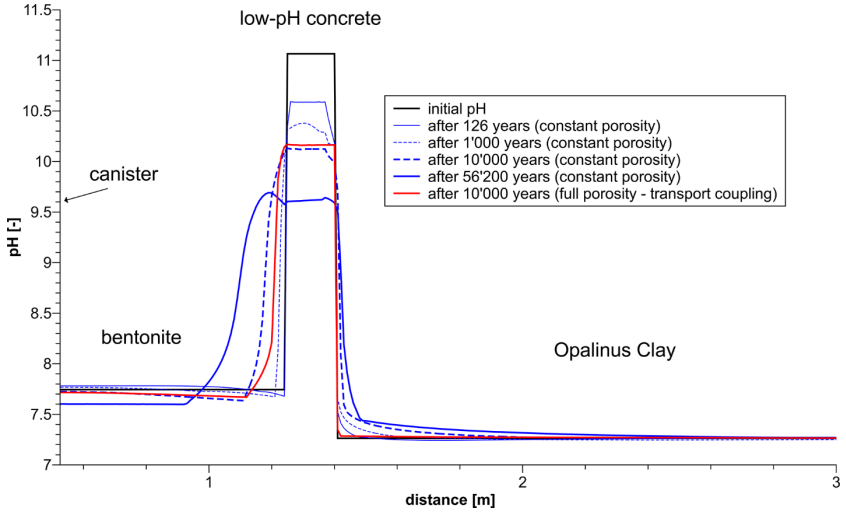

Fig. 6-6: Predicted pH profiles across the Opalinus Clay/ESDRED liner/bentonite interfaces for different repository evolution times assuming instantaneous equilibration of minerals, compared with initial values

Case 1: (red curve): with porosity feedback
Case 2: (blue curves): without porosity feedback

After Bradbury et al. (2014)

Finally, for case 1 Fig. 6-7 shows the total concentrations of the major dissolved conservative ions Na^+ and Cl^- (not involved in the precipitation of secondary minerals), at different reaction times. The simulations predict high initial concentrations for both components in bentonite, ascribed to a small initial NaCl inventory (see Chapter 7). While chloride concentration rapidly drops via out-diffusion to the concentration level in the Opalinus Clay porewater, equilibration of Na concentrations in the three compartments is slower due to the retarding effect of cation exchange reactions in bentonite (replacement of exchanged Na^+ by Ca^{2+} and Mg^{2+}). After 10,000 years, the concentrations of both elements do not show any further significant changes because mass transport across the almost clogged interfaces is strongly reduced.

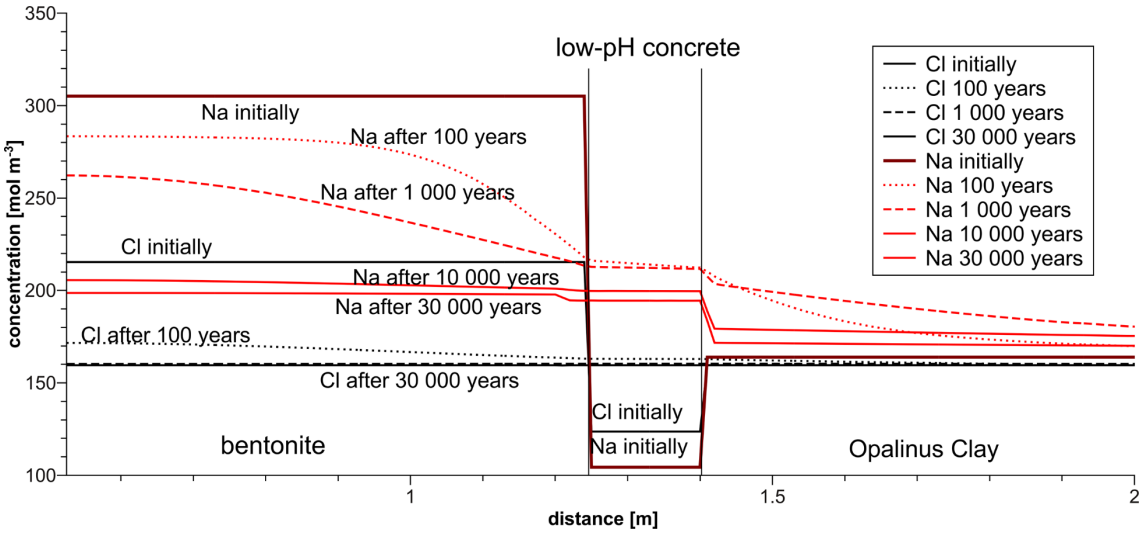

Fig. 6-7: Predicted profiles of dissolved Na and Cl across the Opalinus Clay/ESDRED liner/bentonite interfaces for different repository evolution times, compared with initial values

Case 1, after Bradbury et al. (2014)

6.7 Update of reactive transport calculations for the provisional HLW emplacement drift design

6.7.1 Introduction and model description

The reactive transport calculations presented in Section 6.6 have recently been updated. The update accounts explicitly for the new provisional HLW emplacement drift design with the segmental liner and annulus grout material (see Section 4.5.2) and for the greater depth of the selected site (about 900 m, implying higher temperatures, see Section 5.1.2 and Nagra 2024g). The new calculations were carried out using improved thermodynamic data and considering temperature-dependent parameters. Details on the models and the results are documented in a separate report (Kosakowski 2023).

The approach reported in Cloet et al. (2019) was followed and, as for the previous calculations, the OpenGeoSys-GEMS coupled code (Kosakowski & Watanabe 2014) was used. In analogy with the previous studies of Berner et al. (2013), Bradbury et al. (2014) and Cloet et al. (2019), solute/heat transport is driven solely by diffusion in a fully water-saturated near-field, i.e. the desaturation and convection phenomena predicted during the initial elevated temperature period

are not considered. In all these models, a simplified 1D radial-symmetric geometry is assumed, with a mesh that extends from an inner zero-flux boundary at the canister/bentonite interface (0.55 m from canister/tunnel centre) to an external constant concentration/temperature boundary at 50 m distance from the canister/tunnel centre.

Chemical reactions are modelled using the GEM-Selektor code (Kulik et al. 2013), with a thermodynamic setup analogous to that used in Cloet et al. (2019), i.e. the PSI/Nagra TDB 07/12 (Thoenen et al. 2014) is used together with CEMDATA 18 (Lothenbach et al. 2019) and complementary data on mineral phases imported from Thermoddem DB (Marty et al. 2015a). The older zeolite data in CEMDATA 18 were replaced with those from the new database ZEOLITE DB (Ma & Lothenbach 2020a, Ma & Lothenbach 2020b). Moreover, kinetic data for dissolution/ precipitation reactions, required for some calculations (see below), were taken from the Thermoddem DB.

Several model variants with distinct key assumptions on temperature, porosity coupling and kinetics were considered. This allowed a comparison of results with previous models and to assess the effects of temperature dependence, kinetic constraints and porosity coupling on solute transport and chemical evolution. In the (most realistic) full model variant, the high-temperature transient was considered by assuming an initial heat output from the canister of 1,500 W and the time-dependent temperature profiles calculated by Senger et al. (2014) at different points across the near-field. Heat transport is coupled to solute transport by explicitly considering the temperature-dependence of diffusion coefficients, chemical equilibrium constants and kinetic rate constants of dissolution/precipitation reactions. As an initial condition, a homogeneous temperature profile of 317 K (44.85 ºC) is assumed throughout the simulation domain, representing the average temperature of the near-field in the calculations of Senger et al. (2014), which is roughly comparable to the temperature that can be expected at the depth of the proposed site (~ 47 °C, Section 5.1.2 and Nagra 2024g). At the external boundary (50 m radial distance), the same temperature is fixed for the entire duration of the simulation period.

The setup and materials considered reproduce as closely as possible the most recent near-field description given in Chapter 3 and Chapter 4, but with some deviations. Specifically, the initial mineral inventory and equilibrated porewater composition in bentonite (Chapter 7) are not identical to those defined in this report. This is mostly due to the different thermodynamic databases used in the reactive transport and bentonite porewater (BPW) calculations[20]. The definition of the clay mineral properties in the Opalinus Clay follows the approach adopted in this report, but definitions for the amphoteric sites were taken from Berner et al. (2013). Moreover, the chemical compositions of drift support structure and grout materials (used to fill the gap behind the segmental liner) are based on preliminary recipes, since these materials are currently under development. For both concrete materials, we assumed that aggregates consist mostly of quartz, which will dissolve on the long term and induce aggregate-cement reactions.

[20] In the present reactive transport calculations, an older version of the PSI thermodynamic database had to be used because temperature dependencies and molar volumes of the thermodynamic data are not yet fully integrated in TDB2020 Hummel & Thoenen (2023).

6.7.2 Modelling results and comparison with earlier models

Despite differences in temperature, materials chemistry, geometry, and thermodynamic/kinetic setup, the results of the updated isothermal model reproduce the SGT-E2 simulations reasonably well. Indeed, roughly the same chemical evolution and features are predicted, despite the considerably higher temperature assumed in the new isothermal calculations by Kosakowski (2023) (44.85 °C instead of 25 °C in Berner et al. 2013 and Bradbury et al. 2014).

In the non-isothermal variant of the updated model, a similar temperature evolution to that in the calculations of Cloet et al. (2019) has been assumed. Although the results of Cloet et al. (2019) and Berner et al. (2013) are comparable only to a limited extent to the present ones[21], some analogies remain that allow at least a qualitative comparison. Specifically, all three models include a cement/Opalinus Clay interface: OPC/Opalinus Clay (without bentonite) in Cloet et al. (2019), bentonite/low-pH cement/Opalinus Clay in Berner et al. (2013) and bentonite/low-pH concrete/annulus grout/Opalinus Clay in the present updated model. At least the evolution of the cement/Opalinus Clay interface is expected to be qualitatively similar in the different studies. Indeed, all models predict a tendency towards porosity reduction (complete or partial clogging) at the cement/Opalinus Clay interface due to precipitation of calcite and zeolites over a timescale of several hundred years. At the same time, minor clay dissolution phenomena are observed on a cm scale in the Opalinus Clay.

In the present updated model, both solute diffusion and aggregate-cement reactions are accelerated due to the higher temperature assumed. Consequently, the pH reduction (to values below pH 10) also predicted by the other models in the cement materials is faster. It occurs in a time span ranging from a hundred years (in the model considering the temperature pulse) to a few hundred years (isothermal models). The faster pH reduction strongly mitigates the chemical reactivity between clay and cement materials by reducing hydroxyl fluxes towards the clay and thus slowing down mineral transformations in the clay. As a result, compared to the simulations in Cloet et al. (2019), different amounts of zeolite are formed, clay mineral reaction rates are slower (producing less mineralogical changes) and the evolution of porosity in the model variants with kinetic control is retarded (cf. Fig. 6-8). The extension of the increased pH-region in the Opalinus Clay (not shown) is very limited due to efficient buffering provided by pH-dependent mineral reactions and by the protonation-deprotonation of amphoteric sites in illite, as described in Berner et al. (2013). In contrast, a slight increase by 0.5 pH units is observed in bentonite after about 1,000 years.

For all model variants, changes in spatial extensions and chemical compositions of montmorillonite in MX-80 bentonite and of illite in Opalinus Clay are very limited, specifically after clogging of the pore space has occurred. Compared to former models, the release of calcium from cement dissolution is decreased because of the accelerated degradation of cement materials caused by the enhanced aggregate-cement reactions at elevated temperatures.

---

[21] In Cloet et al. (2019), the entire bentonite buffer is replaced by a self-compacting concrete containing Ordinary Portland Cement (OPC) and carbonate aggregates. In addition, the aggregates are assumed to be inert, while the models described in this report explicitly consider a pozzolanic reaction driven by the dissolving siliceous aggregates. For the differences between the updated calculations and those of Berner et al. (2013), see Section 6.6.

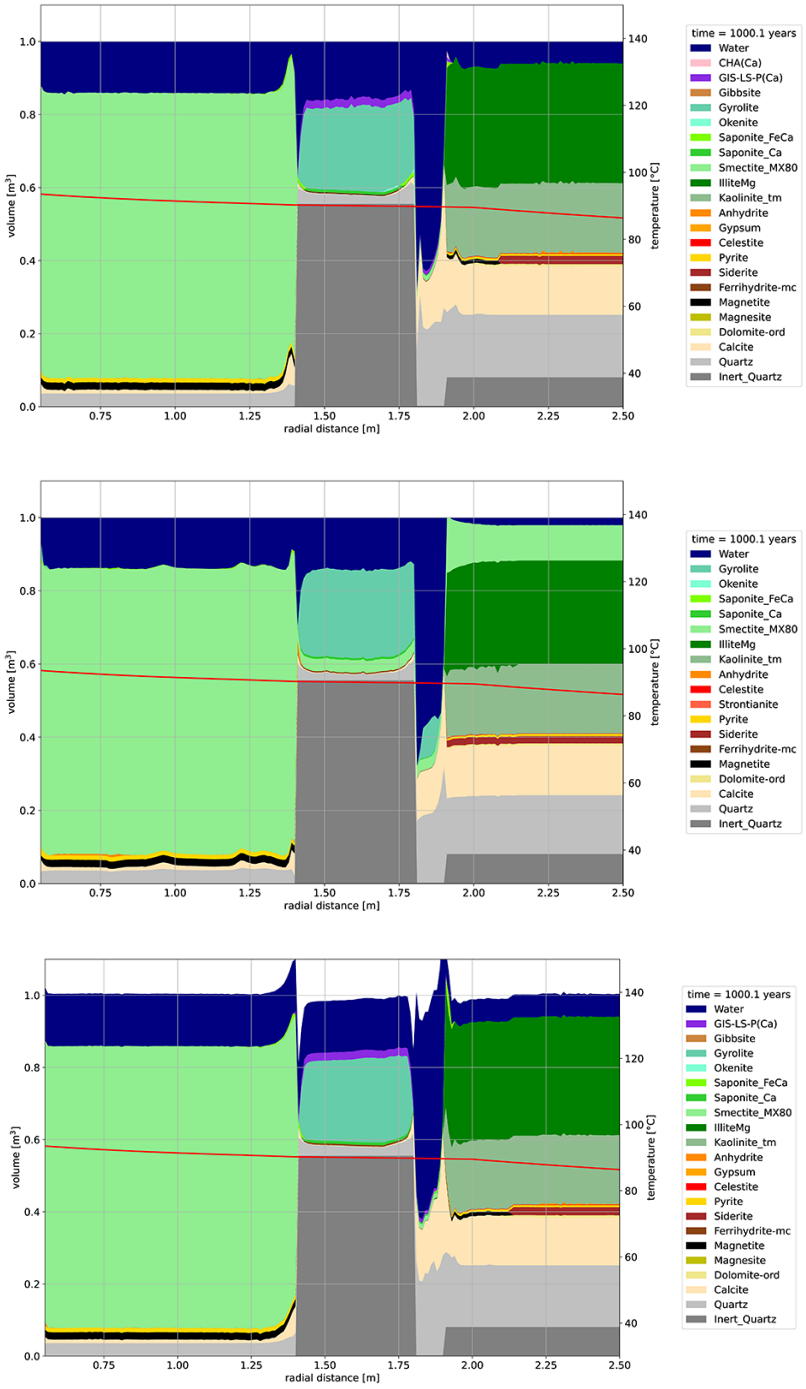

Fig. 6-8: Spatial mineralogical profiles for model variants with temperature increase (this page) and at constant temperature (next page) after 1,000 years simulation time

The x-axis starts at the contact between canister and bentonite at 0.55 m from the drift centre, the bentonite extends between 0.55 and 1.4 m, tubbing concrete between 1.4 and 1.8 m, the annular grout between 1.8 and 1.9 m, and Opalinus Clay beyond 1.9 m. Top row: With kinetic control of reactions and with porosity coupling. Second row: Without kinetic control of reactions and with porosity coupling. Bottom row: With kinetic control of reactions and without porosity coupling. CHA: chabazite type zeolite; GIS-LS-P: gismondine type zeolite; SOD: sodalite type zeolite

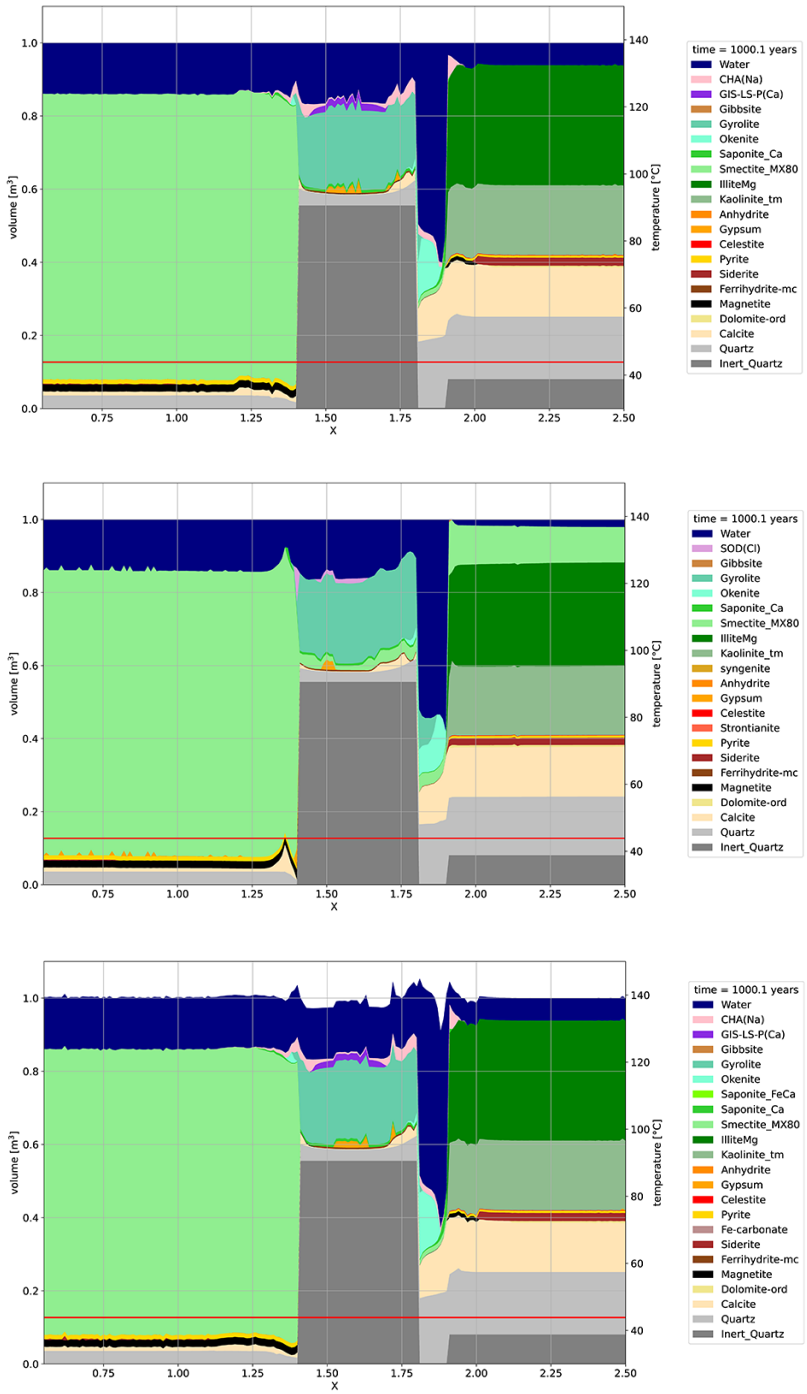
volume [m³]
temperature [°C]
X
time = 1000.1 years
Water
CHA(Na)
GIS-LS-P(Ca)
Gibbsite
Gyrolite
Okenite
Saponite_Ca
Smectite_MX80
IlliteMg
Kaolinite_tm
Anhydrite
Gypsum
Celestite
Pyrite
Siderite
Ferrihydrite-mc
Magnetite
Dolomite-ord
Calcite
Quartz
Inert_Quartz
time = 1000.1 years
Water
SOD(Cl)
Gibbsite
Gyrolite
Okenite
Saponite_Ca
Smectite_MX80
IlliteMg
Kaolinite_tm
syngenite
Anhydrite
Gypsum
Celestite
Strontianite
Pyrite
Siderite
Ferrihydrite-mc
Magnetite
Dolomite-ord
Calcite
Quartz
Inert_Quartz
time = 1000.1 years
Water
CHA(Na)
GIS-LS-P(Ca)
Gibbsite
Gyrolite
Okenite
Saponite_FeCa
Saponite_Ca
Smectite_MX80
IlliteMg
Kaolinite_tm
Anhydrite
Gypsum
Celestite
Pyrite
Fe-carbonate
Siderite
Ferrihydrite-mc
Magnetite
Dolomite-ord
Calcite
Quartz
Inert_Quartz

Fig. 6-8: Cont.

All models predict porosity reduction in the clay materials close to their interface with the cementitious tunnel support structure. In model variants that do not consider kinetic control of clay reactivity, complete porosity clogging is reached “rapidly”, within few hundred years, while model variants that include kinetic control of clay dissolution/precipitation show a slower porosity decrease and do not reach complete porosity clogging within the calculated times. Similarly to Cloet et al. (2019), in all variants the present updated model calculates a strong porosity increase in the grout due to enhanced transformation of C-S-H phases upon temperature increase after 1,000 years. In the long term, however, the degradation of cement via carbonation, aggregate-cement reactions and cement-clay interactions is expected to reverse the porosity evolution (i.e. porosity reduction after porosity increase).

As in Cloet et al. (2019), in the updated model calculations considering the thermal pulse, ettringite or AFt phases, present in cement materials are mostly destabilised at elevated temperature. Interestingly, there is no reprecipitation of ettringite when ambient host rock temperatures are recovered, because the elevated sulphate concentrations generated in the cement materials at high temperature by dissolution of ettringite are reduced via out-diffusion towards the Opalinus Clay. In the isothermal model variants, ettringite is dissolved via a dual mechanism: by carbonation/degradation fronts at the contact with clay materials and, on the other hand, by aggregate-cement reactions. Most of the released sulphate is then used to form anhydrite, the stable calcium sulphate phase above 40 °C.

For the variants considering the temperature pulse, the increase in diffusivity with temperature induces an additional significant carbonate flux from the cooler Opalinus Clay towards the hotter engineered barrier materials. As carbonate solubility decreases with increasing pH, carbonate is precipitated as a sharp horizon corresponding to the pH front at the contact between Opalinus Clay and the gap-filling grout. Due to the limited availability of free calcium in the Opalinus Clay, the carbonation front moves quickly into the grout. The driving force is the reaction between the carbonate in-diffusion from the Opalinus Clay and the abundant calcium dissolution from C-S-H and other cement phases, which forcefully causes calcite precipitation. The dissolution of C-S-H phases also releases large amounts of silica, which precipitates as quartz. As the dissolution of quartz is kinetically controlled, excess silica in solution will be transported towards the Opalinus Clay and precipitate there.

In the long term, carbonates and, to a lesser degree, quartz, which is more stable than amorphous silica, accumulate near the grout/Opalinus Clay interface. In addition, for the investigated provisionalary repository design the grout layer is completely carbonated in less than a thousand years (see first page in Fig. 6-8). The isothermal model variants (see second page in Fig. 6-8) do not show such a strong carbonation effect.

6.8 Summary and conclusions

Overall, the review of reactive transport calculations applied to different repository types and in-situ experiments indicates formation of alteration zones at the contact of clay (engineered barrier materials or host rocks) with concrete (OPC or low-pH cement). Such alteration zones are predicted to be thin, in the order of a few mm to cm, despite different initial mineral compositions, codes and thermodynamic data (see e.g. Figs. 3-2, 3-3 and 3-4 in Savage & Cloet 2018). Broadly, the predicted thicknesses agree with experimental evidence, whenever available. Estimations based on simple mass balance considerations generally lead to much larger thicknesses. For the Swiss HLW repository, using such methods Savage et al. (2010b) and Savage & Cloet (2018) estimated conservative alteration thicknesses of 13 cm in the Opalinus Clay and 4 cm in the bentonite at the corresponding interfaces with the concrete liner. From an analysis of simulations

of clay/concrete barriers in various repository setups and up to 100,000 years simulation time, Savage & Cloet (2018) conclude that perturbed zones in clay are always predicted to be narrow and less porous than in the initial conditions.

New calculations for the documentation of the general licence application, considering both temperature pulse and mineral/porewater evolution across the Opalinus Clay/drift support/bentonite transition, indicate that the altered thickness at the external side of the drift support structure will not exceed about 10 – 20 cm. In both bentonite and Opalinus Clay domains, the total amount of dissolved clay minerals is very small at the end-time of the simulations (several thousands of years). Moreover, on both clay sides alkaline zones with pH > 9 arising from cement alteration are very limited. This is because the alkalinity in the degraded cement materials is mitigated to pH < 10 by aggregate-cement reactions and by extended carbonation after several thousand years, when the temperature pulse has faded. It is anticipated that any pH contrast will be eliminated in the long term. Taking into account the initial high-temperature pulse in the new calculations accelerates cement degradation and cement/clay interactions compared to former isothermal simulations. As in most other repository-related simulations, precipitation of secondary minerals causes a reduction in porosity in both bentonite and Opalinus Clay at the respective interfaces to cementitious drift support materials. The effect is more pronounced and rapid in the Opalinus Clay. The simulations predict precipitation of calcite and hydrotalcite as the main secondary solids in the perturbed bentonite and partial replacement of exchanged Na and Mg by Ca and K in montmorillonite. In the altered Opalinus Clay, kaolinite and illite are dissolved and replaced by montmorillonite. Depending on time and distance from the interface, quartz, calcite and pyrite may dissolve, and precipitation of calcite and illite may occur. Within the tunnel support, C-S-H phases are eventually dissolved completely and replaced by hydrotalcite, phillipsite, clay minerals (illite, montmorillonite), gypsum and calcite.

Verification of reactive transport predictions has recently become possible thanks to detailed experimental data on mineralogical changes collected during the 10-year-long Cement-Clay-Interface (CI) experiment in the Mont Terri Rock Laboratory. Modelling of the CI experiment has recently been carried out using two distinct approaches: a classical single-porosity model (Kosakowski 2023) and a dual-porosity model in which saturated montmorillonite is treated as a uniform Donnan phase (Jenni et al. 2017, Jenni & Mäder 2021). Both models broadly reproduce the major observed features (thickness of alteration zones, porosity evolution and most compositional changes) despite some discrepancies (see below). For instance, neither model correctly reproduces the Mg peak observed in the Opalinus Clay about 7 mm away from the interface.

Despite the largely congruent results obtained in the modelling of the CI experiment, fundamental differences remain between the two approaches used to model compact clays, as discussed in Section 6.1.2. The most prominent concerns the coupling to cation diffusion: while in the classical single porosity model both cation and anion diffusion come to an end once the free porosity is completely clogged, only anion diffusion terminates in such a situation when applying the Donnan-based dual porosity model. In spite of total physical clogging, the latter model permits further diffusion of cations and neutral species through the clay via interlayer and diffuse double layer, a phenomenon which has been verified experimentally (Chagneau et al. 2015, Luraschi et al. 2020).

To conclude, the following issues remain to be solved when modelling cement/clay interfaces at the repository scale over geological timescales:

- Modelling the long-term chemical and mechanical stability of clogged interfaces is still challenging due to uncertainties in the choice of minerals (including solid solutions), insufficient or uncertain thermodynamic data (e.g. clay minerals, C-S-H).
- Further experimental verification of diffusion of neutral species and cations through interlayers and diffuse double layers (DDL) is required and the long-term consequences of this phenomenon have still to be explored.
- The kinetics of dissolution/precipitation reactions is difficult to assess. Dissolution and precipitation rate data are still affected by large uncertainties, as is the case of reactive surface areas.

7 Modelling of bentonite porewater (BPW) chemistry

7.1 Introduction

The knowledge of aqueous compositions in compacted bentonite, the engineered barrier material foreseen for backfilling of the HLW emplacement drifts, is essential as a prerequisite to deriving solubility limits and sorption coefficients (K_d) of considered dose-relevant radionuclides for safety assessment calculations. Bentonite porewaters (BPW) were regularly defined and updated in the context of the earlier safety assessments Kristallin-I, Entsorgungsnachweis and SGT-E2 (Curti 1993, Curti & Wersin 2002, Bradbury et al. 2014). Each update, including the present one, reflects the specificity of host rock type (crystalline basement for Kristallin-I, Opalinus Clay in later assessments), available underground water data, and improvements of thermodynamic data and of chemical models for the prediction of aqueous-solid equilibria in compacted clay. This chapter presents the final BPW update for the documentation of the general licence application, considering the specific geochemical data obtained during the borehole campaign in the proposed Nördlich Lägern siting region. A "classical" approach, based on the "ClaySor" model (Kulik et al. 2018), was preferred to recently developed "Donnan-type" models. A comparison of "classical" vs. "Donnan" approaches is given in Section 6.1.2, along with arguments supporting this choice.

After an outline of the "ClaySor" model used for the modelling of BPW compositions (Section 7.2), this chapter presents a section devoted to the initial state of the system, which includes initial mineralogy of bentonite, as well as exchanged cation populations and amphoteric edge site occupancies in montmorillonite (Section 7.3). Thereafter, the key results of the BPW calculations are presented and discussed (Section 7.4), including the results of a sensitivity analysis carried out to explore the effects of variations in key input parameters (e.g. degree of compaction, initial state of the clay, pCO_2) and the long-term evolution of BPW composition[22]. Finally, some additional key issues potentially affecting the BPW composition are discussed, such as the role of minor minerals in bentonite and the inhibition of redox reactions.

7.2 Outline of the bentonite porewater model for the general licence application

The bentonite porewater model adopted here for the documentation of the general licence application is an adaption of the ClaySor model described in Kulik et al. (2018). The ClaySor model is based on GEM-Selektor (Kulik et al. 2013) and is originally an implementation of the long-standing 2SPNE SC/CE clay sorption model of Bradbury & Baeyens (1997). For the present BPW calculations, it was slightly adapted to the conditions foreseen in the HLW repository. All details on the BPW model development and testing are given in a separate report (Curti 2023). Here, only an outline of the essential features is presented.

[22] The long-term BPW evolution is predicted using a sequential batch reaction model in which the bentonite reacts sequentially with multiple batches of Opalinus Clay porewater filling the anion-accessible porosity of bentonite. An update of the full reactive transport calculations carried out for SGT-E2 (Berner et al. 2013), including the effect of a concrete liner, is currently ongoing and will be presented in a later report (Kosakowski 2023). Preliminary results from the update are presented in Section 6.7.

The following chemical processes are modelled:

- cation exchange in the interlayer of montmorillonite
- pH-dependent protonation/deprotonation on amphoteric surface hydroxyl functional groups
- complexation reactions among solute species in the interparticle ("external") porewater
- dissolution/precipitation of reactive minor minerals

Unlike Donnan-type models (see Section 6.1.2), ClaySor is a single porosity model with no explicit treatment of interlayer and DDL, since the 2SPNE SC/CE approach deliberately excludes an explicit electrostatic term. In spite of this "unphysical" assumption, Bradbury & Baeyens (1997) were able to obtain excellent fits of experimentally determined pH-dependent sorption edges for a variety of cations. The ClaySor model nevertheless considers electrostatic effects implicitly by including and "averaging" the cation-dominated DDL water into the uncharged interparticle water residing in the anion-accessible porosity. As shown in Section 6.1.2, it is currently not possible to calculate a full set of radionuclide solubility limits and sorption coefficients (K_d) using Donnan-based models, so there is presently no alternative. The reasonably good predictions and congruent modelling results obtained with either approach to reproduce the experimental data of the CI experiment (Section 6.5) gives confidence that ClaySor yields reliable predictions also for the bentonite porewater compositions.

Because modelling of protonation/deprotonation reactions of surface functional groups is explicitly included in the ClaySor model, a pH-dependent charge is generated on the surface of the montmorillonite. This charge is usually negative at the pH values of interest and must be balanced by an equivalent positive charge in the porewater to avoid unphysical charge imbalance in the bulk system. This is achieved in ClaySor by adding an appropriate excess of Na^+ ions (or by adding Cl^- anions if the pH is sufficiently low to generate a positive clay charge) to the porewater, so that is electrically balanced. Because ClaySor is a single porosity model, this cation excess cannot be assigned to a separate DDL water and is uniformly distributed through the interparticle water filling the anion-accessible porosity. As a result, the equilibrated interparticle water is positively (or negatively) charged. Anion-accessible porosities in compacted bentonite can be determined via empirical equations as a function of dry density and ionic strength of the porewater (van Loon et al. 2007).

Schematic illustrations of the bentonite microstructure and its conceptualisation as implemented in the ClaySor model are shown in Fig. 7-1. The clay is regarded as consisting of insoluble tetrahedral-octahedral-tetrahedral (TOT) layers intercalating with expanded interlayers hosting hydrated exchangeable cations (2). The edges of the TOT layers carry amphoteric functional groups that can be protonated or deprotonated (1). Minor reactive minerals such as calcite, gypsum and soluble NaCl present in the initial bentonite are allowed to dissolve or precipitate until saturation is reached (3), and a constant CO_2 partial pressure is imposed via exchange with an external reservoir (4). Although the interparticle water is treated as a single homogeneous phase in ClaySor, the DDL water in contact with the clay mineral surface is highlighted in Fig. 7-1 in blue-green colour. In a real system, at neutral to basic pH, excess cations (mainly Na^+) compensating the negative non-permanent charge on the clay are confined in the nanometer-thick DDL (5). The corresponding realistic charge density profile is shown at the bottom of the figure by the green broken line, whereas the continuous orange line shows the "averaging" approximation made in the ClaySor model (the charge-balancing Na^+ cations are distributed uniformly in the external water). The three shaded areas indicate total positive or negative charges, which must sum to zero.

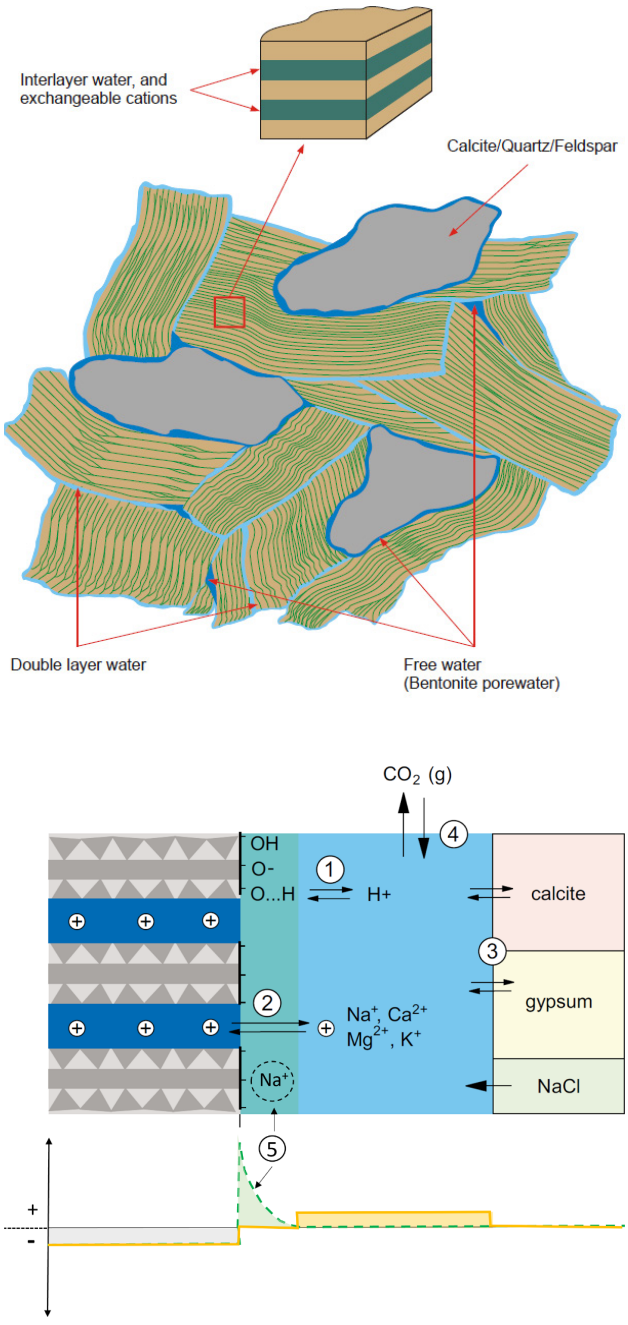

Fig. 7-1: Schematic illustrations showing the microstructure (top, from Bradbury & Baeyens 2002) and the chemical reactions modelled in the ClaySor model (bottom, adapted from Curti & Wersin 2002)

Circled numbers show the different processes considered in the model: (1) protonation/ deprotonation of clay surface sites, (2) cation exchange, (3) precipitation/dissolution, (4) CO_2 exchange and (5) non-specific adsorption of Na^+ in the DDL counteracting the negative pH-dependent charge on the clay surface. The lower graph shows schematic charge density profiles in the real system (green broken line) and in the ClaySor model (orange continuous line). The three shaded areas indicate total positive or negative charges, which must sum to zero.

The architecture of the BPW model is shown in the flow diagram of Fig. 7-2. The calculations simulate cation exchange and mineral dissolution/precipitation reactions in a system consisting of MX-80 bentonite and Opalinus Clay porewater (OPAw) filling the anion-accessible porosity (ε_{an}) at a given solid/water (S/W) ratio. The latter parameter is correlated to the dry bulk density (ρ_{dry}) of bentonite. The initial state of the bentonite is considered by specifying initial populations of exchangeable interlayer cations (Na^+, K^+, Ca^{2+}, Mg^{2+}, Sr^{2+}, Ba^{2+}), an initial protonation state of surface hydroxyl groups and initial inventories of reactive minerals.

The BPW calculations presented later in this chapter include, besides H and O, 16 elements (Al, Ba, Br, C, Ca, Cl, F, Fe, K, K, Mg, Mn, Na, S, Si, Sr)[23] and were carried out with Version 3.9.0 of the GEM-Selektor code (Kulik et al. 2013) using the updated PSI thermodynamic database TDB 2020 (Hummel & Thoenen 2023). Ionic strength corrections were made using the Specific Ion Interaction (SIT) activity model. In the calculations, a pre-defined volume of Opalinus Clay porewater (OPAw) filling the anion-accessible porosity is equilibrated once with the bentonite as described above. The equilibrated output system then consists of bentonite porewater (BPW), a final exchanged ion population, an equilibrium distribution of protonated and deprotonated surface sites and a final inventory of minor solids.

All calculations were carried out at standard state conditions (25 °C, 1 bar), although eventually moderately higher temperatures and pressures will be established in the repository, see Section 5.1. This decision was taken to ensure full consistency of the thermodynamic data used, thus avoiding generating non-defendable results when calculating radionuclide solubility limits and sorption coefficients for safety assessment calculations. While quite reliable parameters for temperature-pressure extrapolations of equilibrium constants exist for the major chemical elements, it is not possible to find equivalent sets of internally consistent temperature/pressure coefficients for *all* dose-determining radioelements, for which solubility limits and sorption coefficients are needed. A way out of this dilemma would be to use generic extrapolation methods, such as the SUPCRT92 database (Johnson et al. 1992), which provide generalised coefficients of heat capacity functions over a large range of temperatures and pressures. Such data were implemented in the former version of the PSI database (12/07), see Thoenen et al. (2014); however the implementation in the updated PSI database (TDB2020) was still ongoing at the time when the BPW calculations were run. The effect of the mismatch in temperature on the equilibria of interest was however estimated via data reviews (Section 5.3) and dedicated reactive transport calculations (Section 6.7). It was shown that assuming standard state conditions has only a minor impact on the results of the OPAw and BPW calculations.

[23] Only results for major elements and those determining key parameters (pCO_2, pH, Eh) will be listed in Tables. Minor elements such as Br, F, Mn are not shown, although they were calculated.

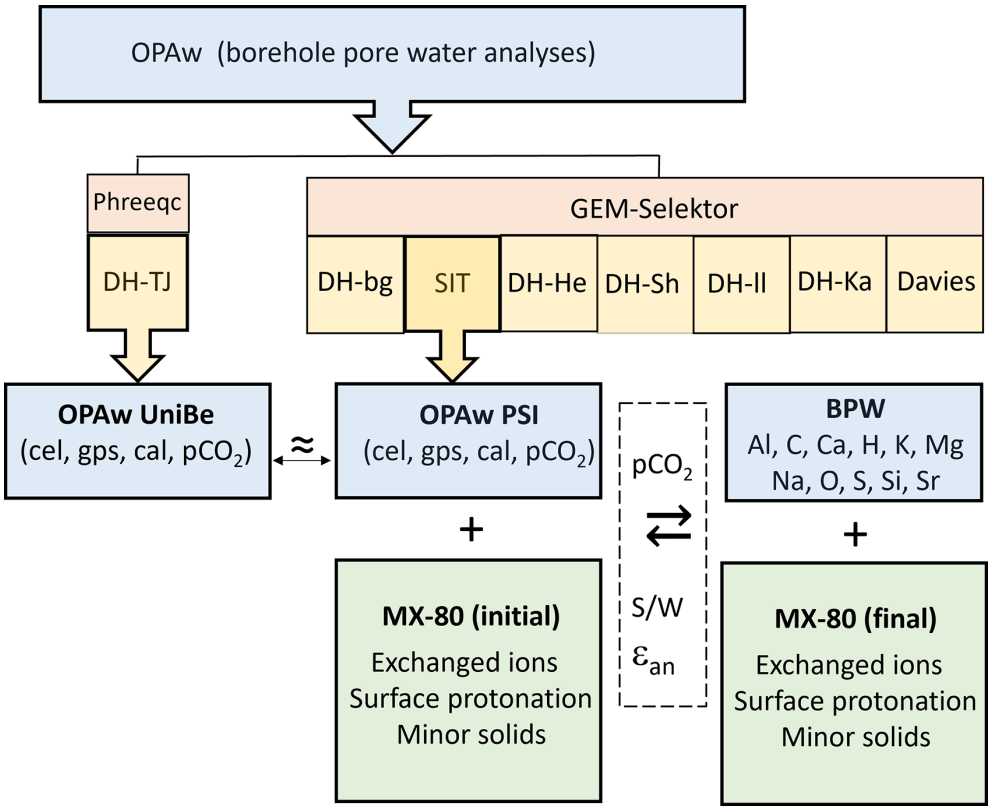

Fig. 7-2: Development and architecture of the SGT-E3 bentonite porewater model

7.3 Initial state of bentonite

The composition and characteristics of bentonite porewaters will depend on the initial state of the compacted bentonite (Bradbury & Baeyens 2002). The initial state of the compacted bentonite includes the initial exchanged cation populations and the protonation state of edge sites in montmorillonite at the time of emplacement, as well as the initial inventory and masses of reactive minerals in bentonite. Generic information on the chemical-physical properties and mineralogical variability of natural bentonite is given in Section 4.4. In compacted clays, aqueous composition, pH and ionic strength of the equilibrated porewater may be very sensitive to dissolution or precipitation of reactive solids due to the very high solid/water (S/W) ratio. Even trace solids may thus have a significant impact on the BPW composition.

To date, no final decision has been taken on which type of bentonite will be used as repository backfill. As in previous safety assessments, MX-80 Na-bentonite was selected here as a representtative material, using the properties determined in previous characterisation studies (Müller-Vonmoos & Kahr 1983, Bradbury & Baeyens 2002) and summarised in Tab. 7-1.

Further parameters defining the initial state in the BPW calculations are the S/W ratio and the fractions of the different types of water present in saturated compacted bentonite. This information is essential to define the volume of solution in which aqueous chemical reactions proceed to thermodynamic equilibrium, which in this BPW model is set equal to the anion-accessible porosity (AAP) (see Curti 2023 for details). As already mentioned in Section 7.2, the AAP corresponds to the uncharged fraction of interparticle water, i.e. the interparticle water volume minus the volume occupied by the diffuse double layer (DDL), where cations are in excess and anions are almost totally excluded.

Empirical equations to calculate AAPs as a function of dry bulk density and ionic strength are provided by van Loon et al. (2007). Their application for an ionic strength of 0.6 M (corresponding the highest expected salinity) leads to volumetric AAPs (Fig. 7-3) of 21.2%, 13.8% and 9% for dry bulk densities of 1,300, 1,450 and 1,600 kg m^{-3}, respectively (the same values are expressed as porosities, ε_{an}, in Tab. 7-2). The bulk density of 1,450 kg m^{-3} is the current reference value for the general licence application, while the other two values (already used in SGT-E2 BPW calculations) define boundaries for the sensitivity analysis. Fig. 7-3 shows the resulting volumetric distribution of solids ("mineral") and water types in compacted bentonite for the three aforementioned bulk dry densities. In the BPW calculations presented later in Section 7.4, slightly lower S/W ratios were assumed, corresponding to the limiting (maximum) values of AAPs at a given dry bulk density ($\varepsilon_{an,max}$ in Tab. 7-2). The rationale behind this choice can be found in Curti (2023).

Tab. 7-1: Initial state of MX-80 bentonite used as reactant material in the calculation of BPW compositions

GEMS name	Species/ mineral	mol/kg	Site fraction*	Mole fraction
Amphoteric edge sites				
=SsO-	$=S^{S}O^{-}$	8.5×10^{-4}	0.567	0.567
=SsOH@	$=S^{S}OH$	6.5×10^{-4}	0.433	0.433
=SsOH2+	$=S^{S}OH_2^{+}$	2.1×10^{-7}	1.4×10^{-4}	1.4×10^{-4}
Ess	$=S^{S}$(total)	1.5×10^{-3}	1	1
=SvO-	$=S^{W1}O^{-}$	1.7×10^{-2}	0.567	0.567
=SvOH@	$=S^{W1}OH$	1.3×10^{-2}	0.433	0.433
=SvOH2+	$=S^{W1}OH_2^{+}$	4.2×10^{-6}	1.4×10^{-4}	1.4×10^{-4}
Esv	$=S^{W1}$(total)	3.0×10^{-2}	1	1
=SwO-	$=S^{W2}O^{-}$	3.0×10^{-4}	0.010	0.010
=SwOH@	$=S^{W2}OH$	2.96×10^{-2}	0.987	0.987
=SwOH2+	$=S^{W2}OH_2^{+}$	9.4×10^{-5}	0.003	0.003
Esw	$=S^{W2}$(total)	3.0×10^{-2}	1	1
Exchanged ions[&]				
NaClay@	NaZ	0.668	0.843	0.907
KClay@	KZ	0.013	0.016	0.018
MgClay@	MgZ_2	0.020	0.051	0.027
CaClay@	CaZ_2	0.033	0.083	0.045
SrClay@	SrZ_2	0.002	0.005	0.003
BaClay@	BaZ_2	5×10^{-4}	0.001	0.001
Clay-	Z(total)	CEC = 0.792[&]	1	1
Reactive minor minerals[+]				
Gypsum		0.0235		
Quartz		1.66		
Kaolinite		0.039		
Calcite		0.3		
Siderite		0.086		
Magnetite		0.43		

[*] Synonym of "equivalent fraction"
[&] Data correspond to Tab. 4-5.
[+] Same inventories as assumed in SGT-E2 BPW, corresponding to the MX-80 mineralogy given in Tab. 4-3, with the addition of magnetite, representing canister corrosion products.

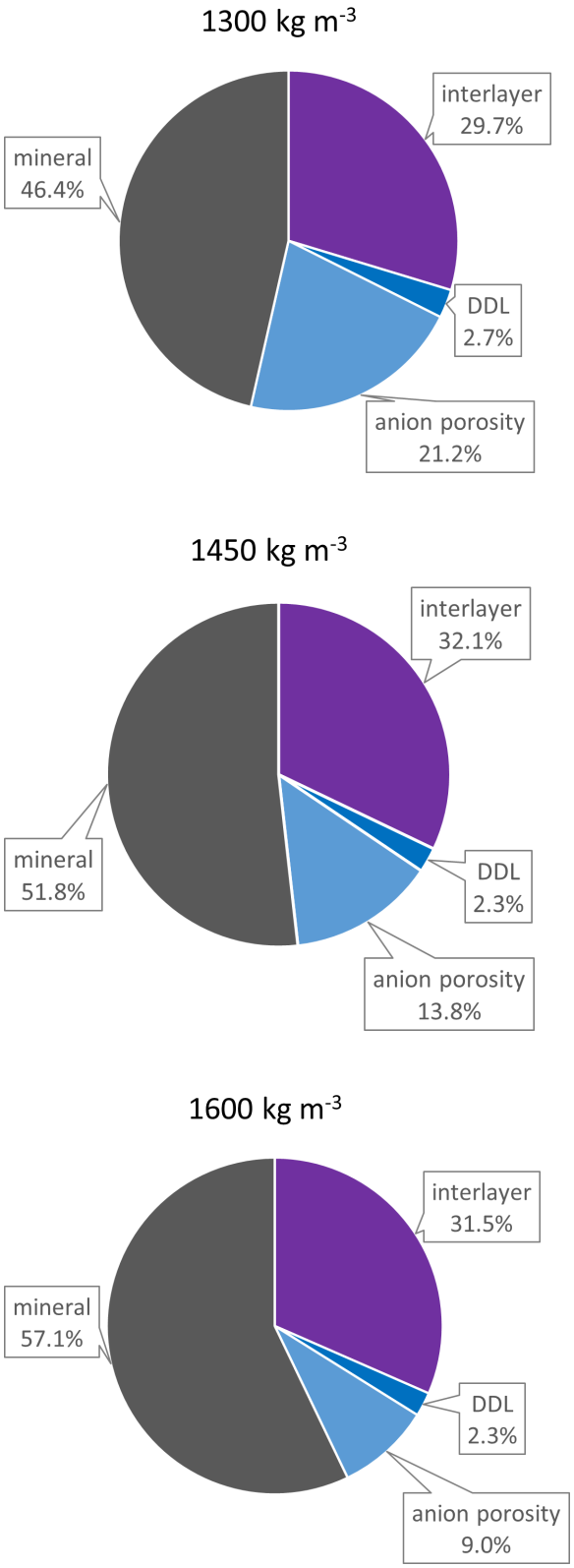

Fig. 7-3: Calculated volumetric distribution of water types and solids in compacted bentonite for three different dry bulk densities

Tab. 7-2: Total porosity, maximum anion-accessible porosity and anion-accessible porosity at I = 0.61 m for 3 different degrees of compaction of MX-80 bentonite

Based on van Loon et al. (2007)

ρ_b (kg m^{-3}) =>	1,300	1,450	1,600
ε_{tot}	0.536	0.482	0.429
$\varepsilon_{an,max}$	0.239	0.161	0.113
ε_{an}	0.212	0.138	0.090

7.4 Calculation and results of bentonite porewaters (BPW) for the documentation of the general licence application

7.4.1 Results of bentonite porewater (BPW) calculations

The BPW calculations were performed with the GEM-Selektor code (Kulik et al. 2013). In the reference case simulations, 114.1 g of OPAw are equilibrated with 1 kg of dry MX-80 bentonite, reflecting the maximum anion porosity at a dry bulk density of 1,450 kg m^{-3} (16.1% see Tab. 7-2). The bentonite equilibrates by dissolving/precipitating selected reactive minerals and by adjusting the cation exchange and surface protonation equilibria in montmorillonite. As in previous safety assessments, no dissolution or precipitation of montmorillonite, nor its transformation to other clay minerals such as illite, is allowed, i.e. the TOT structural units of montmorillonite are considered to remain intact and inert at the low temperatures considered. This approach is consistent with the conclusions reached in Section 5.2 regarding the potential extent of illitisation of montmorillonite.

The key results of the BPW calculations are shown in Tab. 7-3 and Tab. 7-4 together with the corresponding OPAw compositions (in grey). Tab. 7-3 shows the results for the NL-ZNO siting region obtained at the three selected fixed pCO_2. The water denoted E3-BPW-Ref (pCO_2 of $10^{-2.2}$ bar) is the reference BPW used for the calculation of solubility limits and sorption coefficients of the considered dose-relevant radionuclides. The other two compositions define a low-pH and a high-pH variant corresponding to the expected limiting values of pCO_2 in the Opalinus Clay formation ($10^{-1.8}$ and $10^{-2.8}$ bar, respectively, see Mäder & Wersin 2023). Tab. 7-4 lists the BPW results obtained by equilibrating MX-80 bentonite with a high-salinity OPAw variant, defined based on data obtained from the Bülach borehole in the NL region.

Compared to the reacting Opalinus Clay waters, the equilibrated BPWs are slightly more alkaline and more saline. In general, dissolved elemental concentrations change only to a minor extent, except for the considerable increase in sulphate and sodium concentrations and a significant decrease in calcium. The decrease in calcium is caused by uptake via cation exchange of Ca^{2+} in the interlayer of montmorillonite, which in turn triggers gypsum dissolution, thus explaining the increase in dissolved sulphate. On the other hand, the release of exchanged Ba^{2+} and Sr^{2+} from montmorillonite, and of Ca^{2+} through gypsum dissolution, lead to precipitation of baryte, celestine and calcite.

Another effect observed is the destabilisation of siderite. The dissolution of the initial siderite inventory in MX-80 bentonite releases aqueous Fe^{2+}, which reprecipitates as pyrite and magnetite. Combined with gypsum dissolution, this leads to the following Eh/pH/pCO_2-dependent net reaction, which always proceeds to the right in our model calculations:

$$\begin{aligned} & 22\ FeCO_3(s) + 2\ CaSO_4 \cdot H_2O(s) \\ & \quad (siderite) \qquad (gypsum) \\ \rightarrow\ & FeS_2(s) + 7\ Fe_3O_4(s) + 2\ CaCO_3(s) + 2\ H_2O + 20\ CO_2(g) \\ & \quad (pyrite) \quad (magnetite) \quad (calcite) \end{aligned} \tag{7-1}$$

Although no protons or hydroxyl ions appear explicitly, this reaction is pH-dependent since CO_2 degassing produces basicity, inducing as predicted a slight increase in pH (compared with the initial pH of the reacting OPAw). If the reaction were to proceed to the left, CO_2 would be taken up and the pH would decrease. At fixed pCO_2, and provided that all five solids are present at equilibrium, the above combined reaction would fix the pH to a unique (pCO_2-dependent) value. In all cases considered in this report, however, the small siderite inventory dissolves completely, leaving some degree of freedom to the pH. The above reaction also controls the Eh via stability of the iron phases (siderite, pyrite, magnetite), as discussed in Section 7.4.3.

Tab. 7-3: Upper section: pCO_2, pH, Eh, ionic strength and total element concentrations of bentonite porewaters computed for the NL-ZNO region compared to the reacting Opalinus Clay waters (in grey)

Lower section: initial and final amounts of exchanged cations and minor reactive solids in MX-80 bentonite.

All calculations were carried out at 25 °C, 1 bar.

Description	**Low pCO_2**		**Reference BPW**		**High pCO_2**	
GEMS ID => **Nagra ID =>**	OPAw_NL-ZNO-28 **E3-OPW_lowpCO2**	BPW_NL-ZNO-28 **E3-BPW_lowpCO2**	OPAw_NL-ZNO-22 **E3-OPW-Ref**	BPW_NL-ZNO-22 **E3-BPW-Ref**	OPAw_NL-ZNO-18 **E3-OPW_highpCO2**	BPW_NL-ZNO-18 **E3-BPW_highpCO2**
log $p(CO_2)$/bar	-2.79	-2.80	**-2.20**	**-2.20**	-1.80	-1.80
pH	7.40	7.51	**7.10**	**7.24**	6.90	7.05
Eh	-0.190	-0.194	**-0.167**	**-0.173**	-0.152	-0.159
IS /m	0.317	0.452	**0.319**	**0.452**	0.321	0.453
Aqueous concentrations *[mol/kgw]*						
Al	2.13×10^{-8}	2.45×10^{-8}	$\mathbf{2.09 \times 10^{-8}}$	$\mathbf{2.08 \times 10^{-8}}$	2.86×10^{-8}	2.39×10^{-8}
Ba	1.56×10^{-7}	7.84×10^{-8}	$\mathbf{1.57 \times 10^{-7}}$	$\mathbf{7.19 \times 10^{-8}}$	1.58×10^{-7}	6.85×10^{-8}
C(IV)	1.07×10^{-3}	1.37×10^{-3}	$\mathbf{2.21 \times 10^{-3}}$	$\mathbf{2.94 \times 10^{-3}}$	3.68×10^{-3}	4.99×10^{-3}
Ca	2.01×10^{-2}	1.92×10^{-2}	$\mathbf{2.03 \times 10^{-2}}$	$\mathbf{1.77 \times 10^{-2}}$	2.05×10^{-2}	1.69×10^{-2}
Cl	0.239	0.238	**0.240**	**0.239**	0.241	0.240
F	1.74×10^{-4}	1.74×10^{-4}	$\mathbf{1.74 \times 10^{-4}}$	$\mathbf{1.74 \times 10^{-4}}$	1.74×10^{-4}	1.74×10^{-4}
Fe	7.14×10^{-6}	6.42×10^{-6}	$\mathbf{2.56 \times 10^{-5}}$	$\mathbf{2.09 \times 10^{-5}}$	5.95×10^{-5}	4.65×10^{-5}
K	2.13×10^{-3}	1.92×10^{-3}	$\mathbf{2.13 \times 10^{-3}}$	$\mathbf{1.83 \times 10^{-3}}$	2.14×10^{-3}	1.79×10^{-3}
Mg	1.43×10^{-2}	1.12×10^{-2}	$\mathbf{1.45 \times 10^{-2}}$	$\mathbf{1.02 \times 10^{-2}}$	1.46×10^{-2}	9.77×10^{-3}
Mn	8.16×10^{-5}	1.82×10^{-5}	$\mathbf{8.24 \times 10^{-5}}$	$\mathbf{1.84 \times 10^{-5}}$	8.33×10^{-5}	1.86×10^{-5}
Na	0.215	0.391	**0.215**	**0.375**	0.216	0.366
S(VI)	2.29×10^{-2}	7.16×10^{-2}	$\mathbf{2.29 \times 10^{-2}}$	$\mathbf{7.86 \times 10^{-2}}$	2.29×10^{-2}	8.29×10^{-2}
Si	1.73×10^{-4}	1.70×10^{-4}	$\mathbf{1.72 \times 10^{-4}}$	$\mathbf{1.70 \times 10^{-4}}$	1.72×10^{-4}	1.70×10^{-4}
Sr	3.67×10^{-4}	1.87×10^{-4}	$\mathbf{3.70 \times 10^{-4}}$	$\mathbf{1.72 \times 10^{-4}}$	3.73×10^{-4}	1.64×10^{-4}
Exch. *[mol/kg clay]*	*Initial*	*Final*	***Initial***	***Final***	*Initial*	*Final*
BaZ_2	5.00×10^{-4}	1.56×10^{-7}	$\mathbf{5.00 \times 10^{-4}}$	$\mathbf{1.53 \times 10^{-7}}$	5.00×10^{-4}	1.52×10^{-7}
CaZ_2	3.30×10^{-2}	3.68×10^{-2}	$\mathbf{3.30 \times 10^{-2}}$	$\mathbf{3.62 \times 10^{-2}}$	3.30×10^{-2}	3.58×10^{-2}
KZ	1.30×10^{-2}	1.30×10^{-2}	$\mathbf{1.30 \times 10^{-2}}$	$\mathbf{1.30 \times 10^{-2}}$	1.30×10^{-2}	1.30×10^{-2}
MgZ_2	2.00×10^{-2}	1.95×10^{-2}	$\mathbf{2.00 \times 10^{-2}}$	$\mathbf{1.91 \times 10^{-2}}$	2.00×10^{-2}	1.89×10^{-2}
NaZ	6.68×10^{-1}	6.66×10^{-1}	$\mathbf{6.68 \times 10^{-1}}$	$\mathbf{6.68 \times 10^{-1}}$	6.68×10^{-1}	6.69×10^{-1}
SrZ_2	2.00×10^{-1}	3.74×10^{-4}	$\mathbf{2.00 \times 10^{-3}}$	$\mathbf{3.68 \times 10^{-4}}$	2.00×10^{-3}	3.64×10^{-4}
Solids *[mol/kg clay]*	*Initial*	*Final*	***Initial***	***Final***	*Initial*	*Final*
Barite	0	5.00×10^{-4}	**0**	$\mathbf{5.00 \times 10^{-4}}$	0	5.00×10^{-4}
Calcite	3.00×10^{-1}	3.11×10^{-1}	$\mathbf{3.00 \times 10^{-1}}$	$\mathbf{3.12 \times 10^{-1}}$	3.00×10^{-1}	3.13×10^{-1}
Dolomite	0	9.04×10^{-4}	**0**	$\mathbf{1.36 \times 10^{-3}}$	0	1.63×10^{-3}
Pyrite	5.00×10^{-1}	5.04×10^{-1}	$\mathbf{5.00 \times 10^{-1}}$	$\mathbf{5.04 \times 10^{-1}}$	5.00×10^{-1}	5.04×10^{-3}
Celestine	0	1.65×10^{-3}	$\mathbf{1.00 \times 10^{-12}}$	$\mathbf{1.66 \times 10^{-3}}$	0	1.66×10^{-3}
Kaolinite	3.90×10^{-2}	3.90×10^{-2}	$\mathbf{3.90 \times 10^{-2}}$	$\mathbf{3.90 \times 10^{-2}}$	3.90×10^{-2}	3.90×10^{-2}
Gypsum	2.35×10^{-2}	7.95×10^{-3}	$\mathbf{2.35 \times 10^{-2}}$	$\mathbf{7.14 \times 10^{-3}}$	2.35×10^{-2}	6.64×10^{-3}
Siderite	8.60×10^{-2}	0	$\mathbf{8.60 \times 10^{-2}}$	**0**	8.60×10^{-2}	0
Magnetite	4.30×10^{-1}	4.57×10^{-1}	$\mathbf{4.30 \times 10^{-1}}$	$\mathbf{4.57 \times 10^{-1}}$	4.30×10^{-1}	4.57×10^{-1}
Quartz	1.66	1.66	**1.66**	**1.66**	1.66	1.66
Rhodochrosite	0	7.23×10^{-6}	**0**	$\mathbf{7.30 \times 10^{-6}}$	0	7.37×10^{-6}
Fluorite	0	0	**0**	**0**	0	0

Tab. 7-4: Left section: pCO_2, pH, Eh, ionic strength and total element concentrations of bentonite porewaters computed for the NL region (Bülach) compared to the reacting Opalinus Clay water (in grey)

Right section: initial and final amounts of exchanged cations and minor reactive solids in MX-80 bentonite.

All calculations were carried out at 25 °C, 1 bar.

	Bülach water			**Bülach water**	
GEMS ID **Nagra ID**	OPAw_BUL -28 **E3-OPW_sal**	BPW_BUL-28 **E3-BPW_sal**	GEMS ID **Nagra ID**	OPAw_BUL -28 **E3-OPW_sal**	BPW_BUL-28 **E3-BPW_sal**
log $p(CO_2)$/bar	-2.81	-2.80	***Exch.*** *[mol/kg clay]*	*Initial*	*Final*
pH	7.37	7.42	BaZ_2	5.00×10^{-4}	1.47×10^{-7}
Eh	-0.187	-0.189	CaZ_2	3.30×10^{-2}	3.50×10^{-2}
IS /m	0.509	0.592	KZ	1.30×10^{-2}	1.30×10^{-2}
Aqueous concentrations *[mol/kgw]*			MgZ_2	2.00×10^{-2}	1.85×10^{-2}
Al	2.05×10^{-8}	2.21×10^{-8}	NaZ	6.68×10^{-1}	6.71×10^{-1}
Ba	1.81×10^{-7}	1.13×10^{-7}	SrZ_2	2.00×10^{-1}	3.52×10^{-4}
C(IV)	1.02×10^{-3}	1.19×10^{-3}	***Solids*** *[mol/kg]*	*Initial*	*Final*
Ca	2.90×10^{-2}	2.71×10^{-2}	Barite	0	5.00×10^{-4}
Cl	0.407	0.405	Calcite	3.00×10^{-1}	3.10×10^{-1}
F	1.71×10^{-4}	1.70×10^{-4}	Dolomite	0	1.87×10^{-3}
Fe	9.08×10^{-6}	8.49×10^{-6}	Pyrite	5.00×10^{-1}	5.04×10^{-1}
K	2.74×10^{-3}	2.41×10^{-3}	Celestine	0	1.67×10^{-3}
Mg	1.89×10^{-2}	1.56×10^{-2}	Kaolinite	3.90×10^{-2}	3.90×10^{-2}
Mn	1.07×10^{-4}	1.83×10^{-5}	Gypsum	2.35×10^{-2}	1.02×10^{-2}
Na	0.368	0.496	Siderite	8.60×10^{-2}	0
S(VI)	2.98×10^{-2}	5.91×10^{-2}	Magnetite	4.30×10^{-1}	4.57×10^{-1}
Si	1.68×10^{-4}	1.66×10^{-4}	Quartz	1.66	1.66
Sr	4.19×10^{-4}	1.87×10^{-4}	Rhodochrosite	0	1.01×10^{-5}
			Fluorite	0	0

7.4.2 Sensitivity analysis

A sensitivity analysis was carried out to investigate how the results of the BPW model depend on uncertainties of key parameters. It consisted of running the (provisional)[24] reference case calculation, however with a single critical parameter modified across an expected/defined range. In addition to the effect of fixed pCO_2, the effects of the initial protonation state of surface functional groups in montmorillonite and of the dry density of bentonite were investigated. The results of the sensitivity analysis are only summarised here, as they are discussed in detail in Section 3.2 of Curti (2023).

In all BPW calculations mentioned so far, the initial distribution of surface hydroxyl groups (=SOH) reported in Tab. 7-1 was specified in the input. This corresponds to the surface speciation determined by Bradbury & Baeyens (2002) based on the characterisation of a few MX-80 samples. The initial surface protonation state may however vary as a function of history and treatment of the bentonite; therefore the effect of variations in the initial occupancies of the amphoteric surface sites, considering their potential impact on pH, are explored. It turns out that systematically changing the initial protonation state has no or only an insignificant impact on final pH, ionic strength and solution composition of the equilibrated BPW, in spite of the strong predicted release (or uptake) of protons from the amphoteric sites upon equilibration. The latter result is a further indication that the multiphase reaction involving minor reactive minerals discussed in the preceding section plays a major role in buffering the pH.

The influence of different degrees of bentonite precompaction was examined by carrying out two alternative calculations, in which the dry density was set to limiting values (ρ_b = 1,300 kg m^{-3} and ρ_b = 1,600 kg m^{-3}, corresponding to $\varepsilon_{an,max}$ = 0.239 and 0.113, respectively), with all other parameters equal to the reference case. Also in this case, composition, pH and other characteristics of the BPW remained remarkably stable. The main noticeable effect predicted across the dry density range 1,300 – 1,600 kg m^{-3} is a slight increase in ionic strength (from 0.57 – 0.60 m) with increasing compaction. This effect is ascribed to the decrease in anion-accessible porosity as the degree of compaction increases, the Na^+ excess counteracting the negative charge on the clay is distributed over a smaller total volume of external water, so that Na-concentration and thus ionic strength increase.

An additional variation within the framework of the sensitivity analysis was to assess the effect of relaxing the constraint of an externally controlled pCO_2. Technically, this was simply achieved by letting the carbonate-CO_2 system equilibrate internally in the bentonite-porewater system in the GEM-Selektor calculation, i.e. excluding any exchange with external CO_2 gas reservoirs. This procedure is equivalent to treating the saturated bentonite as a locally closed system, an approach that must be used in reactive transport calculations (see Chapter 6 and Berner et al. 2013). It can be anticipated that a lower pH and a higher equilibrium pCO_2 should result in this case, because no CO_2 (i.e. no acidity) is allowed to escape from the aqueous solution. Indeed, after relaxing the fixed pCO_2 constraint, a lower pH (6.9 instead of 7.2) and a higher (unconstrained) equilibrium pCO_2 ($10^{-1.77}$ bar instead of $10^{-2.2}$) are obtained compared to the reference case BPW calculations. The predicted dissolution/precipitation reactions are the same as in the open system, but mass transfer quantities are generally different. Notably, siderite is dissolved only partially, i.e. it remains a stable phase. The aqueous composition did not change much, except for a slight increase in carbonate and sulphate and slight decrease in Ca. Due to the lower pH, the speciation of =SOH sites shifted towards enrichment of protonated species, so that a slightly positive surface charge results, implying that a corresponding enrichment of Cl^- (instead of Na^+) must be assumed to preserve overall charge balance of the bentonite-porewater system. In the context of the sensitivity

[24] To distinguish it from the final reference case calculation, the provisional reference case is denoted "source case" in Curti (2023).

analysis, this represents a singular case of positively charged clay with anion-dominated DDL (i.e. cation exclusion in the DDL instead of anion exclusion). This result shows that the impact of the boundary conditions chosen for CO_2 equilibrium in determining pH and composition of the BPW is much larger than the effect of compaction and initial distribution of protonated surface species. Note that the unconstrained pCO_2 of $10^{-1.77}$ bar obtained with internal equilibration is nearly identical to the highest limit of $10^{-1.8}$ bar pCO_2 imposed in the "open system" calculations. Therefore, in practical terms, the selected variation of imposed pCO_2 values also covers the "closed system" case calculation.

7.4.3 Control of oxidation potential (Eh)

As in previous models (Bradbury et al. 2014, Curti & Wersin 2002, Curti 1993), it is assumed that Fe(II)-Fe(III) and sulphate-sulphide equilibria control the Eh of the BPW. In MX-80 bentonite, an initial assemblage of minor Fe minerals has been determined through characterisation studies, including siderite, pyrite and Fe oxy-hydroxide phases (Bradbury & Baeyens 2002). Gypsum, pyrite, siderite and other Fe minerals are ubiquitous minor constituents of natural bentonites (see Section 4.4). Moreover, the pore solution is considered to always be in equilibrium with magnetite (Fe_3O_4), as this phase is expected to be present in excess due to the occurrence of large amounts of anaerobically corroded steel (canister, drift support).

Recent analyses on samples from the FEBEX and ABM2 field experiments have revealed the presence of both primary and secondary Fe(II) and Fe(III) minerals in MX-80 bentonite after prolonged interaction with steel, confirming the high reactivity of the iron redox system, at least during the elevated temperature period (Hadi et al. 2017, Hadi et al. 2019, Jenni et al. 2019). In the ABM2 experiments, steel in contact with bentonite was corroded during five years with synthetic granitic water at 130 °C. In the FEBEX experiment, the interaction proceeded for 18 years in a humid environment at 100 °C under non-saturated conditions. In both studies, goethite formed in a thin oxidised region associated with transient aerobic corrosion, while Fe(II) enrichments arising from later anaerobic corrosion were observed elsewhere across the steel/ bentonite interface, producing siderite and magnetite in the ABM2 samples.

In agreement with the above evidence, in the present BPW calculations the oxidation potential is assumed to be controlled by simple, stoichiometric Fe-bearing phases using the thermodynamic data selected in the TDB2020 database (Hummel & Thoenen 2023). Accordingly, the Fe-phases potentially at equilibrium in the system of interest are siderite ($FeCO_3$), pyrite (FeS_2), melanterite ($FeSO_4 \cdot 7H_2O$), haematite (Fe_2O_3), magnetite (Fe_3O_4), ferrihydrite, $Fe(OH)_3 \cdot nH_2O$ and goethite (FeOOH).

In order to illustrate graphically the expected phase stability fields for the equilibrated BPW and to test the consistency with GEM-Selektor calculations, Eh-pH diagrams in the Fe-O-H-S-C system were constructed using the Phreeplot code (Kinniburgh & Cooper 2004) and the PSI-Nagra database (Fig. 7-4). Fig. 7-4(a) shows the Eh-pH diagram for a composition approximately corresponding to the Bülach-type saline water E3-BPW_sal (Tab. 7-4). At pH 7.4, Phreeplot predicts a reducing Eh of -190 mV at equilibrium with pyrite and magnetite (red broken lines). Siderite does not appear because it is calculated by Phreeplot to be unstable under these conditions. These results fully agree with the corresponding GEM-Selektor calculation (Tab. 7-4), which predicts almost identical pH (7.42) and Eh (-189 mV), as well as complete dissolution of the initial siderite inventory.

Fig. 7-4(b) shows an Eh-pH diagram calculated for the same system, however with a five times higher carbonate concentration. The increased carbonate concentration enforces stability of siderite, as manifested in the appearance of a small siderite region between the magnetite and pyrite stability areas. In this case, Phreeplot predicts a higher pH (8.2) and a lower Eh (-220 mV) at the triple point defining coexistence of siderite, pyrite and magnetite. This means that, if

sufficiently large inventories of the three minerals were present in bentonite, at such high carbonate concentration there would be no degree of freedom, as predicted by reaction (7-1): both pH and Eh would be fixed at the aforementioned values (each perturbation of the system would be compensated by dissolution or precipitation of one or more of the three minerals, but pH and Eh would not vary). Such a triple point situation is, however, unlikely in the HLW near-field due to the limited inventories of siderite and pyrite in bentonite and the smaller carbonate concentrations measured so far in OPAw.

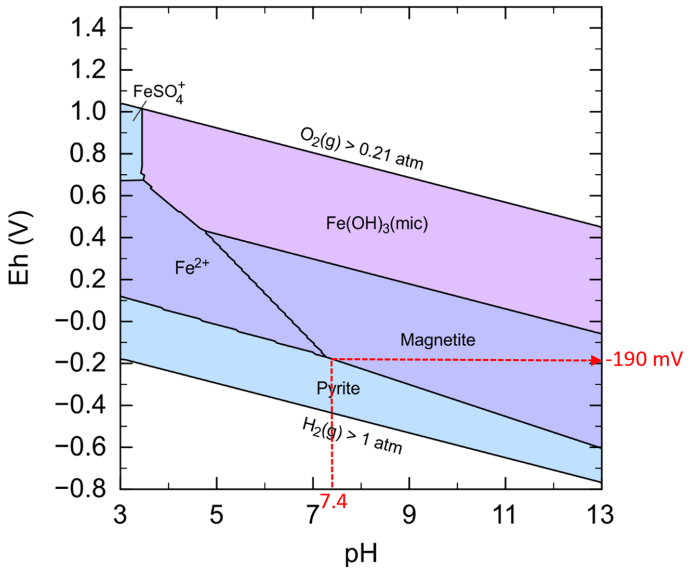

(a)

[Fe] = 2.0×10^{-5} m
[S] = 5.8×10^{-2} m
[C] = 1.1×10^{-3} m
[NaCl] = 0.4 m

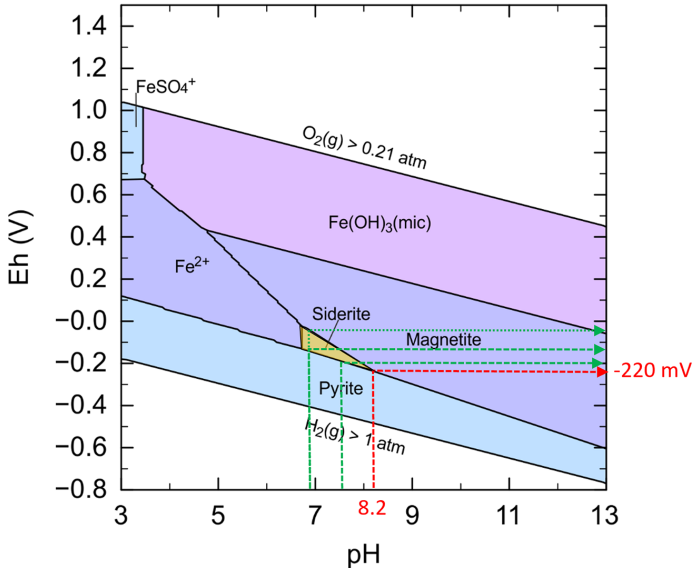

(b)

[Fe] = 2.0×10^{-5} m
[S] = 5.8×10^{-2} m
[C] = 5.0×10^{-3} m
[NaCl] = 0.4 m

Fig. 7-4: Eh-pH diagrams for BPW conditions at 25 °C and 1 bar. See text for explanations

In conclusion, the BPW calculations indicate that the pH will be mainly constrained within a restricted range (pH 6.9 – 7.5) determined to a large extent by the externally controlled pCO_2 values specified for the Opalinus Clay porewaters (see Section 4.5 in Mäder & Wersin 2023) in conjunction with saturation equilibria determining the Ca^{2+} activity (calcite, gypsum and cation exchange). Within this pH window, possible Eh values at equilibrium with pyrite-magnetite-(siderite) will be constrained in the range from about -220 mV up to -50 mV, see red and green broken lines in Fig. 7-4.

7.4.4 Evolution of bentonite porewater

The calculated BPW compositions (Tab. 7-3 and Tab. 7-4) reflect an initial stage in the evolution of bentonite porewater, since they were calculated through a "single pass" reaction by which the first batch of Opalinus Clay porewater filling the anion-accessible porosity reacts with intact bentonite. To simulate the evolution of BPW compositions upon reaction with an increasingly larger volume of Opalinus Clay porewater, calculations were carried out using the GEM2MT module of GEM-Selektor. In such calculations, a 1D column of MX-80 bentonite is flushed with an increasing amount of fresh OPAw (Fig. 7-5). The bentonite is discretised into a number of equivalent boxes ("nodes") in which a given amount of fluid entering on the left side reacts with a batch of solid. Time cannot be calculated explicitly and is replaced by the number of "water exchange cycles" to express reaction progress. At the start of each new cycle, the reacted water volume in each box is transferred to the next node on the right, while the anion porosity of the first box directly in contact with the bentonite is simultaneously filled with an equivalent volume of fresh OPAw and that in the farthest box is flushed away. After this transport step, the ClaySor BPW reaction model is run in all boxes, taking into account the previously recorded changes in bentonite composition (i.e. exchanged ion populations and solid inventories) and then a new cycle starts.

Although this sequential reactor model does not faithfully represent the diffusive regime established in the repository near-field but rather pure advection, it provides a simple method for evaluating the expected mineralogical and chemical evolution of the bentonite-porewater system in the HLW repository. Another limitation of this model is that perturbations due to interactions with the concrete liner are not included. These are considered in a separate reactive transport model (Section 6.7).

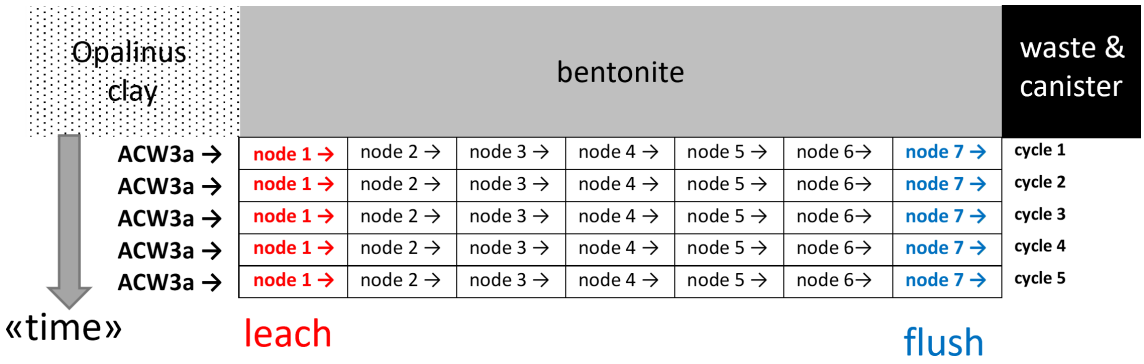

Fig. 7-5: Principle of the sequential reactor model applied to simulate the evolution of the MX-80 bentonite/BPW system

The discretisation of the applied model included 20 nodes.

Calculations were performed with Bülach-type OPAw (the most saline water extracted in the NL region despite the borehole not being located within the repository perimeter, denoted ACW3a in Fig. 7-5) assuming internal CO_2 equilibration in order to avoid complications related to constrained pCO_2 conditions. The bentonite column was discretised into 20 nodes, each containing 1 kg of dry MX-80 bentonite and filled with 0.1411 kg of pristine OPAw, consistent with a bentonite dry density of 1,450 kg m^{-3}.

Fig. 7-6 shows selected results for node 1, i.e. at the external bentonite boundary. In addition to Eh and pH, the evolution of Na and Ca in porewater, of exchanged cations and the mole amounts of minor reactive minerals (calcite, celestine, gypsum pyrite, magnetite and siderite) are plotted as a function of the number of water exchange cycles. The ionic strength is not shown as it remains remarkably constant (0.502 – 0.543 m). The model predicts complete dissolution of the initial inventories of gypsum, celestine and siderite after 2, 95 and 297 water exchange cycles, respectively.

The release of carbonate from the dissolving siderite does not lead to precipitation of calcite. On the contrary, slight dissolution of calcite is predicted due to the uptake of Ca for Na via cation exchange during the first 100 cycles. After about 100 exchange cycles, the Na and Ca molalities in the BPW become equal to the respective concentrations in ACW3a and do not evolve further, indicating that the exchanged cation populations in the bentonite have evolved to reach equilibrium with the incoming OPAw. Eventually, as expected, a final BPW with composition, pH and ionic strength almost identical to the reacting OPAw is obtained (see Tab. 7-5).

Note that after complete dissolution of siderite, the Eh decreases abruptly from -136 mV to -177 mV, while the pH rises sharply from 6.8 to 7.3. Qualitatively, these changes can be understood with the help of the Eh-pH diagrams in Fig. 7-4. As long as siderite coexists with magnetite and pyrite, both pH and Eh are fixed at the triple point siderite-magnetite-pyrite. Once siderite disappears, pH and Eh are free to "move" along the univariant magnetite-pyrite equilibrium line. Any Eh decrease must then induce an increase in pH, and vice versa. Note, however, that the triple point of the calculation corresponding to the Eh/pH discontinuity in Fig. 7-6 lies at different (pH, Eh) coordinates than the triple point shown in Fig. 7-4b, because of different (and variable) pCO_2 and Fe, S, C concentrations during the exchange cycle calculations[25].

The results of the same GEM2MT calculations for nodes 10 and 20 (not shown), which represent the BPW compositions and mineral contents in the middle and downstream boundary of the modelled bentonite column, indicate a similar evolution as for the upstream bentonite boundary (node 1), but the processes are delayed (onset occurs at a higher exchange cycle number).

[25] The Eh-pH diagrams refer to selected *fixed* aqueous concentrations of C, S, Fe and to a *fixed* pCO_2. In the GEM2MT calculations there is no such restriction, so that the triple point "moves" at each subsequent iteration.

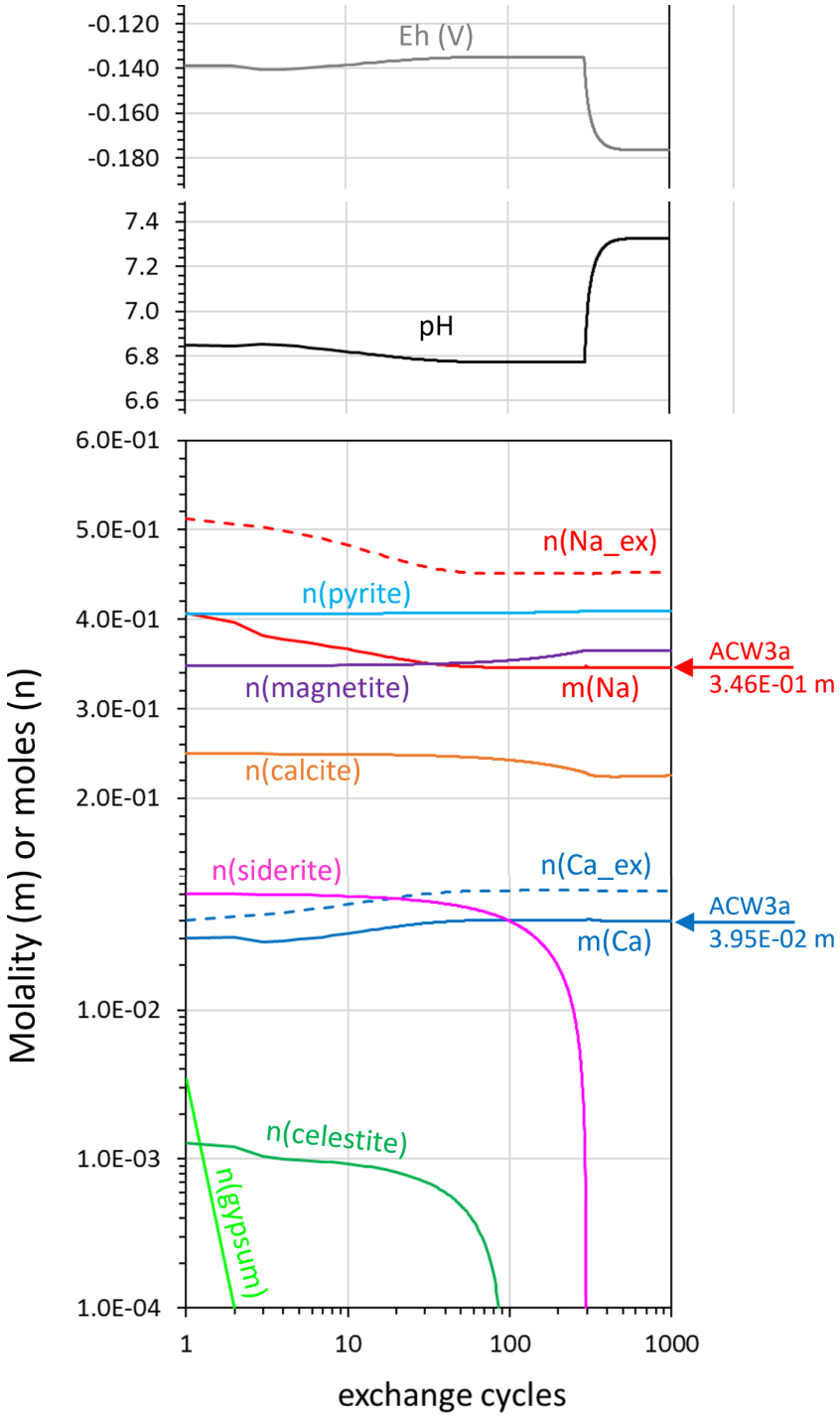

Fig. 7-6: Calculated evolution of bentonite porewater, exchanged cations (denoted as "_ex") and mineral inventories as a function of water exchange cycles at the external boundary of MX-80 bentonite

The arrows indicate the initial molalities of Ca and Na in ACW3a water (Bülach-type OPAw).

Tab. 7-5: Results of BPW sequential reactor calculations for MX-80 bentonite (ρ_{dry} = 1,450 kg m^{-3}) interacting with Bülach-type OPAw "ACW3a" for Node 1 (external bentonite boundary) after 1 and 1,000 water exchange cycles

A system closed to CO_2 exchange was assumed. The composition of the reacting ACW3a is also given for comparison.

	OPAw (ACW3a)	**Cycle 1 Node 1**	**Cycle 1000 Node 1**
T [°C]	25	25	25
p(tot) [bar]	1	1	1
log (pCO_2 [bar])	*-2.83*	-	-
pH	7.28	6.86	7.33
Eh [V]	-0.204	-0.140	-0.177
IS [m]	0.510	0.543	0.510
Aqueous solution	(molality)	(molality)	(molality)
Al	-	5.64×10^{-9}	1.38×10^{-8}
Ba	-	1.52×10^{-7}	2.26×10^{-7}
C (inorganic)	8.42×10^{-4}	3.92×10^{-3}	8.20×10^{-4}
Ca	3.95×10^{-2}	2.89×10^{-2}	3.95×10^{-2}
Cl	4.06×10^{-1}	4.05×10^{-1}	4.06×10^{-1}
Fe	-	1.23×10^{-4}	1.65×10^{-5}
K	1.93×10^{-3}	2.20×10^{-3}	1.93×10^{-3}
Mg	1.78×10^{-2}	1.51×10^{-2}	1.78×10^{-2}
Na	3.46×10^{-1}	4.16×10^{-1}	3.46×10^{-1}
S	2.84×10^{-2}	5.00×10^{-2}	2.84×10^{-2}
Si	-	1.77×10^{-4}	1.78×10^{-4}
Sr	3.13×10^{-4}	2.52×10^{-4}	3.13×10^{-4}

7.4.5 Kinetic inhibition of multielectron redox reactions

The customary procedure in simulating porewater compositions in the host rock and near-field of planned radioactive waste repositories is to assume overall thermodynamic equilibrium, including all redox reactions. This principle is followed in the present BPW derivation, consistently with the modelling procedures adopted for OPAw calculations (Mäder & Wersin 2023). Unlike mono-electronic transitions such as Fe(II)-Fe(III) equilibria, multielectron transitions are frequently sluggish at low temperatures and may be kinetically inhibited in the absence of appropriate microbial mediation. For instance, there is experimental evidence that the abiotic reduction of sulphate and methanogenesis does not proceed at measurable rates at temperatures below 100 °C (Karri et al. 2005, Truche et al. 2009, Miao et al. 2012), contrary to sulphide to sulphate oxidation, which can proceed as a pure inorganic process even at ambient temperatures (e.g. in acid mine tailings, where pyrite is oxidised upon release of sulphuric acid). Considering that microbial activity is suppressed or at least strongly limited in the highly confined environment of compacted bentonite (Stroes-Gascoyne 2011), the adopted principle of overall thermodynamic equilibrium may be questioned. It is therefore imperative to understand the consequence of this choice.

The previously discussed BPW simulations predict that only a tiny fraction of the aqueous sulphate (either inherited from the OPAw or derived from the dissolution of gypsum in bentonite) is reduced to sulphide, producing minor amounts of newly formed pyrite. It can thus be anticipated that the outcome of our BPW calculations should not differ significantly if sulphate reduction is suppressed in the calculations, except for the (redox-sensitive) Fe concentrations. This anticipation was tested by repeating the reference calculation E3-BPW-Ref after "switching off" all reduced C and S species in GEM-Selektor. This procedure allows calculation of a partial equilibrium system, in which sulphate and carbonate species are conserved but formation of any reduced species of sulphur and carbon (e.g. methane, sulphuric acid, graphite, elemental sulphur) is prevented. The comparison of the full and partial equilibrium calculations (Tab. 7-6, column a vs. column b) shows only minimal differences between the two calculations. As expected, significant differences are predicted only for the final Fe concentrations, which increase from 21 to 74 micromolal in the partial equilibrium calculation, due to the prevented formation of secondary pyrite. The calculated Eh changes for the same reason (no buffering along the pyrite-magnetite pH-Eh equilibrium line possible) and is even lower.

Tab. 7-6: BPW variants computed for the NL-ZNO region

(a) Full thermodynamic equilibrium obtained with the ClaySor model (identical to E3-BPW-Ref in Tab. 7-3). (b) Equivalent partial equilibrium calculation with sulphate and carbonate species reduction suppressed. (c) Full equilibrium variant obtained after removing the net positive charge predicted in E3-BPW-Ref. Results showing significant differences from E3-BPW-Ref are highlighted in bold. All calculations were carried out at 25 °C, 1 bar.

GEMS ID => Nagra ID =>	**BPW_NL-ZNO-22 E3-BPW-Ref (a)**	**BPW_NL-ZNO-22x E3-BPW-Ref-nored (b)**	**BPW_NL-ZNO-22un E3-BPW-Ref-uncharged (c)**
log $p(CO_2)$/bar	-2.20	-2.21	-2.22
pH	7.24	7.24	7.25
Eh	-0.173	**-0.223**	-0.175
IS /m	0.452	0.452	**0.434**
Al	2.08×10^{-8}	2.08×10^{-8}	2.08×10^{-8}
Ba	7.19×10^{-8}	7.20×10^{-8}	6.94×10^{-8}
C(in)	2.94×10^{-3}	2.92×10^{-3}	2.94×10^{-3}
Ca	1.77×10^{-2}	1.77×10^{-2}	1.71×10^{-2}
Cl	0.239	0.240	0.239
F	1.74×10^{-4}	1.74×10^{-84}	1.74×10^{-4}
Fe	2.09×10^{-5}	$\mathbf{7.40 \times 10^{-5}}$	2.05×10^{-5}
K	1.83×10^{-3}	1.84×10^{-3}	1.83×10^{-3}
Mg	1.02×10^{-2}	1.03×10^{-2}	1.02×10^{-2}
Mn	1.84×10^{-5}	1.84×10^{-5}	1.84×10^{-5}
Na	0.375	0.376	**0.341**
S	7.86×10^{-2}	7.85×10^{-2}	7.80×10^{-2}
Si	1.70×10^{-4}	1.70×10^{-4}	1.70×10^{-4}
Sr	1.72×10^{-4}	1.72×10^{-4}	1.66×10^{-4}

7.4.6 Charge-balanced BPW variant

As previously discussed, application of the ClaySor model produces water compositions with a net positive (or negative) charge representing cation (or anion) enrichment in the diffuse double layer of montmorillonite. This charge in the aqueous phase balances the non-permanent surface charge generated by amphoteric species sorbing on frayed edges of the clay. Because of the net charge, this water cannot be extracted and used "in isolation" for other purposes (i.e. without the associated charged clay. This issue arises, e.g., if one attempts to calculate the chemical speciation inside a breached canister following intrusion of the BPW (Chapter 9).

For such geochemical simulations, a charged-balanced variant of the reference BPW was defined by eliminating the excess positive charge from the chemical vector of the system (subtraction of Na^+ from the bulk composition), then re-adjusting the water to required saturation equilibria. The result of this calculation (column 'c' Tab. 7-6) yields, as expected, a small decrease in ionic strength (from 452 m to 434 m) as the only major effect. All other element concentrations, as well as pH and Eh, remain almost unchanged with respect to the original calculation.

7.4.7 Role of reactive minor minerals

The results of the BPW calculations show that minor reactive minerals such as gypsum, calcite, siderite, Fe-oxides and sulphides play a relevant role in determining equilibrium composition, pH and Eh of the porewater in compacted bentonite. However, natural bentonites present variable assemblages of such impurities, even within the same formation. The question therefore arises how such variations in mineralogy could affect the composition and properties of bentonite porewaters.

The review of the mineralogy of natural bentonites presented in Section 4.4 showed that MX-80 as described by Bradbury & Baeyens (2002) has a typical minor mineral inventory, similar to that determined in other bentonites. The data in Tab. 4-4 and Fig. 4-3 indicate that some of the impurities (e.g. anatase, feldspars, illite, muscovite) will either be unstable at the expected repository temperatures, or their reactivity kinetically hindered. Such phases were therefore considered to be inert and thus excluded in the BPW calculations, whereas phases known to be reactive under repository conditions, such as gypsum, carbonates (calcite, siderite, dolomite), pyrite or similar Fe-sulphides, Fe(III) oxy-hydroxides and soluble salts (NaCl), were included as potential equilibrium phases.

Most of the cited minerals were detected in MX-80 and their initial inventories considered in the BPW calculations. It is therefore of interest to explore how the *lack* of a given reactive mineral would affect the results of BPW calculations. To this end, several variants of the reference porewater system E3-BPW-Ref were recalculated while setting the inventories of a single or several minor minerals to zero. The results of such calculations revealed that the outcome for the equilibrated solution is significantly different from that obtained in the reference calculation only in the case of gypsum exclusion. The comparison of E3-BPW-Ref with the equivalent calculation without gypsum (column a vs. column b in Tab. 7-7) indicates a slightly higher pH, as well as lower Eh and ionic strength for the case without gypsum present. Moreover, lower Na, Mg, Mn and S concentrations result, while Ba is higher. The decrease in S concentration to trace levels compared to the reference BPW is simply a consequence of the missing contribution of gypsum dissolution. The sulphate "inherited" from the OPAw is almost completely converted to sulphide, which precipitates as pyrite. The absence of gypsum dissolution also leads to lower Ca concentrations, both in solution and as exchanged cation in the interlayer of montmorillonite. This in turn reduces the displacement of exchanged Mg and Na towards the solution, explaining the lower concentrations of these elements compared to the BPW reference case. The increased final Ba concentration results from the fact that no baryte can precipitate due to the absence of sufficient sulphate at equilibrium.

As discussed in Section 7.4.5, reduction of sulphate to sulphide, which is allowed in the BPW calculations to comply with the principle of overall thermodynamic equilibrium, is possibly inhibited in compacted bentonite due to the limitation of microbial activity in such a confined environment. Therefore, the impact of redox inhibition also for the case without initial gypsum has to be explored. To this end, a test calculation was carried out (column c of Tab. 7-7) in which the full equilibrium calculation without gypsum inventory (E3-BPW-Ref-nogps) was repeated with the additional constraint that reduction of sulphate is kinetically inhibited (E3-BPW-Ref-nored-nogps). The results show that this additional constraint mitigates the drastic decrease in aqueous sulphur concentration predicted by the full equilibrium model in the absence of gypsum, leaving 17.6 mmol/kgw sulphate in the final solution (instead of 0.105 μmol/kg). This concentration is nevertheless still four times lower than in the reference calculation, due to the missing contribution of sulphate from gypsum dissolution. Similar effects as previously described apply (reduction of Na, Mg, Mn concentrations and increase in Ba), although to a lesser extent.

Tab. 7-7: pCO_2, pH, Eh, ionic strength and total element concentrations of reference BPW: three variants with different assumptions concerning redox equilibria and initial mineral inventories

Column (a): with gypsum and assuming full thermodynamic equilibrium (identical to E3-BPW-Ref, Tab. 7-3). Column (b): without inclusion of a gypsum inventory and assuming full thermodynamic equilibrium. Column (c): without inclusion of a gypsum inventory and partial equilibrium (sulphate reduction suppressed). Results showing significant differences from column (a) are highlighted in bold. All calculations were carried out at 25 °C, 1 bar.

GEMS ID => Nagra ID =>	**BPW_NL-ZNO-22** E3-BPW-Ref with gypsum (full eq.) **(a)**	**BPW_NL-ZNO-22a** E3-BPW-Ref-nogps no gypsum (full eq.) **(b)**	**BPW_NL-ZNO-22e** **E3-BPW-Ref-nored-nogps** **no gypsum** **(partial eq.)** **(c)**
log $p(CO_2)$/bar	-2.20	-2.20	-2.20
pH	7.24	**7.36**	**7.33**
Eh	-0.173	**-0.223**	**-0.227**
Ionic strength /m	0.452	**0.278**	**0.318**
Al	2.08×10^{-8}	2.18×10^{-8}	2.15×10^{-8}
Ba	7.19×10^{-8}	$\mathbf{8.93 \times 10^{-5}}$	1.88×10^{-7}
C(in)	2.94×10^{-3}	3.62×10^{-3}	3.44×10^{-3}
Ca	$1.77E \times 10^{-2}$	5.67×10^{-3}	7.89×10^{-3}
Cl	0.239	0.240	0.240
F	1.74×10^{-4}	1.74×10^{-4}	1.74×10^{-4}
Fe	2.09×10^{-5}	2.43×10^{-5}	3.33×10^{-5}
K	1.83×10^{-3}	1.32×10^{-3}	1.44×10^{-3}
Mg	1.02×10^{-3}	$\mathbf{3.40 \times 10^{-3}}$	$\mathbf{4.66 \times 10^{-3}}$
Mn	1.84×10^{-5}	$\mathbf{3.09 \times 10^{-7}}$	$\mathbf{3.47 \times 10^{-6}}$
Na	0.375	**0.274**	**0.298**

Tab. 7-7: Cont.

GEMS ID => Nagra ID =>	**BPW_NL-ZNO-22** E3-BPW-Ref with gypsum (full eq.) **(a)**	**BPW_NL-ZNO-22a** E3-BPW-Ref-nogps no gypsum (full eq.) **(b)**	**BPW_NL-ZNO-22e** **E3-BPW-Ref-nored-nogps** **no gypsum** **(partial eq.)** **(c)**
S	7.86×10^{-2}	1.05×10^{-7}	1.76×10^{-2}
Si	1.70×10^{-4}	1.72×10^{-4}	1.71×10^{-4}
Sr	1.72×10^{-4}	3.57×10^{-4}	4.44×10^{-4}

7.4.8 Effect of initial exchanged ion population

Differences in the initial exchanged cation population of montmorillonite in a particular bentonite may have a potentially large impact on the chemistry of the equilibrated BPW. Effects would be of relevance if the main exchanged cation is replaced. For instance, it can be anticipated that the reaction of the (NaCl-rich) OPAw with a Ca-bentonite would proceed in a different way compared to the Na-dominated MX-80 bentonite, e.g. by affecting the gypsum and calcite equilibria and producing a $CaCl_2$-dominated porewater.

Tab. 7-8 shows the results of a test calculation carried out to verify the former expectation, in which the input of the reference BPW (E3-BPW-Ref) was modified by replacing most of the exchanged Na with Ca, with all other input data remaining unchanged. As expected, the results show that replacing Na with Ca in the exchanger causes calcite precipitation in larger amounts, while gypsum dissolves in smaller amounts, compared with the reference calculation. In the aqueous solution, the dominant cation is now Ca (increase from 17.7 to 92.3 mmol/kgw) at the expenses of Na (decrease from 375 to 44.1 mmol/kgw). Dissolved sulphate also decreases considerably (from 78.6 to 11.4 mmol/kgw) due to equilibrium with gypsum at a higher Ca concentration. Sulphate depletion is the main reason for the lower ionic strength calculated with the Ca-dominated bentonite.

The pH decrease by 0.5 units (from 7.24 to 6.78) cannot be understood intuitively, considering that the same carbon dioxide partial pressure was imposed in both calculations. However, it can be demonstrated that, in a system at equilibrium with both calcite and gypsum at a fixed pCO_2 and at constant pressure and temperature, the pH is only a function of the sulphate ion activity. The following simple relationship can be derived from the combination of the following equilibria involving gypsum, calcite and carbon dioxide:

$$CaCO_3(s) \quad <=> \quad Ca^{2+} + CO_3^{2-} \qquad \log K^0_{cal} = -8.47 \qquad (7\text{-}2a)$$

$$CO_3^{2-} + 2\,H^+ \quad <=> \quad CO_2(g) + H_2O \qquad \log K^0_{CO2} = 18.15 \qquad (7\text{-}2b)$$

$$Ca^{2+} + SO_4^{2-} + 2\,H_2O \quad <=> \quad CaSO_4 \cdot 2H_2O(s) \qquad \log K^0_{gps} = 4.581 \qquad (7\text{-}2c)$$

Combined reaction:

$$CaCO_3(s) + 2\,H^+ + SO_4^{2-} + H_2O <=> CaSO_4 \cdot 2H_2O(s) + CO_2(g) \quad \log K^0_{com} = 14.26 \qquad (7\text{-}3)$$

The following equation can then be derived:

$$\text{Log}\, K^0_{com} = \log p_{CO_2} + 2\,\text{pH} - \log a_{SO_4^{2-}} \;\rightarrow\; \text{pH} = \frac{\log K^0_{com} - \log p_{CO_2} + \log a_{SO_4^{2-}}}{2} \qquad (7\text{-}5)$$

Application of the latter equation yields pH values (Tab. 7-9) coinciding with those calculated by GEM-Selektor's full calculations (see Tab. 7-8), thus verifying the above relationship.

The results discussed in this section emphasise that reactive minor minerals in bentonite have a large impact on the composition of porewaters in compacted bentonite. When present, they provide a robust buffering of pH and Eh in the porewater. As long as both calcite and gypsum are present, and no significant sulphate reduction occurs, the pH will be a linear function of the logarithm of sulphate activity only at a given fixed pCO_2. Even a total replacement of exchanged Na by Ca would induce only a moderate change in pH under such circumstances.

Tab. 7-8: BPW computed for the NL-ZNO region assuming reaction with either Na-montmorillonite or Ca-montmorillonite

Column 1: reference calculation (identical to E3-BPW-Ref in Tab. 7-3). Column 2: after replacement of Na with Ca in the exchanger. Results showing significant differences are highlighted in bold. Both calculations were carried out at 25 °C, 1 bar.

GEMS ID => **Nagra ID =>**	**BPW_NL-ZNO-22** **E3-BPW-Ref** **Na-exchanger**	**BPW_NL-ZNO-22Ca** **E3-BPW-Ref-Ca** **Ca-exchanger**
Initial exchanged Na and Ca *[meq/kg clay]*		
Na	668	34
Ca	66	700
log p(CO_2)/bar	-2.20	-2.20
pH	7.24	**6.78**
Eh	-0.173	**-0.147**
IS /m	0.452	**0.341**
Total element molality *[mol/kgw]*		
Al	2.08×10^{-8}	1.78×10^{-8}
Ba	7.19×10^{-8}	$\mathbf{3.91 \times 10^{-7}}$
C(in)	2.94×10^{-3}	$\mathbf{1.27 \times 10^{-3}}$
Ca	1.77×10^{-2}	$\mathbf{9.23 \times 10^{-2}}$
Cl	0.239	0.240
F	1.74×10^{-4}	9.00×10^{-5}
Fe	2.09×10^{-5}	$\mathbf{9.50 \times 10^{-5}}$
K	1.83×10^{-3}	2.03×10^{-3}
Mg	1.02×10^{-2}	$\mathbf{6.54 \times 10^{-3}}$

Tab. 7-8: Cont.

GEMS ID => **Nagra ID =>**	**BPW_NL-ZNO-22** **E3-BPW-Ref** **Na-exchanger**	**BPW_NL-ZNO-22Ca** **E3-BPW-Ref-Ca** **Ca-exchanger**
Mn	1.84×10^{-5}	1.90×10^{-5}
Na	0.375	**4.41×10^{-2}**
S	7.86×10^{-2}	1.14×10^{-2}
Si	1.70×10^{-4}	1.74×10^{-4}
Sr	1.72×10^{-4}	**5.34×10^{-4}**
SI: Mineral precipitation (+) or dissolution (-) *[mol/kg clay]*		
Kaolinite	0.000	0.000
Calcite	0.012	0.018
Gypsum	-0.016	-0.007
Baryte	0.001	0.001
Siderite	-0.086	-0.086
Magnetite	0.027	0.027
Pyrite	0.004	0.004
Quartz	0.000	0.000

Tab. 7-9: Verification of predicted relationship between pH and K^{o}_{com} (combined constant for simultaneous calcite, gypsum and fixed pCO_2 equilibria)

log K^{o}_{com} = 14.26 in both cases

	log pCO_2	**log $a(SO_4^{2-})$***	**pH (equation)**	**pH (GEMS)**
E3-BPW-Ref	-2.20	-2.01	7.23	7.24
E3-BPW-Ref-Ca	-2.20	-2.91	6.78	6.78

* Taken from GEM-Selektor output

7.5 Summary and conclusions

The main purpose of this chapter is to derive the chemical composition and characteristics (pH, Eh, ionic strength) of porewaters permeating the bentonite buffer in the planned Swiss HLW repository after resaturation, considering the specificity of the proposed site in the Nördlich Lägern region. These waters serve as a basis for deriving solubility limits and sorption coefficients (K_d) of dose-determining radionuclides for the safety calculations. The task is achieved using a classical single porosity thermodynamic model (ClaySor) implemented in the GEM-Selektor code (Kulik et al. 2018) using the TDB2020 database (Hummel & Thoenen 2023). In the simulations, Opalinus Clay porewaters derived from water samples extracted from the boreholes in the region of interest (Mäder & Wersin 2023) are equilibrated with a batch of MX-80 Na-bentonite, the representative buffer material, at the foreseen degrees of compaction (1,300 – 1,600 kg m^{-3}) and within the expected pCO_2 range ($10^{-2.8}$ – $10^{-1.8}$ bar). The chemical reactions modelled comprise cation exchange as well protonation/deprotonation at frayed edge sites in montmorillonite, and saturation equilibria of minor minerals known to be reactive at repository temperatures (taking into account their initial inventories in bentonite). Following previous models, it is assumed that Fe(II)-Fe(III) and sulphate-sulphide equilibria control the oxidation potential (Eh) of the system.

A sensitivity analysis was carried out to explore the dependence of the calculated bentonite porewater compositions on critical parameters such as pCO_2 constraints, the degree of compaction of the bentonite, initial occupancy of amphoteric surface sites and exchanged cations, initial inventory of reactive minor minerals (e.g. presence or absence of gypsum), and partial equilibrium of redox reactions (inhibition of sulphate and/or carbonate reduction in the absence of bacteria). Reactive transport calculations using a simple flow-through model have been carried out to estimate the evolution of bentonite porewater as it reacts with increasing amounts of Opalinus Clay porewater. As expected, the bentonite porewater eventually approaches the pH and composition of the reacting Opalinus Clay porewater.

Overall, the results of the extensive sensitivity analysis indicate a narrow range of compositions, Eh and pH across all the simulated bentonite porewaters. Calculated pH values range from 6.8 to 7.5, Eh values are always reducing and lay between -227 mV and -135 mV, ionic strengths are in the range 0.278 – 0.592 m and, except for the trace elements Ba and Mn, variations in dissolved elemental concentrations are well within one order of magnitude. The narrow pH and Eh windows are explained by internal chemical buffering mechanisms provided by the interplay of carbonate-CO_2, sulphate-sulphide and Fe(II)-Fe(III) mineral equilibria in conjunction with cation exchange.

8 Interactions of the steel canister with the surrounding bentonite buffer

8.1 Introduction

As indicated in Chapter 2 and Section 4.3, the provisional disposal system for spent fuel (SF) and reprocessed high-level waste (RP-HLW) will include considerable amounts of iron-based materials, mostly in the form of the 14 cm thick carbon steel canisters enclosing the waste packages. Steel is thermodynamically unstable in any natural aqueous environment and will start to corrode as soon as it comes into contact with water, initially aerobically and then anaerobically, after consumption of all residual O_2 introduced during repository construction. Under anaerobic conditions, iron corrosion products such as magnetite, siderite, green rust, etc. will form, as well as H_2 gas and dissolved Fe(II) that will interact with the surrounding materials.

The purpose of this chapter is to assess the effect of Fe release from the canister on the mineralogical stability of bentonite, and its potential effect on the functionality of the buffer. The dissolved Fe(II) released during steel corrosion interacts with bentonite and could potentially alter its properties. It is therefore of relvance to evaluate such interactions to ensure that the bentonite buffer maintains its sealing and radionuclide retention properties.

Bradbury et al. (2014), Leupin et al. (2014) and Savage (2014) discussed the potential impact of corrosion-derived Fe(II) on bentonite in the near-field of a HLW repository in the context of SGT-E2. Since then, numerous papers and reports have appeared on various aspects of Fe-bentonite interaction. This chapter is intended to provide a review of recent studies, focusing on the reported mineralogical changes in bentonite. Based on the evidence from such studies and conservative estimates of the amount of potentially altered bentonite (App. A), conclusions on the possibility of loss of the safety function of the buffer will be provided.

The reviewed studies can be divided in two broad categories: (1) Experiments with a focus on the influence of corrosion-derived dissolved iron on bentonite or natural claystones (as analogues of bentonite) (Section 8.2), and (2) Experiments with a focus on the influence of bentonite or claystones on the corrosion behaviour of metallic iron, which obviously has a feedback effect on the amounts of bentonite altered (Section 8.3). The former category usually involves the use of iron powders to enhance reactivity and maximise the alteration of bentonite, while in the second type of tests monolithic Fe or steel samples are used in order to simulate the effects on the HLW disposal canister and facilitate post-mortem examination of the corrosion products and of corrosion thickness. In addition to laboratory-scale experiments, this review also considers large-scale in-situ experiments in underground laboratories, which provide the closest analogy to a repository setup.

8.2 Influence of Fe on bentonite and claystone mineralogy

8.2.1 Laboratory-scale experiments

In this section, the results of laboratory-scale experiments on Fe interacting with bentonites, smectites or claystones are briefly discussed. Most of the studies investigated Callovo-Oxfordian claystone (COx), the host rock selected for the French HLW repository; only a few have been conducted with MX-80 bentonite.

Callovo-Oxfordian claystone (COx) contains on average 40 wt.% clay minerals (15 wt.% illite and micas, 20 to 25 wt.% illite-smectite mixed layers, < 5 wt.% kaolinite and chlorite), 25 wt.% quartz, 30 wt.% carbonates (calcite and dolomite with minor amounts of ankerite), and 5 wt.% of pyrite, feldspar and organic matter (Pignatelli et al. 2014 and references therein). Its mineralogical

composition thus differs considerably from that of MX-80 bentonite (Tab. 4-3), which contains only minor amounts of illite and other minerals and is dominated by montmorillonite (> 75 wt.%) a smectitic clay mineral responsible for its very high CEC.

Several types of experiments were performed. Lanson et al. (2012) carried out batch experiments with three different smectite powders (beidellite, montmorillonite, nontronite), each one mixed with powdered iron in suspension with pure water, under anoxic conditions at 80 °C for 45 days. Combarieu et al. (2011) used an assembly consisting of an iron foil inserted between a glass disk (simulating vitrified HLW waste) and an initially dry COx claystone sample. The assembly was placed in a high-pressure cell, saturated with pure water, and kept under anoxic conditions at 90 °C for 18 months. Rivard et al. (2013) and Rivard et al. (2015) carried out batch experiments in simplified COx saline solutions with mixtures of iron powder and other suspended materials (kaolinite, COx claystone with/without calcite/pyrite/quartz) at 90 °C. The suspensions were kept under anoxic conditions. Bourdelle et al. (2014) kept suspensions of ground COx mixed with (a) iron powders and (b) iron grains (smaller surface area) in simplified COx saline solutions under anoxic conditions at 90 °C for 3 months. Other experiments involving metallic Fe and COx claystone were performed by Jodin-Caumon et al. (2012), Pignatelli et al. (2013), Pignatelli et al. (2014), Bourdelle et al. (2014), Mosser-Ruck et al. (2016), Bourdelle et al. (2017) and Mosser-Ruck et al. (2020). Comparable experiments involving MX-80 or other bentonites were carried out in various studies (Jodin-Caumon et al. 2010, Osacký et al. 2010, Osacký et al. 2013, Ueno et al. 2011, Mosser-Ruck et al. 2016, Davies et al. 2017, Idemitsu et al. 2017).

Kaufhold et al. (2015) carried out a special experiment in which iron samples were corroded anaerobically in the presence of bentonite, from which kaolinite and chlorite (which could have obscured XRD identification of secondary corrosion products) had previously been separated. After one month, the corroded iron rods were removed from the slurry with a magnet; the slurry was dried in the glove box and finally ground. The ground products were characterised by XRD, revealing neoformation of berthierine, the Fe end-member of the kaolinite/serpentine clay mineral group. Formation of other corrosion products, such as magnetite and other iron oxides or hydroxides, was not reported.

Smart et al. (2017a) carried out anaerobic corrosion experiments on carbon steel wires embedded in compacted MX-80 bentonite saturated with synthetic Opalinus Clay porewater, using barometric gas cells. The tests were conducted at 60 °C for a duration of more than 5 years. Gas generation was used to monitor steel corrosion during the experiment. The bentonite in one of the cells opened after ~ 3.4 years showed a strong reddish-brown to ochreous staining adjacent to the steel wires. The bentonite matrix itself showed patchy staining within apparently unaffected domains. Secondary iron oxides were found particularly along a network of microfractures permeating the bentonite. The microfractures were apparently generated via shrinking induced by dehydration (caused by the consumption of the water required to generate hydrogen during anaerobic corrosion). XRD diffractograms of corroded both unstained and stained bentonite were not distinguishable from the initial (pre-corrosion) pattern. The d(001) spacings derived from XRD analyses confirmed that, in spite of the intense red colour, the stained bentonite was still dominated by montmorillonite, the measured d(001)/d(002) ratios pointing however to Fe enrichment. Moreover, a peak at 10.55 Å was found that may be assigned to neoformation of palygorskite $(Mg, Al, Fe)_2Si_4O_{10}(OH)\cdot 4H_2O$, a 2:1 clay mineral belonging to the palygorskite-sepiolite group.

To summarise, the aforementioned studies indicate that, in most cases, after reaction with metallic iron, the initial smectitic or illitic clay becomes enriched in Fe(II) and increasingly trioctahedral (i.e. the trivalent Al in octahedral sites was progressively substituted by divalent metals, mainly ferrous iron). Moreover, a variety of newly formed Fe-silicate minerals was often reported in the altered materials. Tab. 8-1 gives an overview of the identified secondary minerals as well as the

associated reacting materials, together with the experimental conditions and references. The nominal compositions of the minerals as given from the International Mineralogical Association (IMA, see https://rruff.info/ima/) are reported in Tab. 8-2.

Tab. 8-1: Summary of mineralogical results from laboratory-scale experiments involving metallic Fe and clay materials

T [°C]	Fe source	Clay type	Initial solution	Conditions	Exp. time	Alteration products	Reference
60	Fe wires	MX-80 bentonite	OPA water	Ar atm.	3.4 a	Fe-rich mtm, palygorskite	Smart et al. (2017a)
50 – 90	Fe powder + Fe plate	COx + quartz	COx water (I ~ 0.2)	Ar atm.	6 – 11 m	Mag / cronstedtite greenalite	Pignatelli et al., Pignatelli et al. (2013, 2014)
75	Fe powder	7 smectites	Pure water	N_2 atm.	35 d	Mag / 7 Å	Osacký et al. (2010)
75	Fe powder	6 smectites	Pure water	Aerobic	35 d	Mag / 7 Å	Osacký et al. (2013)
80	Fe powder	Beidellite, montmorillonite, nontronite	Pure water	Ar atm.	45 d	Odinite/ cronstedtite	Lanson et al. (2012)
80	Fe powder + mag	MX-80 bentonite	Pure or COx water (I ~ 0.2)	Ar atm.	1 – 10 m	7 Å/ chlorite ?	Jodin-Caumon et al. (2010)
90	Fe foil	COx	Pure water	Ar/H_2	6 – 18 m	Sid / 7 Å	De Combarieu et al. (2011)
90	Fe powder	Kaolinite / COx	COx water (I ~ 0.2)	N_2 atm. or air	1 – 9 m	Mag/ 7 Å, berthierine	Rivard et al., Rivard et al. (2013, 2015)
90	Fe grains/ powder	COx	COx water (I ~ 0.2)	Ar atm.	3 m	7 Å, odinite-greenalite	Bourdelle et al. (2014)
90	Fe powder + Fe foils	COx	Dilute $NaHCO_3$ solution	Ar atm.	107 d	prh/ 7 Å,	Mosser-Ruck et al. (2020)
300	Fe powder + mag	MX-80 bentonite	Pure or COx water (I ~ 0.2)	Ar atm.	1 – 10 m	chl	Jodin-Caumon et al. (2010)
300	Fe powder + mag	MX-80 bentonite	COx water (I ~ 0.2)	Ar atm.	2 – 9 a	Chamosite, IS chl-sme	Mosser-Ruck et al. (2016)

mtm = montmorillonite, mag = magnetite, sid = siderite, prh = pyrrhotite, chl = Fe-chlorite, IS chl-sme = interstratified chlorite-smectite, 7 Å = Fe-enriched phyllosilicate with 7 Å interlayer spacing (serpentine structure)

The results in Tab. 8-1 are sorted in order of increasing temperature to facilitate the distinction of tests carried out at the expected HLW repository temperatures from those carried out under a different thermal regime. The inspection of the table readily reveals that Fe-chlorites (e.g. chamosite) only form at much higher temperatures than those expected in any planned geological repository. In the more realistic 50 – 90 °C range, Fe-enriched, poorly to well-crystallised 1:1 clay minerals of the kaolinite/serpentine group are commonly detected.

Corrosion of the steel canister will continue after failure, i.e. also at the lower temperatures established after the initial thermal pulse (≈ 47 °C, see Fig. 5-2, Chapter 5). Unfortunately, only scarce data are available in this range of temperatures. The only study known to the authors is that of Pignatelli et al. (2013) who observed almost complete dissolution of cronstedtite at 40 °C (previously formed at higher temperature in the same experiment). These results would suggest that Fe-serpentine minerals might not be stable at thermal equilibrium in the HLW repository, however these data are not sufficient to draw such a conclusion.

Potential corrosion products of metallic iron known to form at low temperatures under anoxic conditions are so-called “green rusts”. This is a generic term for Fe(II,III)-rich layered double hydroxides (LDH), consisting of positively charged $Mg(OH)_2$ (brucite) layers intercalated with sheets of anions. Cui & Spahiu (2002) showed formation of carbonate “green rust” with formula $Fe(II)_4Fe(III)_2\,(OH)_{12}CO_3$ during corrosion of a metal foil in carbonate water under strictly anoxic conditions at room temperature, but in the absence of clay minerals or other silicates. This result was confirmed by Scheidegger et al. (2003).

In summary, it can be concluded that laboratory experiments on the aqueous interaction of bentonite and claystones with metallic iron (with/without magnetite) lead systematically to the formation of Fe-enriched clay minerals of the serpentine/kaolinite clay mineral group between 50 – 90 °C. Fe-chlorites can be excluded, as they only form at much higher temperatures. Because of slow kinetics, comparable laboratory experiments at temperatures below 50 °C are scarce. The few data available, although inconclusive, suggest destabilisation of Fe-rich serpentine/kaolinite clay minerals and possibly formation Fe-rich LDH phases.

Because the range of predicted temperatures at the canister/bentonite interface after bentonite resaturation is in the 50 – 120 °C range (see Fig. 5-2), the laboratory data discussed above indicate that serpentine/kaolinite type Fe-clays should be the main newly formed Fe-corrosion products in the altered bentonite during the high temperature pulse. In the long term, thermal equilibrium at ~ 47 °C would be reached, which is slightly below the apparent stability limit of 50 °C for these minerals. Therefore, it is not clear whether such minerals would remain stable in the long term. The data from underground laboratory experiments discussed in the next section, more closely reproducing repository conditions, will possibly give more clarity.

Tab. 8-2: Summary of primary and secondary clay minerals observed in the reviewed experimental studies on Fe-clay interaction

Only idealised end-member formulae are reported, and no mention is made of the changes observed in the primary clay minerals (usually, Fe-enrichment and interstratifications).

Mineral	Ideal Formula	Type	Structure*	Group
Primary clay minerals (reactants)				
Nontronite	$Na_{0.3}\,(Fe^{3+}{}_2)[Si,Al]_4O_{10}(OH)_2{\cdot}nH_2O$	2:1	TOT-H...	Smectite
Montm.	$Na_{.14}K_{.01}Ca_{.05}(Al_{1.56}Fe^{3+}{}_{.21}Mg_{.23})[Si_{3.95}Al_{.05}]O_{10}(OH)_2$	2:1	TOT-H...	Smectite
Beidellite	$Na_{.08}K_{.08}Ca_{.10}(Al_{1.80}Fe^{3+}{}_{.12}Mg_{.08})[Si_{3.71}Al_{.29}]O_{10}(OH)_2$	2:1	TOT-H...	Smectite
Illite	$K_{0.83}(Al_{1.51}Fe^{2+}{}_{0.375}Mg_{0.23})[Si_{3.4}Al_{0.6}]O_{10}(OH)_2$	2:1	TOT-K...	Mica
Secondary clay or clay-like minerals (alteration products)				
Berthierine	$(Fe^{2+},Fe^{3+},Al)_3[Si,Al]_2O_5(OH)_4$	1:1	TO...	Kao-ser
Greenalite	$(Fe^{2+},Fe^{3+})_{2\text{-}3}\,[Si_2O_5](OH)$	1:1	TO...	Kao-ser
Cronstedtite	$(Fe^{2+},Fe^{3+})_3[(Si,Fe^{3+})_2O_5](OH)_4$	1:1	TO...	Kao-ser
Odinite	$(Fe^{2+},Mg,Al,Fe^{3+})_{2.5}[(Si,Al)_2O_5](OH)_4$	1:1	TO...	Kao-ser
7Å	unspecified, poorly crystalline	1:1	TO...	Kao-ser
Chamosite	$(Fe^{2+},Mg,Al,\,Fe^{3+})_3[(Si,Al)_2O_5](OH,O)_4$	2:1	TOT-B...	Chlorite
chl	unspecified, poorly crystalline	2:1	TOT-B...	Chlorite

* T = tetrahedral unit, O = octahedral unit, B = brucite layer, H = hydrated cation layer, K= non-hydrated K^+
Montm. = montmorillonite, kao-ser = kaolinite-serpentine series

8.2.2 Large-scale in situ experiments

8.2.2.1 Introduction

The laboratory-scale experiments presented in Section 8.2.1 indicate that the release of dissolved Fe(II) during anaerobic corrosion of metallic iron (simulating a steel canister) leads to formation of Fe-enriched clay minerals upon interaction with bentonite and claystone. The original clay minerals (smectites or illites) become Fe(II)-enriched and progressively trioctahedral. Moreover, 1:1 Fe clay minerals (serpentine/kaolinite group) could form in the initial "hot" phase, which could however be destabilised below 50 °C. These results are however inconclusive, for various reasons.

In the first place, laboratory experiments cannot faithfully reproduce the conditions encountered in the repository, either in terms of geometry, scale or material properties. In addition, the frequent use of finely ground, highly reactive zerovalent iron in laboratory experiments to accelerate the reactions, may bias the reaction path. Such an effect was demonstrated by Bourdelle et al. (2014) by carrying out two (otherwise identical) batch experiments in which COx claystone reacted either with fine Fe powder or coarse Fe grains in $NaCl/CaCl_2$ solution. The corrosion rate measured for the test with Fe powder was more than 50 times faster than in the other experiment. Moreover, the pH and solute concentration evolutions were different, and XRD analyses revealed a surprisingly discrepant clay mineralogy at the end of the experiments (after 90 days). With Fe powder as reactant, the alteration products evolved towards Fe-mica end-members and Fe-chlorite compositions, while with Fe grains the final products were close to kaolinite (i.e. Al-rich and Fe-poor, see Fig. 5 in op. cit.).

These findings suggest that large-scale experiments in underground laboratories, typically conducted with the proper materials in environments similar to those expected in the planned repository, are more realistic and representative of the chemical evolution at the bentonite/canister interface under repository conditions. The following sections therefore summarise in some detail the results of three major large-scale experiments conducted under the supervision of international consortia: FEBEX at the Grimsel Test Site (Switzerland), ABM at the Äspö Hard Rock Laboratory (Sweden) and IC-A at the Mont Terri Rock Laboratory (Switzerland).

8.2.2.2 The FEBEX experiment

The FEBEX (Full-Scale Engineered Barriers Experiment) in-situ test at the Grimsel Test Site, deep underground in crystalline rock, was designed to test a typical HLW disposal concept. The main objective was to demonstrate the feasibility of manufacturing and assembling a repository-scale engineered barrier system with a bentonite buffer, and to develop methodologies to assess the thermo-hydro-mechanical (THM) and geochemical (THMC) behaviour of the engineered barrier system (Lanyon & Gaus 2016).

The experiment was conducted in a horizontal drift of 2.28 m diameter drilled into the Grimsel granodiorite. It consisted of two cylindrical carbon steel heaters of size representative of a waste canister (diameter 0.97 m, length 4.54 m) placed horizontally in the axis of the drift (Villar 2018) and surrounded by a carbon steel liner. The drift was backfilled with blocks of compacted Ca-Mg bentonite (named FEBEX bentonite). Both host rock and bentonite were equipped with more than 600 sensors for real-time monitoring of parameters such as temperature, water content and swelling pressure. The heaters were set at 100 ºC, which represents the highest (constant) temperature reached during the experiment, exactly at the steel/bentonite contact. Saturation of the bentonite was achieved via natural influx of water from the surrounding granodiorite and started in 1997. After 5 years of continuous operation, Heater #1, lying closer to the drift entrance, was turned off, dismantled for post-mortem analyses, and replaced by a dummy steel cylinder

sealed with shotcrete (Villar 2018). In-situ monitoring in the intact part of the system (Heater #2) continued until final dismantling in 2015, after a total operation time of 18 years. All papers discussed below refer to samples extracted during this final dismantling of the experiment.

Torres et al. (2017) examined three samples of bentonite located in the vicinity of Heater #2 and one situated near the contact to the granite. They found that, following evaporation in the partially saturated region at the bentonite/heater interface, the concentration of most soluble ions correlated with the temperature gradient (Na, Cl, Mg and Ca) and increased steeply towards the heater (while sulphate remained constant). CEC values remained within the ranges expected for unreacted FEBEX bentonite; however limited Fe enrichments (from 0.2 mmol/kg in contact with the heater to 12.4 mmol/kg close to the host rock) were detected and attributed to adsorption. From these preliminary data, Torres et al. (2017) concluded that no significant changes in the physical/ chemical characteristics in the bentonite sampled in the vicinity of the heater had occurred.

Fernández et al. (2018) investigated bentonite blocks collected from front, rear and sides of Heater #2, from the external part of the steel liner, as well as from bentonite protrusions inside the liner holes, using additional characterisation techniques compared to Torres et al. (2017) (e.g. XRF, XRD, FTIR, thermal analysis, SEM/TEM). The results revealed that, during bentonite saturation with surrounding granitic groundwater, soluble salts (initially homogeneously distributed as minor components in the bentonite) were dissolved and transported towards the inner parts of the bentonite via advective-diffusive transport, locally modifying the bentonite porewater composition and the cation exchange populations. The highest salinity values were detected at the liner/heater contact (Na-Mg-Ca-Cl-type water with an ionic strength of 0.41 M), resulting in the precipitation of carbonates (aragonite, dolomite, magnesite, and siderite). Most of the exchangeable Na in the smectite interlayer was replaced by Ca or Mg and the Ca/Mg ratio increased. The high Mg content at the liner/heater contact was ascribed to the neoformation of saponite (a trioctahedral Mg-smectite), brucite and Fe-rich chlorite. Modifications of the dehydroxylation temperature peaks, compared to the unaltered dioctahedral smectites initially present in bentonite, were detected, indicating formation of saponite, chlorite and possibly interstratified smectite particles (e.g. illite/smectite or chlorite/smectite mixed layer minerals).

Although the FEBEX in-situ experiment was carried out under aerated conditions, anoxic steel corrosion was detected in localised zones at the liner/heater contact, as indicated by green and black colourations of the bentonite. Steel corrosion resulted in an increase in Fe content in bentonite samples taken from the first mm thin layer of bentonite near the liner/heater contact (from 3.1 wt.% to 6 – 19 wt.%) and in the formation of corrosion products, which include iron oxides and oxyhydroxides (i.e. goethite, maghemite, haematite, ferrihydrite), as well as magnetite, titanomagnetite, siderite and sulphides (i.e. pyrrhotite, mackinawite, FeS). Fernández et al. (2018) further inferred that both solid-state (topotactic) and dissolution/precipitation transformations of the original smectite occurred. In the former case, montmorillonite was replaced by vermiculite-like clays, while in the latter case the result was formation of trioctahedral Mg-smectite (saponite), brucite and chlorite in localised zones. The observed smectite transformations resulted in modifications of the physico-chemical properties of the bentonite, namely a decrease in the total cation exchange capacity and in the BET surface area. These changes were, however, restricted to the immediate vicinity of the liner/heater contact (up to a few mm from the interface), leaving most of the bentonite unaffected.

Hadi et al. (2019) examined two bentonite blocks from the FEBEX experiment, both contacting the steel liner in the section between Heater #2 and the dummy steel element replacing the previously extracted Heater #1, but placed asymmetrically on opposite sides of the liner. Both samples had been exposed to temperatures of only 30 – 60 °C. However, they showed different extents of alteration: the upper left block showed a distinct coloured halo extending from the contact with the corroded steel liner into the bentonite, with red (first 45 mm from the liner contact), followed by orange and blue further away (up to about 125 mm from the liner). There

was clear evidence from XRF data that the colouration in the bentonite correlates with the amount and nature of corrosion-derived Fe diffusing from the steel liner into the bentonite. The Fe accumulated in the red-orange zone consists predominantly of Fe(III) precipitates (goethite and haematite). In the more reduced blue zone, Mössbauer data indicate the presence of both Fe(II) and Fe(III), the latter in concentrations comparable to those in unreacted FEBEX bentonite.

A surprising result was that the bentonite block at the lower right side of the liner tube did not develop a coloured alteration halo. Hadi et al. (2019) explained this difference as the result of an unintended artefact: a plastic sheet placed at the lower right side of the section onto the granodiorite during the build-up of the experiment was unintentionally left after emplacement of the bentonite blocks, preventing the ingress of aerated water from the underlying granodiorite. Only oxygen-free water (previously deaerated via oxidation of the overlying steel liner) could penetrate the lower bentonite section, protecting it from oxidation.

Based on their sample analyses, Hadi et al. (2019) proposed the following evolution of the corrosion process for the FEBEX experiment, see also Wersin & Kober (2017):

Stage 1: Under partially saturated conditions, humidity is sufficiently high to provide water vapour for the aerobic corrosion of steel. Fe(III) species are generated at the surface of steel and in the corrosion layer beneath. Depending on moisture content, Fe(III) oxides (haematite, maghemite) or Fe(III) oxy-hydroxides (mainly goethite and lepidocrocite) are formed. With reaction progress, the thickening of the corrosion layer limits the diffusion of O_2 and H_2O from the bentonite to the unreacted steel, reducing its corrosion rate. Replenishment of O_2 at the steel surface is also limited by its low diffusivity in bentonite.

Stage 2: Anaerobic corrosion starts as soon as O_2 is consumed and no longer available on the steel surface, leading to the formation of Fe(II) species and precipitation of magnetite and siderite in the steel corrosion layer. Electron transfer across the corrosion layer generates soluble Fe(II) at the interface between corrosion layer and bentonite, which starts to diffuse into the bentonite. Reaction with in-diffusing O_2 from the bentonite towards the steel surface leads to the oxidation of the out-diffusing Fe(II). The resulting Fe(III) precipitates mainly as goethite and haematite, forming the red and orange coloured zones.

Stage 3: Oxygen is completely consumed in the bentonite buffer, so that Fe(II) diffuses into and sorbs on the bentonite without further oxidation (blue coloured zone).

In their synthesis of the FEBEX-DP (dismantling project), Wersin & Kober (2017) point out that the thickness of these interaction zones is highly variable (from zero to dm thick, however in most cases only a few mm thick) and that the Fe content correlates with the extent of the coloured reaction zones. The thicker the reaction zone, the larger the increase in Fe content compared to the unaffected bentonite. Close to the corroded steel, the Fe content was generally found to be higher by a factor of 1.5-3 than in areas where the bentonite showed no visible signs of alteration.

Wersin & Kober (2017) also emphasised that the major driving force for steel corrosion and bentonite alteration must have been the availability of H_2O and O_2. In the FEBEX experiment, water availability was limited through evaporation induced by heating up to 100 °C; moreover, the corrosion of metallic iron itself consumes water. Both processes resulted in the accumulation of chloride (likely enhancing corrosion) and, to a lesser extent, of sulphate and carbonate salts near the heater (in analogy with the results of Sena et al. 2010, see Section 5.2.1), resulting in the precipitation of calcite and aragonite close to the heater. The cation exchange capacity showed only minor changes (decrease of $\leq 10\%$ as a function of distance from the heater) and was interpreted as the result of "dilution of the bentonite" by the precipitated iron corrosion products. Alteration of smectite was very limited as documented by the constant Al/Si ratio even across the alteration zones. In some samples close to the heater, minor domains of trioctahedral smectite (saponite) were found by XRD and, in one sample, an Mg-rich zeolite (chabazite) was identified.

8.2.2.3 The ABM experiment

The ABM (Alternative Buffer Materials) test was an in-situ experiment started in the Äspö Hard Rock Laboratory in Sweden in 2006 with the objective of testing different buffer materials (bentonites and other clays) under representative near-field conditions. Three test packages (ABM1, ABM2, ABM3) were devised, each consisting of a borehole drilled in the granite host-rock and then filled with a central heating element surrounded by annular blocks of various bentonite and clay materials stacked upon each other. The heating system contained a central steel tube, serving as surrogate canister material subject to potential corrosion (Wersin et al. 2015). The outer diameter of the individual blocks was 280 mm, the inner diameter 110 mm and the height 100 mm (Kaufhold et al. 2017). Nine different types of compacted bentonites and two marine claystones were tested.

Wetting of ABM1 with artificial Äspö porewater and slow heating started in December 2006 to reach a maximum heater temperature of ~ 130 °C after about 1 year. During the test period, technical problems enforced a temporary decrease in temperature in order to avoid boiling. The ABM1 package was retrieved after 2.5 years (881 days) by overcoring (Wersin et al. 2015). ABM2 was dismantled after 6.5 years from the start of the experiment, with 2.5 years of water saturation and 3 – 4 years of heating to a maximum temperature of up to 141 °C (Kaufhold et al. 2017).

Apart from the exchangeable cations (see below), compositional and mineralogical alterations in all materials tested in the ABM1 experiment were restricted to a thin zone at the contact between steel and clay (Kaufhold et al. 2013), notably an Fe enrichment. Neoformation of Fe solids, however, was detected only in Kunigel V1 bentonite, which showed the largest iron accumulation. No Fe corrosion products were found in any of the other samples. For instance, no trace of the typical 7 Å or 14 Å phyllosilicates routinely found in laboratory experiments with Fe powder was detected in any of the clay blocks. Some samples showed formation of anhydrite or accumulation of organic carbon. No significant alteration of montmorillonite was observed.

The exchangeable cation populations of the ABM1 clay blocks were found to be spatially uniform after the experiment, but largely different from the initial populations (Dohrmann et al. 2013). This finding was systematic (21 blocks were investigated). After the experiment, the average cation exchange capacities of all nine tested bentonites were reduced (on average by 5.5 meq/100 g), with a range from 1.1 to 8.8 meq/100 g). In general, exchanged Na^+ and Mg^{2+} were partially replaced by Ca^{2+} supplied by the in-diffusing groundwater.

Wersin et al. (2015) investigated MX-80 samples from the ABM1 experiment in detail using SEM-EDX, μ-Raman spectroscopy, spatially resolved XRD, and XRF. Steel corrosion resulted in a ~ 100 μm thick layer containing siderite, magnetite, goethite and lepidocrocite associated with the montmorillonitic clay. Most of the Fe released via steel corrosion was detected within the first 10 mm of the bentonite adjacent to the corrosion layer and increased levels of iron did not exceed a maximum distance of about 22 mm.

The exact nature of the iron deposited in the altered bentonite could not be identified. Wersin et al. (2015) suspected formation of fine-grained or microcrystalline Fe oxy-hydroxides, not detectable by conventional XRD analysis (Hadi et al. 2017). No signs of structural modification of the pristine montmorillonite or of newly formed clay minerals were observed. Precipitation of anhydrite close to the heat source was detected by Raman spectroscopy, while XRD data indicated the presence of gypsum (possibly derived from anhydrite by exposure to moisture during sample preparation for XRD). The detection of siderite and magnetite is evidence that, during the experiment, reducing conditions were established, while the formation of the Fe(III) oxy-hydroxides may be related to initially oxic conditions or to oxygen contamination during sample preparation and/or μ-Raman analysis.

Kumpulainen et al. (2016) examined four clay blocks of the ABM2 test, including two MX-80 blocks. In general, the chemical and mineralogical changes observed were more pronounced than in the ABM1 test, which is not surprising considering the longer duration of ABM2. Analyses of water-soluble ions revealed sulphate, Ca and Mg accumulation, and K and chloride depletion, towards the heater tube. At the interface between heater tube and bentonite, an increase in Fe and a decrease in Al and Si were observed, as well as the formation of gypsum and anhydrite and dissolution of cristobalite and feldspars. Exchangeable cations showed changes (similar in all materials studied) with respect to the initial populations. Specifically, exchanged Ca increased at the expense of Na, Mg, and K. As for ABM1, ABM2 clay samples showed no or negligible gradients in the total exchange capacities (CEC) and exchanged cation loadings (Na^+, Ca^{2+}, Mg^{2+}) perpendicular to the heater tube. No formation of new Fe-bearing minerals was detected, nor changes in the Fe-content of smectites. However, based on XRD spectra taken on samples of Friedland clay and MX-80 bentonite within 1 mm from the heater tube surface, there were indications of the formation of a trioctahedral phase (indicated by a peak between 1.52 and 1.54 Å, see also Kaufhold et al. 2017). No changes in hydraulic conductivity were found in any of the materials studied.

Hadi et al. (2017) studied the redox evolution and iron-bentonite interaction of the ABM2 test using a novel multi-method approach involving SEM, SEM-EDX, μ-Raman spectroscopy, XRD, XRF, and ^{57}Fe Mössbauer spectroscopy. They sampled 8 blocks, comprising 7 different bentonites, including MX-80. At the surface of the heater tube, a corrosion layer consisting mainly of magnetite and siderite formed, which indicates anoxic corrosion in this region. Away from the external surface of the corrosion layer, a ~ 5 – 10 mm thick Fe-enriched front extended into the bentonite in most blocks. The Fe enrichments in bentonite mainly consisted of Fe(III) oxides (goethite and, to a lesser extent, lepidocrocite) with minor Fe(II) enrichments in some cases, the nature of which could not be determined (possibly sorbed Fe(II), reduced structural Fe in smectite, amorphous "green rust"). Based on these observations, Hadi et al. (2017) proposed an interpretation of the corrosion-alteration process that is essentially identical to that proposed in Wersin & Kober (2017) for the FEBEX experiment. Overall, the results from exchanged cation analyses confirmed the findings of Kumpulainen et al. (2016) and Kaufhold et al. (2017) i.e. the replacement of Na by Ca in the sodic bentonites (MX-80, Ibeco Seal, Ikosorb, and Kunigel), and almost unmodified and nearly constant CEC values with increasing distance from the heater tube.

8.2.2.4 The IC-A experiment

A currently ongoing experiment, the Iron Corrosion in Bentonite Experiment (IC-A), was set up at the Mont Terri Rock Laboratory with the primary objective of investigating the corrosion of carbon steel in contact with MX-80 bentonite under ambient conditions (no heating). Twelve cylindrical modules made of stainless steel were emplaced in a vertical borehole within the Opalinus Clay. Each module has holes and filters, enabling the exchange of porewater with the host rock, and contains compacted MX-80 bentonite (dry density 1,250 to 1,550 kg m^{-3}) with embedded carbon steel coupons. Samples were retrieved and characterised periodically (Reddy et al. 2021b).

The characterisation of the bentonite adjacent to the corroded carbon steel coupons showed that they were strongly stained to a reddish-brown to ochreous colour, extending into the grey bentonite matrix up to a sharply defined depth of ~ 2 mm. A series of radial microfractures developed perpendicular to the steel-bentonite interface, forming an interconnected network in combination with discontinuous hairline fractures parallel to the interface. No evidence was found for secondary Fe-oxide corrosion products or other alteration products within these microfractures. Although the reddish-brown zone extended up to ~ 2 mm into the bentonite, enhanced concentrations of Fe were detected by EDXA only within the first 100 μm. Calcium and sulphur were seen to be enriched within the first 10 – 20 μm, which was interpreted by Smart et al. (2017b) as either

gypsum or anhydrite. Calcium sulphate was also found as fillings of up to 10 μm-wide micro-fractures penetrating the bentonite from the steel-bentonite interface, and as fillings of grain boundary cracks around bentonite aggregate particles. The apparently unaffected grey bentonite was found by XRD determination of d_{002}/d_{003} ratios to consist primarily of montmorillonite without significant Fe enrichment. In contrast, the high d_{002}/d_{003} value of 0.74 measured for stained bentonite in module 3 points to a significant Fe enrichment, which was however not confirmed in a similar sample from module 2.

8.2.2.5 Comparison of large-scale in-situ experiments with laboratory experiments

In general, the FEBEX and ABM experiments yielded comparable results that differ remarkably from those obtained in laboratory experiments. Except in the study of Fernández et al. (2018), no 7 Å or 14 Å phyllosilicates (Fe-serpentines and Fe-chlorites, respectively) were reported in any type of tested clays, in spite of comparable temperatures and longer experimental times (18 years for FEBEX, 6.5 years in the case of ABM2). Also, the structural and hydraulic properties of the smectites were not significantly modified during the in-situ tests, contrary to the results of most laboratory-scale experiments. These differences are probably the result of unrealistically high Fe mobilisation in the laboratory tests, arising from the use of highly reactive Fe powder and very high Fe/clay ratios. The results from FEBEX and ABM are essentially confirmed by preliminary data from the ongoing IC-A experiment in the Mont Terri Rock Laboratory, obtained after 20 months since the start.

Another outcome of the in-situ experiments is the usually limited extent of Fe mobilisation and clay alteration induced by the steel corrosion process. Only a tiny fraction of the clay thickness is affected by significant chemical/physical modifications of the initial material. In addition, the mobilisation appears to be mainly associated with a transient oxic phase. Most of the subsequent corrosion process take place anaerobically under reducing conditions, as shown by formation of magnetite, siderite and sometimes sulphides in the corroded steel. These minerals form crusts that progressively hinder the migration of dissolved Fe(II) from the steel into bentonite.

8.2.3 Potential extent of bentonite alteration

Clearly, the results of in-situ experiments in underground facilities are more representative of the true evolution in a HLW repository and should be assigned more credibility than evidence obtained from laboratory-scale tests. In general, the in-situ tests indicate a much weaker and spatially limited bentonite degradation compared to laboratory tests, suggesting that the favourable radionuclide retention and transport properties of compacted bentonite, as well as its excellent swelling capacity, will not be compromised by the release of iron from the canister. Nevertheless, due to the necessarily limited time of such experiments, degradation of buffer functionality via chemical alteration over the timescale of repository evolution cannot be categorically excluded merely on the basis of in-situ experiments. Fe-clays identified after Fe-bentonite interaction, such as berthierine and chamosite, have a lower sorption capacity and expandability compared to montmorillonite and would compromise the functionality of bentonite as a barrier material if a large part of the buffer thickness were affected by Fe-alteration in the long term. Therefore, in order to complement the results of in-situ experiments, it is necessary to extrapolate such results to the timescale of interest, i.e. 1 Ma in the case of the Swiss HLW repository.

Usually, mass balance calculations under pessimistic assumptions are made to estimate the maximum possible alteration thickness of the buffer material over such timescales, as done in Section 7.4 of Bradbury et al. (2014). In that calculation, it was assumed that *all* Fe(II) formed via anaerobic canister degradation at a corrosion rate of 1 μm/a would be released as aqueous

species into the bentonite buffer and react there with montmorillonite, producing a stoichiometrically equivalent amount of berthierine or chamosite. The results led to the conclusion that, under this pessimistic assumption, degradation of a substantial part of the bentonite buffer (30 – 70%) within 100,000 – 150,000 years cannot be excluded.

From today's perspective, this calculation appears overconservative since:

(i) more recent data point to slower long-term steel corrosion rates of 0.5 μm/a (Smart et al. 2017a) or even lower (0.3 μm/a, see Diomidis et al. 2023)

(ii) more importantly, the assumption of total mobilisation of the corroded Fe is unreasonably pessimistic

Indeed, considering the low solubility of Fe(II) solids under repository conditions (in the range 6 – 72 μmol/kgw, see Tab. 7-3, Tab. 7-4 and Tab. 9-1), it is difficult to conceive that all Fe released via canister corrosion would be transferred to the bentonite. In fact, most of the metallic Fe oxidised to Fe(II) or Fe(III) during canister corrosion will not migrate, but reprecipitate in-situ within the canister in the form of solid corrosion products (e.g. magnetite, siderite, pyrite).

To account for the in-situ precipitation of iron corrosion products, the estimates of Bradbury et al. (2014) were updated with the help of a more realistic model. This is based on the assumption that a diffusive flux of dissolved Fe(II) will be established between the water permeating the corroding canister and the (Fe-poorer) Opalinus Clay porewater penetrating the external part of the buffer. The details of the calculations are presented in App. A. Briefly, it is assumed that, at the canister/bentonite interface, the dissolved Fe concentration is fixed at $7.22 \cdot 10^{-5}$ M by equilibrium with magnetite and siderite, according to calculation "INCAN 2a_2" (Tab. 9-2). At the outer bentonite boundary, a lower Fe concentration is assumed, fixed by the Fe concentrations predicted for Opalinus Clay waters (see Tab. 7-3 in this report). Transport of dissolved iron is considered to occur at steady state, yielding a constant flux of dissolved Fe from the canister into the bentonite. Two cases were calculated: a realistic estimate, corresponding to reference values for OPAw Fe concentration and effective diffusion coefficient, and a conservative case with the Fe flux into the bentonite maximised, but still using realistic parameters for diffusivity and Fe concentration (see header row in Tab. 8-3). An effective diffusion coefficient of $7 \cdot 10^{-11}$ m^2 s^{-1} is assumed for the realistic estimate, while 3×10^{-10} m^2 s^{-1} is assumed for the conservative case. These values are quoted for chemically analogue transition metals such as Ni and Co in Nagra 2014b (Tab. A3.4-6, p. A-92).

As in Bradbury et al. (2014), all the dissolved Fe entering the bentonite is consumed by conversion of montmorillonite into an Fe-silicate. For the sake of comparability, the same volumetric and mass data given in App. B2.1 (Tab. B1) of Bradbury et al. (2014) are used. The calculations are performed for a spent fuel canister and transformation of the released Fe to the 1:1 Fe-silicate berthierine. Both assumptions are conservative, as (i) the spent fuel canister is larger than the vitrified waste canister, thereby maximising the Fe release rate, and (ii) transformation to berthierine consumes about three times more Fe than chamosite (Fe-chlorite). Formation of the latter phase is unlikely in any case, as the laboratory data indicate that formation of Fe-chlorites requires high temperatures beyond those established in the repository (Section 8.2.1).

The results of the new estimations are summarised in Tab. 8-3. As expected, much lower percentages of bentonite alteration are predicted compared to the mass balance calculations of Bradbury et al. (2014). Using the "reference case" Fe concentration at the outer boundary (realistic estimate), only about 3% of the bentonite would be altered after 1,000,000 years, i.e. 97% of the bentonite would not be affected by Fe alteration. Even in the conservative case, in which a much higher Fe concentration gradient and a larger effective diffusivity are assumed,

more than 80 % of the bentonite would would remain intact after 1,000,000 years. These calculations thus indicate that a loss of the safety function of the compacted bentonite due to Fe-alteration is very unlikely.

Tab. 8-3: Estimation of percentage of bentonite altered, assuming steady-state Fe diffusion with fixed concentrations at the canister/bentonite and bentonite/Opalinus Clay boundaries, compared with the results of the previous mass balance model

Bradbury et al. (2014)

Time [a]	**Realistic estimate** $D_e = 7 \times 10^{-11}$ m^{2}s^{-1} $C_1 = 7.22 \times 10^{-5}$ M $C_2 = 2.56 \times 10^{-5}$ M	**Conservative estimate** $D_e = 3 \times 10^{-10}$ m^{2}s^{-1} $C_1 = 7.22 \times 10^{-5}$ M $C_2 = 7.14 \times 10^{-6}$ M	**Bradbury et al. (2014)***
10,000	0.03%	0.16%	15%
100,000	0.3%	1.7%	100%
1,000,000	2.8%	16.5%	100%

* Values extracted from Fig. 7-1 in Bradbury et al. (2014), upper-left plot. Assumption: all Fe released by a canister corroding at 1 μm/a is transferred to bentonite and converted to berthierine.

8.3 Corrosion of steel in contact with bentonite

8.3.1 Introduction

Section 8.2 was devoted to the potential effect of Fe corrosion on the chemical alteration of the bentonite buffer. In this section the focus is on the "opposite" process, i.e. on how the presence of bentonite may affect the corrosion of the HLW disposal canister made of carbon steel. The two topics are not always clearly distinguishable, as most of the results come from the same experiments and even the same samples presented in Section 8.2. Here, a summary of this topic is presented, again distinguishing laboratory-scale and in-situ experiments in underground facilities.

8.3.2 Laboratory-scale experiments

Several types of experiments were carried out, mostly involving steel samples in contact with COx claystone or MX-80 bentonite.

Schlegel et al. (2014) monitored the in-situ corrosion of ferrite iron samples inserted into a block of COx claystone saturated with porewater. Two configurations were studied, one with and the other without glass specimens (simulating vitrified radioactive waste). The experiments were run under anoxic conditions at 90 °C for over two years. After dismantling, the corroded surfaces of the iron samples were studied using X-ray tomography, SEM-EDS, Raman micro-spectroscopy, micro XRD, and μ-XAFS, yielding similar (though not identical) results for the two configurations. In the most corroded zones, a suite of alteration products was found: a discontinuous inner layer of magnetite in contact with unreacted iron, followed by an intermediate layer of chukanovite, $Fe_2CO_3(OH)_2$, (but only for the test with glass), and an outer layer of Fe-silicates. In less corroded areas, only Fe-silicates were found. More externally, near the former external boundary of the iron surface, a compact mass of secondary products developed, consisting of

ankerite, $(Fe,Ca,Mg)CO_3$, progressively intermixed with clay minerals towards the claystone matrix. The mineralogy of the Fe-silicates could not be determined; however, the comparison of the Si K-edge μ–XAFS spectra with linear combinations of reference spectra gave best fits for mixtures of berthierine, chamosite, minnesotaite and montmorillonite.

Schlegel et al. (2019) repeated similar tests using carbon steel rods inserted into holes drilled in COx clay. The setup was saturated with synthetic COx water in a high-pressure cell, at a constant temperature of 90 °C for a duration of 6 years. Post-mortem analyses revealed, in addition to other corrosion products, formation of an Fe-silicate phase accumulated in depressions of the corroded steel surface (possibly nontronite, $Na_{0.3}Fe_2(Al_{0.3}Si_{3.7})O_{10}(OH)_2$, based on the Si K-edge μ-XAFS spectra).

Le Pape et al. (2015) investigated the corrosion of an iron foil at 90 °C. On one side, the foil was in contact with a clay slurry soaked in a moderately saline solution (0.0207 m NaCl and 0.0038 m Ca_2Cl); on the opposite side it was in contact with humid N_2 gas. At the end of the 2 month test, the side exposed to the gas was covered with magnetite, which was explained as a corrosion product resulting from anaerobic reaction between Fe and water vapour present in the anoxic N_2 atmosphere. At the interface with the clay slurry, a sequence of precipitates was observed. A greenalite-like Fe-serpentine, probably in association with a few magnetite crystals, was formed directly on the iron foil surface. Further away from the surface, a heterogeneous precipitate of spherical serpentine particles was found, with variable amounts of Al replacing Fe in the octahedral layer.

Lotz et al. (2021) studied the corrosion of two different steel types in contact with MX-80 bentonite at 120 °C for a duration of 30 days. The steel coupons were corroded in an evacuated autoclave filled with synthetic, carbonate-free COx water with 30 wt.% of MX-80 bentonite. After the experiment, an inner corrosion layer consisting mainly of magnetite and an outer layer characterised by the presence of Fe-Si-Al-O phases were observed. SEM-EDS and HR-TEM analyses yielded compositions compatible with Fe-bearing serpentine and hydrated smectites.

Kaufhold et al. (2015) investigated the anaerobic corrosion of iron pellets in contact with 40 different types of bentonite gels. The corrosion tests were carried out at 60 °C for a duration of 6 months. After the experiments, the mass loss of the iron pellets was determined as a measure of corrosion and correlated with different parameters characterising the bentonites (e.g. chemical composition, exchangeable cations, layer charge and densities of the smectites, smectite content). The main outcome was that the iron pellets in contact with bentonites containing high-layer-charge smectites were less corroded than those in contact with bentonites containing low-layer-charge smectites. Moreover, Fe corrosion was slightly weaker for iron pellets in contact with Na-bentonites compared to those in contact with Ca-bentonites.

In a follow up study, Kaufhold et al. (2020b) repeated the former Fe corrosion tests at 80 °C, using six bentonites selected on the basis of different smectite layer charges and the absence of any other Fe-containing minerals. Magnetite and Fe-silicates were the main identified corrosion products observed after completion of the tests. Moreover, an increase in total Fe and Fe^{2+} was observed in the bentonites, which was explained as the result of the reduction of structural Fe^{3+} in the smectites by H_2 produced via anaerobic Fe corrosion. This process would destabilise the smectite and release the silica needed for the formation of the observed Fe-silicates. Kaufhold et al. (2020b) stated that the enhanced corrosion of iron in contact with low-layer-charge smectites can be explained by the fact that the Fe^{3+} in the clay is more easily reducible in the latter compared to high-layer-charge smectites (see also Gorski et al. 2013). This would lead to greater consumption of H_2 and Fe^{2+}, accelerating the steel corrosion.

In another study, Kaufhold et al. (2020a) investigated two different Ca-bentonites, one with low (0.5 wt.%), the other with high (1.7 wt.%) amounts of reactive silica (opal, which is more soluble than quartz or cristobalite). Bentonite gels were brought into contact with iron pellets and kept under anoxic conditions at 80 °C for up to 30 days. Fe-silicates (probably of the serpentine group) and Fe-oxides were detected in both bentonites. Formation of Fe-silicates was, however, clearly favoured in the sample with the higher content of reactive silica, whereas at low contents of reactive silica magnetite was the predominant end-corrosion product. The authors concluded that the availability of silica has a strong influence on the reaction route of the Fe corrosion process.

In a further series of experiments, Kaufhold et al. (2021) measured the pH evolution in four different carbonate-free bentonites mixed with Fe powder and saturated with deionised water. The tests lasted for 100 days and were carried out at room temperature. Conditions within the reacting mixture remained anoxic, as shown by nearly identical pH evolutions in samples kept inside and outside an anoxic glovebox. Values of around pH 9 were established for the samples with Ca-Mg bentonites, while about pH 10 was attained in samples with Na-bentonites. Based on studies on the stability of smectite minerals under alkaline conditions, Kaufhold et al. (2021) argued that pH values of 10 or less would not be sufficient to destabilise the smectites. Therefore, such a moderate increase in the initially near-neutral pH should not affect iron corrosion rates. The authors concluded that the effect of reductive dissolution (as shown for low-layer-charge smectites in Kaufhold et al. 2020b) should be the more important process leading to enhanced steel corrosion.

Cheshire et al. (2018) investigated the corrosion of low-carbon and stainless steel in contact with Wyoming bentonite saturated with a dilute K-Ca-Na-Cl solution, however at much higher temperatures and pressures (up to 300 °C at 15 – 16 MPa) than expected in the planned Swiss HLW repository. Bentonite and aqueous solution were loaded in a 9:1 mass ratio into gold reaction cells together with Fe_3O_4 grains, iron filings and stainless/low-C steel plates. After 4 weeks to 6 months, the steel plates were removed and examined using XRD, SEM-EDS and EPMA. Generally, four corrosion layers were found, starting from the reacting intact Fe surface outwards: (1) an $FeCr_2O_4$-like spinel phase, (2) Si-Cl-S mixed phases, (3) discrete pentlandite, $(Ni, Fe)_9S_8$, and millerite, NiS, (4) an outermost layer consisting of Fe-saponite, $M_{0.33}Fe_3(Si_{3.67}Al_{0.33})O_{10}(OH)_2$, with minor chlorite. Except for saponite, these corrosion products, particularly the sulphide and spinel phases, are typical of hydrothermal conditions and are not expected to form under the conditions in the Swiss HLW repository.

8.3.3 Large-scale in-situ experiments

An experiment dedicated to the study of canister corrosion was conducted at the Mont Terri Rock Laboratory in Switzerland (IC, Iron Corrosion Experiment), mainly aimed at determining the corrosion rate of carbon steel, but also including mineralogical characterisation. Carbon steel samples were placed in direct contact with in-situ Opalinus Clay and corroded at 90 °C during 7 years. Necib et al. (2018) reported formation of several iron corrosion products on the surface of carbon steel: magnetite, akaganeite, β-$Fe_2(OH)_3Cl$, chukanovite, siderite, goethite, lepidocrocite, Fe-sulphides and an unidentified iron silicate. In the first carbon steel samples retrieved after 20 months interaction from the (currently ongoing) follow-up IC-A experiment, magnetite, haematite, and an oxyhydroxide were detected as corrosion products (Necib et al. 2018). Preliminary SEM-EDS results indicate Si and Al enrichments on the corroded steel surface, interpreted as residues of bentonite rather than newly formed alteration products. Smart et al. (2017b) detected minor changes in the Fe(III) content in the adjacent montmorillonite, but no new phases.

Kaufhold et al. (2018) investigated the contact zone between steel heater and bentonite at the end of the FEBEX-DP experiment at the Grimsel Test Site (after 18 years interaction, see also Section 8.2.2). They identified goethite, siderite and magnetite in corrosion crusts formed on the

steel. In addition, they observed newly formed brucite and Mg-rich trioctahedral domains within the smectite of the bentonite in direct contact with the front of the heater (where no visible steel corrosion was observed). Limited to these regions, a marked decrease in CEC compared to the intact bentonite was measured (by almost 40%). In addition, exchanged Na^+ was partially replaced by Mg^{2+}. Predominantly oxic corrosion, explained by air entrapment between heater and liner during emplacement, was observed at the bentonite/steel liner interface, characterised by a reddish colour and formation of goethite.

Finally, data are available from the Materials Corrosion Test (MaCoTe) at the Grimsel Test Site, started in 2014 and still ongoing (Reddy et al. 2021a). The purpose of this test is to investigate the in-situ corrosion of various candidate canister materials in the presence of compacted bentonite. The experiment consists of eight cylindrical modules containing compacted bentonite of 1,250/1,500 kg m^{-3} dry density intercalated with metal coupons (carbon steel, stainless steel, and copper) open to access of granitic porewater. The experimental setup is very similar to that of the IC-A experiment at the Mont Terri Rock Laboratory (Necib et al. 2018), however the tests were carried out without heating, i.e. at an ambient temperature of 13 °C. Preliminary data on samples retrieved 394 days after the start of the experiment show a black staining, as well as enrichments in S, Al and Ca in the bentonite directly in contact with the steel. This thin black zone is followed by an Fe-rich reddish-brown front extending about 1 mm further into the bentonite. Fe enrichments were found to be heterogeneously distributed, forming discrete paths radiating from the steel coupons into the bentonite, associated with microfractures formed during the evolution of the system. The microfractures are interpreted as the result of partial dehydration and shrinkage due to water consumption during the anaerobic corrosion of iron. XRD analyses of bentonite adjacent to the carbon steel revealed d_{060} spacings practically identical to those of non-altered bentonite (1.496 – 1.497 Å), indicating that neither alteration of the dioctahedral mont-morillonite structure nor formation of new clay minerals occurred in this initial phase of the experiment.

8.4 Summary and conclusions

Small-scale experiments conducted in the laboratory usually yield results that cannot be directly extrapolated to repository conditions. This is mainly a consequence of the preferred use of highly reactive Fe powders and unrealistically high Fe/clay mass ratios. In contrast, setups of large-scale experiments conducted in underground laboratories attempt to reproduce repository conditions as closely as possible (realistic canister and buffer materials in the appropriate size, geometry and Fe/clay ratios, embedded in the host rock selected for the planned disposal site). In such tests, the higher temperatures expected in the repository are frequently reproduced by means of heating systems, increasing the level of relevance for the assessment case. The results of such large-scale in-situ experiments are thus more representative and provide the basis for the following summary of evidence and conclusions.

Based on the FEBEX and ABM experiments, Wersin & Kober (2017) and Hadi et al. (2017) proposed the following evolution for the steel/bentonite interface under repository-like conditions:

Phase 1: Corrosion of steel under unsaturated, initially aerobic conditions leads first to formation of Fe(III) oxides. The transport rates of O_2 and H_2O to the unreacted steel surface is progressively reduced as the corrosion layer increases in thickness and density.

Phase 2: As O_2 no longer reaches the reacting interface, the steel continues to corrode anaerobically. This leads to release of dissolved Fe(II) and formation of magnetite and siderite in the internal part of the corrosion layer. Moreover, electron transfer across the corrosion layer leads to the generation of Fe(II) at the interface between corrosion layer and bentonite, which then dissolves and reacts with residual O_2 to produce further Fe(III) oxy-hydroxides at the external side.

Phase 3: Once O_2 is totally consumed, anaerobic steel corrosion, generation of Fe(II), formation of magnetite and siderite, and rapid electron transfer across the corrosion layer all proceed simultaneously. Fe(II) diffuses into bentonite, sorbing on smectite and possibly interacting with structural Fe(III).

No signs of smectite destabilisation or formation of iron-rich silicates due to steel corrosion could be observed, either in the FEBEX or in the ABM experiments. In laboratory-scale experiments accelerated by using reactive Fe powder, formation of Fe-silicates is frequently observed, suggesting that similar phases may form in a repository setup over geological timescales. In addition, the experiments of Kaufhold et al. (2020b) show that formation of Fe-silicates is enhanced by the presence of reactive silica[26] (e.g. opal) occasionally found in the bentonite instead of, or in addition to, quartz or cristobalite. Because opal is generally XRD-amorphous, the occurrence of opal-containing bentonite could be more frequent than generally assumed (Önal et al. 2007). The implication is that formation of Fe-silicates at the interface with a steel canister cannot be excluded even if bentonites are used in which no XRD-visible silica has been detected.

For the above reasons, extensive transformation of montmorillonite to Fe-silicates, which could impair the bentonite buffer functionality, cannot be excluded categorically. It is therefore necessary to provide estimates of the potential extent of such transformations in the long term. To this end, the former exceedingly conservative mass balance calculations of Bradbury et al. (2014) have been updated by applying a new estimation method (App. A) relying on out-diffusion of soluble Fe(II) combined with in-situ precipitation of Fe solids at saturation equilibrium. The new calculations point to maximum degrees of bentonite alteration of 1.7% and 16.5% after 100,000 and 1,000,000 years from resaturation, respectively, assuming conservative Fe concentration gradients and diffusivities. Applying more realistic parameters (reference case) reduces these figures to 0.3% and 2.8%, respectively. These calculations indicate that at least ~ 80% of the initial bentonite would remain intact after 1,000,000 years from repository closure even in the conservative case, excluding a loss of buffer functionality.

The collected experimental evidence shows a clear dependence of the Fe-silicate mineralogy on temperature. At 80 – 90 °C, the formation of the kaolinite-serpentine (1:1) Fe-rich clay minerals predominates. At 150 °C, formation of Fe-saponite (trioctahedral smectite) was observed in addition to the latter and, at 300 °C, Fe-chlorite or mixed-layer chlorite interstratified with smectite and/or corrensite become stable. The laboratory experiments demonstrate that Fe-silicates are stable over a wide range of temperatures, suggesting that, although they are not observed in (short-term) field experiments, they could well form during the long-term repository evolution. On the other hand, the results of most experiments seem to confirm that the original (swelling/sorbing) properties of the smectites in bentonite are not significantly altered by the uptake of Fe(II) at repository-relevant temperatures. This implies that interaction of Fe(II) with montmorillonite will not compromise the radionuclide retention and rheological properties of the bentonite buffer.

---

[26] Opal and amorphous silica are more reactive than crystalline silica phases due to their larger specific surface area and solubility products.

9 Chemical interactions of reprocessed high-level waste and spent fuel with surrounding near-field materials

9.1 Introduction

In this chapter, specific chemical effects arising from the chemical interaction between the dissolving waste matrix (spent fuel or borosilicate glass) and the surrounding engineered barrier materials are addressed. Other subjects related to waste matrix degradation, namely the mechanisms and kinetics of dissolution and radionuclide release, are not discussed as they are treated in two separate reports (Johnson et al. 2023, Curti 2022).

More specifically, the present chapter has a dual purpose:

- To illustrate the chemical evolution inside a failed canister after saturation with porewater infiltrated from the bentonite buffer, either in contact with spent fuel (Section 9.2) or vitrified waste (Section 9.3). This task is achieved by calculating the aqueous and solid speciation at thermodynamic equilibrium with the reacting materials (spent fuel or glass, encasing structural materials and the HLW disposal canister made of carbon-steel).
- To determine the aqueous speciation of the water inside the canister in the presence of boron released from the dissolution of vitrified RP-HLW, including the effect of borate complexes on the solubility limits of considered dose relevant radionuclides[27].

For the calculations involving vitrified waste, experimental data from long-term glass dissolution experiments (Curti et al. 2006) were used to estimate the boron concentrations that could build up inside the canister. As boron is not included in the list of critically reviewed elements for the TDB2020 update of Hummel & Thoenen (2023), a correlation method from the literature (Bousher 1995) was applied here to estimate the formation constants of borate complexes. These constants were then implemented into the GEM-Selektor model used for the calculation of porewater composition inside the HLW disposal canister.

9.2 Assessment of "inside canister" chemistry during spent fuel dissolution

9.2.1 Introduction

Knowledge of the chemical conditions at the interfaces between spent fuel, waste package materials and the partially corroded HLW disposal canister is essential, since both spent fuel dissolution kinetics (and thus radionuclide release rates) as well as radionuclide solubility limits are sensitive to local chemical parameters such as pH, Eh, ligand concentrations. Indeed, these parameters may affect the stability of solubility-limiting solids, for instance the solubility of UO_2 is known to increase in oxidising, carbonate-rich solutions due to formation of strong U(VI)-carbonate complexes (Grenthe et al. 2004). Moreover, the type of secondary solids limiting the solubility of redox-sensitive nuclides may change as a function of Eh and pH. Therefore, it can be anticipated that the evolution of Eh and pH inside the canister will largely determine the source-term functions of radionuclide release from spent fuel to the near-field.

Reliable predictions of chemical conditions inside a failed canister filled with water penetrating from the bentonite buffer are difficult, because of the complexity and heterogeneity of the system.

---

[27] This evaluation is of relvance, because – due to lack of reliable thermodynamic data – the release of boron from the glass is generally ignored in calculations of near-field porewater chemistry, although it is one of the major soluble elements released during vitrified waste dissolution and a potential complexant of radionuclides.

It includes a large number of elements distributed over different materials in close vicinity to each other (spent fuel, Zircaloy, steel canister and other structural materials). Moreover, concurrent localised chemical processes operate simultaneously, increasing the complexity. For instance, α–radiation from the fuel will induce radiolysis in a few µm-thick layer of water in direct contact with the spent fuel surface. This may potentially lead to oxidising conditions and lower the pH close to the fuel surface, and thus adversely affect spent fuel dissolution rates. On the other hand, there is ample experimental and theoretical evidence that dissolved molecular hydrogen, continuously released from the corroding canister over hundreds of thousands of years, will be catalytically activated at the surface of spent UO_2 and MOX fuel. The activated hydrogen will react with the oxidants (mainly oxygen peroxide) generated by alpha radiolysis, thus suppressing any oxidation of U(IV) to U(VI) at the fuel surface. This mechanism ensures that spent fuel dissolution rates will remain very low during the entire evolution of the HLW repository (see Chapter 5 in Johnson et al. 2023 for details on this topic).

Other potential complications are the consumption of water via anaerobic Fe corrosion, which could temporarily and locally provide desaturated conditions and increase salinity (Leupin et al. 2021), and inhibition of redox reactions such as sulphate and carbonate reduction in the absence of microbial activity. Finally, some radionuclides are likely to be trapped in solid solutions. A reliable determination of solubility limits at equilibrium with solid solutions is however possible only in exceptional cases, when mixing parameters are known for all ions occupying a given site in the solid solution (e.g. ^{226}Ra in ternary Ba-Sr-Ra sulphates, see Curti et al. 2010 and Vinograd et al. 2018).

In the present model, fully saturated conditions inside the HLW disposal canister are assumed and the potential effect of water radiolysis is ignored, based on the previously discussed evidence that molecular hydrogen from canister corrosion will protect the fuel surface from radiolytic oxidation. The modelling involves batch thermodynamic calculations, using only selected data of the TDB2020 database (Hummel & Thoenen 2023) and formation of stoichiometric solids (i.e. without solid solutions, as for the BPW and OPAw models). Aqueous and solid speciation are determined by equilibrating *kinetically scaled* amounts of the interacting materials (fuel, encasing structural materials and carbon-steel canister) with bentonite porewater filling the canister cavity. *Kinetically scaled means* indicates that the amounts of materials allowed to react with the water are proportional to the respective degradation rates (see Section 9.2.2).

Boundary/initial conditions, near-field geometry and chemical inventories of the materials are based on the current reference repository setup (see Chapter 2 , Chapter 3 and Chapter 4). The major aim is to provide an update of analogous calculations carried out within the framework of SGT-E2 (Bradbury et al. 2014, Section 9.5) taking into account the (partly revised) chemical inventories of the involved materials, revised thermodynamic data and the specific degradation rates of the reacting materials.

9.2.2 Model description and assumptions

A major aim of these calculations was to take into account the chemical complexity of all the materials present. Because differences in the chemical inventories of the six waste types specified in Chapter 3 of Johnson et al. (2023) are small, it was not judged necessary to carry out calculations for all waste sorts. Calculations were thus performed only for BE-L-UO2-U-HAA (Leibstadt), as reported in the MIRAM14 inventory for Zircaloy, structural materials and spent fuel (the latter with a simplified chemical composition[28]). For the HLW disposal canister, the carbon-steel composition specified by (Nagra 2024b) and reported in Tab. 4-2 was used.

Conservatively, it is assumed that bentonite porewater (E3-BPW-Ref-uncharged composition, Tab. 7-6) will intrude "instantaneously" and fill all empty cavities inside the packed HLW disposal canister once it is breached (saturated conditions). It is further assumed in the model that the spent fuel cladding (Zircaloy) has failed and offers no transport resistance, implying that the E3-BPW-Ref water will immediately interact with all exposed material surfaces, i.e. spent fuel, Zircaloy, carbon-steel canister and other structural materials. To account for partial corrosion prior to failure, the chemical composition of the canister is taken to consist of a 1:1 mixture of magnetite and intact carbon-steel.

Based on the provisional HLW disposal canister design (Nagra 2024b), the empty space in the intact loaded canister is 2 m^3 for PWR fuel (4 assemblies/canister) and 1.7 m^3 for BWR fuel (12 assemblies/canister). In the model, the void volume is conserved and completely filled with water. This is a conservative assumption, because in reality the free volume may be largely reduced through formation of Fe corrosion products (which have a much higher molar volume than carbon steel), thereby restricting the transport of solutes to or from the bentonite buffer.

In the calculations, carried out using version 3.9.0 of the GEM-Selektor code (Kulik et al. 2013) with data from the recently updated PSI-Nagra database TDB 2020 (Hummel & Thoenen 2023), predefined amounts of the solids (spent fuel, Zircaloy, canister, structural materials) are allowed to equilibrate with BPW filling the empty spaces in the canister interior. As already mentioned, the amounts of solids and water allowed to react with the intruded bentonite water were *kinetically scaled*, i.e. the amounts of each solid material involved in the equilibration were specified in proportion to its own corrosion rate and to the diffusive flux of water from the bentonite. The scaling procedure is in detailed described in Johnson et al. (2023), Section 3.5.

Briefly, we first determined the diffusive water flux integrated across the bentonite/waste package interface. This value was estimated at 1.1×10^{-4} mol s^{-1} based on a mean water self-diffusion coefficient of 5.97×10^{-11} m^2 s^{-1} obtained from experimental data on the diffusion of tritiated water in compacted bentonite (Bestel et al. 2018). At this flux, the initial water and solutes filling the void volume inside the canister (1.7 m^3) will be exchanged (without any advection) within 28.2 years under the hypothetical assumption of a steady-state flux. At a corrosion rate of 2 μm/a (Diomidis et al. 2016) and constant water flux, the mass fraction of steel canister material corroded during a single "water renewal cycle" was then calculated to be 4.03×10^{-4} [-] inside the canister, which defines the amount of canister material allowed to react with a unit water volume (1 L) filling the canister space. The mass fractions of reacting spent fuel, Zircaloy and structural materials were then calculated by scaling with a factor equal to the ratio of the respective corrosion

[28] The following approximations were made: (i) UO_2 spent fuel is treated as a mixture of UO_2 and PuO_2 with a standardised fission product and actinide inventory for a burnup of 60 GW/t_{iHM}; (ii) Cr and Cu inventories in structural materials were ignored as these elements are not included in the TDB2020 database (Hummel & Thoenen 2023).

rate to the carbon steel corrosion rate (see details in Section 3.7.2 of Johnson et al. 2023). Because all these materials degrade more slowly than the canister, the resulting mass fractions are much smaller than 4.03×10^{-4}.

In the simulations, the scaled amounts are equilibrated with E3-BPW-Ref-uncharged water, assuming either unconstrained or externally imposed pCO_2 (see Section 9.2.3). Based on the experimental evidence that sulphate reduction and methanogenesis are inhibited in the absence of microbial activity at near-field temperatures established at 10,000 years (Section 7.4.5) and considering that the γ-radiation field inside the canister will make microbial life even more unlikely, reduction of carbonate and sulphate species was intentionally suppressed.

9.2.3 Results of speciation calculations

Two distinct cases were calculated (Tab. 9-1), differing only in the treatment of the gas phase. In the calculation denoted "INCAN 2a_3", thermodynamic equilibrium is computed without setting any constraint on the gas phase, specifically without requiring an externally imposed pCO_2. This assumption implies that no exchange of dissolved gaseous species (CO_2 or any other dissolved gas component) can take place between the water inside the HLW disposal canister and the porewater permeating the bentonite buffer. In other words, the chemical system inside the canister is assumed to be closed to transfer of CO_2 (and also H_2) to or from any external reservoir. This calculation yields a mildly alkaline, strongly reduced solution (pH 8.4, Eh = -495 mV) in equilibrium with H_2-rich and CO_2-poor gas ($pH_2 = 10^{-0.03}$ bar, $pCO_2 = 10^{-4.5}$ bar). The pCO_2 resulting from the internal equilibrium is more than two orders of magnitude lower than the fixed value assumed in the reference case BPW calculations ($pCO_2 = 10^{-2.2}$ bar), implying that CO_2 would diffuse from the bentonite towards the canister hull if the system were "opened" to gas transfer.

The calculation denoted "INCAN 2a_2 is identical to the former, except that an externally imposed pCO_2 of $10^{-2.2}$ bar equal to that of E3-BPW-Ref water is implemented. There will therefore be no tendency for CO_2 diffusion from or to the bentonite buffer, since the two compartments are in mutual pCO_2 equilibrium. In this case, the equilibrated solution inside the HLW disposal canister has similar concentrations and characteristics to the intruding BPW, specifically a nearly neutral pH, a moderately reducing Eh and a low hydrogen partial pressure.

The two calculations can be regarded as opposite limiting cases of the expected chemical evolution inside the HLW disposal canister. "INCAN 2a_3" simulates short-term equilibration soon after canister failiure and filling of the canister cavity, before CO_2(aq) from the bentonite porewater diffuses in, while INCAN 2a_2 represents long-term equilibrium conditions after annihilation of the initial CO_2(aq) gradient when iron corrosion is almost complete and the generated hydrogen has escaped.

The results of "INCAN 2a_3" represent an update of the analogous calculation presented in Tab. 9-3 of Bradbury et al. (2014). The comparison of the two calculations shows, somewhat surprisingly, significant differences ascribed to a combination of factors: different compositions of the incoming BPW, different types and amounts of reacting solid materials (e.g. carbon-steel instead of stainless steel), different volumes of the water-filled canister cavities, and the updated thermodynamic data. A much lower equilibrium phosphate concentration is predicted in "INCAN 2a_3" due to the lower P contents in the updated steel formulation (Tab. 4-2) and following improvements in the thermodynamic data for this element. Specifically, the precipitation of Ca-phosphate (apatite), a mineral that has been newly included in the TDB2020 database (Hummel & Thoenen 2023), now limits the dissolved P concentration to the nanomolar range. In the calculation of Bradbury et al. (2014), this saturation equilibrium was not included, with the consequence that unrealistically high phosphate concentrations in the millimolar range were calculated. A side-result of such high P concentration was the exceedingly low predicted Pu

solubility controlled by $PuPO_4$ (< 10^{-12} mol/kgw). Note that, in spite of the lower P concentration in the steel, in the present update $PuPO_4$ remains the solubility-limiting phase for Pu; however due to the lower P concentration the Pu solubility is now higher and more realistic (~ 6×10^{-8} mol/kgw).

Compared to Bradbury et al. (2014), considerably lower U concentrations ($9 \times 10^{-10} – 3 \times 10^{-11}$ mol/kgw instead of 3.5×10^{-9} mol/kgw) are predicted, and precipitation of coffinite ($USiO_4$) instead of U(IV) hydrous oxide occurs. The discrepancy is mainly a consequence of new thermodynamic data for coffinite in the TDB2020 update (see Section 6.3 in Johnson et al. 2023 for details). The solubility limits of other dose-relevant elements reported in Tab. 9-1 remain in most cases identical to those predicted in Bradbury et al. (2014).

As previously mentioned, in the present calculations only equilibrium with stoichiometric solids was considered. This explains the considerably higher Ra concentrations (3.5×10^{-8} mol/kgw, equilibrium with pure $RaSO_4$) compared to the value of 2×10^{-10} mol/kgw calculated at equilibrium with $(Ra,Ba)SO_4$ solid solution by Bradbury et al. (2014).

An objective of the present calculations was to determine the elemental solubility limits of dose-relevant radionuclides in the water inside the canister, for the purpose of comparison with those determined in bentonite porewater, which are used in safety assessment calculations (*cf.* Hummel et al. 2023). A detailed discussion of the results is provided in Section 3.8 in Johnson et al. (2023). It should be noted that, in some cases, however (Cs, Am, Ra, Sr, Np and Se), the amount of a given element released through reaction of the "scaled amount" of spent fuel with BPW was insufficient to reach saturation with any solid. Therefore, for these elements (except for Cs[29]), small arbitrary amounts of the element were "added" in the input in order to reach the elemental solubility limit. Note that since this procedure was not adopted in Bradbury et al. (2014), the concentrations obtained for Am, Ra, Sr, Np and Se in the two calculations are not comparable.

[29] Cs is very soluble. Under the expected repository conditions, Cs aqueous concentrations will not be solubility-limited.

Tab. 9-1: Results of speciation calculations to determine aqueous, gas and solid equilibria in the water filling the open space inside a failed HLW disposal canister loaded with BWR UO_2 fuel, compared with the initial composition of the reacting bentonite porewater

	E3-BPW-Ref-uncharged (reacting BPW)	**INCAN 2a_2 constrained pCO_2**	**INCAN 2a_3 unconstrained pCO_2**
IS(m)	0.434	0.434	0.432
pH	7.25	7.24	8.40
Eh(V)	-0.175	-0.222	-0.495
log $p(CO_2)$	-2.22	-2.20	-4.51
log $p(H_2)$	-8.58	-6.95	**-0.03**
log $p(N_2)$	-0.008	-0.007	**-1.162**
log $p(O_2)$	-65.9	-69.2	-83.0
Main elements	***mol/kgw***	***mol/kgw***	***mol/kgw***
Al	2.08×10^{-8}	2.08×10^{-8}	2.08×10^{-8}
Ba	6.94×10^{-8}	7.00×10^{-8}	8.34×10^{-8}
C(in)	2.94×10^{-3}	2.94×10^{-3}	2.20×10^{-4}
Ca	1.71×10^{-2}	1.69×10^{-2}	1.64×10^{-2}
Cl	0.239	0.239	0.239
F	1.74×10^{-4}	1.65×10^{-4}	1.65×10^{-4}
Fe	2.05×10^{-5}	7.22×10^{-5}	7.08×10^{-5}
K	1.83×10^{-3}	1.83×10^{-3}	1.83×10^{-3}
Mg	1.02×10^{-2}	1.01×10^{-2}	9.58×10^{-3}
Mn	1.84×10^{-5}	6.21×10^{-5}	5.94×10^{-5}
Na	0.341	0.341	0.341
P	---	9.59×10^{-9}	6.59×10^{-10}
S	7.80×10^{-2}	7.70×10^{-2}	7.78×10^{-2}
Si	1.70×10^{-4}	1.95×10^{-4}	2.06×10^{-4}
Considered dose-relevant radionuclides	***Limiting solid***	***mol/kgw***	***mol/kgw***
Am	$AmOHCO_3w_{0.5}$(cr)	7.61×10^{-8}	2.43×10^{-8}
Cs*	---	1.05×10^{-8}	1.05×10^{-8}
Mo	MoO_2(cr)	1.70×10^{-8}	4.32×10^{-13}
Ni	$Ni(OH)_2$(cr)	1.85×10^{-4}	3.70×10^{-5}
Np	NpO_2(am_hyd)	2.04×10^{-8}	1.07×10^{-9}
Pd	Pd(cr)	3.12×10^{-10}	3.13×10^{-10}

Tab. 9-1: Cont.

	E3-BPW-Ref-uncharged (reacting BPW)	**INCAN 2a_2 constrained pCO_2**	**INCAN 2a_3 unconstrained pCO_2**
Pu	$Pu(OH)_3(am)$/ $PuPO_4(am\_hyd)$	3.61×10^{-8}	6.32×10^{-8}
Ra	$RaSO_4$	3.55×10^{-8}	3.49×10^{-8}
Se	$FeSe_{2-x}(cr)$	8.53×10^{-10}	1.21×10^{-8}
Sn	$SnO_2(cr)$	8.96×10^{-9}	1.71×10^{-8}
Sr	$SrSO_4(cr)$	1.67×10^{-4}	1.64×10^{-4}
Tc	$TcO_2(am\_hyd\_ag)$	2.05×10^{-9}	1.87×10^{-9}
U	$USiO_4(cr)$	8.86×10^{-10}	3.14×10^{-11}
Zr	$ZrO_2(cr)$	6.23×10^{-10}	6.23×10^{-10}

* The reported aqueous Cs concentrations result from total dissolution of the ^{135}Cs inventory present at an assumed canister failure time at 10,000 years after closure in the reacted spent fuel amount. The inventory of waste sort BE-L-UO2-U-HAA (Leibstadt UO_2 fuel) specified in the MIRAM14 (Nagra 2014a) database was used.

An interesting result of the calculations is that equilibrium U concentrations are predicted to depend on the pCO_2 conditions established inside the HLW disposal canister. Shortly after canister failure (INCAN_2a_3), a very low equilibrium pCO_2 of $10^{-4.51}$ bar is calculated, implying low contributions of U-carbonate complexes. In the long-term (INCAN_2a_2), the CO_2 supply following pCO_2 equilibration with the bentonite pore water would reduce the pH of the water inside the canister and increase the Ca and total carbonate concentration via calcite equilibrium, stabilising ternary Ca-uranium-carbonate complexes and thus leading to a higher U concentration. The predicted increase in U concentration is however minor (from 0.03 to 0.9 nM), in any case negligible compared to the potential effect of radiolytic oxidation. Therefore, it will not have an impact on the dissolution of the spent fuel matrix.

A further notable result of the calculations is that the U(IV) silicate coffinite is predicted to limit uranium solubility instead of amorphous U(IV) oxide. This result is a direct consequence of the new data selected for this compound in the TDB2020 thermodynamic database (Hummel & Thoenen 2023). Considering the still large uncertainties remaining in thermodynamic data for this solid, the question whether coffinite or amorphous UO_2 will be the most stable U(IV) phase in the system of interest cannot be resolved conclusively. This issue is not purely academic, considering the potential consequences of coffinitisation on spent fuel dissolution kinetics and radionuclide release (see Chapter 6.3 in Johnson et al. 2023).

If sufficient dissolved silica were available, extensive transformation of UO_2 to coffinite may conceivably occur. The comparison of bentonite porewater (Tab. 7-3) and “inside canister” water compositions (Tab. 9-1) however indicate similar silica concentrations in both compartments, as imposed by saturation equilibrium with an SiO_2 phase (quartz). This implies negligible fluxes of Si from bentonite towards the fuel (if any), provided that the buffer material does not contain large amount of reactive silica, e.g. opal (cf. Section 8.4). Under such circumstances, extensive coffinitisation of spent fuel can be ruled out.

9.3 Effect of RP-HLW dissolution on near-field chemistry

9.3.1 Introduction

The chemical environment inside a failed HLW disposal canister containing vitrified RP-HLW will be similar to that inside a spent fuel canister, particularly with regard to the highly reducing conditions, Fe(II) supply and hydrogen production provided by the degradation of the HLW disposal canister made of carbon-steel. As for spent fuel, the glass is encased in a slowly corroding metallic envelope (stainless steel instead of Zircaloy), for which - although it could serve as an additional protective barrier - no credit is given in safety assessment calculations. Water radiolysis also takes place, but this process is weaker than in the case of spent fuel due to the much lower content of alpha emitters in vitrified waste and is not expected to affect the kinetics of glass dissolution in the long term (see Section 4.3.3.3 in Curti 2022).

In spite of such analogies, the chemical environment in the vicinity of the two types of waste will be significantly different due to the higher reactivity of borosilicate glass compared to UO_2/MOX spent fuel. After containment failure and water intrusion, RP-HLW will release considerable amounts of boron, molybdate and alkalis into the solution. The release of these soluble components will be of relevance shortly after the first contact between water and vitrified waste, due to the initial fast kinetics of borosilicate glass (in the order of 0.1 g m^{-2} d^{-1}, see Curti 2022).

Glass dissolution rates are then expected to decrease by 3 – 4 orders of magnitude due to silica saturation effects and the formation of a passivating nanoporous “gel layer” at the glass/water interface. However, uncertainties remain regarding the timing and extent of such a decrease in glass corrosion rates. The presence of large amounts of iron and iron corrosion products has been shown to maintain high corrosion rates in laboratory experiments simulating (at small scale) repository near-field conditions up to the end of leach tests lasting two years (Rébiscoul et al. 2015). Moreover, recent experiments with radioactive glass doped with rapidly decaying alpha emitters indicate that the alpha dose accumulated in the vitrified waste up to realistic canister failure times leads to enhanced glass dissolution rates compared to the non-active vitrified waste simulants normally used in leach experiments (Tribet et al. 2021). Even in the long term, small amounts of soluble glass components will be continuously released to the near-field at low rates because there is no thermodynamic solubility limitation for glass (glass is a metastable phase in aqueous solutions). These topics are treated thoroughly in a separate report by Curti (2022), to which the reader is referred for more details.

Soluble elements released from the glass such as B, Mo and Li interact only weakly with solid phases and may therefore reach appreciable concentrations in the water in contact with the glass. Moreover, Mo and B form poorly sorbing anionic species, MoO_4^{2-} and $B(OH)_4^-$, that could act as ligands for actinides and fission products. Li^+ may play a role by forming complexes with anions, particularily with phosphate (Curti et al. 2006). In static leaching experiments with the RP-HLW simulant MW (from reprocessing of UK Magnox waste), total concentrations as high as 65 mM for B and 29 mM for Li have been reached, whereas for Mo a maximum of 0.7 mM was measured (Curti et al. 2006).

Within the framework of SGT-E2, Bradbury et al. (2014) carried out scoping calculations to estimate the effect of boron release from RP-HLW on the solubility of Eu(III), taken as an analogue of trivalent actinides. The estimation was based on the assumption that the borate anion[30], $BO(OH)_2^-$ or $B(OH)_4^-$, behaves as a ligand similarly to silicate, $SiO(OH)_3^-$, therefore the same formation constants as for the corresponding monomeric silicate complexes were assumed for the borate complexes of Eu(III). Based on this crude analogy, Bradbury et al. (2014) argued that *"Eu-borate complexes would be the major dissolved* [europium] *species, even at a relatively low total B concentration of 0.1 mM, which would lead to a doubling of the Eu solubility"* and concluded that *"the issue of radionuclide complex formation with borate is still unresolved"*. The estimation made in Bradbury et al. (2014) was indeed not conclusive and presumably overconservative, since it did not include the effects of borate complexes of other major cations, i.e. all dissolved borate was assumed to be available for the formation of Eu(III) complexes and possible sharing with borate complexes of other cations present in the water was ignored. Moreover, the calculation did not consider the full speciation for the environment of interest and thus did not account for possible chemical cross-effects.

In this section, an updated assessment of the influence of boron released from RP-HLW waste on the near-field chemistry is presented, considering boron complexes of all major cations and a full speciation inside the canister. The main aim is to determine the effect of boron release and complexation on the solubility of dose-relevant radionuclides. Because boron was not part of the TDB2020 update, empirical methods were used to estimate borate formation constants.

9.3.2 Modelling approach

To predict the chemical environment inside a HLW disposal canister containing RP-HLW, we applied the same model as presented in Section 9.2 for the spent fuel canister, but considering in addition the release of soluble elements from the MW glass. This was done by adding 65 mM of boron as a mixture of 19.7 mM $B(OH)_3$ and 45.3 mM $NaB(OH)_4$ to the system defined for the INCAN 2a_3 calculation (Tab. 9-1). The added components represent the (simplified) composition of the final solution in contact with the UK MW glass after 12.2 years of corrosion in initially distilled water at 90 °C (see Table 8 in Curti et al. 2006). Na^+ represents the sum of all soluble alkalis (Na^+, Li^+ and to a minor extent K^+)[31]. The assumed B concentrations are conservative and represent a maximum boundary, since the experiments of Curti et al. (2006) were carried out under closed conditions, whereas in a repository setup the released boron would slowly diffuse out into the bentonite, thus mitigating the B concentration levels inside the HLW disposal canister.

With respect to the original calculation for a spent fuel canister, the following effects can be anticipated following the addition of $B(OH)_3$ and $NaB(OH)_4$:

(i) a pH increase, since boric acid/borate is a mildly alkaline pH buffer (pK_a = 9.23 at 25 °C, Manov et al. 1944)

(ii) possibly an increase in solubility of radionuclides forming strong complexes with borate

(iii) a slight increase in ionic strength due to the addition of Na^+ and $B(OH)_4^-$

---

[30] Both formulae are found in the literature for the borate anion. They can be considered as equivalent as they differ by a single water molecule. In the following discussion we adopt $B(OH)_4^-$ for consistency with the discussed literature.

[31] Li^+ was excluded, since this element is not part of the TDB2020 update (Hummel & Thoenen 2023) and has a similar chemical behaviour to Na^+. The concentrations of K^+ measured in the MW glass leachant were minor.

9.3.3 Estimation of borate complexation constants

Borate is by far the most abundant ligand released from the glass and could thus become a major complexant. Because boron was not reviewed in TDB2020 (Hummel & Thoenen 2023) and to our knowledge there is no published review of thermodynamic data for this element, a necessary key step for the modelling of porewater in contact with vitrified waste was the determination of stability constants of monomeric borate complexes, both for radionuclides and major cations. To this end, the estimation method developed by Bousher (1995) was used and is briefly discussed below.

The method is based on the empirical correlation between acid dissociation constants of metal aquaions (K_x^o for the formation of mono-hydroxo complex of metal x) and measured or independently estimated stability constants for the formation reaction of the borate complex from the mono-hydroxo complex (β_x^o). The general form of the two reactions from which the correlation is derived is:

$$M^{z+} + H_2O = H^+ + MOH^{z-1} \qquad \log_{10} K_x^o = \log_{10}(a_{MOH^{z-1}}) - pH - \log_{10}(a_{M^z}) \tag{9-1}$$

$$MOH^{z-1} + B(OH)_3 = MB(OH)_4^{z-1} \qquad \log_{10} \beta_x^o = \log_{10}(a_{MB(OH)_4^{z-1}}) - \log_{10}(a_{MOH^{z-1}}) - \log_{10}(a_{B(OH)_3}) \tag{9-2}$$

The linear relationship derived by Bousher (1995) based on the available data takes the following form:

$$log_{10}\,\beta_x^o = (0.55 \pm 0.04)\, pK_x^o - (2.71 \pm 0.47) \tag{9-3}$$

The equation predicts that the *value* of the borate complex formation constant ($log_{10}\,\beta_x^o$) will increase with decreasing acidity (increasing pK_x^o) of the corresponding mono-hydroxo complex. One therefore expects the highest $log_{10}\,\beta_x^o$ values to be reached for large monovalent cations such as Cs^+ and K^+ and the smallest for highly charged metal cations, e.g. tetravalent to hexavalent actinides. Bousher's relationship was applied using the K_x^o values reported in the TDB2020 update (Hummel & Thoenen 2023). Because no constant was recommended in TDB2020 for caesium, pK_{Cs}^o was taken from Baes & Mesmer (1986). The resulting best estimates are reported in Tab. 9-2 along with bounding values derived from the uncertainties stated in Bousher's equation. The correlation is shown graphically in Fig. 9-1.

9.3.4 Results of speciation calculations

The speciation calculations were carried out with GEM-Selektor using the Debye-Hückel activity model instead of the SIT model used so far. The reasons for this choice are twofold: on one hand the lack of reliable SIT coefficients for the borate complexes, on the other hand technical complications when implementing the new data in the SIT aqueous phase. The same model with no external pCO_2 equilibration as described in Section 9.2 was used.

The results of the speciation calculations are reported in Tab. 9-3. The first column (INCAN 2a_3_B1, *no boron*) refers to the system without any addition of boron. This calculation is thus fully equivalent to that reported as INCAN 2a_3 in Tab. 9-1 for a spent fuel canister environment,

except that it was carried out using Debye-Hückel activity model instead of the SIT activity model[32]. The comparison of INCAN_ 2a_3_B1 with column INCAN 2a_3 in Tab. 9-1 shows, as expected, only minimal differences between the results obtained with either activity model.

Tab. 9-2: Estimated formation constants of borate complexes (in order of decreasing values) determined using the empirical correlation of Bousher (1995), pK_x^o-values from Hummel & Thoenen (2023) and pK_{Cs}^o from Baes & Mesmer (1986)

	pK_x^o	**log β_x^o min.**	**log β_x^o best estimate**	**log β_x^o max.**
Cs^+	14.7	4.32	5.37	6.43
K^+	14.5	4.22	5.27	6.32
Na^+	14.4	4.16	5.21	6.26
Ra^{2+}	13.7	3.81	4.83	5.84
Ba^{2+}	13.32	3.61	4.62	5.62
Sr^{2+}	13.15	3.53	4.52	5.52
Ca^{2+}	12.57	3.23	4.20	5.18
Mg^{2+}	11.7	2.79	3.73	4.66
Ni^{2+}	9.54	1.69	2.54	3.39
Fe^{2+}	9.43	1.63	2.48	3.32
Am^{3+}	7.2	0.49	1.25	2.01
Cm^{3+}	7.2	0.49	1.25	2.01
Pu^{3+}	6.9	0.34	1.09	1.83
Np^{3+}	6.8	0.29	1.03	1.77
Sn^{2+}	3.53	-1.38	-0.77	-0.16
Fe^{3+}	2.2	-2.06	-1.50	-0.94
Pd^{2+}	2	-2.16	-1.61	-1.06
U^{4+}	0.54	-2.90	-2.41	-1.92
Pu^{4+}	0	-3.18	-2.71	-2.24
Zr^{4+}	-0.32	-3.34	-2.89	-2.43
Np^{4+}	-0.55	-3.46	-3.01	-2.56

The two columns labelled INCAN 2a_3_B0 in Tab. 9-3 present the results for the same system, but including 20 mM $B(OH)_3$ + 45 mM $NaB(OH)_4$ to simulate the effect of glass dissolution and considering borate complexation using the estimated constants (B.E. = best estimates; max. = maximum values, see Tab. 9-2).

It is to be realised that a high value of the stability constants listed in Tab. 9-2 does not necessarily imply a high concentration of the corresponding metal borate complex. This is because of multiple superposed effects in the chemical simulations, which include not only the effect of borate complexation, but also the effects of pH increase (induced by the addition of the boric acid/borate

[32] The Debye-Hückel model was used because no SIT coefficients are available for B species in TDB2020.

mixture), of competition with other ligands and of solubility limitations (the limiting solids were those listed in Tab. 9-1). Furthermore, it must be understood that the *value* of $\log \beta_x^o$ is not an intrinsic measure of the strength of the borate complex of metal x, as β_x^o is related to the strength of the mono-hydroxo complex, which is pH-dependent. The effective contribution of $MB(OH)_4^{z-1}$ to the total metal concentration will thus be a non-linear function of pH and competition by other ligands (hydroxide, carbonate, sulphate, chloride). In conclusion, only the full equilibrium calculation will reveal the true strength of borate complexes.

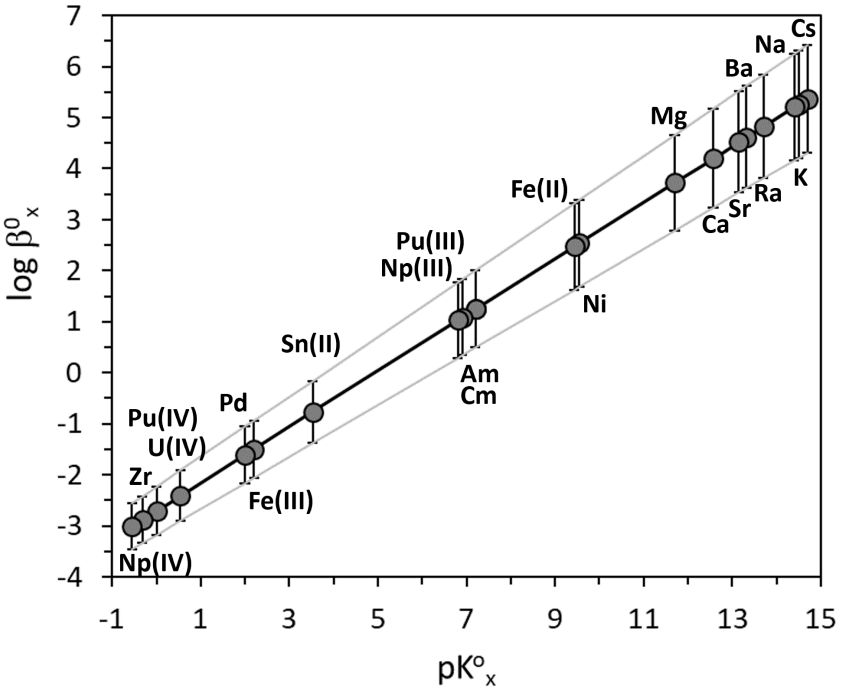

Fig. 9-1: Formation constants and uncertainties of unidentate monomeric metal borate complexes estimated with the empirical correlation of Bousher (1995)

To facilitate the discussion of the results listed in Tab. 9-3, the concentrations of dose-relevant elements are highlighted in red whenever a significant increase with respect to the reference calculation (*no boron*) is predicted, and in green in the case of a significant decrease. Red values thus indicate that the addition of 65 mM $B(OH)_3$ + $NaB(OH)_4$ to the system leads to a significant increase in the specific radionuclide solubility limit, whereas green values indicate that this addition leads even to "improved" (lower) solubility limits. Values in black imply that no significant effect on the solubility limit is predicted through the addition of the borate-boric acid mixture.

For Am, Ni and Pu, a *decrease* in solubility limit with respect to the reference system devoid of boron is predicted, which is readily explained by the increase in pH caused by the $NaB(OH)_4$ addition and the fact that solubility-limiting solids of these elements are hydroxides: the increased OH^- activity leads to a reduction of the free (and total) metal ion equilibrium activity, and the formation of the borate complex is not sufficient to compensate this effect.

The reduction in U concentration has another explanation: it arises from the decrease in carbonate concentration upon B addition, which leads to a decrease in the $UCO_3(OH)_3^-$ contribution to total uranium concentration. No U(IV) borate complex is formed at all as the derived formation

constant is too small. In contrast to U, the Np concentration increases in the most conservative calculation due to the partial stabilisation of Np(III) and consequent formation of Np(III)-borate complex in significant amounts (about 40% of the total Np concentration).

The predicted strong increase in Mo concentration deserves a more detailed explanation. According to the equilibrium equation (9.3) discussed in Bradbury et al. (2014), the solubility of Mo is a function of both pH and hydrogen partial pressure when controlled by Mo(IV) oxide. Because the hydrogen partial pressure is fixed at about 1 bar in all three calculations and no borate complex can form with molybdate, according to the relationship mentioned in Bradbury et al. (2014), the calculated increase in Mo must be attributed to the pH increase alone. The increase in the decimal logarithm of the total Mo concentration should then be about twice the pH increase (0.43 pH units for the *max.* case), i.e. an increase by a factor of about 7 – 8 is predicted by the equation of Bradbury et al. (2014), which is confirmed by the speciation results presented here.

The marked increase in Se solubility in the *B.E.* calculation (about 1 order of magnitude) is a direct consequence of the decreased equilibrium Fe(II) concentration in conjunction with the specific solubility control by $FeSe_{2-x}$(cr), ferroselite: the decrease in Fe^{2+} activity must be compensated by an increased Se^{2-} activity to maintain equilibrium with this solid.

The only elements for which the increased solubility limits can be attributed solely to the formation of borate complexes are Ra and Sr. The effect is however minor, the increase in equilibrium concentrations with respect to the B-free calculation being less than 10% in both cases.

To evaluate the effective efficiency of boron in complexing the cations present in the modelled water, a simplified calculation was carried out using the best estimates of the borate complex constants. In the calculation, all other competing ligands were eliminated (Cl^-, SO_4^{2-}, CO_3^{2-}, etc., but obviously not OH^-), i.e. the calculation was carried out in a pure 19.7 mM $B(OH)_3$ + 45.3 mM $NaB(OH)_4$ solution, to which equal small amounts of the metals of interest (1 μmol/kg_{H2O}) were added. Moreover, the precipitation of all solids was suppressed, so that in the equilibrated system all metals (except Na) conserve the common concentration level of 1 μmol/kg_{H2O}. The calculation yields a water with pH 9.49 and Eh -467 mV, similar to the preceding full model water INCAN 2a_3_B0 (*B.E.*). The resulting percentages of total element occurring as borate complex in the water are plotted as a function of pK^o_x in Fig. 9-2 (blue open symbols).

Tab. 9-3: Results of speciation calculations to determine aqueous, gas and solid equilibria in the water filling the open space inside a failed HLW disposal canister loaded with RP-HLW, assuming no B (*no boron*) present or 65 mM B using either best estimates (*B.E.*) or maximum values (*max.*) of the estimated borate complex stability constants

Calculation ID ==>	**INCAN 2a_3_B1 (no boron)**	**INCAN 2a_3_B0 (B.E.)**	**INCAN 2a_3_B0 (max.)**
IS(m)	0.432	0.470	0.448
pH	8.40	9.27	8.84
Eh(V)	-0.495	-0.546	-0.521
log p(CO_2)	-4.51	-6.12	-5.22
log p(H_2)	-0.03	-0.03	-0.03
log p(N_2)	-1.16	-1.18	-1.18
log p(O_2)	-83.0	-83.0	-83.0
Main elements	***mol/kgw***		
Al	2.08×10^{-8}	2.08×10^{-8}	2.08×10^{-8}
B	---	6.50×10^{-2}	6.50×10^{-2}
Ba	8.34×10^{-8}	8.19×10^{-8}	8.21×10^{-8}
C(in)	2.20×10^{-4}	6.06×10^{-5}	1.29×10^{-4}
Ca	1.64×10^{-2}	1.57×10^{-2}	1.47×10^{-2}
Cl	0.239	0.239	0.239
F	1.65×10^{-4}	1.65×10^{-4}	1.65×10^{-4}
Fe	7.08×10^{-5}	2.83×10^{-6}	3.23×10^{-5}
K	1.83×10^{-3}	1.83×10^{-3}	1.83×10^{-3}
Mg	9.58×10^{-3}	8.91×10^{-3}	9.97×10^{-3}
Mn	5.94×10^{-5}	5.81×10^{-5}	5.24×10^{-5}
Na	0.341	0.386	0.386
P	6.59×10^{-10}	1.93×10^{-10}	4.58×10^{-10}
S	7.78×10^{-2}	7.78×10^{-2}	7.78×10^{-2}
Si	2.06×10^{-4}	2.57×10^{-4}	2.15×10^{-4}
Considered dose relevant radionuclides	***mol/kgw***		
Am	2.43×10^{-8}	1.45×10^{-8}	2.35×10^{-8}
Cs	1.05×10^{-8}	1.05×10^{-8}	1.05×10^{-8}
Mo	4.32×10^{-13}	2.59×10^{-11}	3.51×10^{-12}
Ni	3.70×10^{-5}	5.10×10^{-6}	1.75×10^{-5}
Np	1.07×10^{-9}	1.00×10^{-9}	1.68×10^{-9}

Tab. 9-3: Cont.

Calculation ID ==>	**INCAN 2a_3_B1 (no boron)**	**INCAN 2a_3_B0 (B.E.)**	**INCAN 2a_3_B0 (max.)**
Pd	3.13×10^{-10}	3.16×10^{-10}	3.16×10^{-10}
Pu	6.32×10^{-8}	2.02×10^{-9}	1.31×10^{-8}
Ra	3.49×10^{-8}	4.11×10^{-8}	4.07×10^{-8}
Se	1.21×10^{-8}	1.01×10^{-7}	3.15×10^{-8}
Sn	1.71×10^{-8}	6.37×10^{-8}	3.40×10^{-8}
Sr	1.64×10^{-4}	1.99×10^{-4}	2.01×10^{-4}
Tc	1.87×10^{-9}	1.94×10^{-9}	1.90×10^{-9}
U	3.14×10^{-11}	1.96×10^{-11}	2.44×10^{-11}
Zr	6.23×10^{-10}	6.28×10^{-10}	6.29×10^{-10}

Not surprisingly, Fig. 9-2 shows that the strongest borate complexes are those with metals having a pK^{o}_{x} close to the pK of the boric acid dissociation constant ($pK_a = 9.23$), i.e. Fe(II) and Ni(II). Appreciable degrees of borate complexation are also calculated for other alkaline earth cations, while weak or no complexation is found for monovalent, trivalent and tetravalent cations.

When the pH is adjusted to near-neutral values through addition of HCl (red dots in Fig. 9-2), the efficiency of borate complexation again shows a peak value for the Fe(II), however there is a shift in favour of the trivalent actinide borate complexes, whereas the strength of the Ni(II) and alkaline earth borate complexes is significantly reduced. This illustrates the point made earlier: it is not possible to anticipate a priori the effective abundance of a given metal borate complex only from the numerical value of the stability constant, because of the high sensitivity to pH.

Overall, it can be concluded that the effect of boron release from RP-HLW on radionuclide solubility limits will be minor, even under the conservative assumptions made to obtain the results listed in Tab. 9-3 (in particular, the assumption of a closed system leads to exceedingly high B concentrations and to a pH increase that will hardly be reached inside the HLW disposal canister or in the internal section of the bentonite buffer, due to out-diffusion of B). Therefore, it can safely be concluded that complexation of dose-relevant radionuclides with borate released from the RP-HLW and the associated pH increase should be not a safety-relevant issue.

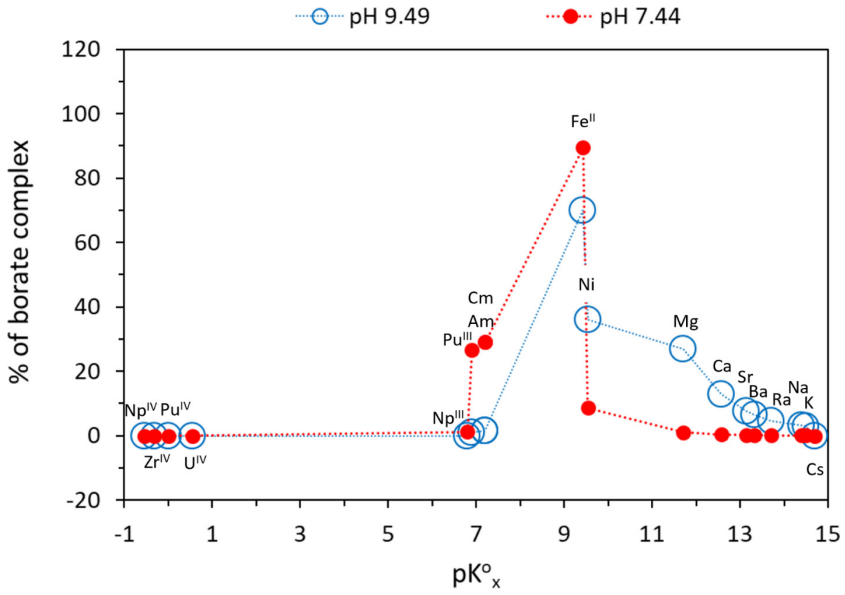

Fig. 9-2: Percentages of total element concentration as monoborate complex for different cations as a function of first hydrolysis constant in a simplified $B(OH)_3/NaB(OH)_4$ solution devoid of competing ligands and suppressing precipitation, calculated at mildly alkaline and neutral pH using the best estimates of the constants reported in Tab. 9-2

9.4 Summary and conclusions

In this chapter, specific issues related to bulk chemical effects arising from the interaction between the dissolving waste (spent fuel or borosilicate glass) with the surrounding engineered barrier materials were discussed. Other subjects related to waste degradation, namely dissolution kinetics and radionuclide release, are not addressed here as they are covered in detail in two separate reports (Johnson et al. 2023, Curti 2022).

Thermodynamic equilibrium calculations were carried out to estimate the chemical conditions established inside a failed HLW disposal canister made of carbon steel hosting either spent UO_2 fuel or RP-HLW. The calculations were carried out assuming estimated bentonite porewater infiltration rates and material-specific waste dissolution and canister corrosion rates. Based on currently available evidence, it was postulated that sulphate and carbonate reduction reactions are inhibited due to the absence of microbial activity.

In the case of a HLW disposal canister loaded with spent fuel, two distinct speciation calculations, representing the initial and advanced stages of canister degradation, were carried out. The former calculation leads to a mildly alkaline, strongly reduced water (pH =8.4, Eh = -495 mV) rich in H_2, while the calculation representative of advanced degradation conditions produces a nearly neutral, moderately reducing H_2-poor water (pH =7.2, Eh = -222 mV) resembling the bentonite porewaters discussed in Chapter 7. Compared to the earlier calculation of Bradbury et al. (2014), lower Fe and higher carbonate concentrations are predicted. Most calculated solubility limits of radionuclides are similar, with some exceptions (Np, Pd, Pu, Ra). The discrepancies can be ascribed to a combination of effects (differences in the assumed boundary conditions, water and material compositions and updated thermodynamic data, specifically for P and Fe).

The effect of glass dissolution on the chemical environment in the failed HLW disposal canister loaded with RP-HLW was evaluated through speciation calculations including amounts of B corresponding to the concentrations measured in long-term glass corrosion experiments (Curti et al. 2006, Kerleguer 2020), in conjunction with values for borate complex formation constants estimated with the free energy relationship of Bousher (1995). The results indicate that the effect (if any) of borate complexation and/or local pH increase induced by the initial dissolution of borosilicate glass on the solubility limits of considered dose-relevant radionuclides will be negligible or minor, even assuming the upper uncertainty boundaries of the borate complexation constants and conservatively high concentrations. It is therefore concluded that release of boron and pH increase due to RP-HLW dissolution is not a safety-relevant issue.

Scoping calculations indicate that the strongest borate complexes will be formed with transition metals (Fe and Ni). Depending on pH, alkali-earth metals (Mg, Ca, Sr, Ba, Ra) and trivalent actinides (Am, Cm) could also form borate complexes to a limited extent. In contrast, monovalent (Na, Cs, K) and tetravalent to hexavalent cations (U, Np, Pu, Tc) should not form borate complexes in significant concentrations.

10 Overall summary and conclusions

This report provides a detailed description and a critical discussion of the chemical processes expected in the near-field of the HLW repository in Switzerland according to the provisional design and expected thermo-hydro-mechanical evolution (Nagra 2024d). It updates, complements and replaces an analogous earlier report (Bradbury et al. 2014) released within the framework of Stage 2 of the Sectoral plan for Deep Geological Repositories (SGT-E2). The focus is primarily on the chemical stability of engineered barrier materials (bentonite buffer) during the elevated temperature phase immediately following waste emplacement, on the reactivity of material interfaces (bentonite/drift support/Opalinus Clay, HLW disposal canister/bentonite and HLW disposal canister/waste), as well as on porewater chemistry. The potential impact of these chemical processes on waste degradation, solubility and sorption of dose-relevant radionuclides, transport and swelling properties of bentonite, is discussed and where appropriate evaluated. HLW disposal canister and waste degradation kinetics, and the associated radionuclide release from spent fuel and RP-HLW, are not treated in this report, since these topics are discussed in detail in separate reports (Nagra 2024b, Curti 2022, Johnson et al. 2023).

The main chemical processes identified to have the largest potential impact on the long-term performance of the near-field barrier system are:

- the reaction between the cementitious support structure of the emplacement drifts with Opalinus Clay (external interface) and bentonite (internal interface) during and after the resaturation phase
- the increased reactivity of near-field materials during the post-closure, elevated temperature transient
- the reaction of the degrading HLW disposal canisters made of carbon-steel with bentonite at their external interface
- the reaction of the slowly dissolving waste materials (spent fuel or RP-HLW) with structural materials and the internal HLW disposal canister interface.

The focus of the report is on mineral transformations and porewater chemistry, since these two categories of chemical processes have the potential to directly affect properties of considered dose-relevant radionuclides (solubilities, sorption coefficients and diffusion coefficients in bentonite). The first introductory part (Chapters 2 – 5) presents generic, brief descriptions of the provisional repository setup, of initial chemical composition and properties of the near-field materials, and of the expected physical-chemical evolution of the repository. The subsequent chapters (6 – 9) are dedicated to in-depth discussion of specific chemical subsystems within the repository near-field.

Chapter 2 provides a description of the provisionalary design of the repository, including geometry and functionality of the components and the expected evolution. The generic repository project foresees a single repository site with two spatially separated disposal sections, one for high-level waste (HLW section, hosting spent fuel and RP-HLW) and one for low- and intermediate-level waste (L/ILW section). Because of the large distance between the two sections, the two waste types are not expected to interact chemically, so that the phenomenological evolution of each disposal section can be treated separately. The present report addresses only the HLW section. While some of the processes considered in this report will proceed in a similar way in both disposal sections (e.g. interactions at tunnel support interfaces), those involving specifically the waste and its containment refer only to the HLW section. Following a comparison of the siting

regions, Nagra concluded that NL is the safest and most flexible siting region and is therefore applying for a general licence for a combined repository for both HLW and L/ILW at the Haberstal site. The waste will be, according to the provisionalary design, disposed of in a system of dead-end emplacement drifts, supported by segmental lining elements and annular gap-filling material, both made of cementitious materials. The waste packages consist of HLW disposal canisters made of carbon-steel with wall thickness of around 14 cm encasing the waste forms (Nagra 2024b) according to the provisionalary design. They will be emplaced at the centre of the drifts on pedestals of compacted bentonite blocks. The drifts will then be backfilled with highly compacted granular bentonite. The repository components and environmental conditions are selected for their ability to ensure large safety margins during the entire safety-relevant performance period (up to 1,000,000 years), for example preventing human intrusion, ensuring resilience towards disruptive geological events (e.g. glaciations), and minimising radionuclide transport (low hydraulic conductivities, low diffusivities, high sorption capacities and low solubility limits for most dose-relevant radionuclides, as well as low waste dissolution rates). The performance of the repository will also rely on the chemical evolution of the engineered barrier materials and of the Opalinus Clay host rock under the environmental conditions established during the period of assessment.

Chapter 3 describes the expected geomechanical and thermal evolution of the repository system. Construction and operation will unavoidably affect the initial in-situ conditions. Drift excavation will cause stress redistribution within the adjacent host rock, leading to formation of fracture networks, the excavation-damaged zone, EDZ. Ventilation will introduce cool dried air, leading to evaporation and thus partial desaturation in the EDZ. This process will induce salt and gypsum precipitation in the host rock near the drifts, as well as oxidation of pyrite to Fe oxy-hydroxides. Another possible effect of ventilation will be carbonation of concrete in the tunnel support, which should however be minor and limited to the surface. Overall, the evidence collected from experiments in underground research laboratories (Mont Terri Rock Laboratory) indicate that chemical changes during construction at the Opalinus Clay / tunnel support interface are not expected to impair the safety functions of the barriers.

After repository closure, the dehydrated zone in the Opalinus Clay and bentonite buffer will slowly resaturate, resulting in self-sealing of cracks and closing spaces in the EDZ. A steep temperature transient will characterise the early post-closure time, as described in more detail in Chapter 5. Because temperatures in the bentonite buffer will temporarily and locally exceed 100 °C, partially saturated conditions will prevail during this period due to condensation-evaporation cycles driven by the steep temperature gradient between the hot HLW disposal canister surface and the incoming porewater front. Redox conditions will rapidly become anaerobic after consumption of O_2 (gaseous or physisorbed on the bentonite). As soon as the relative humidity within the bentonite is high enough, anaerobic corrosion of the HLW disposal canister made of carbon steel will start and produce hydrogen, which in an early stage is expected to form a separate gas phase. Canister corrosion will result in secondary Fe-oxides, mainly Fe_3O_4 (magnetite). Once the HLW disposal canister is breached, porewater will enter the internal empty space (canister cavity), while intrusion of bentonite is considered to be very unlikely (see App. B). Once the radioactive waste (either spent fuel or RP-HLW) comes in contact with the intruded water, dissolution of the waste and resulting radionuclide release will begin. Due to the hydrogen generated (high partial pressures not necessary, very reducing conditions are guaranteed even at very low $p(H_2)$) by anaerobic steel corrosion, the redox conditions inside the HLW disposal canister will be strongly reducing, ensuring that the dissolution rates of the $U(Pu)O_2$ spent fuel and thus the release rates of redox-sensitive dose-relevant nuclides remain low. After breaching, corrosion of the HLW disposal canister will continue and produce hydrogen for at least several tens of thousands of years, until all metallic Fe is consumed.

In Chapter 4, the physicochemical initial state of the repository near-field is described. The term initial state refers both to boundary conditions and chemical specifications of the repository system, including the adjacent host rock, shortly after repository closure. The chemical and mineralogical compositions of waste (spent fuel and RP-HLW), engineered barrier materials (HLW disposal canister, structural materials, bentonite) and of adjacent natural barriers (Opalinus Clay, including the EDZ) are specified. Compositional variations, e.g. due to mineralogical heterogeneity in bentonite or due to the evolution of the radionuclide inventory in spent fuel, are also discussed. These "initial state" data are needed as input for follow-up chemical calculations, particularly of bentonite porewater in Chapter 7 and "inside canister" water in Chapter 9. While the initial composition of RP-HLW is well-defined through specifications by the two reprocessing plants in France and the U.K., spent fuel and structural material compositions are more variable as they originate from five different reactors and different types of fuel (UO_2 or MOX) with a large variability in burnup, thus giving rise to different initial radionuclide inventories (Johnson et al. 2023).

Due to decay/ingrowth, radionuclide inventories continuously evolve during 1,000,000 years. Our calculations show, however, that after canister failure (Nagra 2024b), the total element inventories of most fission/activation products remain nearly constant because of the dominant contribution of stable isotopes. In contrast, minor actinides and their decay products (e.g. ^{226}Ra) show strong time-dependent inventories, as these elements do not form stable isotopes. Because of the low concentrations involved, however, the time-dependent inventories of such nuclides do not significantly affect the bulk composition of the waste.

Chapter 5 provides an overview of the predicted temperature evolution across the HLW repository near-field. Moreover, the potential effects of the post-closure transient temperature increase on the chemical stability of bentonite, as well as on radionuclide sorption and transport properties, are discussed based on literature data. The chapter starts by reviewing earlier model calculations on the temperature evolution in the HLW repository near-field. All models predict, at least locally, a rise in temperature above 100 °C in the bentonite during a relatively short time span (< 1,000 a after closure). A recent update of the model of Senger et al. (2014) (Fig. 5-1) adapted to a ~ 900 m deep repository at the Haberstal site (Fig. 5-2) shows overall higher temperatures, as a result of more elevated background temperatures at such depths, compared to those assumed in the former SGT-E2 scenario. In the updated calculations, temperatures exceeding 100 °C are predicted across the entire bentonite section during several hundred years. Moreover, contrary to the SGT-E2 predictions, thermal equilibrium with the host rock is not yet achieved at the assumed canister failing time at 10,000 years (Nagra 2024b) after repository closure. At that time, temperatures of around 55 °C are predicted across the entire bentonite annulus, while formation temperatures in the Opalinus Clay are in the order of 47 °C.

The second part of Chapter 5 deals with chemical/mineralogical transformations and change in properties induced by the predicted high-temperature pulse in the HLW near-field. The first topic is the chemical stability of montmorillonite, the main clay mineral in the bentonite buffer, with focus on the potential loss of the buffer functionality through conversion to illite. Laboratory experiments and the geological record indicate that illitisation of montmorillonite is possible at temperatures below 100 °C. However, geochronological data on the diagenesis of natural bentonites clearly show that the kinetics of illitisation is extremely slow at the temperatures of interest (~ 47 – 105 °C). It would take several million years for the conversion of smectite to illite to be complete (Clauer et al. 2014). Moreover, mass balance calculations based on the availability of potassium (from Opalinus Clay porewater and tunnel support structure) show that no more than a few wt.% of the montmorillonite initially present in bentonite could be converted to illite. From the above evidence, it is concluded that the relevant physical and chemical properties of the bentonite buffer will not be compromised during the thermal pulse.

The second topic in Chapter 5 deals with the effect of temperature on the sorption and diffusion of radionuclides and major ions in bentonite. There is clear evidence for a decrease, with increasing temperature, in the sorption of metals taken up preferentially via cation exchange (e.g. Cs^+, K^+, Na^+, Mg^{2+}). For instance, the distribution coefficient (K_d) of Cs^+ decreases by a factor of three when the temperature increases from 25 °C to 90 ºC, which can be explained by the exothermic character of cation exchange reactions in clays. According to the Van't Hoff equation, an increase in temperature then leads to a decrease in cation exchange constant. In contrast, highly charged cations sorbing preferentially via surface complexation show either negligible (e.g. Eu^{3+}, Th^{4+}) or the opposite temperature dependence (e.g. Ni^{2+}). In this case, adsorption is endothermic, leading to an increase in sorption as temperature rises.

Experimental studies in saturated, compacted bentonite show that diffusion coefficients of cationic, anionic and neutral species vary with temperature following Arrhenius' law. For most chemical species, the derived activation energies (E_a) are in general slightly higher (~ 20 kJ mol^{-1}) than in free water (~ 18 kJ mol^{-1}), independent of the compaction of the clay. Increasing the temperature from 20 °C to 80 °C then results in an increase of D_e by a factor of four. An exception is Cs^+, which shows considerably higher activation energies, also increasing significantly with the bulk dry density of the clay (from ~ 30 to ~ 50 kJ mol^{-1} between 1,000 and 1,800 kg m^{-3}).

Because at 10,000 years after waste emplacement, heat transfer calculations predict temperatures only 8 °C above thermal equilibrium with the host rock (55 °C vs. 47 °C, see above), effects on radionuclide sorption and diffusion due to the elevated temperature gradient will be small and can be ignored in a first approximation.

Chapter 6 is devoted to the complex chemical interactions between the cementitious drift support structure and the surrounding clay materials (bentonite buffer and Opalinus Clay host rock) that will be driven primarily by strong pH-gradients between cement and clay materials upon resaturation. Results from many reactive transport calculations conducted for realistic repository conditions consistently indicate thin (generally a few cm thick) alteration zones for clay in contact with concrete (either OPC or low-pH cement), in spite of the different setups and initial clay mineralogy. Qualitatively, the predictions agree with experimental evidence from dedicated underground laboratory experiments.

Earlier reactive transport calculations carried out within the framework of SGT-E2 assuming instantaneous mineral dissolution/precipitation and isothermal-isobaric conditions (25 °C, 1 bar) indicated maximum alteration thicknesses of 10 – 20 cm for the clays in contact with the tunnel support structure, as well as a local reduction in porosity due to precipitation of secondary minerals. In the altered bentonite and Opalinus Clay, only minor amounts of the pristine clay minerals were predicted to dissolve. Alkaline porewater (pH > 9) was predicted not to extend more than 10 cm from the interface with the tunnel support, and to remain stationary before eventually reaching near-neutral conditions everywhere (pH ~ 8 after 100,000 years). In the altered bentonite, precipitation of calcite and hydrotalcite and partial replacement of exchanged Na^+ and Mg^{2+} by Ca^{2+} and K^+ in montmorillonite were anticipated, while in the altered Opalinus Clay, kaolinite and illite dissolved and were replaced by montmorillonite. Within the drift support, C-S-H phases eventually dissolved and hydrotalcite, phillipsite, clay minerals (illite, montmorillonite), gypsum and calcite precipitated.

The SGT-E2 reactive transport calculations have been recently updated (Section 6.7) with a view to the general licence application, taking into account the new near-field geometry, modified formulations of cementitious materials, the pozzolanic reaction with silica aggregates, as well as refined thermodynamic data. Moreover, in addition to isothermal calculations (25 °C), temperature-dependent calculations were carried out using an updated post-closure thermal pulse

(as calculated by Senger et al. 2014). In special calculations, mineral precipitation kinetics was also considered. Overall, the update shows qualitatively similar features and processes to those predicted by the SGT-E2 calculations. However, when the temperature pulse is included, an accelerated degradation of cement materials is predicted due to the enhanced dissolution of siliceous aggregates at higher temperatures. Consequently, the pH at the cement/clay interface decreases more rapidly and the high-pH anomaly therefore has a shorter duration compared to the isothermal calculations at 25 °C. A process predicted in the latter calculations but not observed in any (SGT-E2 and updated) isothermal calculation is the accumulation of carbonate leading to a porosity decrease at the Opalinus Clay/cement interface. This phenomenon is a direct consequence of the temperature increase towards the canister: because the solubility of carbonates (calcite) decreases with both temperature and pH, a flux of dissolved carbonate from the cooler Opalinus Clay (i.e., opposite to the temperature gradient) is generated that causes carbonate precipitation within a high-pH (high-T) front in a thin external zone of the bentonite buffer originating from the cementitious backfill.

Verification of reactive transport predictions with experimental data has recently become possible thanks to detailed data on mineralogical changes that occurred during the 10-year-long Cement-Clay-Interface (CI) experiment in the Mont Terri Rock Laboratory, however limited to isothermal conditions. To this end, a classical single porosity model (Prasianakis et al. 2022), and a dual porosity model in which saturated montmorillonite has been treated as a uniform Donnan phase (Jenni et al. 2017, Jenni & Mäder 2021) have been applied and compared to the experimental findings of the CI experiment. In spite of some discrepancies, both models broadly reproduce the major observed features (thickness of alteration zones, porosity changes and most compositional changes).

Chapter 7 presents the modelling of bentonite porewaters (BPW) for the determination of radionuclide solubility limits and sorption coefficients in safety assessment calculations. For this purpose, a refined classical model was selected (ClaySor, see Kulik et al. 2018) that includes the 2SPNE SC/CE model successfully used for many years for the evaluation of cation exchange and surface adsorption in clays. In the simulations, fully saturated MX-80 Na-bentonite is equilibrated with Opalinus Clay waters (OPAw) taking into account cation exchange reactions, protonation/deprotonation of amphoteric surface sites and solubility equilibria of minor reactive solids, at a clay/water ratio corresponding to the anion-accessible porosity in bentonite with a bulk dry density of 1,450 kg m-3. The OPAw correspond to compositions defined for the Nördlich Lägern (NL) and Zürich Nordost (ZNO) siting regions. Three BPWs in equilibrium with carbon dioxide partial pressures of 10-2.8, 10-2.2 and 10-1.8 bar (corresponding to the expected range) were calculated for average salinity OPAw (ionic strength ≈ 0.32 M). An additional BPW representative of high-salinity OPAw (ionic strength ≈ 0.51 mol/kgw) was calculated. The computed BPWs yield narrow ranges of concentrations, pH (6.9 – 7.4), Eh (-159 – -154 mV) and ionic strength (0.45 – 0.59 mol/kgw), which can be explained by robust internal buffering reactions. A sensitivity analysis revealed only weak dependencies on bentonite compaction, protonation/deprotonation of surface sites and initial mineralogy (except for presence/absence of gypsum). In contrast, there is a high sensitivity to the initial occupancies of exchange sites. As expected, significantly different BPW compositions are obtained when OPAw reacts with Ca-bentonite instead of Na-bentonite. The modelling also includes iterative calculations simulating the evolution of BPW as it reacts with an increasing volume of OPAw. As expected, the results show that, with time, the BPW should evolve towards the composition of the reacting OPAw.

Chapter 8 presents a review of studies on the interaction between iron/steel (representing the HLW disposal canister) and claystones or bentonite (representing the buffer material in the drifts).

The review includes laboratory studies as well as large-scale in-situ experiments carried out in underground facilities. Based on the results of the in-situ FEBEX and ABM experiments, Wersin & Kober (2017) and Hadi et al. (2017) proposed a generalised scheme for the evolution of steel/bentonite interfaces under repository conditions. Initially, aerobic unsaturated conditions prevail, leading to formation of Fe(III) oxides. As O_2 no longer reaches the reacting interface due to the binding to Fe(III) oxides in the external corrosion layer, steel corrosion becomes anaerobic, producing magnetite and siderite at the internal reaction front and, at the same time, releasing considerable concentrations of dissolved Fe(II). Electron transfer across the corrosion layer leads to the generation of Fe(II) at the interface between corrosion layer and bentonite, which then reacts with residual O_2 to produce further Fe(III) oxy-hydroxides at the external side. After O_2 consumption, Fe(II) diffuses into bentonite, sorbing on smectite and probably interacting with structural Fe(III). Contrary to laboratory experiments, in which the chemical evolution is usually accelerated through the use of highly reactive Fe powder, no signs of smectite destabilisation or formation of iron-rich silicates could be observed within the limited time frame of the FEBEX and ABM experiments. The laboratory experiments nevertheless demonstrate that Fe-silicates are stable over a wide range of temperatures, suggesting that, although they are usually not observed in the (necessarily short-term) field experiments, they may form over long-term repository timescales. Estimations based on out-diffusion of Fe(II) from the corroding canister indicate however that the amount of montmorillonite that could be converted to Fe-silicates is limited. Assuming conservative Fe(II) concentration gradients and diffusion coefficients, the amount of bentonite that could be altered in this way would not exceed ~ 17% of the initial mass in 1 Ma. Assuming more realistic parameters (realistic estimate), less than ~ 3% of the bentonite is predicted to be altered during the same time. Therefore, a loss of buffer functionality is unlikely, since a sufficient thickness of bentonite buffer will remain intact during the 1 Ma period required by the regulators for the safety case.

In Chapter 9, the chemical conditions inside a failed HLW disposal canister containing either spent fuel or RP-HLW are assessed, as an update of earlier analogous calculations (Chapter 9 in Bradbury et al. 2014). As for the modelling of BPWs, this is done via thermodynamic equilibrium calculations assuming fully saturated conditions. For the HLW disposal canister containing spent fuel, two distinct calculations were carried out, assuming either unconstrained or a fixed pCO_2 identical to that assumed for the reference bentonite porewater ($pCO_2 = 10^{-2.2}$ bar). The former case simulates early conditions after canister breaching and leads to an H_2-rich, strongly reducing mildly alkaline water (pH = 8.4, Eh = -495 mV). In contrast, the calculation with fixed pCO_2, representing advanced degradation, produces a nearly pH-neutral, moderately reducing H_2-poor water (pH = 7.2, Eh = -222 mV). Compared to Bradbury et al. (2014), lower Fe and higher carbonate concentrations are predicted. Most radionuclide solubility limits remain similar, with notable exceptions (Np, Pd, Pu, Ra) ascribed to various factors, such as different boundary conditions, different compositions of BPW and reacting solids, and updated thermodynamic data (specifically for P and Fe).

The effect of glass dissolution on the chemical environment in the failed HLW disposal canister was evaluated by considering the effect of soluble B and Na released from the glass on the infiltrated bentonite porewater. Beforehand, these calculations required the estimation of borate complex formation constants and their implementation in GEM-Selektor, since boron was not part of the TDB2020 update (Hummel & Thoenen 2023). The estimated constants were determined using a free energy correlation between known borate complexation constants and the corresponding mono-hydroxo complexation constants (Bousher 1995). The results indicate that the combined effect of pH increase (due to release of alkali oxides from the borosilicate glass) and borate complex formation is negligible and will not lead to a significant increase in radionuclide solubility limits, even assuming the upper uncertainty boundaries of the borate complexation constants. It is therefore concluded that release of boron and pH increase resulting from RP-HLW dissolution is not a safety-relevant issue.

This report also includes three appendices. App. A provides the details of the method used to estimate the maximum amounts of bentonite alteration due to interaction with the corroding canister, while App. B deals with the issue of bentonite erosion and infiltration into the cavities of the failed HLW disposal canister (not treated elsewhere in the report). This topic is of relevance since, in the case of bentonite intrusion into the failed canister, the chemical environment inside the canister would differ significantly from the reference system treated in Chapter 9. Moreover, direct contact between borosilicate glass matrix and bentonite could adversely enhance its dissolution kinetics. Application of the "bentonite erosion" model of Birgersson & Karnland (2009) to conservative conditions in the Swiss HLW repository indicate that bentonite intrusion is very unlikely, even in the case of formation of open fissures through the canister. Finally, App. C provides a comparison between the provisional calculations for Opalinus Clay porewater (used to calculate the bentonite porewaters discussed in Chapter 7) and the final ones (released later, based on the complete set of borehole data after completion of the bentonite porewater calculations). The comparison shows that provisional and final OPAw are almost identical, so that the effort of a full recalculation of bentonite porewaters is not necessary.

11 References

Alheid, H.J., Aranyossy, J.F., Bluming, P., Hoteit, N. & van Geet, M. (2005): EDZ development and evolution. State of the art report. European Commission NF-Pro project, 6th EURATOM Framework Programme. European Commission.

Ali, A., Salman, M. & Ahmad, R. (2021): Smectite illitization of the Talhar shale, Lower Goru Formation, Southern Indus Basin, Pakistan. Journal of Petroleum Exploration and Production Technology 11/6, 2315-2325. DOI: 10.1007/s13202-021-01183-5.

Alonso, J., García-Siñeriz, J.L., Barcena, I., Alonso, M.C., Fernandez Luco, L., García, J.L., Fries, T., Pettersson, S. & Boden, A., Salo, J.P. (2009): Module 4 (Temporary sealing technology). Final Report ESDRED Project (Contract Number : F16W-CT-2004-508851). European Commission.

Alt-Epping, P., Tournassat, C., Rasouli, P., Steefel, C.I., Mayer, K.U., Jenni, A., Mäder, U., Sengor, S.S. & Fernández, R. (2015): Benchmark reactive transport simulations of a column experiment in compacted bentonite with multispecies diffusion and explicit treatment of electrostatic effects. Computational Geosciences 19/3, 535-550. DOI: 10.1007/s10596-014-9451-x.

Baes, C.F. & Mesmer, R.E. (1986): The hydrolysis of cations. Robert E. Krieger Publishing Company, Malabar.

Beaufort, D., Berger, G., Lacharpagne, J. & Meunier, A. (2001): An experimental alteration of montmorillonite to a di + trioctahedral smectite assemblage at 100 and 200°C. Clay Minerals 36, 211-225. DOI: 10.1180/000985501750177942.

Bernard, E., Jenni, A., Fisch, M., Grolimund, D. & Mäder, U. (2020): Micro-X-ray diffraction and chemical mapping of aged interfaces between cement pastes and Opalinus Clay. Applied Geochemistry 115, 104538.

Berner, U., Kulik, D. & Kosakowski, G. (2013): Geochemical impact of a low-pH cement liner on the near field of a repository for spent fuel and high-level radioactive waste. Physics and Chemistry of the Earth Parts A/B/C 64. DOI: 10.1016/j.pce.2013.03.007.

Berner, U.R. (1992): Evolution of pore water chemistry during degradation of cement in a radioactive waste repository environment. Waste Management 12/2-3, 201-219.

Bestel, M., Glaus, M.A., Frick, S., Gimmi, T., Juranyi, F., van Loon, L.R. & Diamond, L.W. (2018): Combined tracer through-diffusion of HTO and ^{22}Na through Na-montmorillonite with different bulk dry densities. Applied Geochemistry 93, 158-166. DOI: 10.1016/ j.apgeochem.2018.04.008.

BFE (2008): Sachplan Geologische Tiefenlager: Konzeptteil. BFE 2. April 2008 (Revision vom 30. November 2011). Departement für Umwelt, Verkehr, Energie und Kommunikation UVEK, Bern.

Birgersson, M. (2017): A general framework for ion equilibrium calculations in compacted bentonite. Geochimica et Cosmochimica Acta 200, 186-200. DOI: 10.1016/ j.gca.2016.11.010.

Birgersson, M., Börgesson, L., Hedström, M., Karnland, O. & Nilsson, U. (2009): Bentonite erosion. Final report. Technical Report TR 09-34. Swedish Nuclear Fuel and Waste Management SKB, Stockholm.

Birgersson, M., Hedström, M., Karnland, O. & Sjöland, A. (2017): 12 - Bentonite buffer: Macroscopic performance from nanoscale properties. *In:* Apted, M.J. & Ahn, J. (eds.): Geological Repository Systems for Safe Disposal of Spent Nuclear Fuels and Radioactive Waste (Second Edition) : Woodhead Publishing Series in Energy. Woodhead Publishing, 319-364.

Birgersson, M. & Karnland, O. (2009): Ion equilibrium between montmorillonite interlayer space and an external solution — Consequences for diffusional transport. Geochimica et Cosmochimica Acta 73/7, 1908-1923.

Bock, H., Dehandschutter, B., Martin, C.D., Mazurek, M., Haller, A. de, Skoczylas, F. & Davy, C. (2010): Self-sealing of fractures in argillaceous formations in the context of geological disposal of radioactive waste. Review and synthesis. OECD/NEA, Paris.

Borchardt, G. (1989): Smectites. *In:* Dixon, J.B., Weed, S.B., Dixon, J.B., Weed, S.B. & Dinauer, R.C. (eds.): Minerals in soil environments. 2nd ed. (Soil Science Society of America book series, no. 1). Soil Science Society of America, Madison, Wis., USA, 675-727.

Bossart, P., Trick, T., Meier, P.M. & Mayor, J.-C. (2004): Structural and hydrogeological characterisation of the excavation-disturbed zone in the Opalinus Clay (Mont Terri Project, Switzerland). Applied Clay Science Special Issue: Clays in natural and engineered barriers for radioactive waste confinement: Papers from the ANDRA meeting, Reims, 2002 26/43922, 429-448.

Bourdelle, F., Mosser-Ruck, R., Truche, L., Lorgeoux, C., Pignatelli, I. & Michau, N. (2017): A new view on iron-claystone interactions under hydrothermal conditions (90 °C) by monitoring in situ pH evolution and H2 generation. Chemical Geology 466, 600-607. DOI: 10.1016/j.chemgeo.2017.07.009.

Bourdelle, F., Truche, L., Pignatelli, I., Mosser-Ruck, R., Lorgeoux, C., Roszypal, C. & Michau, N. (2014): Iron–clay interactions under hydrothermal conditions: Impact of specific surface area of metallic iron on reaction pathway. Chemical Geology 381, 194-205. DOI: 10.1016/j.chemgeo.2014.05.013.

Bousher, A. (1995): Review: unidentate complexes involving borate. Journal of Coordination Chemistry 34/1, 1-11. DOI: 10.1080/00958979508024298.

Bradbury, M.H. & Baeyens, B. (1997): A mechanistic description of Ni and Zn sorption on Na-montmorillonite Part II: Modelling. Journal of Contaminant Hydrology 27, 223-248.

Bradbury, M.H. & Baeyens, B. (2002): Porewater chemistry in compacted re-saturated MX-80 bentonite: Physical-chemical characterisation and geochemical modelling. PSI Bericht 02-10. PSI, Nuclear Energy and Safety Department, Waste Management Laboratory, Villigen.

Bradbury, M.H. & Baeyens, B. (2005): Experimental measurements and modeling of sorption competition on montmorillonite. Geochimica et Cosmochimica Acta 69/17, 4187-4197.

Bradbury, M.H., Berner, U., Curti, E., Hummel, W., Kosakowski, G. & Thoenen, T. (2014): The long term geochemical evolution of the nearfield of the HLW repository. Nagra Technical Report NTB-12-01.

Bucher, F. & Spiegel, U. (1984): Quelldruck von hochverdichteten Bentonit. Nagra Technical Report NTB-84-18.

Chagneau, A., Claret, F., Enzmann, F., Kersten, M., Heck, S., Madé, B. & Schäfer, T. (2015): Mineral precipitation-induced porosity reduction and its effect on transport parameters in diffusion-controlled porous media. Geochemical transactions 16, 13. DOI: 10.1186/s12932-015-0027-z.

Cheshire, M.C., Caporuscio, F.A., Jové Colón, C.F. & Norskog, K.E. (2018): Fe-saponite growth on low-carbon and stainless steel in hydrothermal-bentonite experiments. Journal of Nuclear Materials 511, 353-366. DOI: 10.1016/j.jnucmat.2018.09.038.

Cifuentes, G.R., Jiménez-Millán, J., Quevedo, C.P., Nieto, F., Cuadros, J. & Jiménez-Espinosa, R. (2021): Low temperature illitization through illite-dioctahedral vermiculite mixed layers in a tropical saline lake rich in hydrothermal fluids (Sochagota Lake, Colombia). Minerals 11/5, 523. DOI: 10.3390/min11050523.

Clauer, N., Fallick, A.E., Eberl, D.D., Honty, M., Huff, W.D. & Aubert, A. (2013): K-Ar dating and δ^{18}O-δD characterization of nanometric illite from Ordovician. K-bentonites of the Appalachians: Illitization and the Acadian-Alleghenian tectonic activity. American Mineralogist 98/11-12, 2144-2154. DOI: 10.2138/am.2013.4510.

Clauer, N., Honty, M., Fallick, A.E., Šucha, V. & Aubert, A. (2014): Regional illitization in bentonite beds from the East Slovak Basin based on isotopic characteristics (K-Ar, δ^{18}O and δD) of illite-type nanoparticles. Clay Minerals 49/2, 247-275. DOI: 10.1180/claymin.2014.049.2.07.

Cloet, V., Lothenbach, B., Lura, P., Kosakowski, G., Curti, E., Wieland, E., Lanyon, G.W., Diomidis, N. & Leupin, O.X. (2019): Cementitious backfill for a high-level waste repository: impact of repository-induced effects. Nagra Arbeitsbericht NAB 18-41.

Cloet, V., Pekala, M., Smith, P., Wersin, P. & Diomidis, N. (2017): An evaluation of sulphide fluxes in the near field of a HLW repository. Nagra Technical Report NTB 17-04.

Combarieu, G. De, Schlegel, M.L., Neff, D., Foy, E., Vantelon, D. & Barboux, P. (2011): Glass-iron-clay interactions in a radioactive waste geological disposal: An integrated laboratory-scale experiment. Applied Geochemistry 26/1, 65-79.

Couture, R.A. (1985): Steam rapidly reduces the swelling capacity of bentonite. Nature 318/7.Nov, 50-52.

Cremers, A. (1968): Ionic movement in a colloidal environment: Measurement, interpretation and relevance to plant nutrition. Thesis. Katholieke Universiteit te Leuven, Leuven.

Cui, D. & Spahiu, K. (2002): The reduction of U (VI) on corroded iron under anoxic conditions. Radiochimica Acta 90/9-11, 623-628. DOI: 10.1524/ract.2002.90.9-11_2002.623.

Curti, E. (1993): Modelling bentonite pore waters for the Swiss high-level radioactive waste repository. PSI Bericht 93-05. Paul Scherrer Institut, Villigen.

Curti, E. (2022): Aqueous corrosion of vitrified nuclear waste: Current process understanding, Literature Review and Recommended Rates. Nagra Arbeitsbericht NAB 23-09.

Curti, E. (2023): Bentonite pore waters (BPW) for the sectoral plan, phase SGT-3: model development,testing and final calculations. Nagra Arbeitsbericht NAB 22-43.

Curti, E., Croivisier, J.L., Morvan, G. & Karpoff, A.M. (2006): Long-term corrosion of two nuclear waste reference glasses (MW and SON68): A kinetic and mineral alteration study. Applied Geochemistry 21/7, 1152-1168.

Curti, E., Fujiwara, K., Iijima, K., Tits, J., Cuesta, C., Kitamura, A., Glaus, M.A. & Müller, W. (2010): Radium uptake during barite recrystallization at 23 ± 2 ºC as a function of solution composition: An experimental ^{133}Ba and ^{226}Ra tracer study. Geochimica et Cosmochimica Acta 74/12, 3553-3570.

Curti, E. & Wersin, P. (2002): Assessment of porewater chemistry in the bentonite backfill for the Swiss SF/HLW repository. Nagra Technical Report NTB 02-09.

Damian, G., Damian, F., Szakács, Z., Iepure, G. & Aştefanei, D. (2021): Mineralogical and physico-chemical characterization of the Oraşu-Nou (Romania) bentonite resources. Minerals 11/9, 938. DOI: 10.3390/min11090938.

Dauzeres, A., Achiedo, G., Nied, D., Bernard, E., Alahrache, S. & Lothenbach, B. (2016): Magnesium perturbation in low-pH concretes placed in clayey environment—solid characterizations and modeling. Cement and Concrete Research 79, 137-150. DOI: 10.1016/j.cemconres.2015.09.002.

Dauzères, A., Le Bescop, P., Cau-Dit-Coumes, C., Brunet, F., Bourbon, X., Timonen, J., Voutilainen, M., Chomat, L. & Sardini, P. (2014): On the physico-chemical evolution of low-pH and CEM I cement pastes interacting with Callovo-Oxfordian pore water under its in situ CO_2 partial pressure. Cement and Concrete Research 58, 76-88. DOI: 10.1016/j.cemconres.2014.01.010.

Davies, C., Davie, C., Edward, C. & White, M. (2017): Physicochemical and Geotechnical Alterations to MX-80 Bentonite at the Waste Canister Interface in an Engineered Barrier System. Geosciences 7/3, 69. DOI: 10.3390/geosciences7030069.

Diomidis, N., Cloet, V., Leupin, O.X., Marschall, P., Poller, A. & Stein, M. (2016): Production, consumption and transport of gases in deep geological repositories according to the Swiss disposal concept. Nagra Technical Report NTB 16-03.

Diomidis, N., Guillemot, T. & King, F. (2023): Definition of reference corrosion rates for performance and safety assessments. Nagra Arbeitsbericht NAB 23-22.

Dixon, D.A. (2019): Review of the T-H-M-C properties of MX-80 bentonite. Report NWMO-TR-2019-07. Nuclear Waste Management Organisation NWMO, Toronto, Canada.

Dohrmann, R., Genske, D., Karnland, O., Kaufhold, S., Kiviranta, L., Olsson, S., Plötze, M., Sandén, T., Sellin, P., Svensson, D. & Valter, M. (2012a): Interlaboratory CEC and exchangeable cation study of bentonite buffer materials: I. Cu(II)-triethylenetetramine method. Clays and Clay Minerals 60/2, 162-175. DOI: 10.1346/CCMN.2012.0600206.

Dohrmann, R., Genske, D., Karnland, O., Kaufhold, S., Kiviranta, L., Olsson, S., Plötze, M., Sandén, T., Sellin, P., Svensson, D. & Valter, M. (2012b): Interlaboratory CEC and exchangeable cation study of bentonite buffer materials: II. Alternative methods. Clays and Clay Minerals 60/2, 176-185. DOI: 10.1346/CCMN.2012.0600207.

Dohrmann, R., Olsson, S., Kaufhold, S. & Sellin, P. (2013): Mineralogical investigations of the first package of the alternative buffer material test - II. Exchangeable cation population rearrangement. Clay Minerals 48/2, 215-233.

Donnan, F.G. (1995): Theory of membrane equilibria and membrane potentials in the presence of non-dialysing electrolytes. A contribution to physical-chemical physiology. Journal of Membrane Science 100/1, 45-55. DOI: 10.1016/0376-7388(94)00297-C.

ENSI (2018): Präzisierungen der sicherheitstechnischen Vorgaben für Etappe 3 des Sachplans geologische Tiefenlager. Sachplan geologische Tiefenlager, Etappe 3. ENSI 33/649. Eidgenössisches Nuklearsicherheitsinspektorat ENSI, Brugg.

ENSI (2020): Geologische Tiefenlager. Erläuterungsbericht zur Richtlinie ENSI-G03/d. Eidgenössisches Nuklearsicherheitsinspektorat ENSI, Brugg.

ENSI (2023): Geologische Tiefenlager. Ausgabe Dezember 2020 (Änderung vom 1. November 2023). Richtlinie für die schweizerischen Kernanlagen ENSI-G03/d. Eidgenössisches Nuklearsicherheitsinspektorat ENSI, Brugg.

Fernández, A.M., Kaufhold, S., Sánchez-Ledesma, D.M., Rey, J.J., Melón, A., Robredo, L.M. & Clavero, M.A. (2018): Evolution of the THC conditions in the FEBEX in situ test after 18 years of experiment: Smectite crystallochemical modifications after interactions of the bentonite with a C-steel heater at 100 °C. Applied Geochemistry 98, 152-171.

Fox, P.M., Tinnacher, R.M., Cheshire, M.C., Caporuscio, F., Carrero, S. & Nico, P.S. (2019): Effects of bentonite heating on U(VI) adsorption. Applied Geochemistry 109, 104392. DOI: 10.1016/j.apgeochem.2019.104392.

Fukatsu, Y., van Loon, L.R., Shafizadeh, A., Grolimund, D., Ikeda, Y. & Tsukahara, T. (2017): Effect of celestite precipitation in compacted illite on the diffusion of HTO, $^{36}Cl^{-}$, and $^{22}Na^{+}$. Energy Procedia 131, 133-139. DOI: 10.1016/j.egypro.2017.09.450.

Galán, E. & Ferrell, R.E. (2013): Chapter 3 - Genesis of clay minerals. *In:* Bergaya, F. & Lagaly, G. (eds.): Developments in Clay Science : Handbook of Clay Science, vol. 5. Elsevier, 83-126.

Gates, W., Anderson, J., Raven, M. & Churchman, G. (2002): Mineralogy of a bentonite from Miles, Queensland, Australia and characterisation of its acid activation products. Applied Clay Science 20/4, 189-197. DOI: 10.1016/S0169-1317(01)00072-2.

Gaucher, E.C. & Blanc, P. (2006): Cement/clay interactions - A review: Experiments, natural analogues, and modeling. Waste Management 26, 776-788.

Gens, A., Ledesma, A., Pusch, R. & Börgesson, L. (2004): THMC Processes in engineered barriers : The experience from Febex and prototype projects. Euradwaste '04 : Radioactive waste management community policy and research initiatives : Proceedings of the sixth European Commission confererence on the management and disposal of Radioactive waste, 29-31 March 2004, Luxembourg, EUR-21027, 259-270.

Gimmi, T. & Alt-Epping, P. (2018): Simulating Donnan equilibria based on the Nernst-Planck equation. Geochimica et Cosmochimica Acta 232, 1-13.

Giroud, N., Tomonaga, Y., Wersin, P., Briggs, S., King, F., Vogt, T. & Diomidis, N. (2018): On the fate of oxygen in a spent fuel emplacement drift in Opalinus Clay. Applied Geochemistry, Special Issue Clay Conference 2017 97, 270-278.

Gorski, C.A., Klüpfel, L.E., Voegelin, A., Sander, M. & Hofstetter, T.B. (2013): Redox properties of structural Fe in clay minerals: 3. Relationships between smectite redox and structural properties. Environmental Science & Technology 47/23, 13477-13485. DOI: 10.1021/es403824x.

Grenthe, I., Fuger, J. & Konings, R. (2004): Chemical thermodynamics of uranium: Reprint of the 1992 review. (NEA TDB Chemical Thermodynamics 1). OECD/NEA, Paris.

Greve-Dierfeld, S. von, Lothenbach, B., Vollpracht, A., Wu, B., Huet, B., Andrade, C., Medina, C., Thiel, C., Gruyaert, E., Vanoutrive, H., Del Saéz Bosque, I.F., Ignjatovic, I., Elsen, J., Provis, J.L., Scrivener, K., Thienel, K.-C., Sideris, K., Zajac, M., Alderete, N., Cizer, Ö., van den Heede, P., Hooton, R.D., Kamali-Bernard, S., Bernal, S.A., Zhao, Z., Shi, Z. & Belie, N. de (2020): Understanding the carbonation of concrete with supplementary cementitious materials: a critical review by RILEM TC 281-CCC. Materials and Structures 53/6. DOI: 10.1617/s11527-020-01558-w.

Grim, R.E. (1968): Clay mineralogy. (McGraw-Hill international series in the earth and planetary sciences). McGraw-Hill Book Company, Inc, New York.

Hadi, J., Wersin, P., Jenni, A. & Greneche, J.M. (2017): Redox evolution and Fe-bentonite interaction in the ABM2 experiment, Äspö Hard Rock Laboratory. Nagra Technical Report NTB 17-10.

Hadi, J., Wersin, P., Serneels, V. & Greneche, J.-M. (2019): Eighteen years of steel–bentonite interaction in the FEBEX in situ test at the Grimsel Test Site in Switzerland. Clays and Clay Minerals 67/2, 111-131. DOI: 10.1007/s42860-019-00012-5.

Huggett, J.M. (2005): Sedimentary rocks - Clays and their diagenesis. *In:* Selley, R.C., Plimer, I.R. & Cocks, L.M.R. (eds.): Encyclopedia of geology. Elsevier, Amsterdam, Heidelberg, 62-70.

Hummel, W., Kulik, D.A. & Miron, G.D. (2023): Solubility Limits for Bentonite Near Field (Update of NTB 14-06). Nagra Technical Report NTB 23-04.

Hummel, W. & Thoenen, T. (2023): The PSI chemical thermodynamic database 2020. Nagra Technical Report NTB 21-03.

Idemitsu, K., Okubo, N., Inagaki, Y., Arima, T., Akiyama, D., Konashi, K. & Watanabe, M. (2017): Plutonium migration in compacted bentonite with iron corrosion for 15 Years. MRS Advances 2/12, 693-698. DOI: 10.1557/adv.2017.12.

Inoue, A. (1995): Formation of clay minerals in hydrothermal environments. *In:* Velde, B. (ed.): Origin and mineralogy of clays. Clays and the Environment. Springer Berlin Heidelberg, Berlin, Heidelberg, s.l., 268-329.

Jenni, A., Gimmi, T., Alt-Epping, P., Mäder, U. & Cloet, V. (2017): Interaction of ordinary Portland cement and Opalinus Clay: Dual porosity modelling compared to experimental data. Physics and Chemistry of the Earth, Parts A/B/C 99, 22-37. DOI: 10.1016/j.pce.2017.01.004.

Jenni, A. & Mäder, U. (2021): Reactive transport simulation of low-pH cement interacting with Opalinus Clay using a dual porosity electrostatic model. Minerals 11/7, 664. DOI: 10.3390/min11070664.

Jenni, A., Mäder, U., Lerouge, C., Gaboreau, S. & Schwyn, B. (2014): In situ interaction between different concretes and Opalinus Clay. Physics and Chemistry of the Earth 70-71, 71-83. DOI: 10.1016/j.pce.2013.11.004.

Jenni, A., Wersin, P., Thoenen, T., Baeyens, B., Ferrari, A., Gimmi, T., Mäder, U., Marschall, P., Hummel, W. & Leupin, O. (2019): Bentonite backfill performance in a high-level waste repository: a geochemical perspective. Nagra Technical Report NTB 19-03.

Jodin-Caumon, M.-C., Mosser-Ruck, R., Randi, A., Pierron, O., Cathelineau, M. & Michau, N. (2012): Mineralogical evolution of a claystone after reaction with iron under thermal gradient. Clays and Clay Minerals 60/5, 443-455. DOI: 10.1346/CCMN.2012.0600501.

Jodin-Caumon, M.-C., Mosser-Ruck, R., Rousset, D., Randi, A., Cathelineau, M. & Michau, N. (2010): Effect of a thermal gradient on iron-clay interactions. Clays and Clay Minerals 58/5, 667-681. DOI: 10.1346/CCMN.2010.0580506.

Johnson, J.W., Oelkers, E.H. & Helgeson, H.C. (1992): SUPCRT92: A software package for calculating the standard molal thermodynamic properties of minerals, gases, aqueous species, and reactions from 1 to 5000 bar and 0 to 1000°C. Computers & Geosciences 18/7, 899-947. DOI: 10.1016/0098-3004(92)90029-Q.

Johnson, L.H., Curti, E. & Spahiu, K. (2023): A radionuclide release model for spent UO_2 and MOX fuel for safety assessment with application to waste to be disposed of in a deep geological repository in Switzerland. Nagra Arbeitsbericht NAB 23-10.

Johnson, L.H., Niemeyer, M., Klubertanz, G., Siegel, P. & Gribi, P. (2002): Calculations of the temperature evolution of a repository for spent fuel, vitrified high-level waste and intermediate level waste in Opalinus Clay. Nagra Technical Report NTB 01-04.

Kampmeyer, P.M. (1952): The temperature dependence of viscosity for water and mercury. Journal of Applied Physics 23/1, 99-102. DOI: 10.1063/1.1701986.

Karnland, O. (2010): Chemical and mineralogical characterization of the bentonite buffer for the acceptance control procedure in a KBS-3 repository. Technical Report TR 10-60. Swedish Nuclear Fuel and Waste Management SKB, Stockholm.

Karnland, O., Olsson, S. & Nilsson, U. (2006): Mineralogy and sealing properties of various bentonites and smectite-rich clay materials. Technical Report TR 06-30. Swedish Nuclear Fuel and Waste Management SKB, Stockholm, Sweden.

Karri, S., Sierra-Alvarez, R. & Field, J.A. (2005): Zero valent iron as an electron-donor for methanogenesis and sulfate reduction in anaerobic sludge. Biotechnology and bioengineering 92/7, 810-819. DOI: 10.1002/bit.20623.

Kaufhold, S., Dohrmann, R., Götze, N. & Svensson, D. (2017): Characterization of the second parcel of the alternative buffer material (ABM) Experiment – I mineralogical reactions. Clays and Clay Minerals 65/1, 27-41. DOI: 10.1346/CCMN.2016.064047.

Kaufhold, S., Dohrmann, R., Sandén, T., Sellin, P. & Svensson, D. (2013): Mineralogical investigations of the first package of the alternative buffer material test - I. Alteration of bentonites. Clay Minerals 48/2, 199-213.

Kaufhold, S., Dohrmann, R., Ufer, K. & Kober, F. (2018): Interactions of bentonite with metal and concrete from the FEBEX experiment: mineralogical and geochemical investigations of selected sampling sites. Clay Minerals 53/4, 745-763.

Kaufhold, S., Dohrmann, R. & Weber, C. (2021): Evolution of the pH value at the vicinity of the iron-bentonite interface. Applied Clay Science 201, 105929. DOI: 10.1016/ j.clay.2020.105929.

Kaufhold, S., Hassel, A.W., Sanders, D. & Dohrmann, R. (2015): Corrosion of high-level radioactive waste iron-canisters in contact with bentonite. Journal of Hazardous Materials 285, 464-473.

Kaufhold, S., Klimke, S., Schloemer, S., Alpermann, T., Renz, F. & Dohrmann, R. (2020a): About the corrosion mechanism of metal iron in contact with bentonite. ACS Earth Space Chemistry 4, 711-721.

Kaufhold, S., Schippers, A., Marx, A. & Dohrmann, R. (2020b): SEM study of the early stages of Fe-bentonite corrosion—The role of naturally present reactive silica. Corrosion Science 171, 108716. DOI: 10.1016/j.corsci.2020.108716.

KEG (2003): Kernenergiegesetz (KEG) of March 21, 2003, status as of January 1, 2024. Systematische Sammlung des Bundesrechts SR 732.1, Schweiz.

Kerleguer, V. (2020): Apport de l'étude de matériaux modèles $U_{1-x}Pu_xO_2$ à la compréhension des mécanismes d'altération des combustibles UOx et MOx en stockage géologique. Ph.D. thesis. Université PSL, Paris, France.

KEV (2004): Kernenergieverordnung (KEV) of December 10, 2004, status as of January 1, 2024. Systematische Sammlung des Bundesrechts SR 732.11, Schweiz.

Kinniburgh, D.G. & Cooper, D.M. (2004): Predominance and mineral stability diagrams revisited. Environmental Science & Technology 38/13, 3641-3648. DOI: 10.1021/ es034927l.

Kirsimäe, K., Somelar, P. & Jõeleht, A. (2020): Illitization of the lower Cambrian (Terreneuvian) Blue Clay in the northern Baltic Palaeobasin. Estonian Journal of Earth Sciences 69/4, 200. DOI: 10.3176/earth.2020.14.

Kober, F., Villar, M., Turrero, M., Wersin, P. & Gaus, I. (2017): FEBEX-DP: Dismantling FEBEX after 18 years, activities, results, conclusions. Abstract 7. Clay Conference 2017, 24.-27. September, Davos, Switzerland, the 7th International Conference on Clays in Natural and Engineered Barriers for Radioactive Waste Confinement. Book of Abstracts, 9-10.

Komarneni, S. (1979): Cesium sorption by clay minerals and shales at elevated temperatures. Journal of Inorganic and Nuclear Chemistry 41/3, 397-400. DOI: 10.1016/0022-1902(79)80153-0.

Kosakowski, G. (2023): Reactive transport modelling of material interface evolution in the HLW near field. Nagra Arbeitsbericht NAB 23-33.

Kosakowski, G. & Berner, U. (2013): The evolution of clay rock/cement interfaces in a cementitious repository for low- and intermediate level radioactive waste. Physics and Chemistry of the Earth 64, 65-86.

Kosakowski, G., Berner, U., Wieland, E., Glaus, M. & Degueldre, C. (2014): Geochemical evolution of the L/ILW near-field. Nagra Technical Report NTB 14-11.

Kosakowski, G. & Watanabe, N. (2014): OpenGeoSys-Gem: A numerical tool for calculating geochemical and porosity changes in saturated and partially saturated media. Physics and Chemistry of the Earth, Parts A/B/C 70-71, 138-149. DOI: 10.1016/j.pce.2013.11.008.

Krynicki, K., Green, C.D. & Sawyer, D.W. (1978): Pressure and temperature dependence of self-diffusion in water. Faraday Discussions of the Chemical Society 66, 199. DOI: 10.1039/dc9786600199.

Kulik, D.A., Fernandes, M.M. & Baeyens, B. (2018): The 2SPNE SC/CE sorption model in GEM-Selektor v.3.4 code package (ClaySor): Implementation, tests, and user guide. Nagra Arbeitsbericht NAB 18-27.

Kulik, D.A., Wagner, T., Dmytrieva, S.V., Kosakowski, G., Hingerl, F.F., Chudnenko, K.V. & Berner, U.R. (2013): GEM-Selektor geochemical modeling package: revised algorithm and GEMS3K numerical kernel for coupled simulation codes. Comput Geosci 17/1, 1-24. DOI: 10.1007/s10596-012-9310-6.

Kumpulainen, S., Kiviranta, L. & Korkeakoski, P. (2016): Long-term effects of an iron heater and Äspö groundwater on smectite clays: Chemical and hydromechanical results from the in situ alternative buffer material (ABM) test package 2. Clay Minerals 51/2, 129-144. DOI: 10.1180/claymin.2016.051.2.02.

Lanson, B., Lantenois, S., van Aken, P.A., Bauer, A. & Plançon, A. (2012): Experimental investigation of smectite interaction with metal iron at 80 °C: Structural characterization of newly formed Fe-rich phyllosilicates. American Mineralogist 97/5-6, 864-871. DOI: 10.2138/am.2012.4062.

Lanyon, G.W. & Gaus, I. (2016): Main outcomes and review of the FEBEX In Situ Test (GTS) and Mock-up after 15 years of operation. Nagra Technical Report NTB 15-04.

Le Pape, P., Rivard, C., Pelletier, M., Bihannic, I., Gley, R., Mathieu, S., Salsi, L., Migot, S., Barres, O., Villiéras, F. & Michau, N. (2015): Action of a clay suspension on an Fe(0) surface under anoxic conditions: Characterization of neoformed minerals at the Fe(0)/solution and Fe(0)/atmosphere interfaces. Applied Geochemistry 61, 62-71. DOI: 10.1016/j.apgeochem.2015.05.008.

Lerouge, C., Gaboreau, S., Grangeon, S., Claret, F., Warmont, F., Jenni, A., Cloet, V. & Mäder, U. (2017): In situ interactions between Opalinus Clay and Low Alkali Concrete. Physics and Chemistry of the Earth, Parts A/B/C 99, 3-21. DOI: 10.1016/j.pce.2017.01.005.

Leupin, O.X., Bernier-Latmani, R., Bagnoud, A., Moors, H., Leys, N., Wouters, K. & Stroes-Gascoyne, S. (2018): Fifteen years of microbiological investigation in Opalinus Clay at the Mont Terri rock laboratory (Switzerland). *In:* Bossart, P. & Milnes, A.G. (eds.): Mont Terri Rock Laboratory, 20 Years. Two Decades of Research and Experimentation on Claystones for Geological Disposal of Radioactive Waste. 5th ed. (Swiss Journal of Geosciences Supplement). Birkhäuser Cham, 345-356.

Leupin, O.X., Birgersson, M., Karnland, O., Korkeakoski, P., Mäder, U., Sellin, P. & Wersin, P. (2014): Montmorillonite stability under near-field conditions. Nagra Technical Report NTB 14-12.

Leupin, O.X., Smart, N.R., Zhang, Z., Stefanoni, M., Angst, U., Papafotiou, A. & Diomidis, N. (2021): Anaerobic corrosion of carbon steel in bentonite: An evolving interface. Corrosion Science 187, 109523. DOI: 10.1016/j.corsci.2021.109523.

Li, Q., Steefel, C.I. & Jun, Y.-S. (2017): Incorporating nanoscale effects into a continuum-scale reactive transport model for CO_2-deteriorated cement. Environmental Science & Technology 51/18, 10861-10871. DOI: 10.1021/acs.est.7b00594.

Li, Y., Cai, J., Song, M., Ji, J. & Bao, Y. (2016): Influence of organic matter on smectite illitization: A comparison between red and dark mudstones from the Dongying Depression, China. American Mineralogist 101/1, 134-145. DOI: 10.2138/am-2016-5263.

Lothenbach, B., Kulik, D.A., Matschei, T., Balonis, M., Baquerizo, L., Dilnesa, B., Miron, G.D. & Myers, R.J. (2019): Cemdata18: A chemical thermodynamic database for hydrated Portland cements and alkali-activated materials. Cement and Concrete Research 115, 472-506. DOI: 10.1016/j.cemconres.2018.04.018.

Lotz, H., Carrière, C., Bataillon, C., Gardes, E., Monnet, I., Foy, E., Schlegel, M.L., Dynes, J.J., Neff, D., Mercier-Bion, F. & Dillmann, P. (2021): Investigation of steel corrosion in MX80 bentonite at 120°C. Materials and Corrosion 72/1-2, 120-130. DOI: 10.1002/maco.202011777.

Luraschi, P., Gimmi, T., van Loon, L.R., Shafizadeh, A. & Churakov, S.V. (2020): Evolution of HTO and $^{36}Cl^-$ diffusion through a reacting cement-clay interface (OPC paste-Na montmorillonite) over a time of six years. Applied Geochemistry 119, 104581. DOI: 10.1016/j.apgeochem.2020.104581.

Ma, B. & Lothenbach, B. (2020a): Synthesis, characterization, and thermodynamic study of selected Na-based zeolites. Cement and Concrete Research 135, 106111.

Ma, B. & Lothenbach, B. (2020b): Thermodynamic study of cement/rock interactions using experimentallygenerated solubility data of zeolites. Cement and Concrete Research 135, 106149.

Mäder, U., Jenni, A., Lerouge, C., Gaboreau, S., Miyoshi, S., Kimura, Y., Cloet, V., Fukaya, M., Claret, F., Otake, T., Shibata, M. & Lothenbach, B. (2018): 5-year chemico-physical evolution of concrete–claystone interfaces, Mont Terri rock laboratory (Switzerland). *In:* Bossart, P. & Milnes, A.G. (eds.): Mont Terri Rock Laboratory, 20 Years. Two Decades of Research and Experimentation on Claystones for Geological Disposal of Radioactive Waste. 5th ed. (Swiss Journal of Geosciences Supplement). Birkhäuser Cham, 309-329.

Mäder, U. & Wersin, P. (2023): Reference porewaters for SGT Stage 3 of the Opalinus Clay for the siting regions Jura Ost (JO), Nördlich Lägern (NL) and Zürich Nordost (ZNO). Nagra Arbeitsbericht NAB 22-47.

Magill, J. & Dreher, R. (2009): The NUCLEONICA Nuclear Science Portal. AIP Conference Proceedings 1164/1, 100-106. DOI: 10.1063/1.3224690.

Manov, G.G., Lollis, N.J. de & Acree, S.F. (1944): Ionization constant of boric acid and the pH of certain borax-chloride buffer solutions from 0° to 60 °C (Research Paper RP1609). Journal of Research of the National Bureau of Standards 33/4, 287-306.

Marques Fernandes, M., Ishidera, T. & Baeyens, B. (2017): Sorption of Cs(I), Ni(II), Eu(III) and Th(IV) on montmorillonite, MX-80 bentonite and Altered Buffer Material at 25 °C and 90 °C. Nagra Arbeitsbericht NAB 17-49.

Marschall, P., Giger, S., La Vassière, R. de, Shao, H., Leung, H., Nussbaum, C., Trick, T., Lanyon, B., Senger, R., Lisjak, A. & Alcolea, A. (2018): Hydro-mechanical evolution of the EDZ as transport path for radionuclides and gas: insights from the Mont Terri rock laboratory (Switzerland). *In:* Bossart, P. & Milnes, A.G. (eds.): Mont Terri Rock Laboratory, 20 Years. Two Decades of Research and Experimentation on Claystones for Geological Disposal of Radioactive Waste. 5th ed. (Swiss Journal of Geosciences Supplement). Birkhäuser Cham, 175-196.

Martin, L.H., Leemann, A., Milodowski, A.E., Mäder, U.K., Münch, B. & Giroud, N. (2016): A natural cement analogue study to understand the long-term behaviour of cements in nuclear waste repositories: Maqarin (Jordan). Applied Geochemistry 71, 20-34. DOI: 10.1016/j.apgeochem.2016.05.009.

Marty, N.C., Claret, F., Lassin, A., Tremosa, J., Blanc, P., Madé, B., Giffaut, E., Cochepin, B. & Tournassat, C. (2015a): A database of dissolution and precipitation rates for clay-rocks minerals. Applied Geochemistry 55, 108-118. DOI: 10.1016/j.apgeochem.2014.10.012.

Marty, N.C., Tournassat, C., Burnol, A., Giffaut, E. & Gaucher, E.C. (2009): Influence of reaction kinetics and mesh refinement on the numerical modelling of concrete/clay interactions. Journal of Hydrology 364/1, 58-72. DOI: 10.1016/j.jhydrol.2008.10.013.

Marty, N.C.M., Bildstein, O., Blanc, P., Claret, F., Cochepin, B., Gaucher, E.C., Jacques, D., Lartigue, J.-E., Liu, S., Mayer, K.U., Meeussen, J.C.L., Munier, I., Pointeau, I., Su, D. & Steefel, C.I. (2015b): Benchmarks for multicomponent reactive transport across a cement/clay interface. Computational Geosciences 19/3, 635-653. DOI: 10.1007/s10596-014-9463-6.

McGinnes, D.F. (2002): Model radioactive waste inventory for reprocessing waste and spent fuel. Nagra Technical Report NTB 01-01.

Meunier, A. & Velde, B. (2004): Illite. Origins, evolution and metamorphism. 1st ed. Springer Berlin Heidelberg.

Meunier, A., Velde, B. & Griffault, L. (1998): The reactivity of bentonites: a review. An application to clay barrier stability for nuclear waste storage. Clay Minerals 33/2, 187-196. DOI: 10.1180/000985598545462.

Miao, Z., Brusseau, M.L., Carroll, K.C., Carreón-Diazconti, C. & Johnson, B. (2012): Sulfate reduction in groundwater: characterization and applications for remediation. Environmental Geochemistry and Health 34/4, 539-550. DOI: 10.1007/s10653-011-9423-1.

Mills, R. (1973): Self-diffusion in normal and heavy water in the range 1 - 45 °C. The Journal of Physical Chemistry 77/5, 685-688. DOI: 10.1021/j100624a025.

Morcillo, M., Chico, B., Alcántara, J., Díaz, I., Simancas, J. & La Fuente, D. de (2015): Atmospheric corrosion of mild steel in chloride-rich environments. Questions to be answered. Materials and Corrosion 66/9, 882-892. DOI: 10.1002/maco.201407940.

Mosser-Ruck, R., Pignatelli, I., Bourdelle, F., Abdelmoula, M., Barres, O., Guillaume, D., Charpentier, D., Rousset, D., Cathelineau, M. & Michau, N. (2016): Contribution of long-term hydrothermal experiments for understanding the smectite-to-chlorite conversion in geological environments. Contributions to Mineralogy and Petrology 171/11, 97. DOI: 10.1007/s00410-016-1307-z.

Mosser-Ruck, R., Sterpenich, J., Michau, N., Jodin-Caumon, M.-C., Randi, A., Abdelmoula, M., Barres, O. & Cathelineau, M. (2020): Serpentinization and H_2 production during an iron-clay interaction experiment at 90°C under low CO_2 pressure. Applied Clay Science 191, 105609. DOI: 10.1016/j.clay.2020.105609.

Müller-Vonmoos, M. & Kahr, G. (1983): Mineralogische Untersuchungen von Wyoming Bentonite MX-80 und Montigel. Nagra Technical Report NTB 83-12.

Nagra (1985): Project Gewähr 1985: Nuclear Waste Management in Switzerland: Feasibility studies and safety analyses. Nagra Project Report NGB 85-09.

Nagra (2002): Project Opalinus Clay: Safety report: Demonstration of disposal feasibility for spent fuel, vitrified high-level waste and long-lived intermediate-level waste (Entsorgungsnachweis). Nagra Technical Report NTB 02-05.

Nagra (2014a): Modellhaftes Inventar für radioaktive Materialien MIRAM 14. Nagra Technical Report NTB 14-04.

Nagra (2014b): Provisional safety analyses for SGT Stage 2. Models, codes and general modelling approach. Nagra Technischer Bericht NTB 14-09.

Nagra (2014c): SGT Etappe 2: Vorschlag weiter zu untersuchender geologischer Standortgebiete mit zugehörigen Standortarealen für die Oberflächenanlage. Charakteristische Dosisintervalle und Unterlagen zur Bewertung der Barrierensysteme. Nagra Technical Report NTB 14-03.

Nagra (2017): Sachplan geologische Tiefenlager, Etappe 2: Fragen des ENSI und seiner Experten und zugehörige Antworten der Nagra. Nagra Arbeitsbericht NAB 17-01.

Nagra (2022): Module der Lagerarchitektur. Nagra Arbeitsbericht NAB 22-35.

Nagra (2023): Modellhaftes Inventar für radioaktive Materialien MIRAM-RBG. Nagra Technischer Bericht NTB 22-05.

Nagra (2024a): Abfallzuteilung und Betrachtungszeitraum für den Standortvergleich und Nachweiszeitraum für den Sicherheitsnachweis für das geologische Tiefenlager. Nagra Arbeitsbericht NAB 24-05.

Nagra (2024b): Design and performance assessment of HLW disposal canisters. Nagra Technical Report NTB 24-20.

Nagra (2024c): Geosynthesis of Northern Switzerland. Nagra Technischer Bericht NTB 24-17.

Nagra (2024d): Phenomenological Description of the Evolution of a Combined Geological Repository for Radioactive Waste in Opalinus Clay. Nagra Arbeitsbericht NAB 24-20 Rev. 1.

Nagra (2024e): Post-closure safety report. Nagra Technical Report NTB 24-10.

Nagra (2024f): Synthesis of the performance assessment for a combined repository. Nagra Technical Report NTB 24-22.

Nagra (2024g): Thermo-hydraulic modelling of the temperature distribution in the siting regions JO, NL and ZNO. Nagra Arbeitsbericht NAB 24-24.

Nagra (2025a): Rahmenbewilligungsgesuch für das geologische Tiefenlager – Begründung der Standortwahl. Nagra Technischer Bericht NTB 24-03.

Nagra (2025b): Rahmenbewilligungsgesuch für das geologische Tiefenlager – Sicherheitsbericht. Nagra Technischer Bericht NTB 24-01.

Necib, S., Diomidis, N., Keech, P. & Nakayama, M. (2018): Corrosion of carbon steel in clay environments relevant to radioactive waste geological disposals. *In:* Bossart, P. & Milnes, A.G. (eds.): Mont Terri Rock Laboratory, 20 Years. Two Decades of Research and Experimentation on Claystones for Geological Disposal of Radioactive Waste. 5th ed. (Swiss Journal of Geosciences Supplement). Birkhäuser Cham, 329-342.

Newman, A.C.D. (ed.) (1987): Chemistry of clays and clay minerals. New York : J. Wiley; London : Mineralogical Society.

Novozamsky, I., Beek, J. & Bolt, G.H. (1976): Chapter 2 chemical equilibria. *In:* Bolt, G.H. & Bruggenwert, M. (eds.): Soil Chemistry: A. Basic Elements. (Developments in Soil Science, Volume 5, Part A). Elsevier, 13-42.

Önal, M., Kahraman, S. & Sarıkaya, Y. (2007): Differentiation of α-cristobalite from opals in bentonites from Turkey. Applied Clay Science 35/1, 25-30. DOI: 10.1016/j.clay.2006.07.003.

Osacký, M., Šucha, V., Czímerová, A. & Madejová, J. (2010): Reaction of smectites with iron in a nitrogen atmosphere at 75°C. Applied Clay Science 50/2, 237-244. DOI: 10.1016/j.clay.2010.08.004.

Osacký, M., Šucha, V., Czímerová, A., Pentrák, M. & Madejová, J. (2013): Reaction of smectites with iron in aerobic conditions at 75°C. Applied Clay Science 72, 26-36. DOI: 10.1016/j.clay.2012.12.010.

Oscarson, D.W. & Dixon, D.A. (1989): The effect of steam on montmorillonite. Applied Clay Science 4/3, 279-292. DOI: 10.1016/0169-1317(89)90035-5.

Oscarson, D.W. & Dixon, D.A. (1990): Effect of heating unsaturated bentonite on the swelling and hydraulic properties of subsequently saturated clay. *In:* Allen, B.L. (ed.): Engineering in our environment. Proceedings annual conference and 1st Biennial Environmental Speciality Conference May 16-18. 5 volumes. (Proceedings of the CSCE Annual Conference, 1990), Hamilton, Ontario, 312-323.

Palandri, J.L. & Kharaka, Y.K. (2004): A compilation of rate parameters of water-mineral interaction kinetics for application to geochemical modeling. U.S. Geological Survey. U.S. Department of the Interior U.S. Geological Survey.

Papafotiou, A. & Senger, R. (2014): Sensitivity analyses of gas release from a SF/HLW repository in the Opalinus Clay in the candidate siting regions of Northern Switzerland. Nagra Arbeitsbericht NAB 14-10.

Patel, R., Punshon, C., Nicholas, J., Bastid, P., Zhou, R., Schneider, C., Bagshaw, N., Howse, D., Hutchinson, E., Asano, R. & King, S. (2012): Canister design concepts for disposal of spent fuel and high level waste. Nagra Technical Report NTB 12-06.

Pfingsten, W., Bradbury, M. & Baeyens, B. (2011): The influence of Fe(II) competition on the sorption and migration of Ni(II) in MX-80 bentonite. Applied Geochemistry 26/8, 1414-1422. DOI: 10.1016/j.apgeochem.2011.05.014.

Pignatelli, I., Bourdelle, F., Bartier, D., Mosser-Ruck, R., Truche, L., Mugnaioli, E. & Michau, N. (2014): Iron–clay interactions: Detailed study of the mineralogical transformation of claystone with emphasis on the formation of iron-rich T–O phyllosilicates in a step-by-step cooling experiment from 90°C to 40°C. Chemical Geology 387, 1-11. DOI: 10.1016/ j.chemgeo.2014.08.010.

Pignatelli, I., Mugnaioli, E., Hybler, J., Mosser-Ruck, R., Cathelineau, M. & Michau, N. (2013): A multi-technique characterization of cronstedtite synthesized by iron-clay interaction in a step-by-step cooling procedure. Clays Clay Miner. 61/4, 277-289. DOI: 10.1346/CCMN.2013.0610408.

Prasianakis, N.I., Kosakowski, G., Gimmi, T., Luraschi, P., Miron, G.D., Pfingsten, W. & Churakov, S.V. (2022): Cement - Clay : Synthesis of transport across the cement-clay interface. Nagra Arbeitsbericht NAB 22-34.

Pusch, R. (2000): On the effect of hot water vapor on MX-80 clay. Technical Report TR 00-16. Swedish Nuclear Fuel and Waste Management SKB, Stockholm, Sweden.

Pusch, R., Bluemling, P. & Johnson, L. (2003): Performance of strongly compressed MX-80 pellets under repository-like conditions. Applied Clay Science 23/1, 239-244. DOI: 10.1016/S0169-1317(03)00108-X.

Pytte, A.M. & Reynolds, R.C. (1989): The thermal transformation of smectite to illite. *In:* Naeser, N.D. & McCulloh, T.H. (eds.): Thermal History of Sedimentary Basins. Methods and Case Histories. Springer, New York, 133-140.

Rébiscoul, D., Tormos, V., Godon, N., Mestre, J.-P., Cabie, M., Amiard, G., Foy, E., Frugier, P. & Gin, S. (2015): Reactive transport processes occurring during nuclear glass alteration in presence of magnetite. Applied Geochemistry 58, 26-37. DOI: 10.1016/ j.apgeochem.2015.02.018.

Reddy, B., Padovani, C., Rance, A.P., Smart, N.R., Cook, A., Haynes, H.M., Milodowski, A.E., Field, L.P., Kemp, S.J., Martin, A. & Diomidis, N. (2021a): The anaerobic corrosion of candidate disposal canister materials in compacted bentonite exposed to natural granitic porewater containing native microbial populations. Materials and Corrosion 72/1-2, 361-382. DOI: 10.1002/maco.202011798.

Reddy, B., Padovani, C., Smart, N.R., Rance, A.P., Cook, A., Milodowski, A., Field, L., Kemp, S. & Diomidis, N. (2021b): Further results on the in situ anaerobic corrosion of carbon steel and copper in compacted bentonite exposed to natural Opalinus Clay porewater containing native microbial populations. Materials and Corrosion 72/1-2, 268-281. DOI: 10.1002/ maco.202011785.

Rivard, C., Pelletier, M., Michau, N., Razafitianamaharavo, A., Abdelmoula, M., Ghanbaja, J. & Villiéras, F. (2015): Reactivity of Calloyo-Oxfordian claystone and its clay fraction with metallic iron: role of non-clay minerals in the interaction mechanism. Clays and Clay Minerals 63/4, 290-310. DOI: 10.1346/CCMN.2015.0630404.

Rivard, C., Pelletier, M., Michau, N., Razafitianamaharavo, A., Bihannic, I., Abdelmoula, M., Ghanbaja, J. & Villiéras, F. (2013): Berthierine-like mineral formation and stability during the interaction of kaolinite with metallic iron at 90 °C under anoxic and oxic conditions. American Mineralogist 98/1, 163-180. DOI: 10.2138/am.2013.4073.

Ross, C.S. & Shannon, E.V. (1926): The minerals of bentonite and related clays and their physical properties. Journal of the American Ceramic Society 9/2, 77-96. DOI: 10.1111/j.1151-2916.1926.tb18305.x.

Sato, T., Murakami, T. & Watanabe, T. (1996): Change in layer charge of smectites and smectite layers in illite/smectite during diagenetic alteration. Clays and Clay Minerals 44/4, 460-469. DOI: 10.1346/CCMN.1996.0440403.

Savage, D. (2014): An assessment of the impact of the long term evolution of engineered structures on the safety-relevant functions of the bentonite buffer in a HLW repository. Nagra Technical Report NTB 13-02.

Savage, D., Arthur R., Watson C. & Wilson J. (2010a): An evaluation of models of bentonite pore water evolution. Report 2010:12. Swedish Radiation Safety Authority SSM.

Savage, D. & Cloet, V. (2018): A review of cement-clay modelling. Nagra Arbeitsbericht NAB 18-24.

Savage, D., Walker, C. & Benbow, S. (2010b): An analysis of potential changes to barrier components due to interaction with a concrete liner in a repository for SF/HLW in Opalinus Clay. Nagra Arbeitsbericht NAB 10-17.

Scheidegger, A.M., Grolimund, D., Cui, D., Devoy, J., Spahiu, K., Wersin, P., Bonhoure, I. & Janousch, M. (2003): Reduction of selenite on iron surfaces: A micro-spectroscopic study. J. Phys. IV France 104, 417-420. DOI: 10.1051/jp4:20030112.

Schlegel, M.L., Bataillon, C., Brucker, F., Blanc, C., Prêt, D., Foy, E. & Chorro, M. (2014): Corrosion of metal iron in contact with anoxic clay at 90°C: Characterization of the corrosion products after two years of interaction. Applied Geochemistry 51, 1-14. DOI: 10.1016/j.apgeochem.2014.09.002.

Schlegel, M.L., Martin, F., Fenart, M., Blanc, C., Varlet, J., Foy, E., Prêt, D. & Trcera, N. (2019): Corrosion at the carbon steel-clay compact interface at 90°C: Insight into short- and long-term corrosion aspects. Corrosion Science 152, 31-44. DOI: 10.1016/j.corsci.2019.01.027.

Seiphoori, A. (2014): Thermo-hydro-mechanical characterisation and modelling of MX-80 granular bentonite. ETH Lausanne, Thèse No. 6159. École polytechnique fédérale de Lausanne EPFL, Lausanne.

Sena, C., Salas, J. & Arcos, D. (2010): Aspects of geochemical evolution of the SKB near field in the frame of SR-Site. Technical Report TR 10-59. Swedish Nuclear Fuel and Waste Management SKB, Stockholm, Sweden.

Senger, R. & Ewing, J. (2008): Evolution of temperature and water content in the bentonite buffer: Detailed modelling of two-phase flow processes associated with the early closure period. Nagra Arbeitsbericht NAB 08-32.

Senger, R., Papafotiou, A. & Marschall, P. (2014): Thermo-hydraulic simulations of the near-field of a SF/HLW repository during early- and late-time post-closure period. Nagra Arbeitsbericht NAB 14-11.

Shafizadeh, A., Gimmi, T., van Loon, L.R., Kaestner, A.P., Mäder, U.K. & Churakov, S.V. (2020): Time-resolved porosity changes at cement-clay interfaces derived from neutron imaging. Cement and Concrete Research 127, 105924. DOI: 10.1016/ j.cemconres.2019.105924.

Shao, H., Kosakowski, G., Berner, U., Kulik, D.A., Mäder, U. & Kolditz, O. (2013): Reactive transport modeling of the clogging process at Maqarin natural analogue site. Physics and Chemistry of the Earth, Parts A/B/C 64, 21-31. DOI: 10.1016/j.pce.2013.01.002.

Smart, N.R., Reddy, B., Rance, A.P., Nixon, D.J. & Diomidis, N. (2017a): The anaerobic corrosion of carbon steel in saturated compacted bentonite in the Swiss repository concept. Corrosion Engineering, Science and Technology 52/sup1, 113-126. DOI: 10.1080/ 1478422X.2017.1316088.

Smart, N.R., Reddy, B., Rance, A.P., Nixon, D.J., Frutschi, M., Bernier-Latmani, R. & Diomidis, N. (2017b): The anaerobic corrosion of carbon steel in compacted bentonite exposed to natural Opalinus Clay porewater containing native microbial populations. Corrosion Engineering, Science and Technology 52/sup1, 101-112. DOI: 10.1080/ 1478422X.2017.1315233.

Soler, J.M. (2016): Two-dimensional reactive transport modeling of the alteration of a fractured limestone by hyperalkaline solutions at Maqarin (Jordan). Applied Geochemistry 66, 162-173. DOI: 10.1016/j.apgeochem.2015.12.012.

Soler, J.M., Steefel, C.I., Gimmi, T., Leupin, O.X. & Cloet, V. (2019): Modeling the ionic strength effect on diffusion in clay. The DR-A experiment at Mont Terri. ACS Earth and Space Chemistry 3/3, 442-451. DOI: 10.1021/ACSEARTHSPACECHEM.8B00192.

Steefel, C.I. & Lichtner, P.C. (1994): Diffusion and reaction in rock matrix bordering a hyperalkaline fluid-filled fracture. Geochimica et Cosmochimica Acta 58/17, 3595-3612. DOI: 10.1016/0016-7037(94)90152-X.

Steefel, C.I. & Lichtner, P.C. (1998): Multicomponent reactive transport in discrete fractures: II: Infiltration of hyperalkaline groundwater at Maqarin, Jordan, a natural analogue site. Journal of Hydrology 209/1, 200-224. DOI: 10.1016/S0022-1694(98)00173-5.

Stroes-Gascoyne, S. (2011): Microbiological characteristics of compacted bentonite for a dry density of 1'450 kg/m3: A literature review. Nagra Arbeitsbericht NAB 11-05.

Su, D., Xie, M., Mayer, K.U. & MacQuarrie, K.T.B. (2022): Simulation of diffusive solute transport in heterogeneous porous media with dipping anisotropy. Frontiers in Water 4, 974145. DOI: 10.3389/frwa.2022.974145.

Surnam, B.Y.R., Chui, C.-W., Xiao, H. & Liang, H. (2016): Investigating atmospheric corrosion behavior of carbon steel in coastal regions of Mauritius using Raman Spectroscopy. Revista Matéria (Rio de Janeiro) 21/01, 157-168, 11688. DOI: 10.1590/S1517-707620160001.0014.

Svensson, D., Dueck, A., Nilsson, U., Olsson, S., Sanden, T., Lydmark, S., Jaegerwall, S., Pedersen, K. & Hansen, S. (2011): Alternative buffer material : Status of the ongoing laboratory investigation of reference materials and test package 1. Technical Report TR 11-06. Swedish Nuclear Fuel and Waste Management SKB, Stockholm.

Tanaka, K. (1975): Measurements of self-diffusion coefficients of water in pure water and in aqueous electrolyte solutions. Journal of the Chemical Society, Faraday Transactions 1: Physical Chemistry in Condensed Phases 71/0, 1127-1131. DOI: 10.1039/F19757101127.

Thoenen, T., Hummel, W., Berner, U. & Curti, E. (2014): The PSI/Nagra chemical thermodynamic database 12/07. Nagra Arbeitsbericht NAB 14-49.

Tomonaga, Y., Giroud, N., Brennwald, M.S., Horstmann, E., Diomidis, N., Kipfer, R. & Wersin, P. (2019): On-line monitoring of the gas composition in the Full-scale Emplacement experiment at Mont Terri (Switzerland). Applied Geochemistry 100, 234-243. DOI: 10.1016/j.apgeochem.2018.11.015.

Torres, E., Turrero, M.J., Moreno, D., Sánchez, L. & Garralón, A. (2017): FEBEX in-situ test: Preliminary results of the geochemical characterization of the metal/bentonite interface. 15th Water-Rock Interaction International Symposium. Procedia Earth and Planetary Science 17/WRI-15, 802-805. DOI: 10.1016/j.proeps.2017.01.045.

Tournassat, C. & Steefel, C.I. (2015): Ionic transport in nano-porous clays with consideration of electrostatic effects. Reviews in Mineralogy & Geochemistry 80/1, 287-329. DOI: 10.2138/rmg.2015.80.09.

Tournassat, C. & Steefel, C.I. (2019): Reactive transport modeling of coupled processes in nanoporous media. Reviews in Mineralogy and Geochemistry 85/1, 75-109. DOI: 10.2138/rmg.2019.85.4.

Tournassat, C. & Steefel, C.I. (2021): Modeling diffusion processes in the presence of a diffuse layer at charged mineral surfaces: a benchmark exercise. Computational Geosciences 25/4, 1319-1336. DOI: 10.1007/s10596-019-09845-4.

Tribet, M., Marques, C., Mougnaud, S., Broudic, V., Jegou, C. & Peuget, S. (2021): Alpha dose rate and decay dose impacts on the long-term alteration of HLW nuclear glasses. npj Materials Degradation 5/1, 36. DOI: 10.1038/s41529-021-00183-4.

Truche, L., Berger, G., Destrigneville, C., Pages, A., Guillaume, D., Giffaut, E. & Jacquot, E. (2009): Experimental reduction of aqueous sulphate by hydrogen under hydrothermal conditions: Implication for the nuclear waste storage. Geochimica et Cosmochimica Acta 73/16, 4824-4835. DOI: 10.1016/j.gca.2009.05.043.

Ueno, K., Suyama, T., Ishidera, T. & Sato, T. (2011): Ten-year interaction of carbon steel coupon and compacted bentonites. Clay Science 15/2, 89-102. DOI: 10.11362/ jcssjclayscience.15.2_89.

van Loon, L.R. & Glaus, M.A. (2008): Mechanical compaction of smectite clays increases ion exchange selectivity for Cesium. Environmental Science & Technology 42/5, 1600-1604. DOI: 10.1021/es702487m.

van Loon, L.R., Glaus, M.A. & Müller, W. (2007): Anion exclusion effects in compacted bentonites: Towards a better understanding of anion diffusion. Applied Geochemistry 22/11, 2536-2552. DOI: 10.1016/j.apgeochem.2007.07.008.

Villar, M.V. (2018): FEBEX-DP post-mortem THM/THG analysis report. Nagra Arbeitsbericht NAB 16-17 Rev.1.

Vinograd, V.L., Kulik, D.A., Brandt, F., Klinkenberg, M., Weber, J., Winkler, B. & Bosbach, D. (2018): Thermodynamics of the solid solution - Aqueous solution system (Ba,Sr,Ra)SO_4 + H_2O: I. The effect of strontium content on radium uptake by barite. Applied Geochemistry 89, 59-74. DOI: 10.1016/j.apgeochem.2017.11.009.

Vinsot, A., Leveau, F., Bouchet, A. & Arnould, A. (2014): Oxidation front and oxygen transfer in the fractured zone surrounding the Meuse/Haute-Marne URL drifts in the Callovian-Oxfordian argillaceous rock. *In:* Norris, S., Bruno, J., Cathelineau, M., Delage, P., Fairhurst, C., Gaucher, E.C., Höhn, E.H., Kalinichev, A., Lalieux, P. & Sellin, P. (eds.): Clays in Natural and Engineered Barriers for Radioactive Waste Confinement, vol. 400. Geological Society of London, 207-220.

Watson, C., Savage, D., Wilson, J., Benbow, S., Walker, C. & Norris, S. (2013): The Tournemire industrial analogue: reactive-transport modelling of a cement–clay interface. Clay Minerals 48/2, 167-184. DOI: 10.1180/claymin.2013.048.2.02.

Wersin, P., Curti, E. & Appelo, C. (2004): Modelling bentonite–water interactions at high solid/liquid ratios: swelling and diffuse double layer effects. Applied Clay Science 26/1, 249-257. DOI: 10.1016/j.clay.2003.12.010.

Wersin, P., Jenni, A. & Mäder, U.K. (2015): Interaction of corroding iron with bentonite in the ABM1 experiment at Äspö, Sweden: A microscopic approach. Clays and Clay Minerals 63/1, 51-68. DOI: 10.1346/CCMN.2015.0630105.

Wersin, P. & Kober, F. (2017): FEBEX-DP. Metal corrosion and iron-bentonite interaction studies. Nagra Arbeitsbericht NAB 16-16.

Whitney, G. (1990): Role of water in the smectite-to-illite reaction. Clays and Clay Minerals 38/4, 343-350.

Wilson, J., Bateman, K. & Tachi, Y. (2021): The impact of cement on argillaceous rocks in radioactive waste disposal systems: A review focusing on key processes and remaining issues. Applied Geochemistry 130, 104979. DOI: 10.1016/j.apgeochem.2021.104979.

Yariv, S. (1992): Wettability of clay minerals. *In:* Schrader, M.E. & Loeb, G.I. (eds.): Modern approaches to wettability: Theory and applications. Springer US, Boston, MA, 279-326.

Yokoyama, S., Shimbashi, M., Minato, D., Watanabe, Y., Jenni, A. & Mäder, U. (2021): Alteration of bentonite reacted with cementitious materials for 5 and 10 years in the Mont Terri Rock laboratory (CI Experiment). Minerals 11/3. DOI: 10.3390/min11030251.

App. A Estimation of bentonite alteration through Fe corrosion

The present method used to evaluate the potential extent of bentonite alteration induced via chemical interaction with a HLW disposal canister made of carbon steel differs fundamentally from that described in Bradbury et al. (2014) (Section 7.3, App. B in op. cit.). These authors carried out such an evaluation based on a mass balance approach that is now judged to be unrealistically conservative. Briefly, they postulated that the entire amount of Fe dissolved during canister corrosion (at a constant linear rate of 1 μm/a) is transferred to the bentonite buffer and reacts there by transforming the primary montmorillonite to an Fe-silicate (either berthierine or chamosite).

More realistically, in the updated model we take into account the fact that part of the dissolved Fe reprecipitates in-situ (i.e. within the HLW disposal canister) as an Fe-corrosion product (typically magnetite and siderite). Because the corrosion products are in permanent equilibrium with the porewater in the disposal canister, these solids fix the dissolved Fe concentration at the disposal canister/bentonite interface via saturation equilibria. The Fe concentration in the disposal canister environment under the conditions established in the HLW repository after canister failure is predicted to be 7.22×10^{-5} M (Tab. 9-1). In the Opalinus Clay, lower Fe concentration values are predicted, e.g. 2.56×10^{-5} M for the ZNO-NL reference Opalinus Clay porewater, see Tab. 7-3. In the present updated evaluation, these two values are used as boundary conditions to define a stationary concentration gradient for diffusion of Fe from the canister to the bentonite outer boundary, yielding a time-independent flux of Fe into the bentonite.

Considering the radial (cylindrical) geometry of the planned repository, the condition for stationary diffusion is given by:

$$\frac{\partial^2 C}{dr^2} + \frac{1}{r}\frac{\partial C}{dr} = 0 \qquad \text{(A-1)}$$

where C [mol m^{-3}] is the Fe concentration in solution, and r [m] is the radial distance from the centre of the repository drift axis. The general solution of eq. (A-1) is:

$$\frac{dC}{dr} = \frac{A}{r} \qquad \text{(A-2a)}$$

$$C(r) = A \ln r + B \qquad \text{(A-2b)}$$

A and B are integration constants that must be determined by setting appropriate boundary conditions. At the inner boundary, r_1 (HLW disposal canister/bentonite interface), we assume a constant Fe concentration C_1, leading to a constant Fe flux, J_1 [mol m^{-2} s^{-1}] into the bentonite. Applying this condition to eq. (A-2a) and using Fick's 1st law leads to:

$$A = -\frac{r_1\ J_1}{D_e} \qquad \text{(A-3)}$$

where D_e [m^2 s^{-1}] is the effective (sorption-independent) diffusion coefficient. The constant B is evaluated by setting a constant Fe concentration C_2 at the external boundary (bentonite/ host rock interface) and substituting in (A-2b):

$$B = C_2 - A \ln r_2 \qquad \text{(A-4)}$$

Inserting the integration constants (eqs. A-3 and A-4) into the general solutions (A-2a) and (A-2b) yields:

$$\frac{dC}{dr} = -\frac{r_1 J_1}{r\ D_e} \tag{A-5a}$$

$$C(r) = C_2 + \frac{r_1 J_1}{D_e} \ln\frac{r_2}{r} \tag{A-5b}$$

The solution of eq. (A-2a) at the inner boundary ($r=r_1$) is:

$$C_1 = C_2 + \frac{r_1 J_1}{D_e} \ln\frac{r_2}{r_1} \tag{A-6}$$

Rearranging and solving for J_1 yields the Fe flux at the canister/bentonite interface as a function of the geometric parameters, the effective diffusion coefficient and C_1, C_2, which represent the dissolved Fe concentrations inside the canister (buffered by equilibrium with magnetite and other Fe solids) and in the unaffected bentonite (BPW), respectively:

$$J_1 = \frac{D_e(C_1 - C_2)}{r_1 \ln(r_2/r_1)} \tag{A-7a}$$

The explicit solution for the concentration profile can then be obtained by inserting eq. (A-7a) into eq. (A-5b):

$$C(r) = C_2 + \ln(r_2/r) \ = \ C_2 + \frac{r_1}{D_e}\frac{D_e(C_1 - C_2)}{r_1 \ln(r_2/r_1)} \ln(r_2/r) = C_2 + (C_1 - \ C_2)\ \ln(r_1/r) \tag{A-7b}$$

Note that the steady-state concentration profile is only a function of geometry (radial positions of canister/bentonite and bentonite/OPA interface) and the assumed boundary concentrations. It is independent of the diffusion coefficient[33].

The total Fe release rate from a single canister (neglecting for simplicity the contribution from the base and the lid) is then given by:

$$F = 2\pi\, r_1\, L\, J_1 \tag{A-8}$$

where L is the canister length. In order to calculate the fraction of bentonite potentially altered as a function of time by conversion of montmorillonite to an Fe-silicate, one needs information on the moles of montmorillonite present in the buffer per canister, $n_{montpercan}$, and the molar amount of Fe fixed in the Fe-silicate per mole of metallic Fe released from the canister, $n_{montfesi}$. To ensure

[33] The lack of dependence of stationary concentration profile on the diffusion coefficient might at first sight seem contradictory. This is not the case: although the transient concentration profiles and fluxes will differ for two different effective diffusion coefficients (because due to Fick's 1st law fluxes are proportional to D_e) *eventually* the concentration profiles will be equal once steady state is achieved. Of course, the time needed to reach stationary diffusion will differ for the two D_e values.

comparability with the earlier estimations, the aforementioned parameters were kept equal to those reported for spent fuel in Bradbury et al. (2014) (see Tab. B1 and text in op. cit.). The percentage *P(%)* of bentonite altered at a given time *t* with the present diffusion model is then:

$$P(\%) = \frac{100\,Ft}{n_{montfesi}\,n_{montpercan}} \tag{A-9}$$

All parameter values used to apply the present estimation model are listed in Tab. A-1.

Fig. A-1 shows the stationary concentration profiles of Fe calculated with eq. A-5b using the "best estimate" and "conservative estimate" parameter sets of Tab. A-1. The net flux of dissolved Fe into bentonite is proportional to the concentration gradient at the canister/bentonite interface (r = 0.625 m).

Tab. A-1: Parameters used in the model for estimating the release of Fe into the bentonite buffer

Parameter	**Symbol / units**	**Realistic estimate**	**Conservative estimate**
Effective diffusion coefficient	D_e [m^2s^{-1}]	7×10^{-11}	3×10^{-10}
Fe concentration at the bentonite/OPA interface*	C_2 [M]	2.56×10^{-5}	7.14×10^{-6}
Fe concentration at the canister/bentonite interface	C_1 [M]	7.22×10^{-5}	
Radial position at canister/bentonite interface	r_1 [m]	0.625	
Radial position at bentonite/OPA interface	r_2 [m]	1.25	
Canister length (spent fuel)	L [m]	5.35	
Moles of montmorillonite per canister	$n_{montpercan}$	129,400	
Moles of Fe fixed to berthierine per mole of montmorillonite consumed	$n_{montfesi}$	1.4	

* The quoted Fe concentrations come from the waters denoted E3-OPW-Ref and E3-OPW_lowpCO2 in Tab. 7-3.

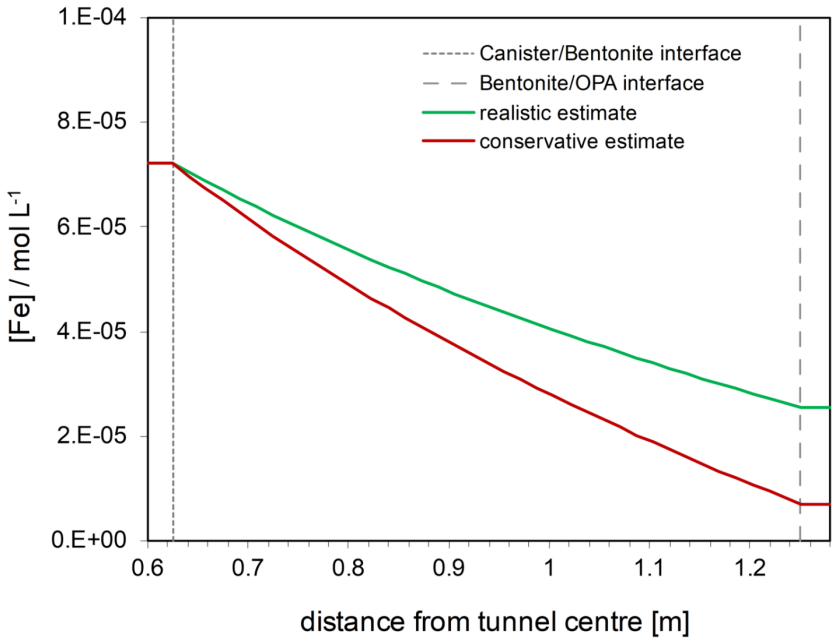

Fig. A-1: Steady-state Fe concentration profiles calculated from eq. A-5b using the parameters of Tab. A-1

Using the parameters listed in Tab. A-1 and applying eqs. A-7a, A-8 and A-9, the percentages of bentonite affected by Fe alteration were calculated at different times for two cases: a realistic estimate based on reference values for diffusion coefficient and Fe concentration at the outer bentonite boundary, and a conservative case based on pessimistic values for both parameters. The results (Tab. A-2) indicate that, even in the worst case, at least 80% of the bentonite would remain unaffected by Fe alteration after 1,000,000 years. Applying the realistic estimate parameters, less than 3% of the bentonite would be affected.

Tab. A-2: Calculated percentages, *P(%)*, of bentonite altered as berthierine at different repository evolution times, assuming steady-state supply of dissolved Fe(II) from the canister according to the parameters listed in Tab. A-1

Time*	**Realistic estimate**	**Conservative**
10,000 a	0.03	0.16
100,000 a	0.3	1.7
1,000,000 a	2.8	16.5

* Time since start of canister corrosion (around the time of completion of the bentonite saturation)

App. B Assessment of the likelihood of bentonite intrusion into the HLW disposal canister

One issue that has not been thoroughly investigated so far is whether bentonite could penetrate the cavities inside a HLW disposal canister following failure. Although this is a more a rock-mechanical and rheological question rather than a geochemical one, the answer has direct consequences for the chemical environment at the waste/canister interface. If bentonite from the buffer were to intrude into the inner side of the canister, it could affect chemical equilibria, e.g. via cation exchange reactions with the intruded clay. Additionally, the presence of clay in direct contact with RP-HLW could impact its dissolution kinetics and thus radionuclide release rates.

To address the issue of bentonite intrusion, we apply the "bentonite erosion" model developed for SKB by Birgersson et al. (2009). Although this model was originally intended to predict the loss of bentonite buffer material and colloids to intersecting water-filled fractures at its external boundary, the formalism dealing with bentonite swelling (op. cit., Section 3.9) may be adapted to predict bentonite intrusion into HLW disposal canister cavities.

After sealing and resaturation, the bentonite will exert a swelling pressure on the drift and canister surfaces. The magnitude of the swelling pressure will depend on several factors, such as the type (Na- or Ca-dominated) and dry density of the compacted bentonite. If the canister fails via formation of a fissure transecting the canister, constant volume conditions in the buffer are locally relaxed, and there will be a tendency for the bentonite to penetrate the fissure and eventually enter the empty space inside it due to the pressure gradient imposed by the swelling pressure.

Saturated and confined compacted bentonite has mechanical properties that are intermediate between a gel and a hard rock, with shear strengths in the order of a few kPa providing a strong internal frictional resistance to flow. The fissure surfaces will provide additional frictional resistance. Birgersson et al. (2009) calculate the equilibrium between the swelling pressure inside the fissure (which decreases with increasing distance from the origin of the fissure at the bentonite side) and the opposing frictional forces using following equation (eq. 3-4 in op. cit.):

$$\sigma(r) = \sigma_1 exp[-2 \tan\Phi \cdot (r/a)] \qquad \text{(B-1)}$$

where:

r = distance from the origin of the fissure[34] [m]
$\sigma(r)$ = swelling pressure at distance r [Pa]
σ_1 = swelling pressure in confined saturated bentonite [Pa]
Φ = friction angle [-]
a = fissure aperture [m]

[34] In the original model, fissures originate at the external bentonite boundary and propagate into the host rock. In the present adaptation of the model, the fissures originate at the HLW disposal canister/bentonite interface and propagate into the canister cavities.

Fig. B-1 depicts a disposal canister containing RP-HLW embedded in bentonite, along with a fissure intersecting the canister, through which bentonite has intruded. The enlarged detail highlights the aperture a and r-coordinate involved in equation (B-1). The frictional angle is an empirical parameter derived from the effective stress theory that is not related to the geometry of the system. It must be fitted to experimental data and is the angle defined in linear plots of shear stress versus normal stress applied to a material sample.

For the modelling, we used a conservative value of 10° for the frictional angle, as suggested by Birgersson et al. (2009) for compacted bentonite. This value is lower than what is typically found for clays and thus maximises the calculated penetration depths into the modelled fissure.

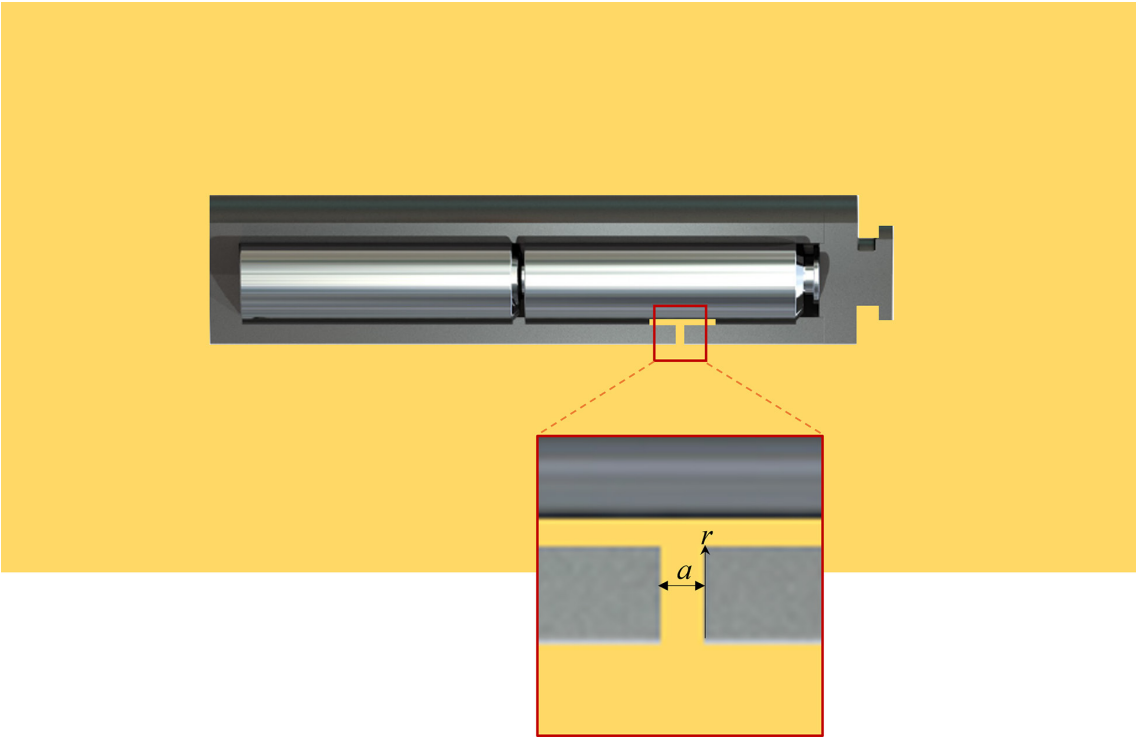

Fig. B-1: Intrusion of saturated bentonite into a HLW canister containing two vitrified waste forms. The enlargement shows the definitions of aperture *a* and *r*-coordinate used in eq. (B-1)

The swelling pressure in the confined bentonite buffer (σ_1) was estimated with the help of the experimental data on swelling pressure for MX-80 bentonite provided by Bucher & Spiegel (1984), reproduced below in Fig. B-2. For the reference dry density of 1,450 kg m^{-3}, we extrapolated 70 bar, which turns out to be identical to the value used by Birgersson et al. (2009). To obtain the estimate, we chose the midpoint between the two bands shown in Fig. B-2. Assuming a hydrostatic pressure gradient of 9.81 bar/100 m depth, it would correspond to the hydrostatic pressure at a repository depth of about 700 m.

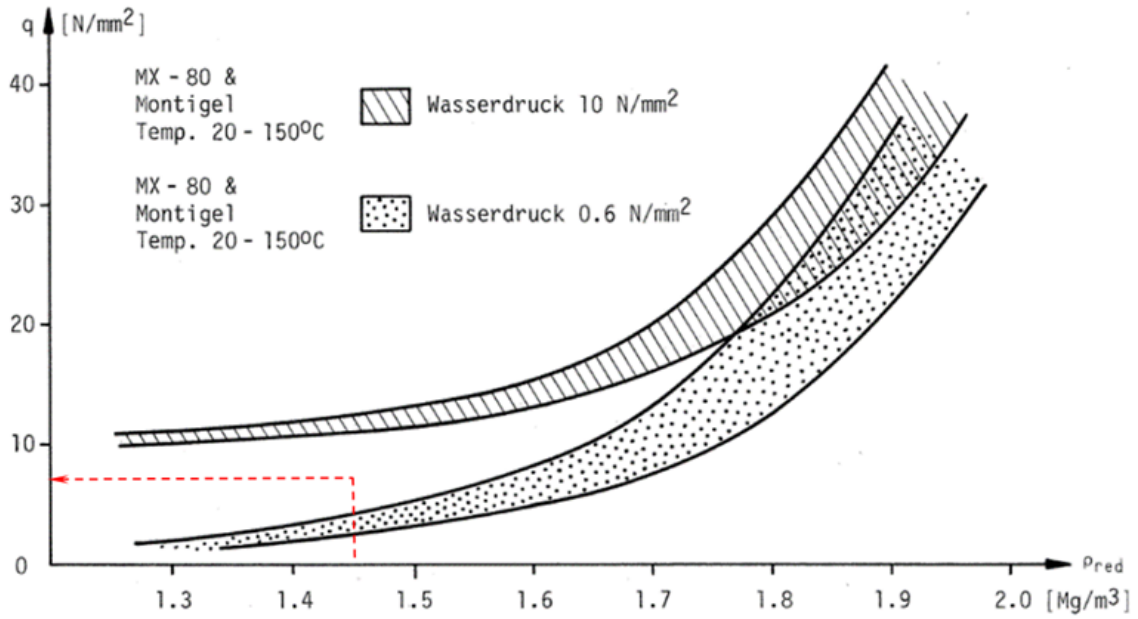

Fig. B-2: Reproduction of Fig. I from Bucher & Spiegel (1984), used to estimate the swelling pressure in confined, saturated MX-80 bentonite subject to a hydrostatic pressure at about 500 m depth

The red broken line shows the extrapolated swelling pressure used in the present calculation.

Taking, as done by Birgersson et al. (2009), a limit of 10 Pa (0.1 mbar) as the equilibrium position where swelling is counterbalanced by the opposing frictional forces, we obtain penetration distances as a function of fissure aperture as indicated in the "70 bar" column of Tab. B-1.

Tab. B-1: Calculated penetration depths of bentonite into a canister fissure using the model of Birgersson et al. (2009)

	Penetration depth [cm]	
Fissure aperture (mm)	$P_{hyd} = P_{sw} = 70$ bar	$P_{hyd} = P_{sw} = 140$ bar
0.1	0.4	0.4
0.5	1.6	1.7
1	3.2	3.4
2	6.3	6.8
5	15.8	16.9
10	38	40

Fig. B-3 shows in graphical form the calculated swelling pressure distributions inside the fissure as a function of fissure aperture (mm) for the latter case. Doubling the pressure, which corresponds to a hydrostatic pressure at about 1,400 m depth, thus covering the reference depth of ~ 900 m for a repository sited at the Haberstal, has only a minor effect on the calculated penetration depths. The results show that only in the case of fissure apertures larger than 5 mm is intrusion of bentonite into the inside cavities of the fissured canister possible, considering the provisional design of the HLW disposal canister made of carbon-steel (thicknesses of 15 – 18 cm, Nagra 2024b). Such large apertures are quite unrealistic, because they will tend to close due to the compressive stress provided by the swelling pressure of bentonite. Thin cracks of less than 1 mm are more realistic. Moreover, soon after fissure formation, HLW disposal canister corrosion products (mainly Fe oxy-hydroxides) will tend to fill and seal the aperture because of their large molar volume. The abovementioned results seem to be confirmed by the limited penetration depth of bentonite through a perforated liner, observed in the FEBEX experiment (Kober et al. 2017).

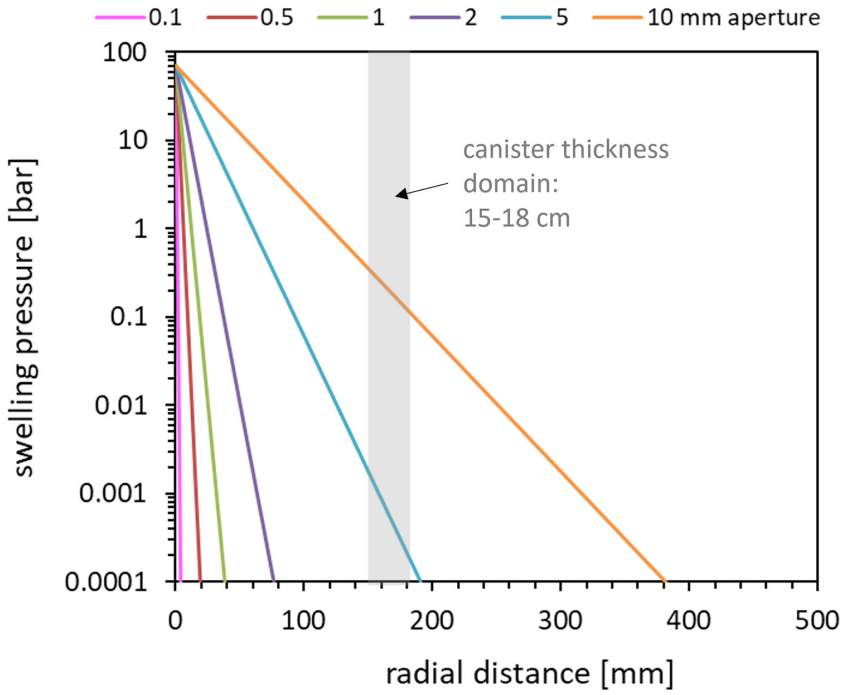

Fig. B-3: Swelling pressure distributions calculated inside a canister fissure as a function of penetration depth (radial distance) for selected fissure apertures at 70 bar swelling pressure

Bentonite intrusion into the canister cavity is predicted only for lines intersecting the shaded canister thickness domain, i.e. for fissure apertures exceeding about 5 mm.

App. C Comparison of preliminary and finalised Opalinus Clay porewaters

One issue addressed in Section 4.6 regards the use of *preliminary* compositions of Opalinus Clay porewaters (OPAw) as reacting solutions for the calculation of bentonite porewaters (BPW), instead of using the *definitive* compositions as documented in Mäder & Wersin (2023). This situation arises because the BPW calculations presented in this report were carried out during Nagra's borehole drilling campaign, at a time when the aqueous data available from borehole samples were not yet complete.

A comparison of the preliminary OPAw used for the present BPW calculations with the corresponding finalised OPAw is given below in Tab. C-1. Inspection of the table shows that, with the notable exception of the Fe concentration, the differences in pH, pe, ionic strength and total element concentrations are negligible. Overall, it can be anticipated that there is no significant impact on the results of BPW calculations when using either preliminary or final OPAw.

The one order of magnitude difference in Fe concentration (see numbers in bold) can be ascribed to different assumptions made on the selected Fe minerals controlling dissolved Fe at equilibrium. While magnetite was selected as equilibrium phase by Curti (2023), leading to its precipitation, in the OPAw calculations of Mäder & Wersin (2023) magnetite was considered to be metastable (the final solution is oversaturated). Details on this issue can be found in App. C of Curti (2023). The rationale for considering magnetite as an equilibrium phase in the present calculations is the expectation that anaerobic corrosion of the steel present in canister and drift support structures should produce magnetite as the main product of anaerobic corrosion. Formation of magnetite under such conditions at repository-relevant temperatures has been amply documented in laboratory and underground experiments (see Chapter 8), therefore it seemed reasonable to include it as equilibrium phase.

Tab. C-1: Preliminary OPAw used as input for the BPW calculations described in this report compared to the corresponding final OPAw

GEMS. ID Nagra ID	**OPAw_NL-ZNO-28** E3-OPW_lowpCO2		**OPAw_NL-ZNO-22** E3-OPW-Ref		**OPAw_NL-ZNO-18** E3-OPW_highpCO2	
	Preliminary[1]	Final[2]	Preliminary[1]	Final[2]	Preliminary[1]	Final[2]
log $p(CO_2)$/bar	-2.8	-2.8	-2.2	-2.2	-1.8	-1.8
pH	7.40	7.37	7.10	7.07	6.90	6.87
pe	-3.22	-3.10	-2.83	-2.76	-2.58	-2.53
Eh	-0.190		-0.167		-0.152	
IS /m	0.317	0.323	0.319	0.324	0.321	0.326
Al	2.13×10^{-8}	2.00×10^{-8}	2.09×10^{-8}	2.00×10^{-8}	2.86×10^{-8}	2.70×10^{-8}
Ba	1.56×10^{-7}	1.60×10^{-7}	1.57×10^{-7}	1.60×10^{-7}	1.58×10^{-7}	1.60×10^{-7}
C(IV)	1.07×10^{-3}	1.01×10^{-3}	2.21×10^{-3}	2.11×10^{-3}	3.68×10^{-3}	3.52×10^{-3}
Ca	2.01×10^{-2}	2.62×10^{-2}	2.03×10^{-2}	2.65×10^{-2}	2.05×10^{-2}	2.68×10^{-2}
Cl	0.239	0.240	0.240	0.240	0.241	0.240
F	1.74×10^{-4}	1.60×10^{-4}	1.74×10^{-4}	1.60×10^{-4}	1.74×10^{-4}	1.60×10^{-4}
Fe	**7.14×10^{-6}**	**1.00×10^{-4}**	**2.56×10^{-5}**	**1.00×10^{-4}**	**5.95×10^{-5}**	**1.00×10^{-4}**
K	2.13×10^{-3}	1.15×10^{-3}	2.13×10^{-3}	1.16×10^{-3}	2.14×10^{-3}	1.16×10^{-3}
Mg	1.43×10^{-2}	1.55×10^{-2}	1.45×10^{-2}	1.56×10^{-2}	1.46×10^{-2}	1.58×10^{-2}
Mn	8.16×10^{-5}	9.70×10^{-5}	8.24×10^{-5}	9.80×10^{-5}	8.33×10^{-5}	9.90×10^{-5}
Na	0.215	0.202	0.215	0.202	0.216	0.203
S(VI)	2.29×10^{-2}	2.34×10^{-2}	2.29×10^{-2}	2.34×10^{-2}	2.29×10^{-2}	2.34×10^{-2}
Si	1.73×10^{-4}	1.70×10^{-4}	1.72×10^{-4}	1.70×10^{-4}	1.72×10^{-4}	1.70×10^{-4}
Sr	3.67×10^{-4}	3.80×10^{-4}	3.70×10^{-4}	3.80×10^{-4}	3.73×10^{-4}	3.80×10^{-4}

[1] Tab. 7-3 in this report or Tab. 4-1 in Curti (2023); [2] Tab. 5-5 in Mäder & Wersin (2023)